

Modelling and simulations of single-molecule sensing supramolecular structure

Natthiti Chiangraeng^{1,2}, Haruyuki Nakano³, Piyarat Nimmanpipug^{1,2}, Norio Yoshida⁴

¹ Department of Chemistry, Faculty of Science, Chiang Mai University, Chiang Mai 50200, Thailand

² Materials Science Research Center, Faculty of Science, Chiang Mai University, 239 Huay Kaew Road, Suthep, Muang, Chiang Mai, 50200, Thailand

³ Department of Chemistry, Graduate School of Science, Kyushu University, 744 Motooka, Nishi-ku, Fukuoka 819-0395, Japan

⁴ Department of Complex Systems Science, Graduate School of Informatics, Nagoya University, Chikusa-ku, Nagoya 464-8601, Japan

Corresponding Author's E-mail: natthiti_c@cmu.ac.th

Abstract

A combination of molecular dynamics (MD) simulations and three-dimensional reference interaction site model (3D-RISM) calculations can provide the solvation properties of host and guest molecules. In this study, glycine, tryptophan, phenylalanine and their derivatives were employed as representatives of guest molecules, while cucurbiturils (CBs) of different sizes were used as host molecules. We found that the glycine or guest 1 can bind with the CB in different binding modes including inclusion and exclusion binding modes. The CB7-1 and CB8-1 complexes also provide the unbound state. Moreover, the unbound state of glycine is pointed out.

Objectives

- To investigate the complexation process of amino acids with CBs in detail as well as the influences of surrounding environments in the aqueous solution
- To propose a method to investigate the CB-guest complex in order to design the complex with a high-binding affinity for specific applications.

Introduction

- The study of molecular recognition of amino acids via supramolecular host-guest chemistry is an essential and challenging task for molecular sensing of biomolecule and disease diagnostic fields.
- The understanding the nature interactions between host CBs and amino acid-based guests would contribute to a fascinating concept to improve the sensitivity and selectivity of the molecular sensors.

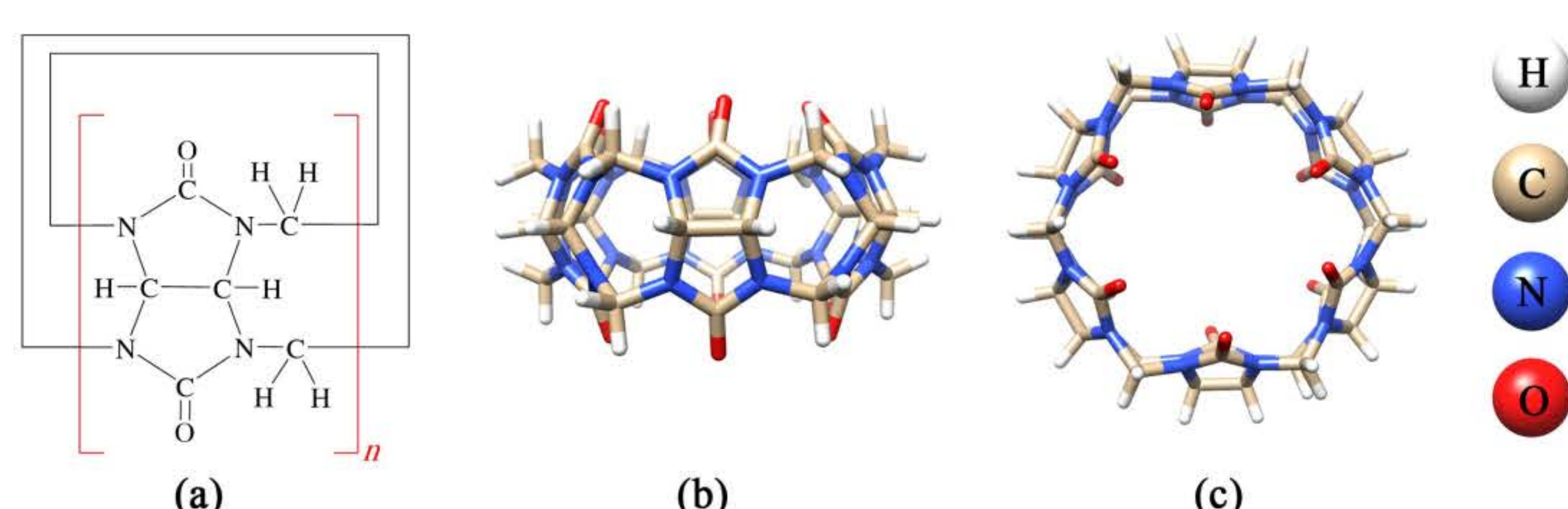


Fig. 1 (a) Chemical structures of cucurbituril, where n is number of glycoluril units of 6-8. (b) and (c) depict the side and top views of CB6 as examples.

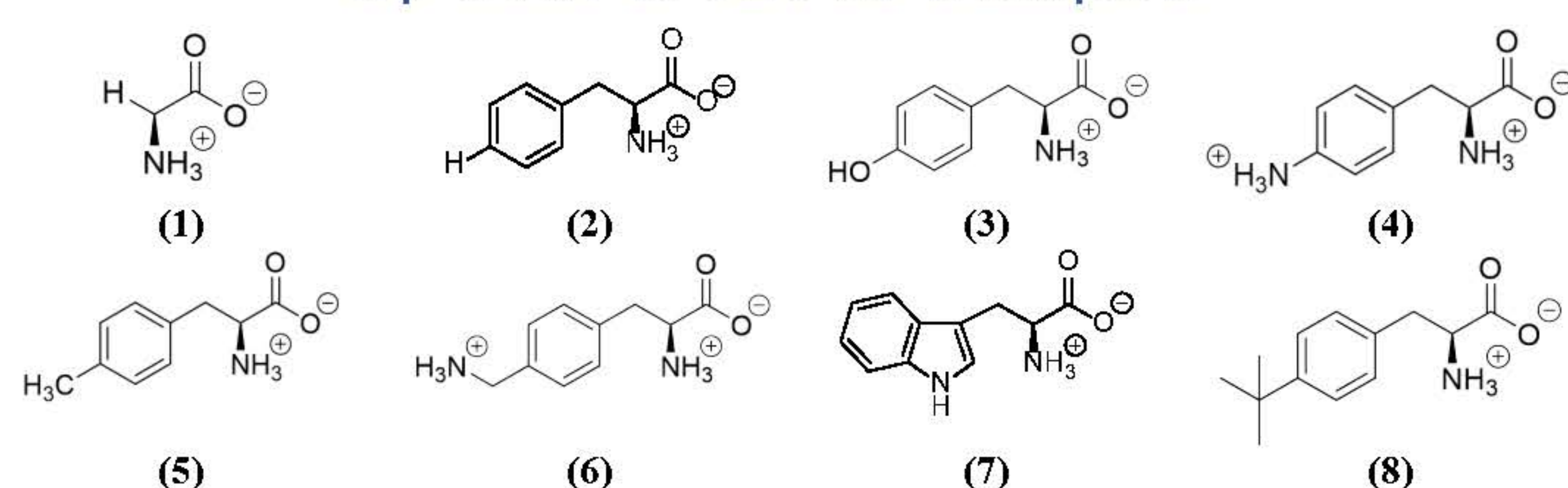
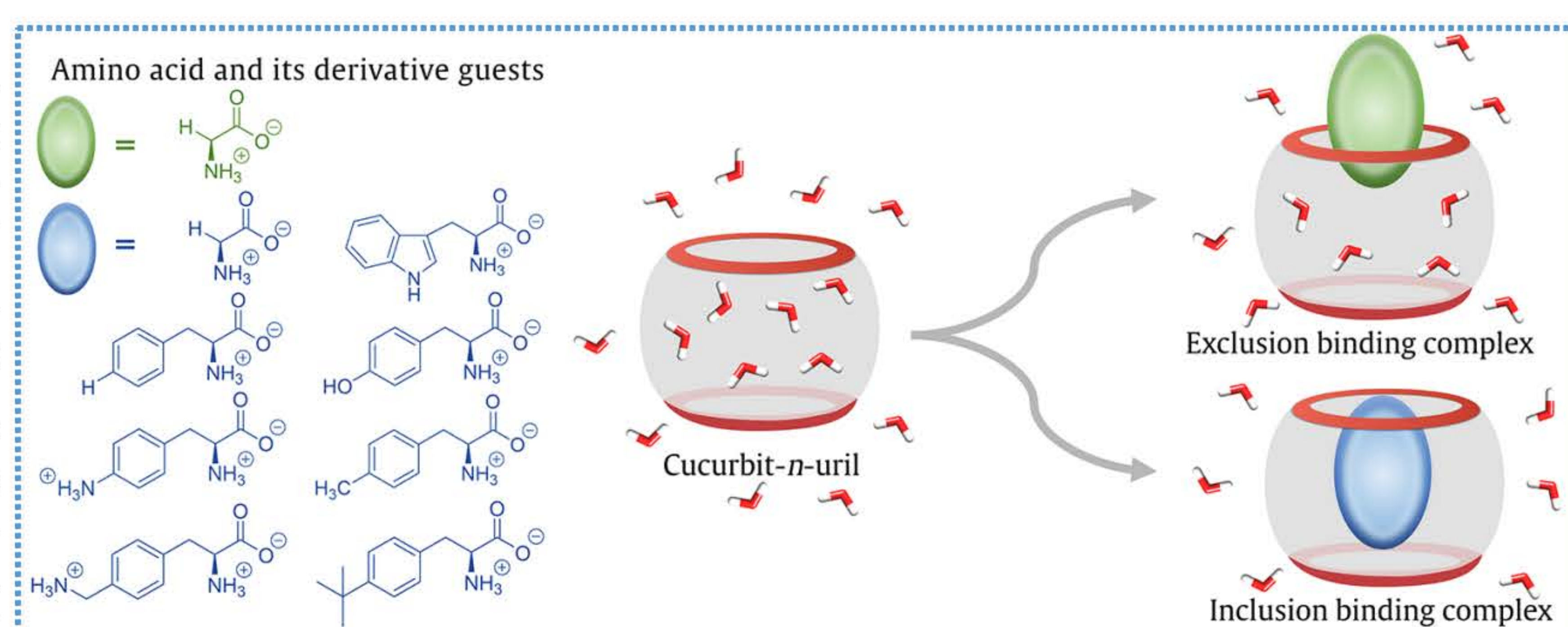


Fig. 2 Chemical structures of guest molecules and corresponding abbreviations were used in this work.



Results

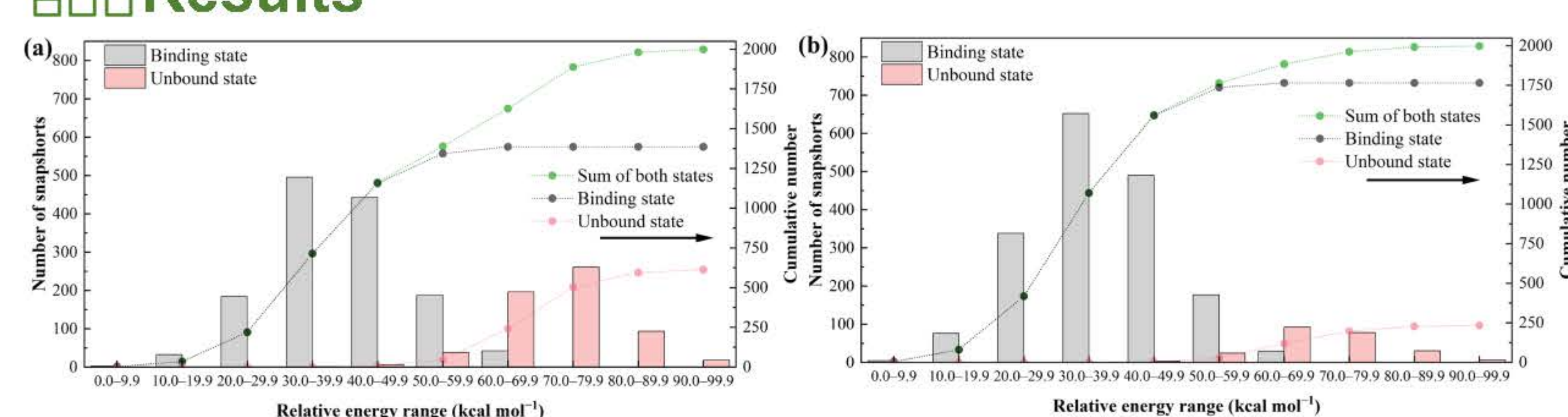


Fig. 3 Number of snapshots in each energy range and its cumulative number: (a) CB7-1 and (b) CB8-1 complexes. These 2000 snapshots were sampled from the last 1 μ s of MD simulations. The axis of abscissa is depicted as the relative energy of a complex.

The unbound states of CB7-1 and (b) CB8-1 complexes have relatively high energy compared with binding state indicating that the binding state is more stable than unbound state.

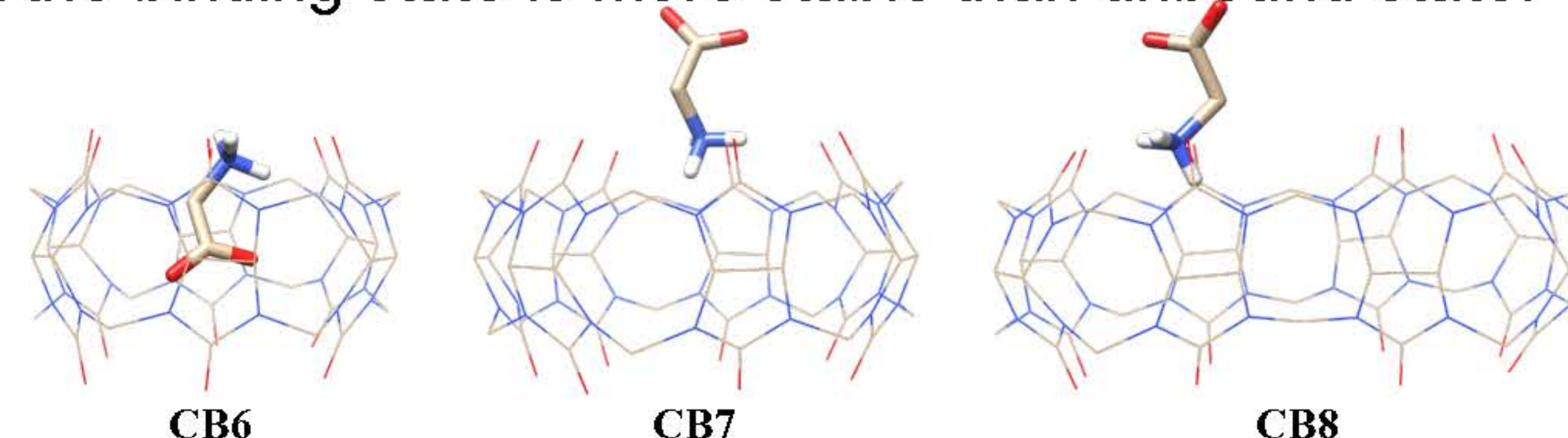


Fig. 4 Snapshots of binding states for CBn-1 complexes.

The guest 1 that is the smallest guest in this study also provided inclusion and exclusion binding complexes.

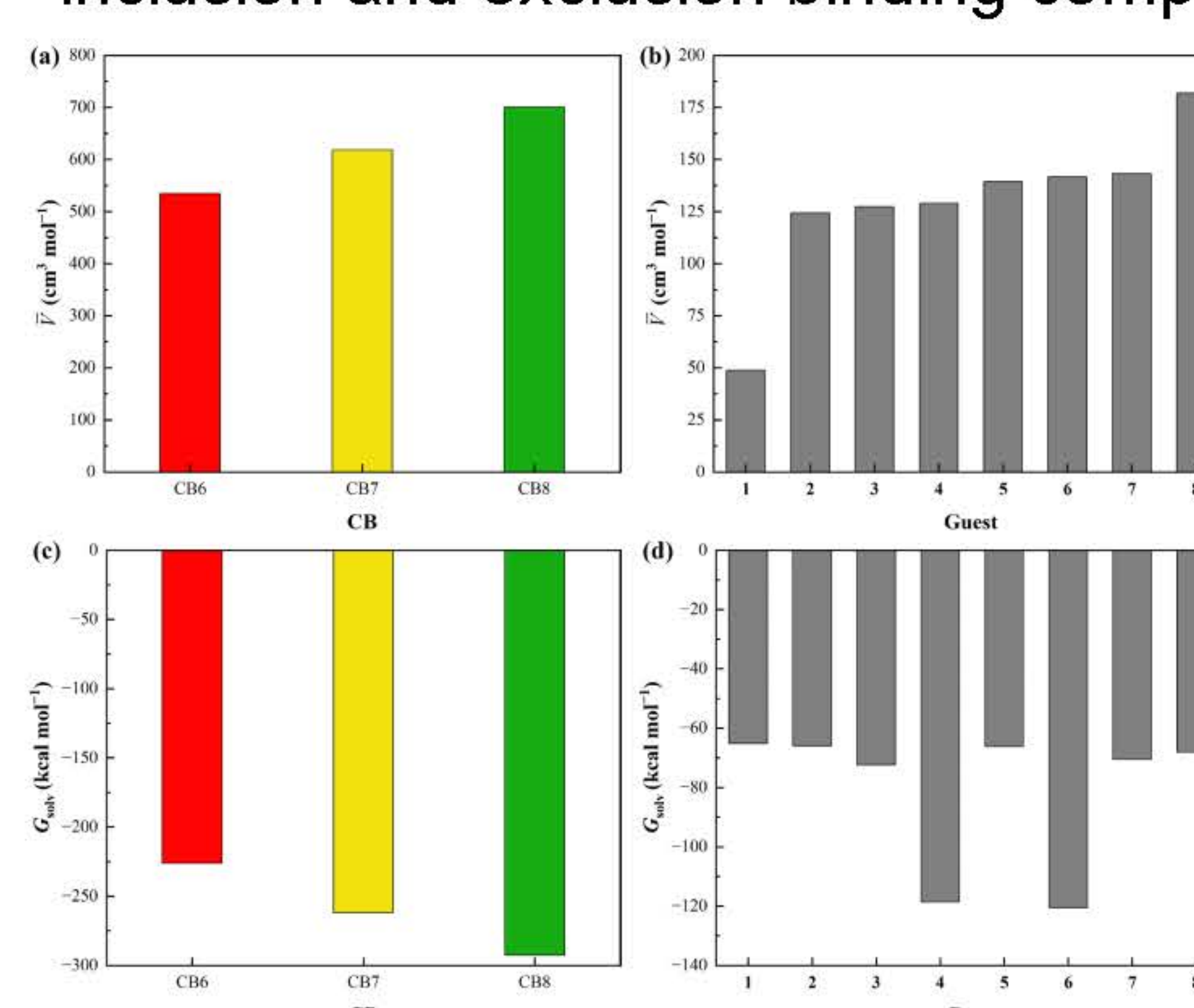


Fig. 5 Partial molar volume (\bar{V}) and solvation free energy (G_{solv}) of (a, c) CBs and (b, d) guests, respectively.

The molecular volume of CBs and guest molecules are reasonable because the relatively large molecular size provide the large value in molecular volume.

Conclusions

- Computational calculations can provide the solvation properties of host and guest molecules.
- The inclusion and exclusion binding modes can be observed from the smallest guest.
- The CB7-1 and CB8-1 complexes also provide the unbound state.

References

- N. Yoshida, *IOP Conf. Ser. Mater. Sci. Eng.*, **2020**, 773, 012062.
- N. Chiangraeng, H. Nakano, P. Nimmanpipug and N. Yoshida, *J. Phys. Chem. B*, **2023**, 127, 3651–3662.

Acknowledgements

This research has received funding support from the NSRF via the Program Management Unit for Human Resources & Institutional Development, Research and Innovation [grant number B13F660056]. The head of the project is Assoc. Prof. Dr. Pisith Singjai.



BRAINPOWER
CONGRESS 2023

ร่วมกันสร้างและขับเคลื่อนงานวิจัยชั้นนำ
สู่อุตสาหกรรมแห่งอนาคต



Study of Quantum Confinement Effect of AlN Thin Film for Application in jewelry industry

Chalermopol Rudradawong ^a, Aparporn Sakulkalavek ^a, Worawat Meevasana ^b

^a Department of Physics, School of Science, King Mongkut's Institute of Technology Ladkrabang, Bangkok, 10520, Thailand

^b School of Physics, Suranaree University of Technology, 111 University Ave., Nakhon Ratchasima, 30000, Thailand

Introduction

Thailand is one of the world's most prominent centers for silver jewelry. The silver products are systematically developed from a cottage industry to a large-scale and export-oriented commerce, generating nearly \$60,000 million in exports. Silver naturally tarnishes in the atmosphere due to sulphur, oxides or carbonates. Tarnishing of the silver forms black or dark grey color as layer or spot on surface. This reduces the optical properties such as reflectivity of silver. The tarnishing of silver is important problem in the industry as well as to the end users of the silver products. In this work, we provide a method for preventing tarnishing of silver with AlN passivation using physical vapor deposition (PVD). The thickness of the coating is adjusted by varying time sputtering. The AlN coating serves resistant to sulphur.

Methods

AlN coating by DC magnetron sputtering

Sandpaper polishing → DI, acetone, methanol ultrasonic cleaner → Drying → Sputtering

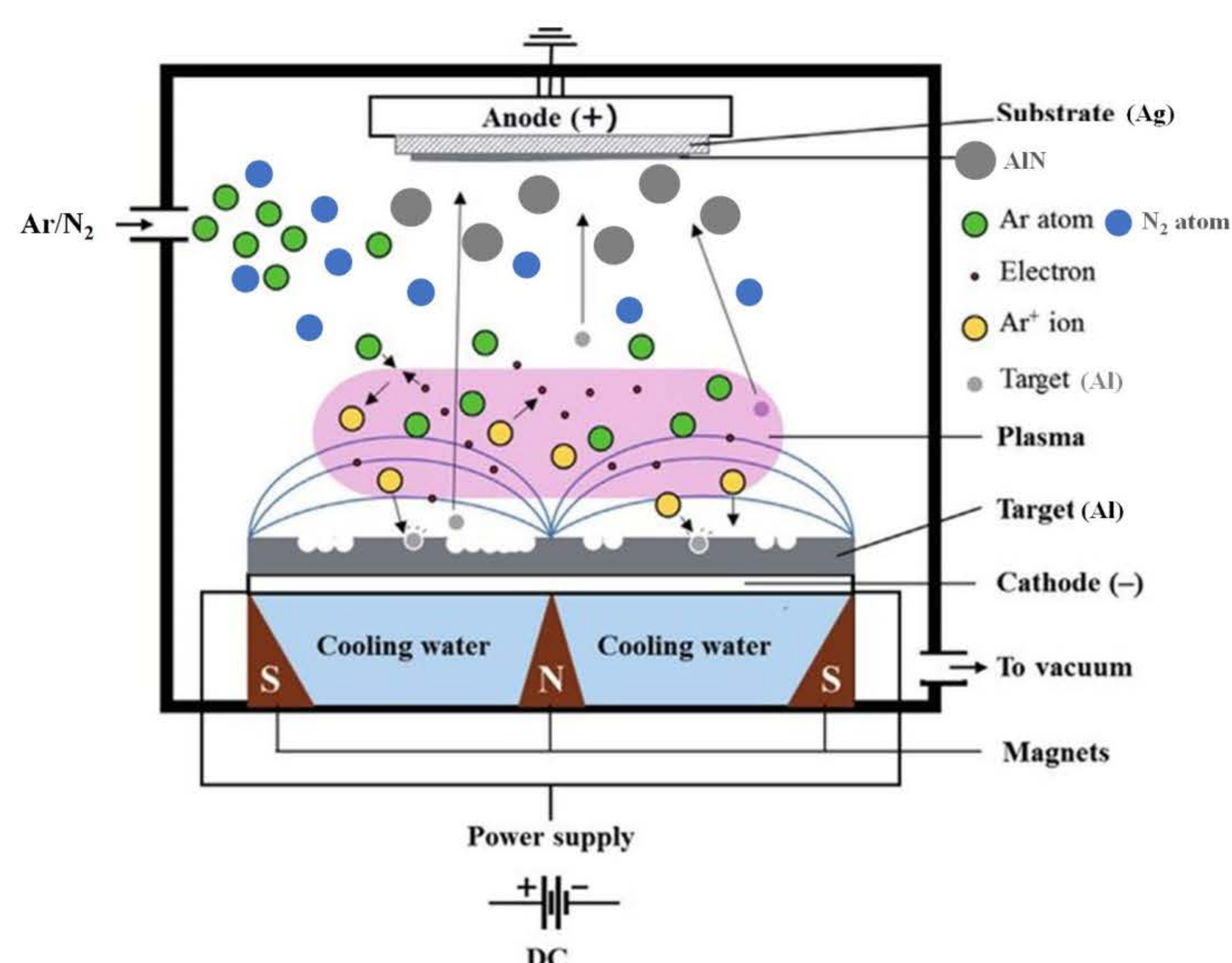


Fig 1 Diagram of DC magnetron sputtering process.

Sputtering parameters	Conditions
Based pressure	8.0×10^{-3} Pa
Ar flow rate	30 sccm
N ₂	20 sccm
Current	3 A
Temperature	60 °C
Rotational speed	15 rpm
Sputtering time	50 - 100 min

Acknowledgements

This research has received funding support from the NSRF via the Program Management Unit for Human Resources & Institutional Development, Research and Innovation [grant number B13F660057]

Results & Discussion

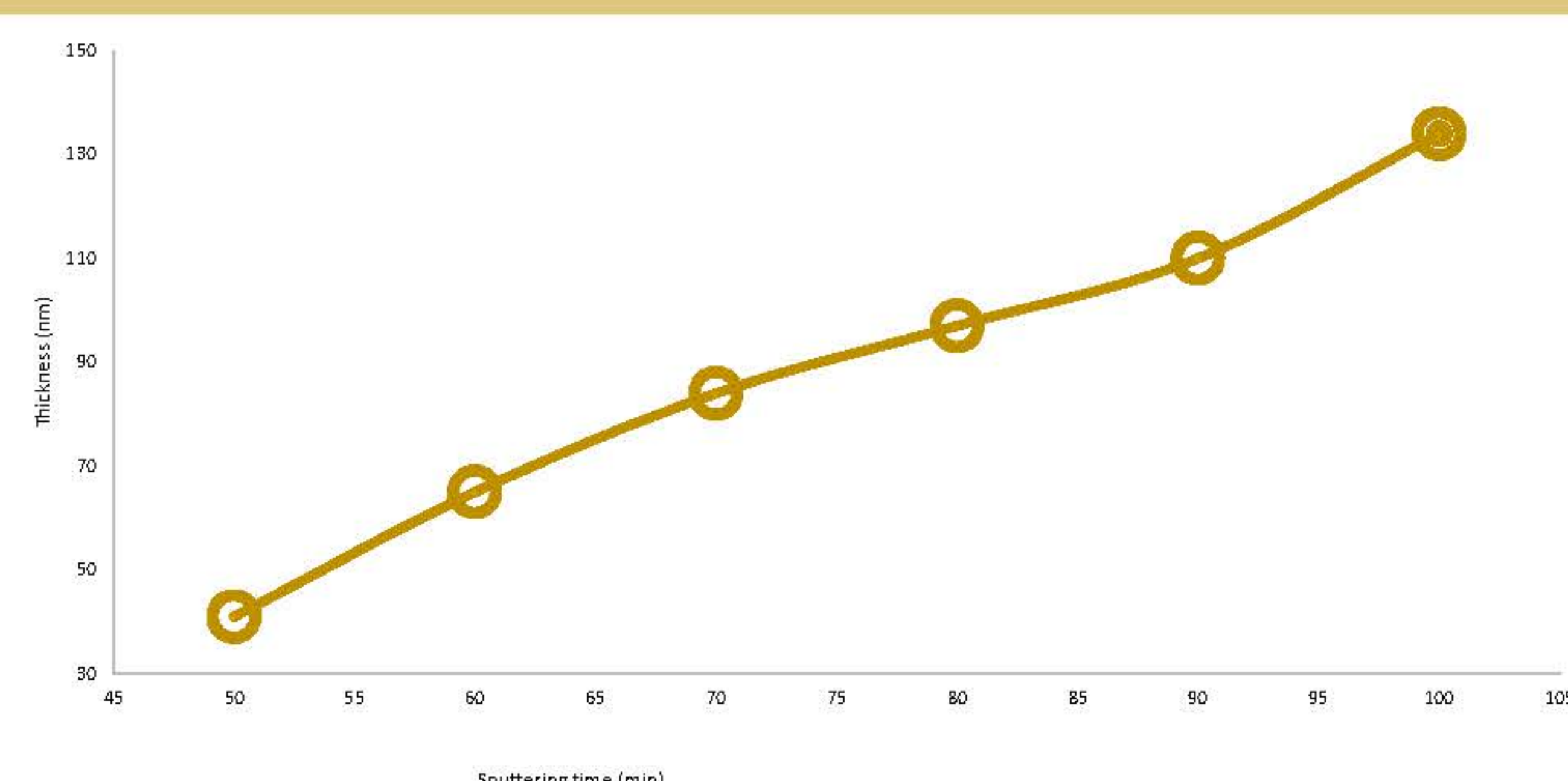


Fig 2 Thickness of AlN with sputtering time from 50-100 min .

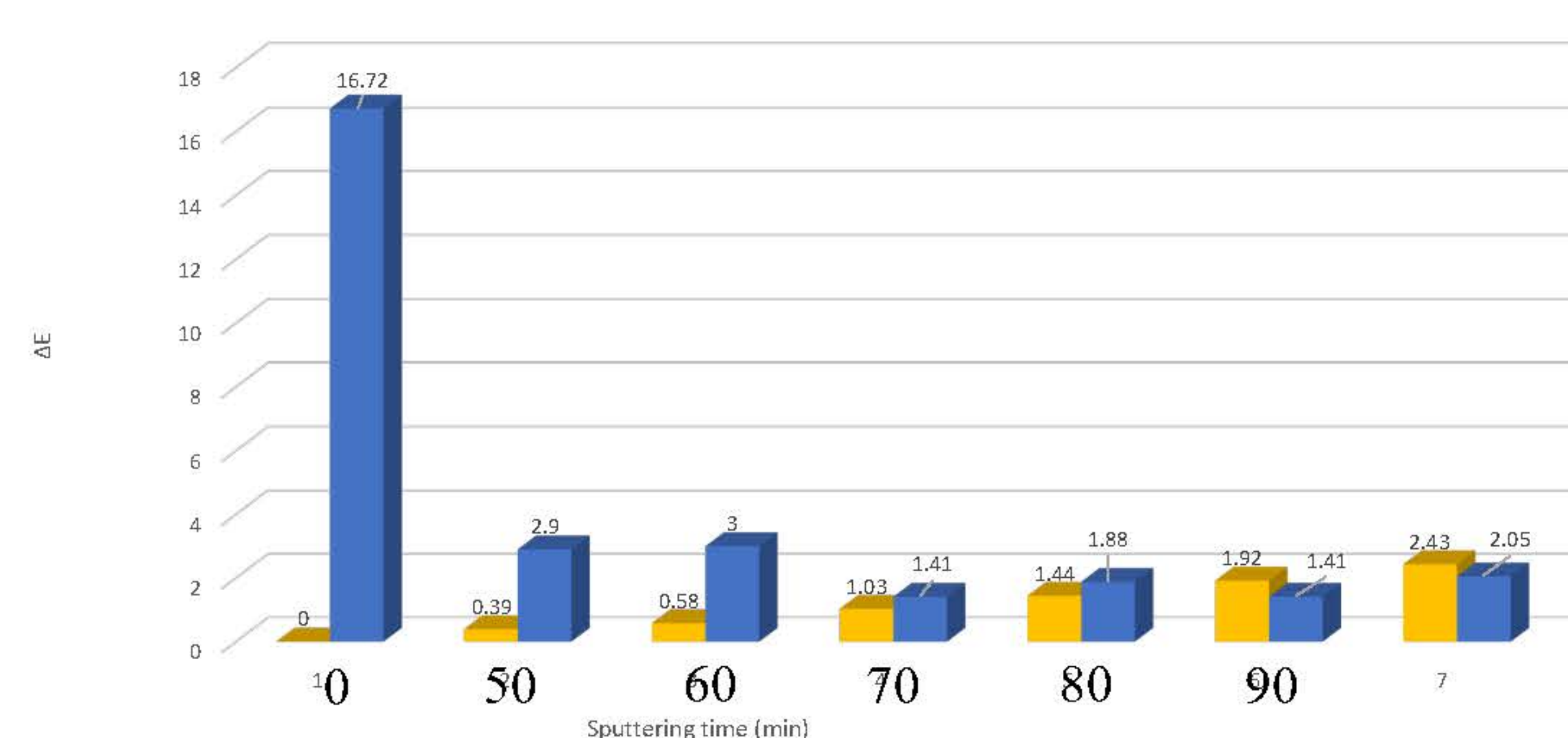


Fig 3 ΔE of Ag plate samples after AlN coating as 1 and 60 days with sputtering time from 50-100 min.

ΔE^* (Total Color Difference) is calculated based on delta L*, a*, b* color differences and represents quantifying the overall color difference between a sample and standard color

$$\Delta E = \sqrt{(\Delta L^*)^2 + (\Delta a^*)^2 + (\Delta b^*)^2}$$

ΔL^* represents a lightness difference between sample and standard colors.

Δa^* represents a redness or greenness difference between sample and standard colors.

Δb^* represents blueness-yellowness difference between sample and standard colors.

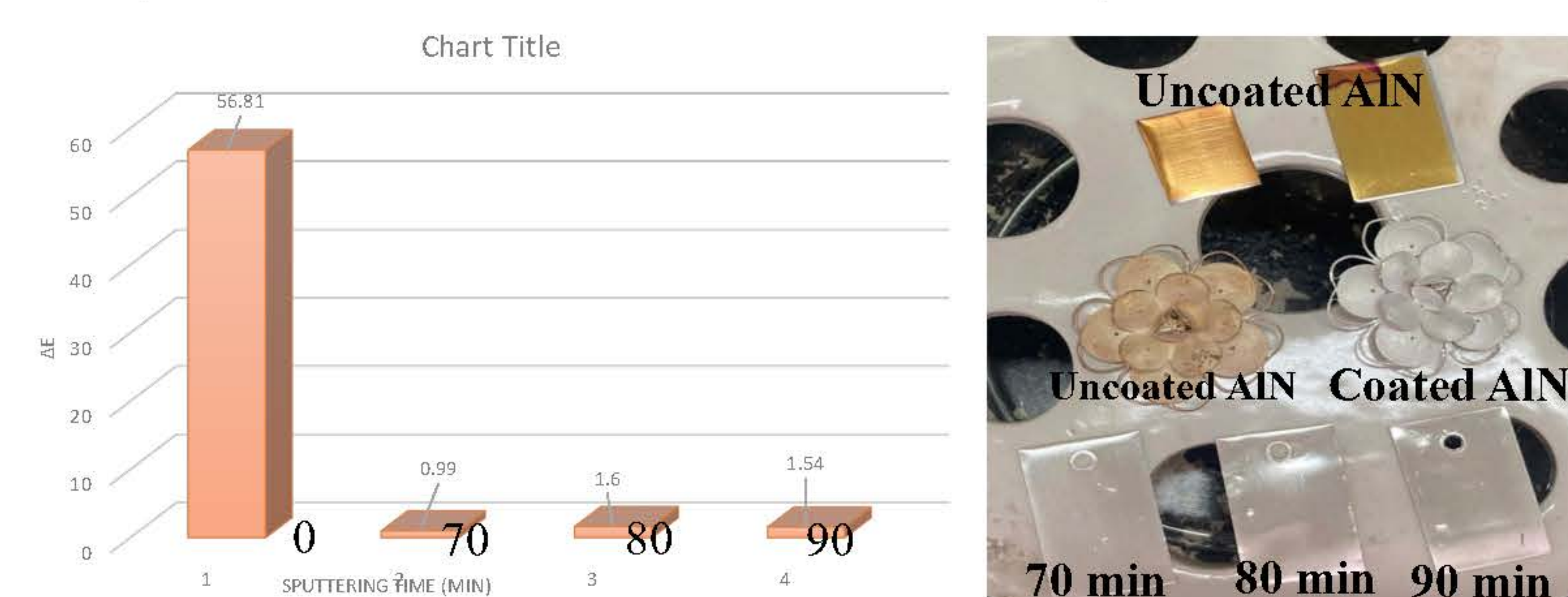


Fig 4 ΔE of AlN coated Ag with sputtering time 0, 70, 80 and 90 min by H₂S atmosphere testing.

Conclusion

- Tarnishing of silver was prevented by AlN coating using DC magnetron sputtering technique.
- ΔE^* was calculated for confirmation of resistant to sulphur.
- AlN coating samples showed outstanding ΔE^* at 1.41 of sputtering time 70 min, 1.88 of sputtering time 80 min and 1.41 of sputtering time 90 min under air atmosphere for 60 days.

Theerapoom Boonprab¹, Peeranuch Pongsripong², Pongkamon Prayongkul², Pinit Kidkhunthod³,
Jonathan A. Kitchen⁴, Pichaya Pattanasattayawong⁵, Pimphaka Harding^{1*}, David J. Harding^{1*}

¹Molecular Magnetic Materials Laboratory, Suranaree University of Technology, Mueang, Nakhon Ratchasima, 30000, Thailand

²Functional Materials and Nanotechnology Centre of Excellence, Walailak University, Thasala, Nakhon Si Thammarat, 80160, Thailand

³Synchrotron Light Research Institute (Public organization), Mueang, Nakhon Ratchasima, 30000, Thailand

⁴Department of Chemistry, University of Southampton, Highfield, Southampton, SO17 1BJ, United Kingdom

⁵Department of Materials Science and Engineering, School of Molecular Science and Engineering, Vidyasirimedhi Institute of Science and Technology, Wang Chan, Rayong, 21210, Thailand

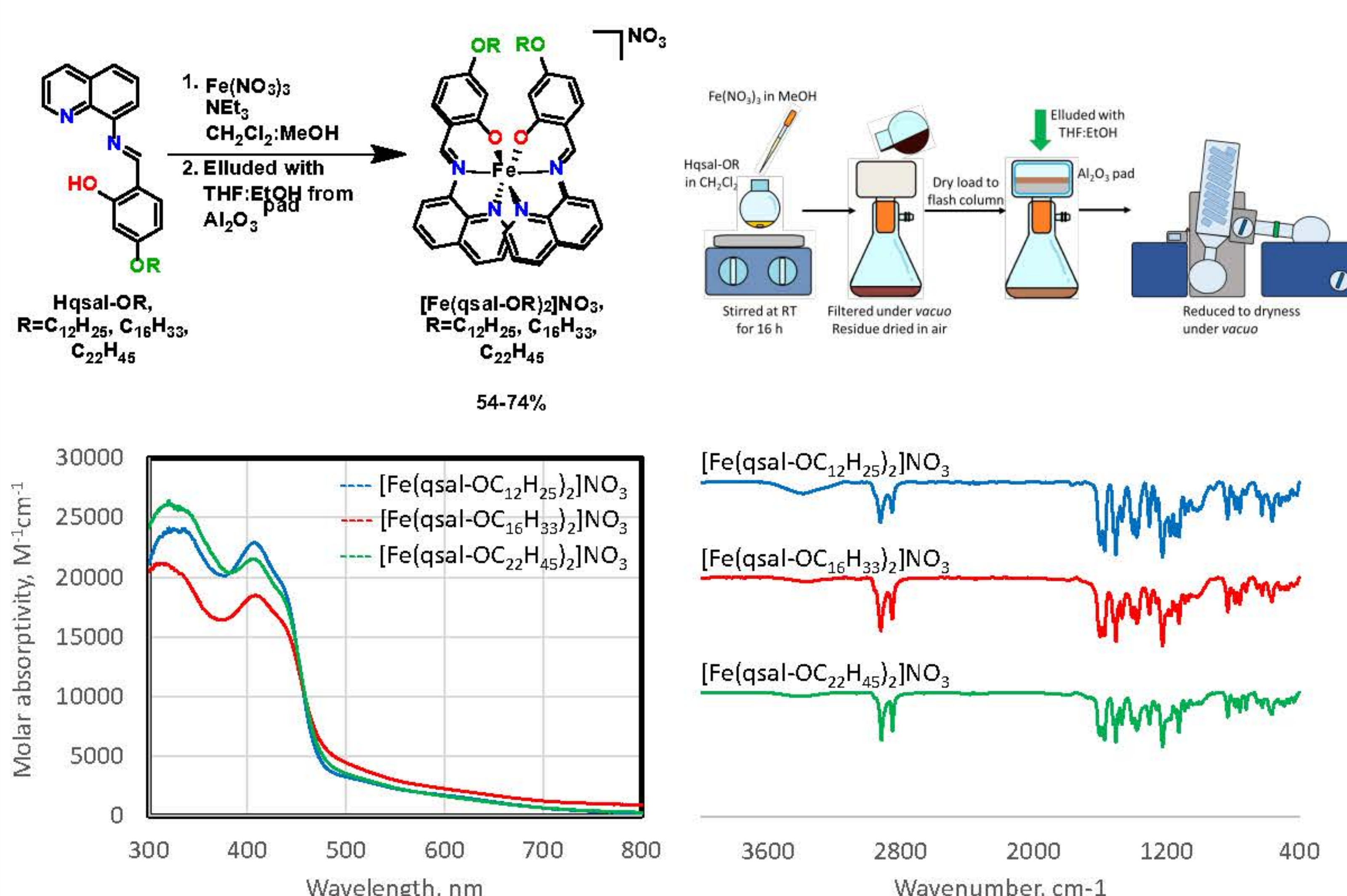
Contact: pimphaka@g.sut.ac.th, david@g.sut.ac.th

Rational and Introduction

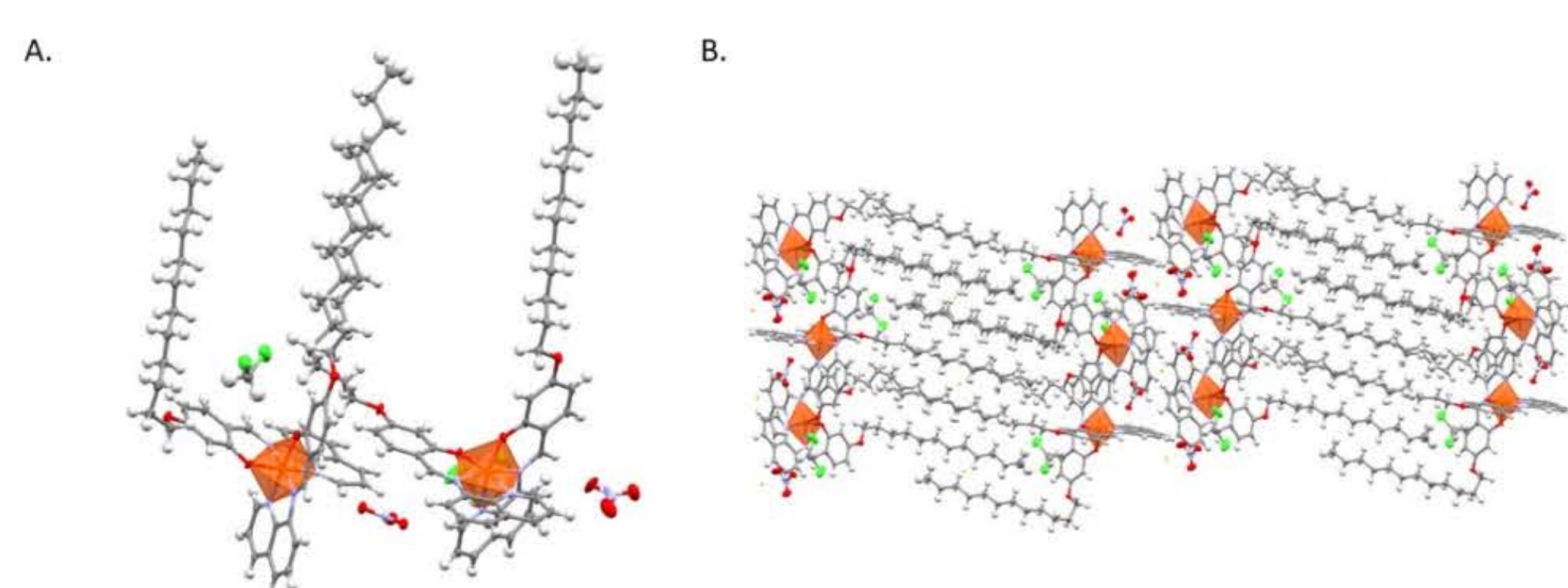
- Spin crossover (SCO) involves switching between two magnetic states, HS and LS upon external stimulation and can potentially act as qubits.
- Commercial application requires arrays of qubits which can be efficiently prepared by self-assembly.

Synthesis and structure of $[\text{Fe}(\text{qsal-OR})_2]\text{NO}_3$

- Long alkyl chains were attached to the qsal ligand platform to create $[\text{Fe}(\text{qsal-OR})_2]\text{NO}_3$; R = $\text{C}_{12}\text{H}_{25}$, $\text{C}_{16}\text{H}_{33}$, $\text{C}_{22}\text{H}_{45}$.
- The bilayer structure of $[\text{Fe}(\text{qsal-OC}_{12}\text{H}_{25})_2]\text{NO}_3$ suggests effective self-assembly on surfaces should be possible.

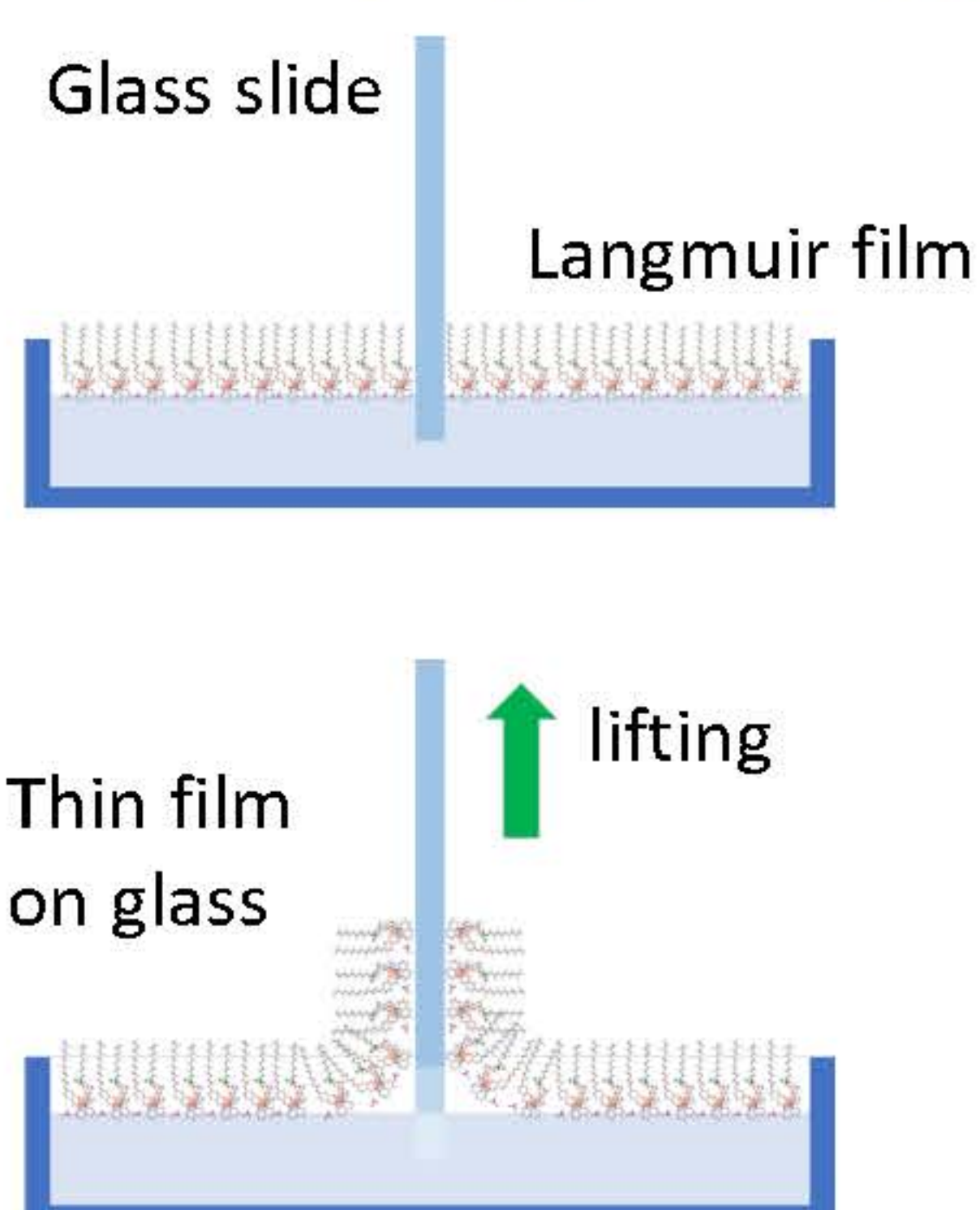


UV-Visible absorption and FT-IR spectra of $[\text{Fe}(\text{qsal-OR})_2]\text{NO}_3$

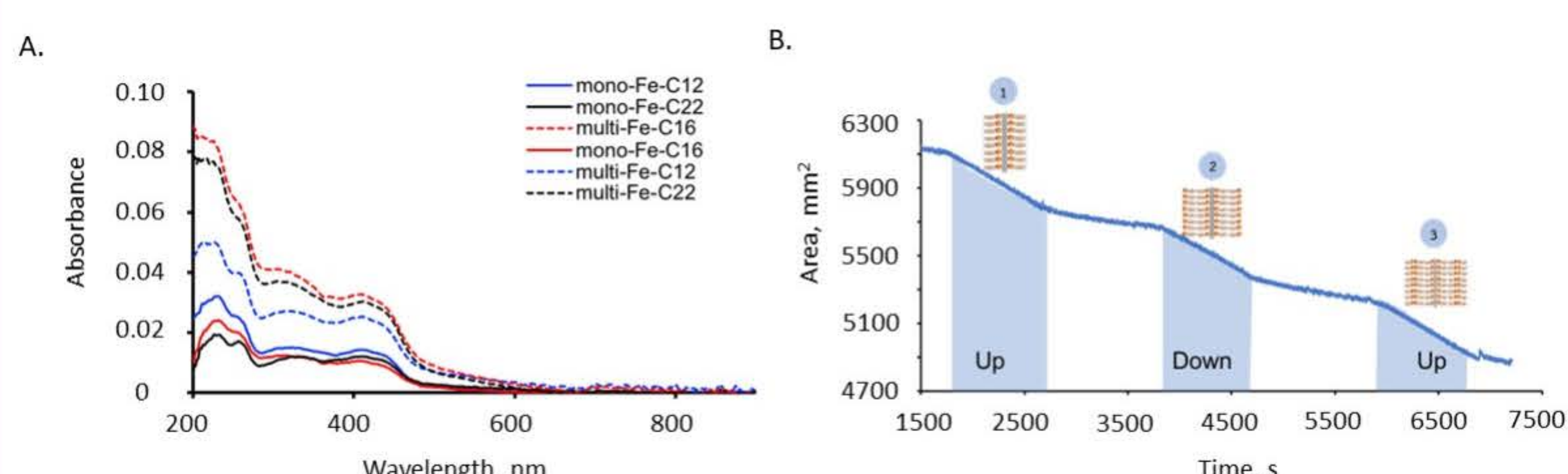


Asymmetric unit of $[\text{Fe}(\text{qsal-OC}_{12}\text{H}_{25})_2]\text{NO}_3$ (A.) and its bilayer solid state packing (B.)

Deposition of $[\text{Fe}(\text{qsal-OR})_2]\text{NO}_3$ Langmuir film on glass



- Deposition of complexes on a glass substrate was achieved by transferring of Langmuir film.
- $[\text{Fe}(\text{qsal-OC}_{16}\text{H}_{33})_2]\text{NO}_3$ exhibited the highest stability and can be stacked up to 3 layers.

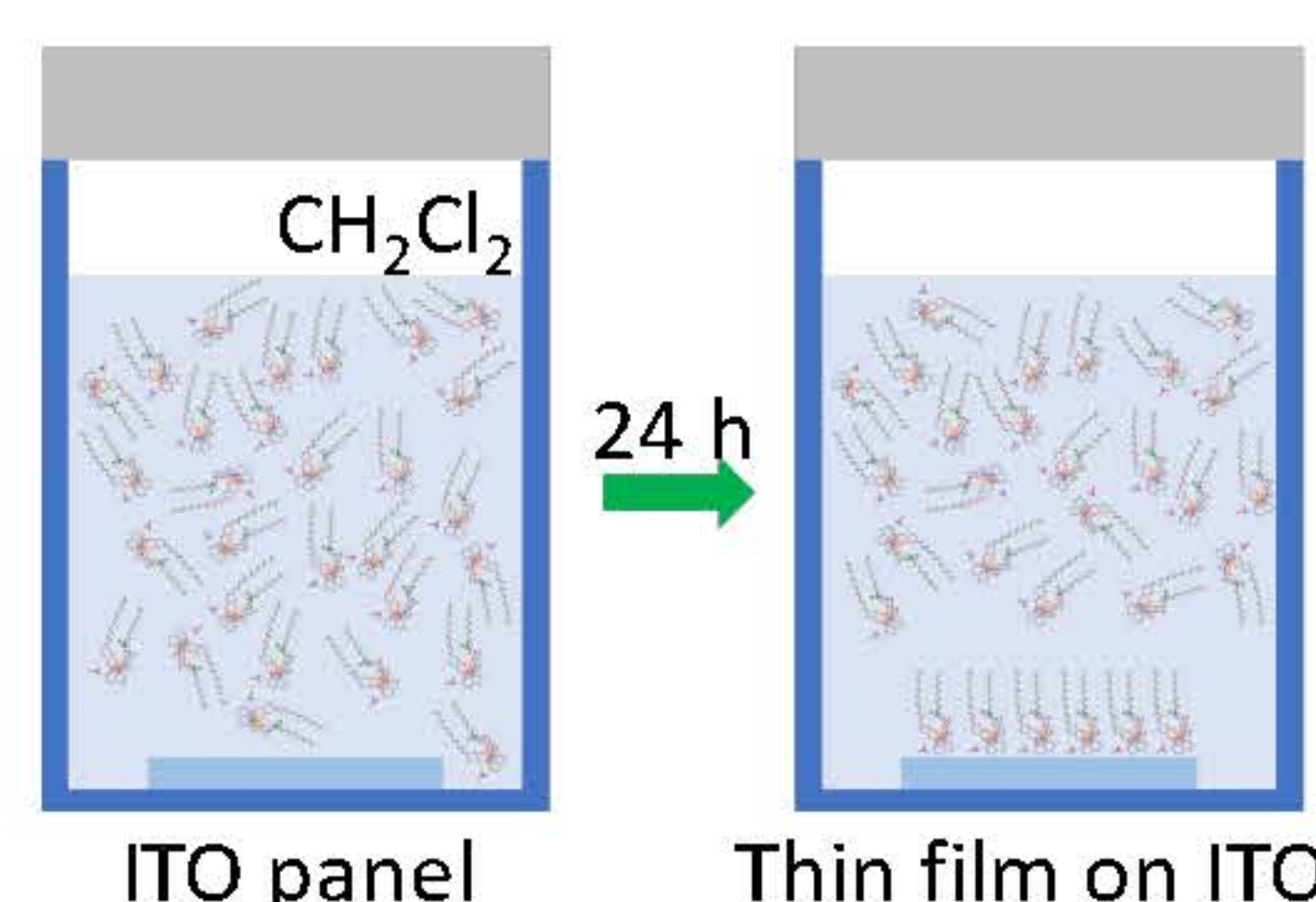


Langmuir film study of $[\text{Fe}(\text{qsal-OR})_2]\text{NO}_3$ showing the films' UV-Vis absorption (A.) and Langmuir film transferring to the glass surface of $[\text{Fe}(\text{qsal-OC}_{16}\text{H}_{33})_2]\text{NO}_3$ (B.).

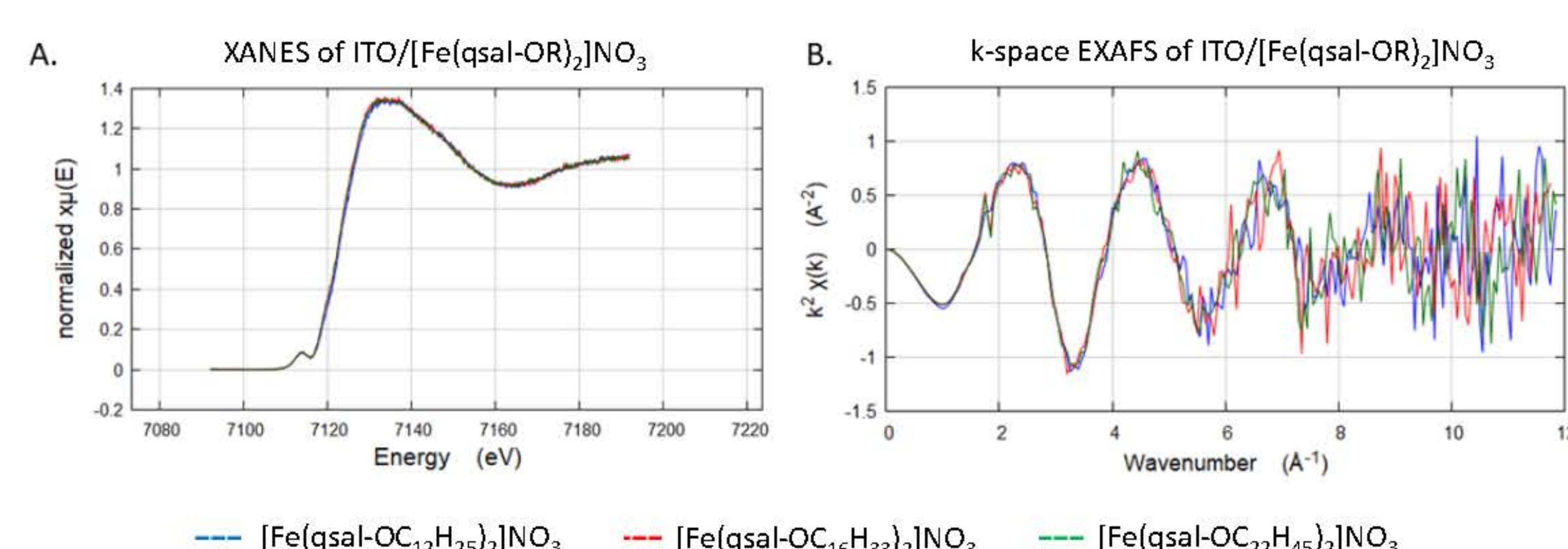
Acknowledgements

This research has received funding support from the NSRF via the Program Management Unit for Human Resources & Institutional Development, Research and Innovation (grant number: B13F660057)

Deposition of $[\text{Fe}(\text{qsal-OR})_2]\text{NO}_3$ on ITO panel

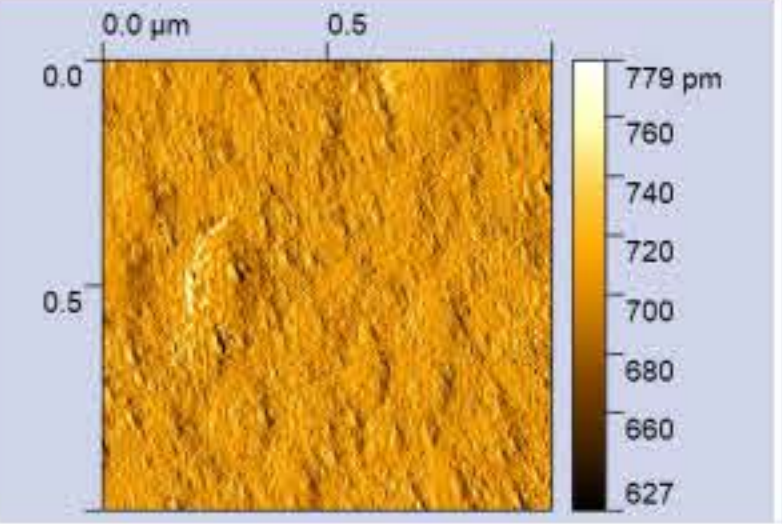
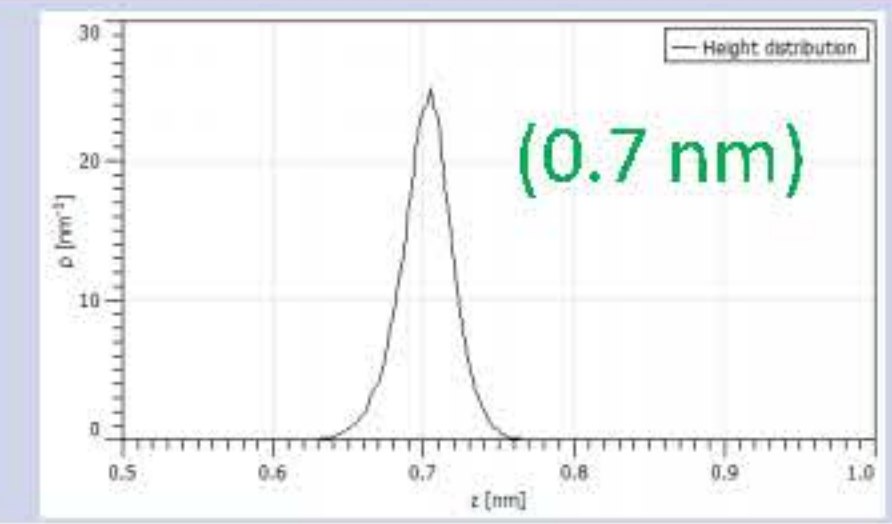
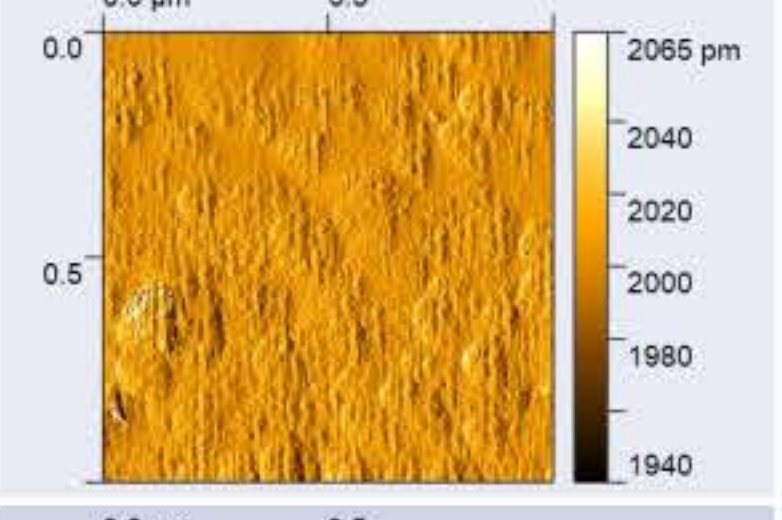
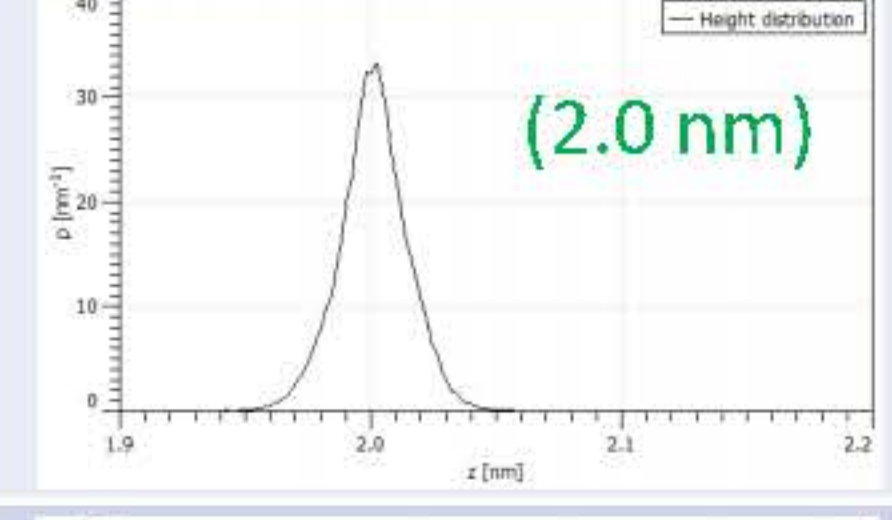
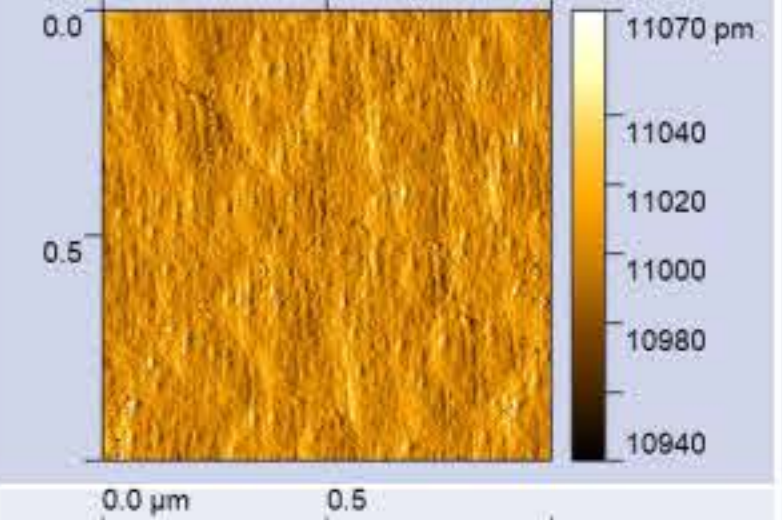
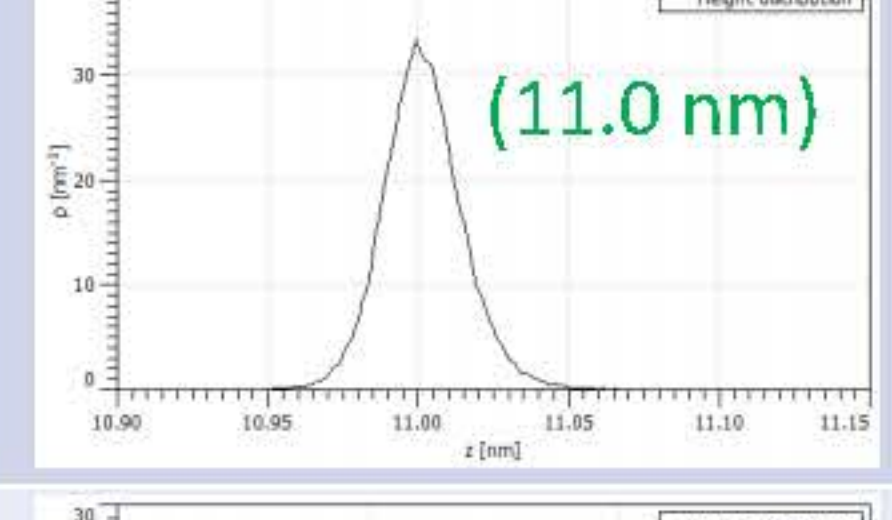
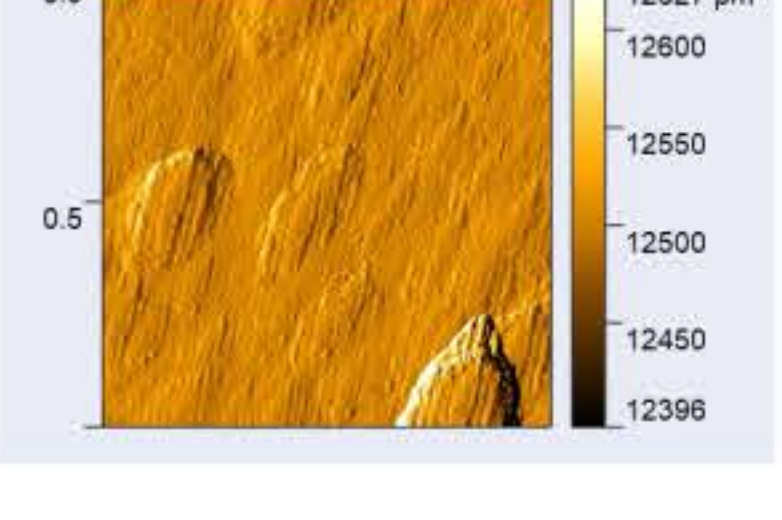
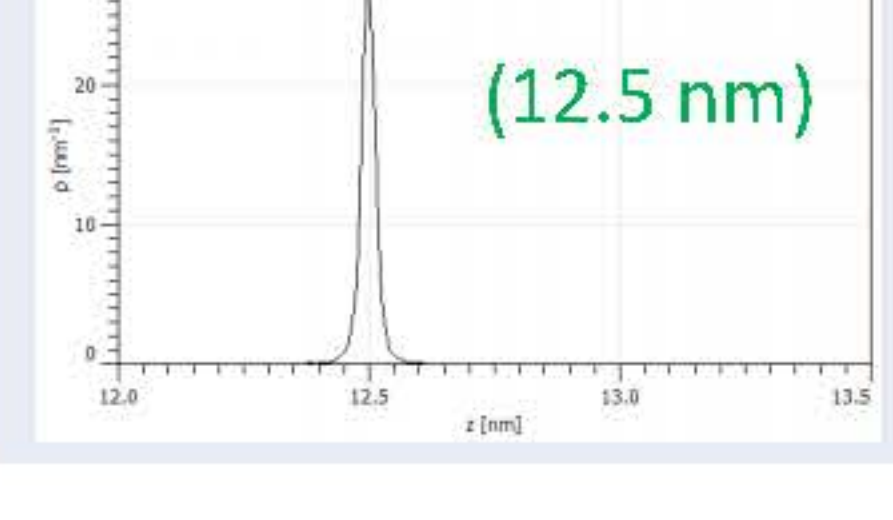


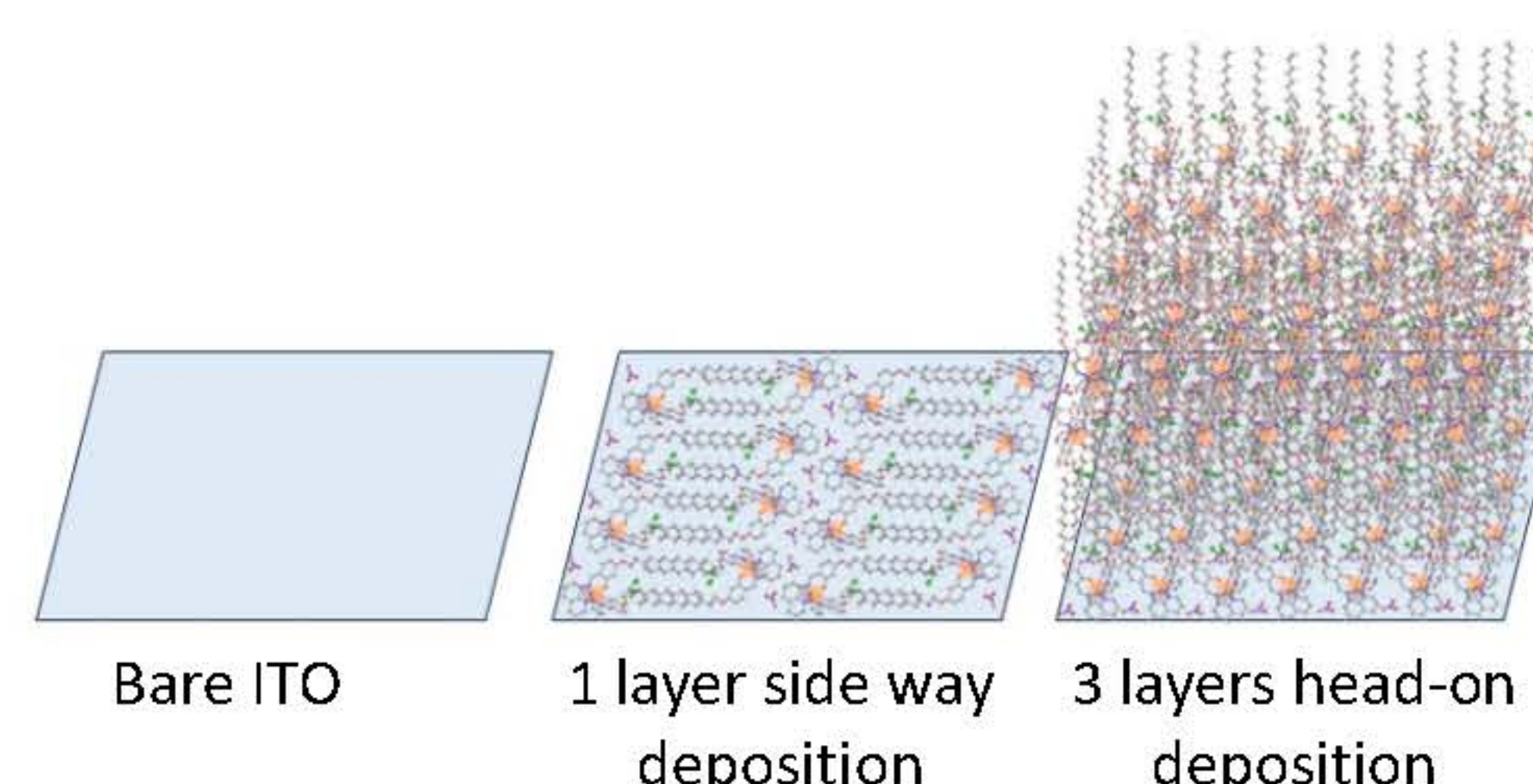
- Deposition of $[\text{Fe}(\text{qsal-OR})_2]\text{NO}_3$ on ITO is readily achieved *via* immersive self-assembly.
- XANES and EXAFS confirm the presence of the Fe(III) complexes on the panel.



XAS results of $[\text{Fe}(\text{qsal-OR})_2]\text{NO}_3$ on ITO panel; XANES (A.), and EXAFS displaying in a k-space (B.)

Surface characterization of the films on ITO by SEM and AFM

	AFM (Amplitude scan, 1.0*1.0 μM)	Surface height distribution
Bare ITO panel		 (0.7 nm)
ITO/ $[\text{Fe}(\text{qsal-OC}_{12}\text{H}_{25})_2]\text{NO}_3$		 (2.0 nm)
ITO/ $[\text{Fe}(\text{qsal-OC}_{16}\text{H}_{33})_2]\text{NO}_3$		 (11.0 nm)
ITO/ $[\text{Fe}(\text{qsal-OC}_{22}\text{H}_{45})_2]\text{NO}_3$		 (12.5 nm)



A schematic illustration of $[\text{Fe}(\text{qsal-OR})_2]\text{NO}_3$ deposition on ITO panel

AFM suggests a monolayer deposition of $[\text{Fe}(\text{qsal-OC}_{12}\text{H}_{25})_2]\text{NO}_3$, while trilayers are present for the other two systems.

Conclusion & Outlook

- $[\text{Fe}(\text{qsal-OR})_2]\text{NO}_3$; R = $\text{C}_{12}\text{H}_{25}$, $\text{C}_{16}\text{H}_{33}$, $\text{C}_{22}\text{H}_{45}$ complexes were successfully synthesized. The SCXRD structure reveals a bilayer packing in solid state.
- Langmuir films of the complexes are easily made with $[\text{Fe}(\text{qsal-OC}_{16}\text{H}_{33})_2]\text{NO}_3$ the most stable and able to stack up to 3 layers.
- Deposition on ITO panel was achieved *via* immersion and confirmed by XANES and EXAFS. AFM suggests a monolayer deposition of $[\text{Fe}(\text{qsal-OC}_{12}\text{H}_{25})_2]\text{NO}_3$, while trilayers are present for $[\text{Fe}(\text{qsal-OC}_{16}\text{H}_{33})_2]\text{NO}_3$ and $[\text{Fe}(\text{qsal-OC}_{22}\text{H}_{45})_2]\text{NO}_3$.
- The electronic properties and potential applications will be explored next.

Mid-IR optical fiber sensor for environment monitoring applications

Teerapat Rutirawut, Sorawis Sangtawesin, Wanvisa Talataisong*
School of Physics, Institute of Science, Suranaree University of Technology

Key tasks of project

A key task of this project is to design and manufacture the microstructured optical fiber (MOF) for the mid-IR guidance. The prototype of a low-cost fiber drawing system in Thailand to fabricate the polymer-based MOFs will be invented. The demonstration of the mid-IR guidance by using the MOF that fabricated in this project will be performed. The environment (gas) sensing system based on the hollow-core optical fiber will be demonstrated.

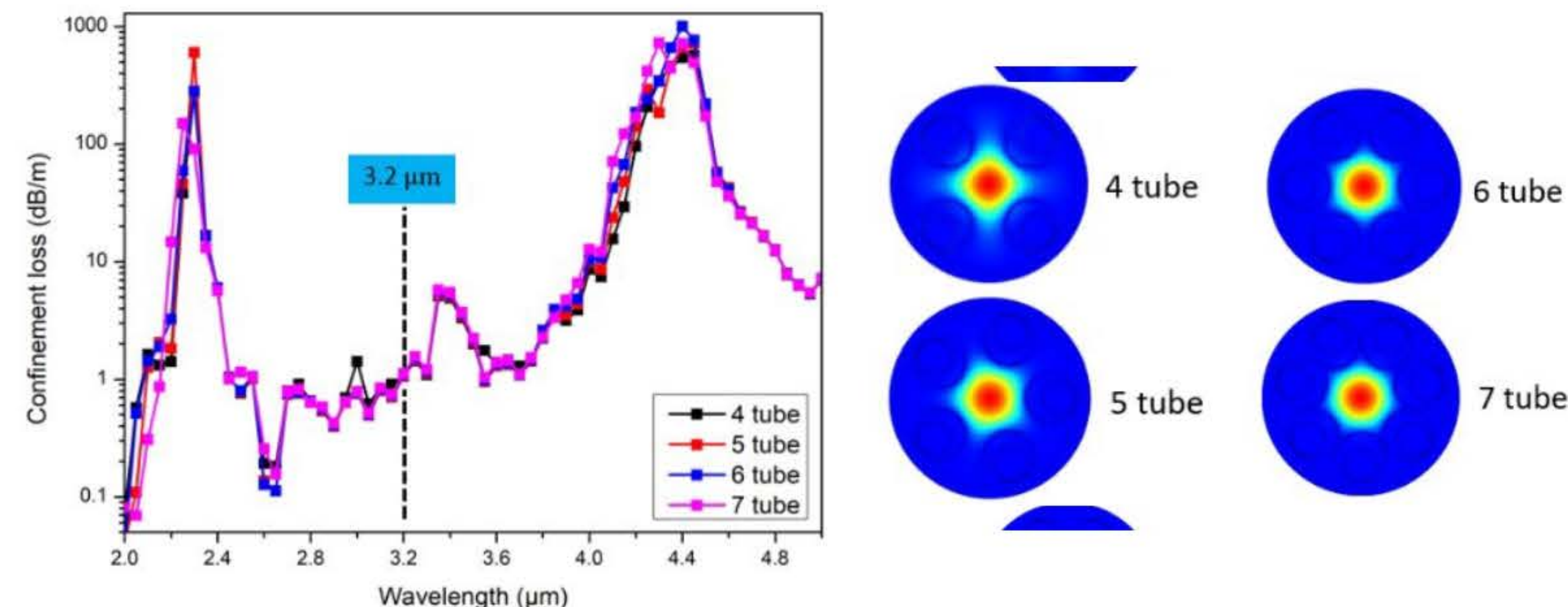
Introduction

Thailand is one of the countries in southeast Asia (ASEAN) that air quality especially in the capital (Bangkok) has been obviously getting worse in the beginning of 2019. The pollution level (PM_{2.5}) and greenhouse gas (CO₂, CO, NO₂) remains at hazardous level in many areas of Bangkok and the surrounding provinces. Therefore, the research on the development of air quality monitoring and take mitigating actions to reduce air pollution are of interest. The monitoring methods based on an optical technique have proven to be an ideal method for remote and real-time particles and gas monitoring.

The above clearly illustrate the need to develop more reliable in situ measurement to tackle the ever-increasing effects of the PM_{2.5} and harmful greenhouse gases on the global health awareness. Thus, the aim of this research project is to develop and design the hollow-core optical fiber for the Greenhouse gas sensing applications.

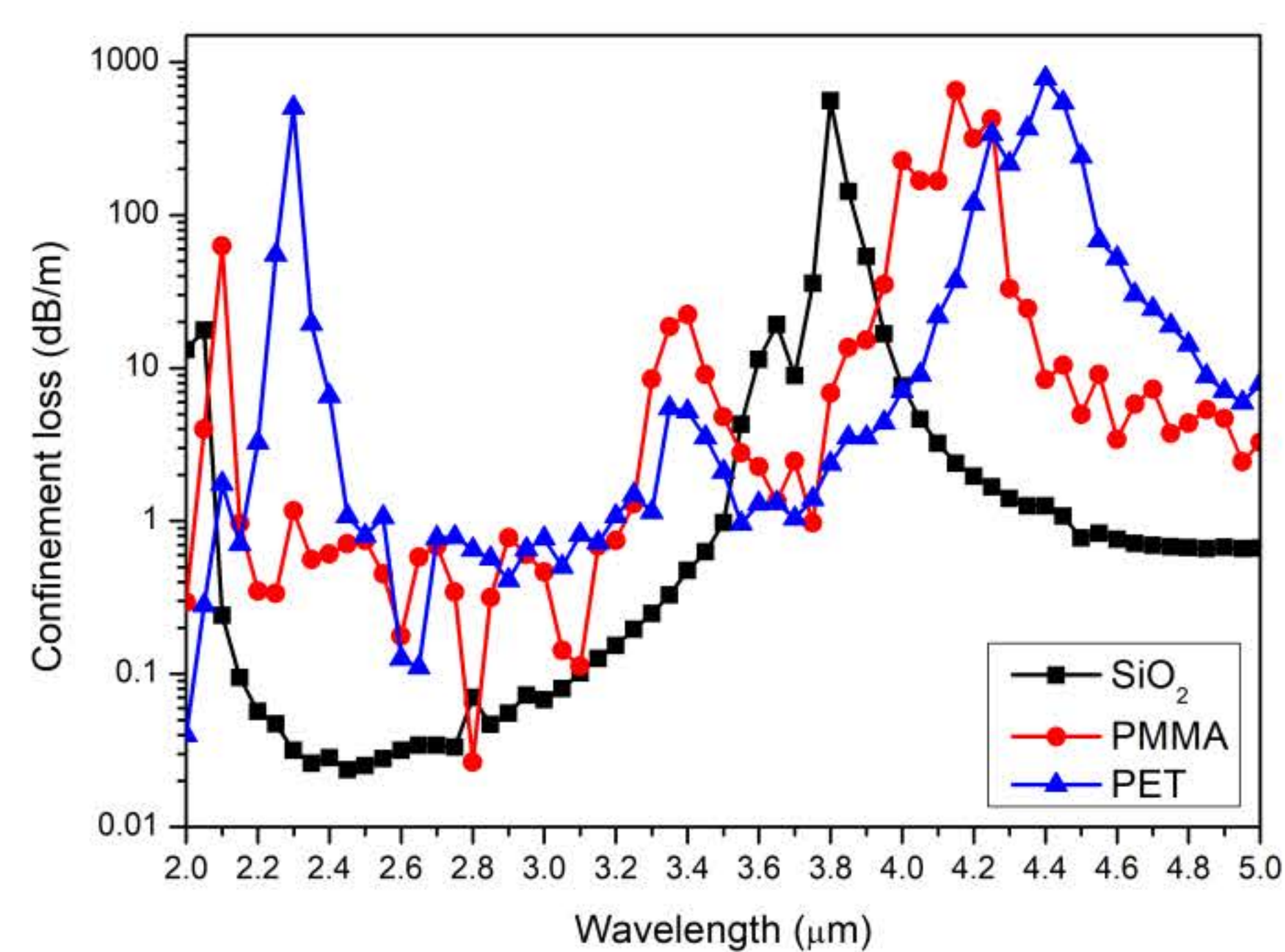
Design optimization of the hollow-core MOF for mid-IR guidance

The mid-IR guidance hollow-core optical fiber, tailored for a wavelength of 3.2 μm crucial for methane (CH₄) gas sensing, is meticulously crafted through optimization using Multiphysics simulation software. Drawing insights from existing literature, the hollow-core antiresonance fiber (HC-ARF) with a cladding tubes structure emerges as the optimal choice, exhibiting the least confinement loss due to double reflection into the fiber core. Simulation results indicate that, at 3.2 μm , the number of cladding tubes has no significant impact on confinement loss, though mode profiles differ between odd and even tube numbers.



Modal analysis of HC-ARF structure for the different numbers of cladding tubes showing the confinement loss and mode field distribution for nested tube from 4-7 tubes.

In the context of sensing applications, PET was chosen for optical fiber design and production. Its chemical compatibility, characterized by resistance to dissolution in basic chemicals such as isopropyl alcohol and acetone, surpasses that of PMMA, making it a fitting material for the surface functionalization process in optical fiber gas sensors.

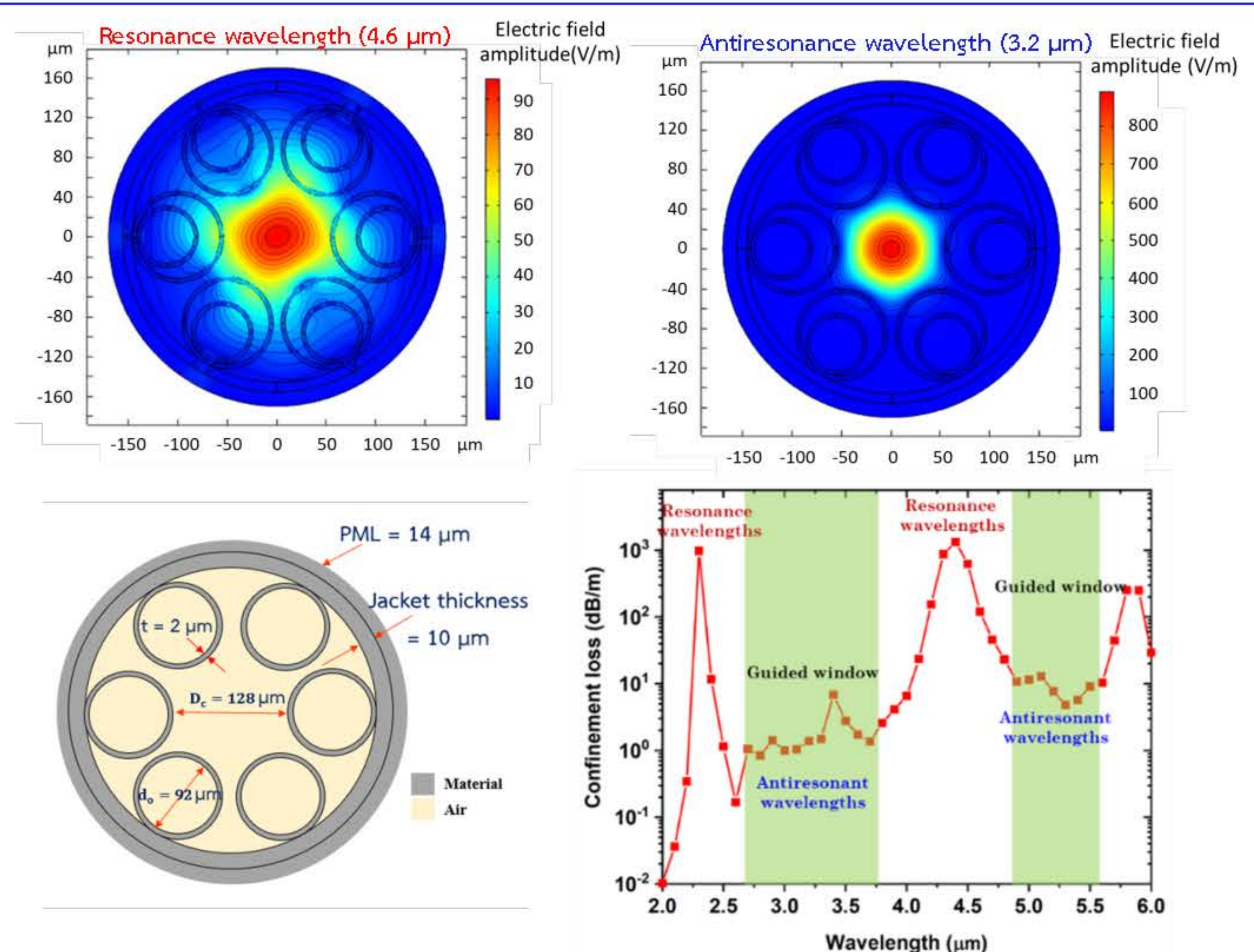


Confinement loss as a function of wavelength for different materials

The simulation reveal that the optimized configuration for Hollow-Core Antiresonance Fiber (HC-ARF) in mid-IR guidance, within the wavelength range of 3-5 μm , involves employing HC-ARF with 6 cladding tubes.

- The tube thickness is set at 2 μm .
- The tube diameter at 92 μm .
- The optical fiber core diameter at 128 μm .
- The overall fiber diameter at 340 μm .

Utilizing PET material results in a confinement loss of 1.06 dB/m. Illustrated in the accompanying figure, the spectra of confinement loss indicate that the optical fiber can effectively guide light in two distinct windows: the wavelength range of 2.6 – 3.6 μm and 5.0-5.5 μm , both pertinent to methane gas sensing applications.

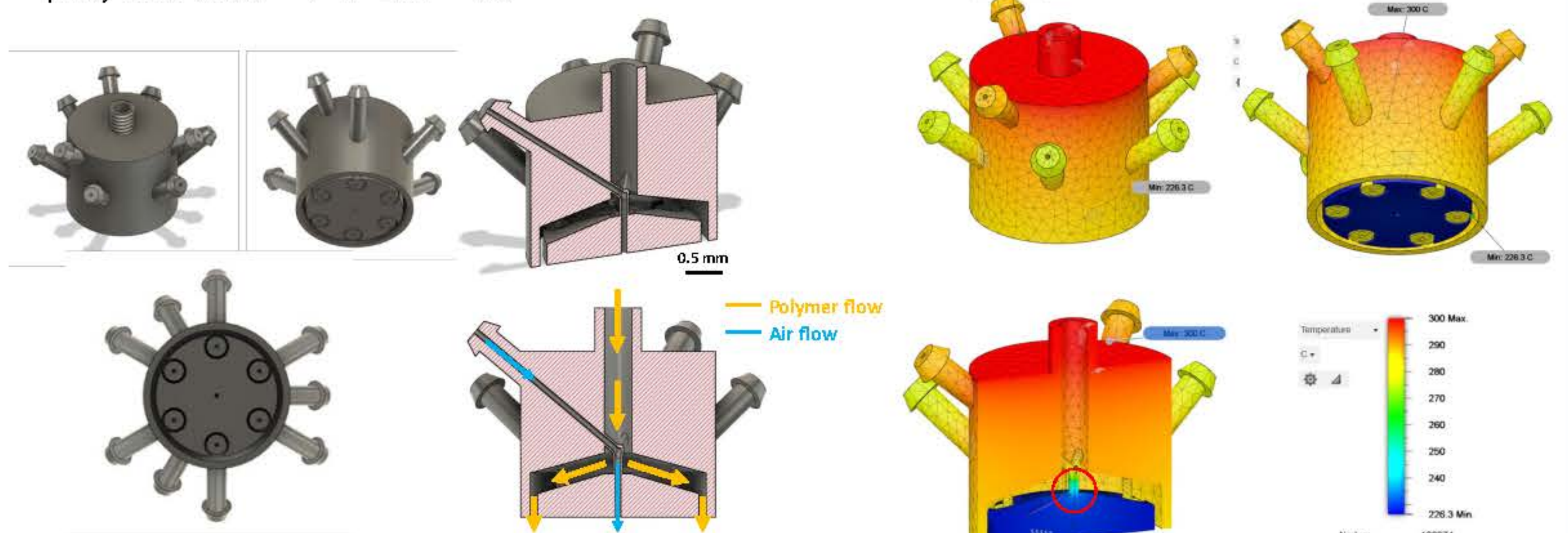


Optimized Structure of HC-ARF for guiding the wavelength of 3.2 μm and the simulated spectrum of the designed fiber.

Optical fiber extruding and drawing system

The nozzle for HC-ARF fabrication has been designed and the structure is optimized to fit with the drawing system. The solid polymer filament will be fed through the heated nozzle where the polymer will be heated via the nozzle. The temperature of the nozzle must be high enough to heat the polymer to a temperature higher than its glass transition temperature ($T_g \sim 110^\circ\text{C}$).

The result shows that the temperature at the nozzle bottom is reduced from the applied temperature of 300.0 $^\circ\text{C}$ to 226.3 $^\circ\text{C}$. The outer part of the nozzle is designed to connect with the nozzle thread, where the heat will be applied, thus the applied heat at the thread will transfer directly to the outer part of the nozzle through heat conduction. The temperature at the bottom of the nozzle body is lower than the cover for the metal 3D printed nozzle but it is in the acceptable rang of the drawing temperature for polymer (100 $^\circ\text{C}$ to 210 $^\circ\text{C}$).



CAD design of the structured nozzle based on the design of the optical fiber from the simulation results. Heat transfer simulation of the designed structured nozzle for hollow-core antiresonance fiber fabrication.

Conclusion

To achieve the optical fiber with confinement loss of 1.06 dB/m by using PET material, the HC-ARF is required to have 6 cladding tubes, where the tube thickness is 2 μm , the diameter of the tube is 92 μm , the optical fiber core diameter is 128 μm , and the overall fiber diameter is 340 μm .

The structured nozzle for fiber fabrication has been created based on the optimal design of the optical fiber from the simulation. Heat transfer simulation is done and shows the acceptable range of temperature which can be used to draw the optical fiber.

Suggestions on the nozzle design is to run the material flow simulation where the result from the simulation can provide the possibility to feed the polymer through the nozzle while the structure inside the optical fiber remains.

Acknowledgement

This research has received funding support from the NSRF via the Program Management Unit for Human Resources & Institutional Development, Research and Innovation [grant number B13F660057]

- W. Talataisong, J. Gorecki, L. D. van Putten, R. Ismaeel, J. Williamson, K. Addinall, D. Schwendemann, M. Beresna, V. Apostolopoulos and G. Brambilla, "Hollow-core antiresonant terahertz fiber-based TOFAS extruded from a 3D printer using a metal 3D printed nozzle". *Photon. Res.* 9, 1513-1521 (2021).
- W. Talataisong, R. Ismaeel, T. Marques, S. Abokhamis Mousavi, M. Beresna, M. Gouveia, S. Sandoghchi, T. Lee, C. Cordeiro, and G. Brambilla "Mid-IR Hollow-core microstructured fiber drawn from a 3D printed PETG preform". *Scientific Reports*, 8, 1-8, (2018).
- W. Talataisong, R. Ismaeel, S. Sandoghchi, T. Rutirawut, M. Beresna, and G. Brambilla, "Novel method for manufacturing optical fiber: extrusion and drawing of microstructured polymer optical fibers from a 3D printer". *Optics Express*, 26 (24), (2018).
- Z. Liu, et al., Microstructured optical fiber sensors. *Journal of Lightwave Technology*, 2017. 35(16): p. 3425-3439.
- K. Cook, et al., Step-index optical fiber drawn from 3D printed preforms. *Optics Letters*, 2016. 41(19): p. 4554-4557.

Enhanced the effectiveness of energy storage system by using quantum technology

Warakorn Jindata¹, Supansa Musikajareon², Unchista Wongpatat², and Worawat Meevasana^{1,2,*}

¹School of Physics, Institute of Science, Suranaree University of Technology, Nakhon Ratchasima 30000, Thailand

²EQ Tech Energy Co. Ltd., Suan Luang Sub-district, Krathum Baen district, Samut Sakhon 74000, Thailand

Introduction:

Integrating renewable energy into microgrids is attracted great attention in industrial plants due to the rapid increase in electric power consumption. However, such integration may affect the stability and safety of the power system, resulting from the complexity and power discontinuity of the system. This project presents the enhancement energy storage by using quantum technology which is divided into two parts. In the first part, we apply the quantum effect of thin films called negative electronic compressibility (NEC) to enhance the electrical capacity of energy storage systems, including supercapacitor and lithium-ion battery. The second part focuses on the cooperation with partner companies in creating the energy management system to supporting the use of quantum-inspired algorithm for improving efficiency of microgrids and save the energy costs.

Methods:

1. Determining the conditions for thin films coating by using the radio frequently (RF) magnetron sputtering technique

1.1 The electrode is coated by the RF magnetron sputtering as the thin film layer is coated on both side of electrode at room temperature.

1.2 The base pressure in vacuum is 1.4 Pa and use Argon gas as the dissolved gas for coated pressure at 1.5 Pa with alternating current with 80 to 100 W.

1.3 A time rate for film coating is 30 to 60 second, and a distance between sputtering target and substrate is 6 to 10 cm.

1.4 After coating the film, an electrode would be weighted which the increased weight is very small as less than 1%.

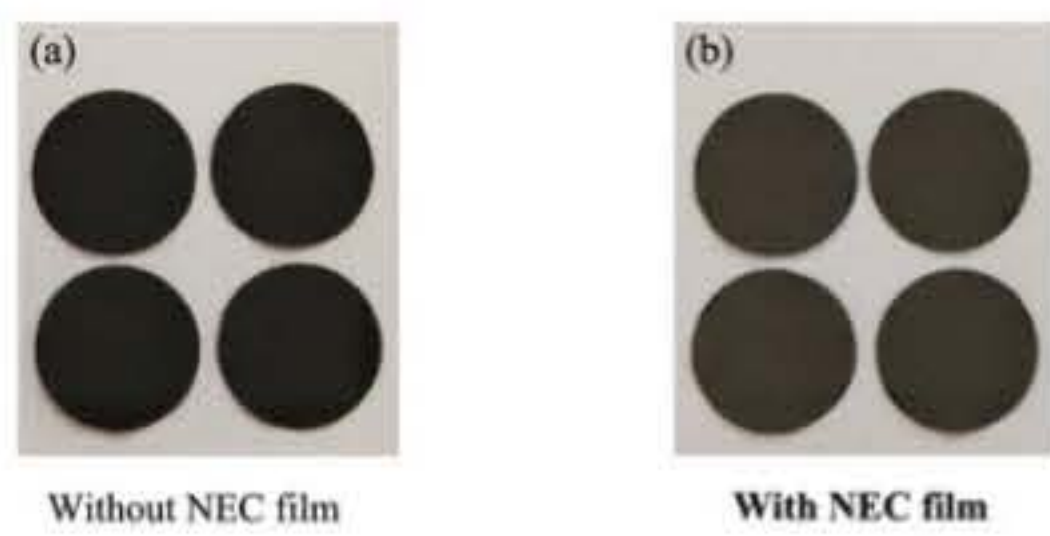


Figure 1. Electrodes without NEC film (a) and electrodes coated with NEC film (b).

2. Design the energy storage and monitoring system (Done by EQ Tech Energy Co. Ltd. and I participated in the research study)

Battery energy storage system (BESS)

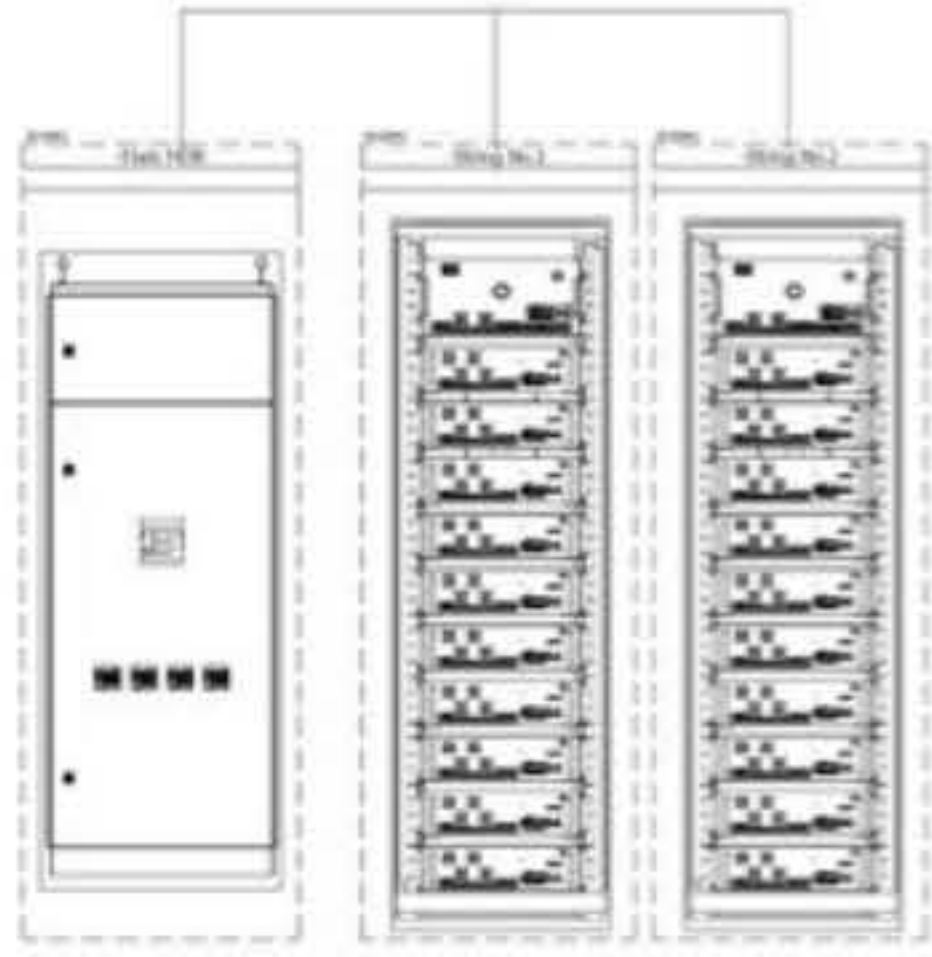


Figure 2. The schematic design of a 100 kWh battery system consisting of a battery module and a control system.

3. Prototype of battery energy storage system (BESS) and energy management system (EMS) (Done by EQ Tech Energy Co. Ltd., I participated in the research study)



Figure 3. Prototype of a 100 kWh LiFePo4 battery with monitoring system.



Figure 4. The screen showing various parameters of the BESS.



Figure 5. The connection between BESS, bi-directional inverter, and EMS.

Conclusion:

1. The research on the increasing of effectiveness of energy storage by using quantum technology showed that coating the metal oxide thin films with the NEC onto electrodes of supercapacitors and lithium-ion batteries can increase the energy density by 29% and 22%, respectively.
2. The research on the coordination in using quantum-inspired algorithm to increase the efficiency of energy management system can develop a prototype of energy storage system (battery energy storage system, BESS) and energy management system (EMS) for applying to use in industrial scale.

Acknowledgements:

This research has received funding support from the NSRF via the Program Management Unit for Human Resources & Institutional Development, Research and Innovation [grant number B13F660057].

Results and Discussion:

1. Testing the charge/discharge process of energy storage

As shown in Fig. 6(a), at a constant current density of 0.1 A/g, the supercapacitor comprising NEC coating shows a significantly longer time from charge to discharge process, indicating that the supercapacitor comprising NEC coating has a greater energy capacity than the supercapacitor without NEC. The supercapacitor comprising NEC coating exhibit an energy density of 16.4 ± 0.1 Wh/kg which is about 29 % greater than the supercapacitor without NEC (12.7 ± 0.1 Wh/kg) shown in Fig. 6(b).

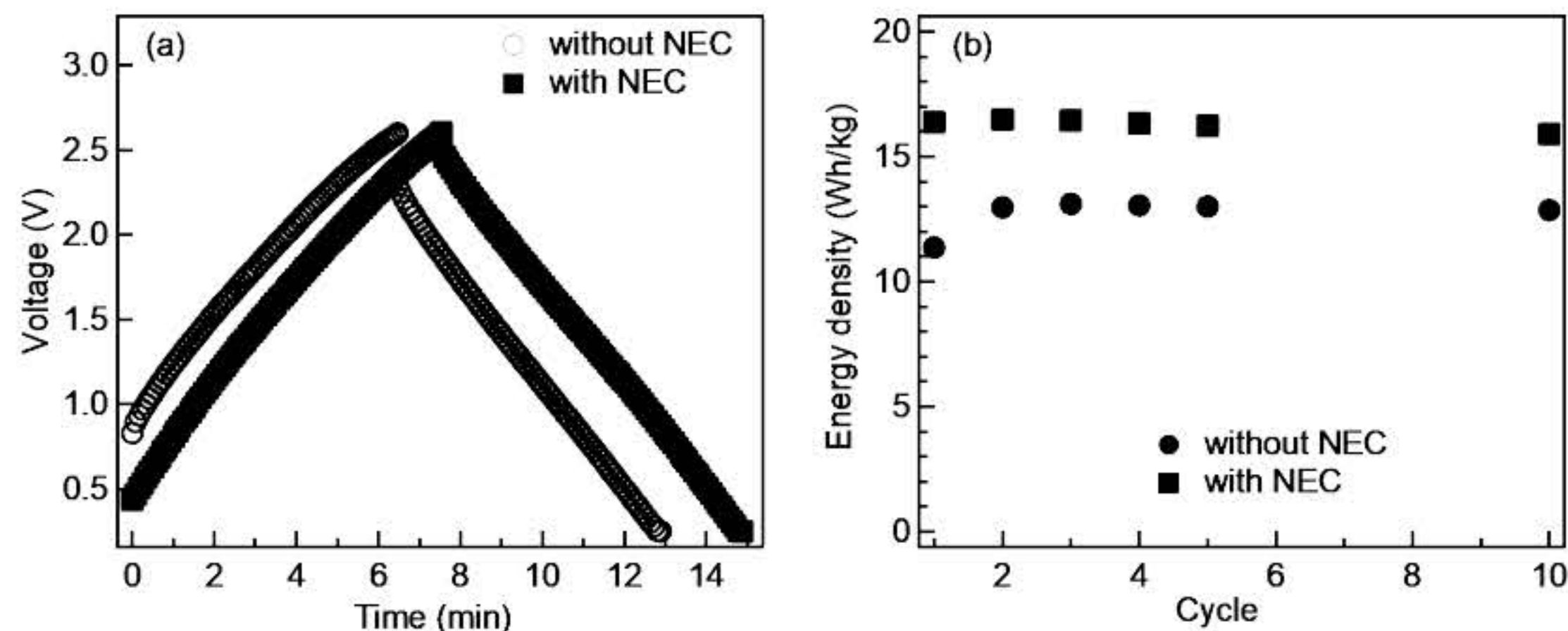


Figure 6. (a) The change of voltage (V) over time (minutes) of a supercapacitor comprising reference electrodes without NEC coating and exemplary electrode with NEC coating. (b) The change of energy density (Wh/kg) over cycles of charge/discharge of a supercapacitor comprising reference electrodes without NEC coating and exemplary electrode with NEC coating.

As shown in Fig. 7(a), at a constant current density of 0.035 A/g, the lithium-ion battery comprising NEC coating shows a significantly longer time from charge to discharge process, indicating that the lithium-ion comprising NEC coating has a greater energy capacity than the lithium-ion without NEC. The lithium-ion battery comprising NEC coating exhibit an energy density of 275 ± 5 Wh/kg which is about 22 % greater than the lithium-ion battery without NEC (225 ± 5 Wh/kg) shown in Fig. 7(b).

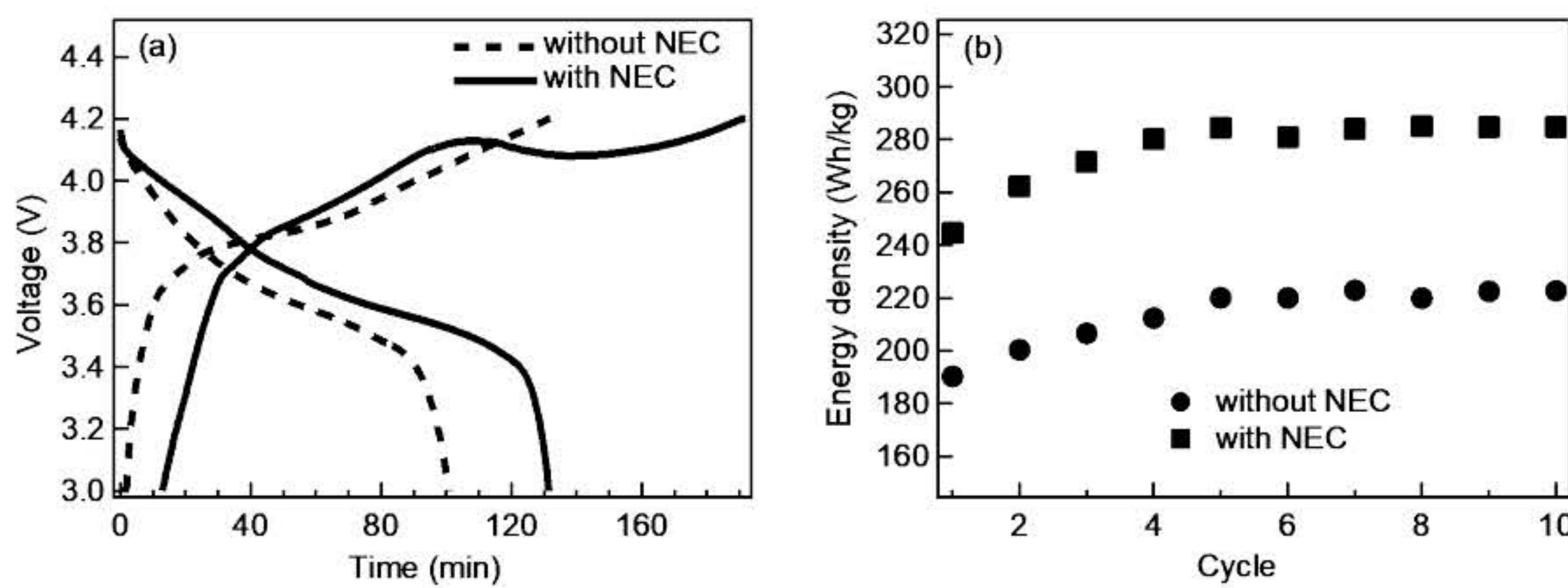


Figure 7. (a) The change of voltage (V) over time (minutes) of a lithium-ion battery comprising reference electrodes without NEC coating and exemplary electrode with NEC coating. (b) The change of energy density (Wh/kg) over cycles of charge/discharge of a lithium-ion battery comprising reference electrodes without NEC coating and exemplary electrode with NEC coating.

2. Testing the capacity of BESS 409.6V 200Ah with module set of 51.2V 200Ah (Done by EQ Tech Energy Co. Ltd., I participated in the research study)

The BESS 409.6V 200Ah with module set of 51.2V 200Ah can support with the maximum power of the Bi-directional inverter 100 kW as designed earlier.

Testing parameters:

- 2.1 Maximum power used for discharging (as designed): 100 kW (approximately 212A)
- 2.2 Maximum power used for discharging (as used in testing): 160 kW (approximately 330A)
- 2.3 Starting voltage (DC): 408.24 Vdc
- 2.4 Final voltage before stopping the test (DC): 326.28 Vdc
- 2.5 Test duration: 15 minutes

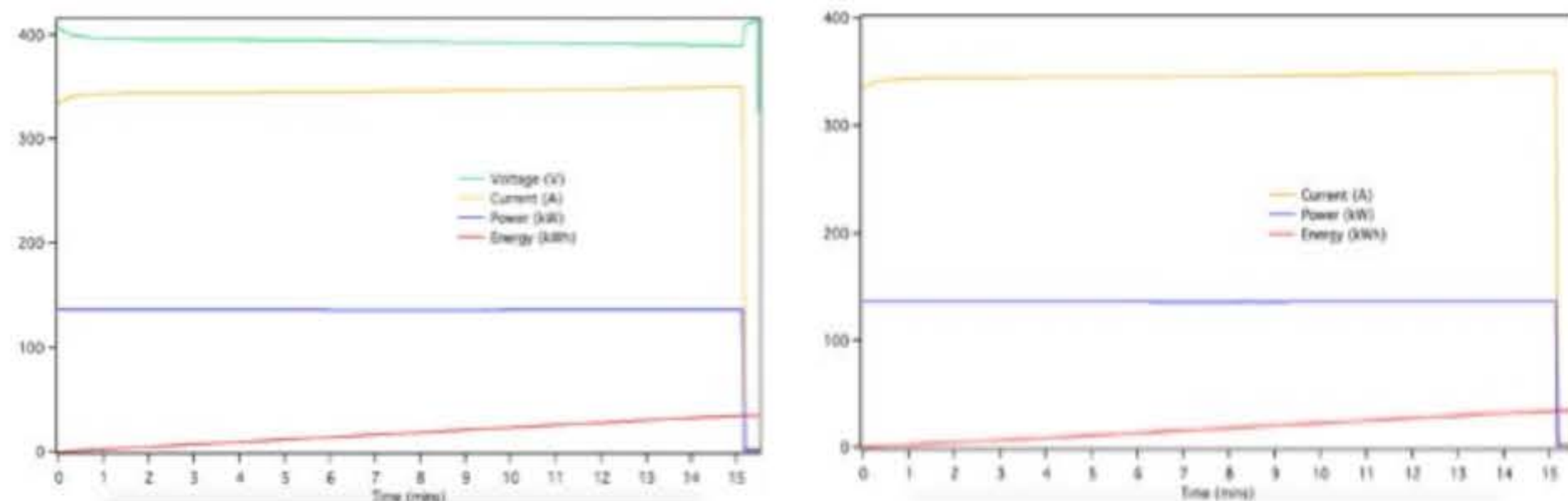


Figure 8. The testing results of battery with specification of 409.6V 200Ah.

Mitesh Kumar Behera ^a, Pawin Ittisamai ^b, Patipan Uttayarat ^c, Chakrit Pongkitivanichkul ^a

Department of Physics, Faculty of Science, Chulalongkorn University, Bangkok – 10330, Thailand ^{a,b}

Department of Physics, Srinakharinwirot University, Wattana, Bangkok, 10110, Thailand^c

Khon Kaen Particle Physics and Cosmology Theory Group (KKPaCT), Department of Physics, Faculty of Science, Khon Kaen University, 123 Mitraphap Rd, Khon Kaen 40002, Thailand^d

miteshbehera1304@gmail.com^a, pawin.i@chula.ac.th^b, patipan@g.swu.ac.th^c, chakpo@kku.ac.th^d



- Neutrino physics is a very interesting field of high energy physics. Its history is rather astonishing and filled with many mysterious clues to the beginning of our Universe. Deciphering these conundrums has kept the high energy physicists occupied for over a decade or two.
- The missing energy in the beta decay experiment led to the contemplation that there is a particle which goes undetectable called neutrino. Wolfgang Pauli and Enrico Fermi were the first to bring it into limelight in around 1930-32. Neutrino is a neutral elementary particle which is not a part of atomic structure.
- They are second in the race in-terms of abundance against photons and were believed to be massless until 1998. However, their existence was experimentally proven by Cowan and Reines in 1954. The other experiments that too have verified the results are Super-Kamiokande, T2K, SNO, Double-Chooz etc.
- A very bizarre behaviour is showcased by neutrino while moving long distances i.e. they change flavor while propagation. Historically, solar neutrino anomaly and atmospheric neutrino anomaly confirmed that lepton flavor is violated in nature. This was further verified by observation of flavor violation of man-made neutrinos after propagating substantial distances in various reactor and long baseline experiments.
- This fascinated the scientific community and made them to think about neutrinos in a new way. Not only neutrino flavor but certain other questions have jolted high energy community, to mention a few, which requires new physics to sweep in are: Why are they almost but not quite massless, could any neutrinos be Majorana spinors, Is there a fourth kind of neutrino, such as a "sterile" neutrino etc.
- After working on it theoretically physicists have arrived at three generation oscillations. If $(\nu_e, \nu_\mu, \nu_\tau)$ are flavor eigenstates which couples to W^\pm through weak interactions are coherent superpositions of three mass eigenstates (ν_1, ν_2, ν_3) with $\nu_\alpha = U_{\alpha i} \nu_i$ with U being the unitary matrix called the PMNS (Pontecorvo, Maki, Nakagawa, Sakata) matrix parametrized by three mixing angles $(\theta_{13}, \theta_{12}, \theta_{23})$ and δ_{CP} phase.
- These neutrino oscillations indicates their are two mass differences and implies that atleast two of the three species have non-zero mass. However, the sign of one of the measured mass splitting is to be decided, after that, one will be sure if neutrinos achieve normal hierarchy (NH) or inverted hierarchy (IH).
- There are many experiments which have given the values for the mass differences, mixing angles and CP phase i.e. δ_{CP} to a 3σ accuracy. Hence, theoretically we explore the cases by model building and try to explain these experimental evidences determined so far.

- The uniqueness of this work is that it employs the type-I seesaw mechanism in SUSY to create a model that explains neutrino oscillation data under S_3 modular symmetry. The Standard Model (SM) is supplemented by three RH neutrinos N_k to construct the superpotential.
- Modular symmetry [1-3] minimizes the use of flavon fields and in addition the modular group is the group of linear fractional transformation acting on a complex variable τ .

$$\tau \rightarrow \gamma\tau = \frac{a\tau+b}{c\tau+d}$$

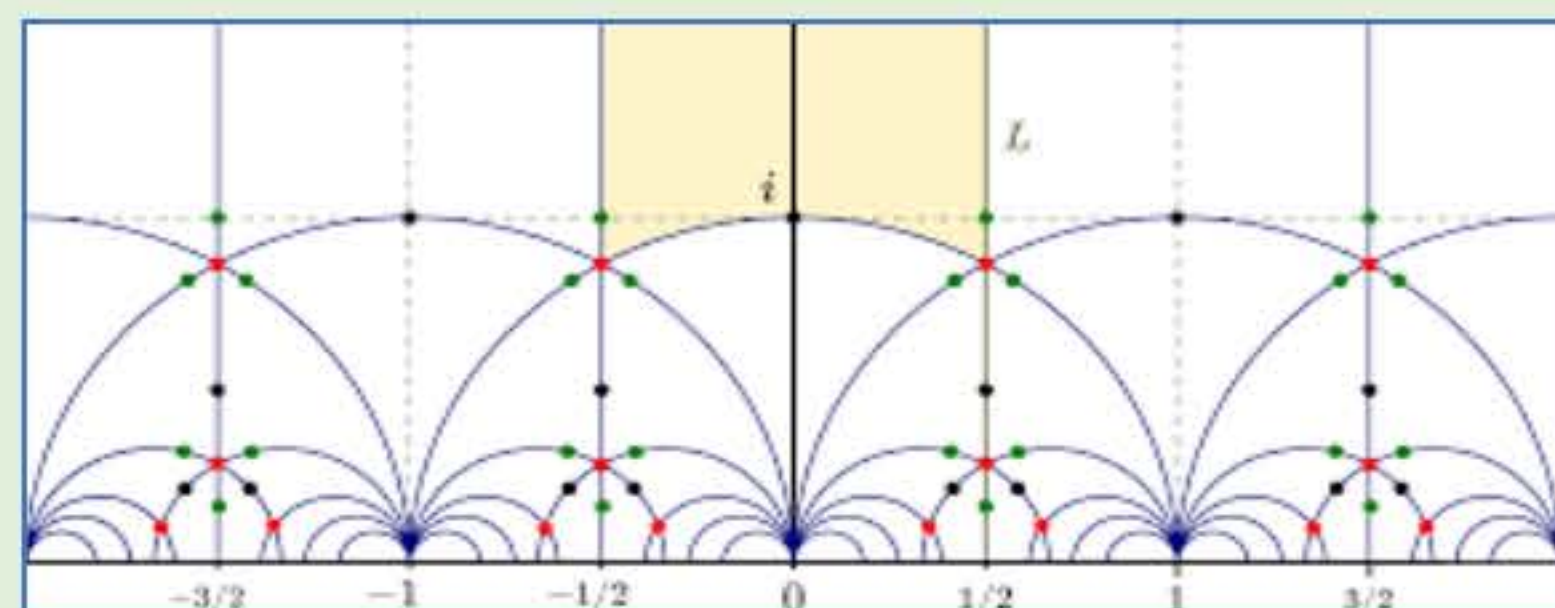
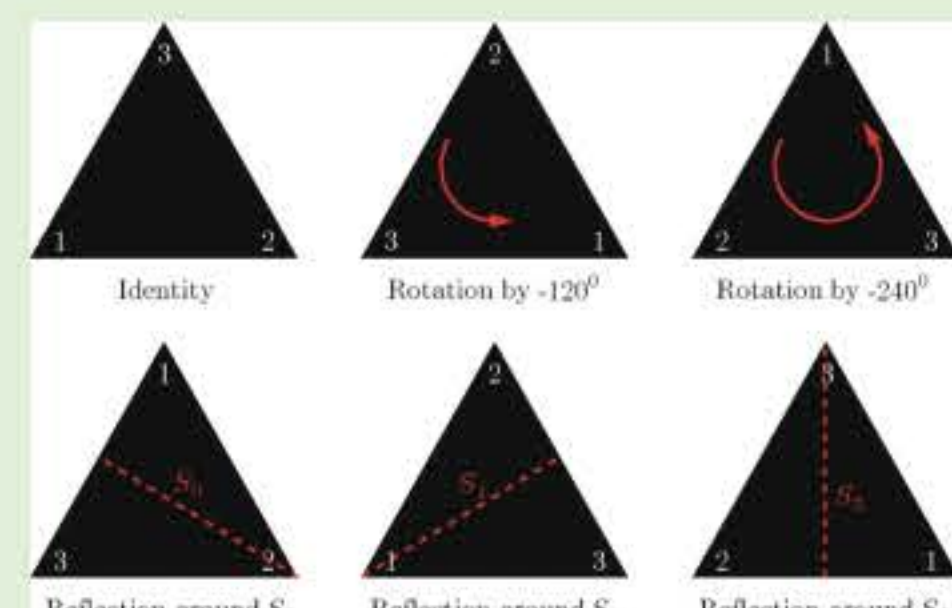
where, $a, b, c, d \in \mathbb{Z}$, $ad - bc = 1$ and $\text{Im}(\tau) > 0$. The Yukawa couplings: $Y = (y_1, y_2)$, transforming as a doublet under S_3 with lowest modular weight $k_l = 2$ can be expressed in terms of Dedekind eta-function $\eta(\tau)$ and its derivative, given as

$$\eta(\tau) = e^{\frac{i\tau\pi}{12}} \prod_{n=1}^{\infty} (1 - e^{2i\tau\pi n})$$

where, $\tau \in H$, $x = e^{2i\tau\pi n}$, $|x| < 1$ (H represents the upper half plane).

- The S_3 group consists of all permutations among three objects, (x_1, x_2, x_3) as its order is equal to $3! = 6$.
- It is also the symmetry group of an equilateral triangle, generated by a reflection with respect to an axis crossing a vertex and orthogonal to the opposite side and a $2\pi/3$ rotation around the centre.
- The irreducible representations for the S_3 symmetry are $1, 1', 2$ which when squared and summed gives the total number of permutations i.e. 6 in S_3 symmetry case and is called the orthogonality condition.
- If $x = \begin{pmatrix} x_1 \\ x_2 \end{pmatrix}$ and $y = \begin{pmatrix} y_1 \\ y_2 \end{pmatrix}$ are two doublets then under S_3 product rule they yield

$$\begin{pmatrix} x_1 \\ x_2 \end{pmatrix}_2 \otimes \begin{pmatrix} y_1 \\ y_2 \end{pmatrix}_2 = (x_1 y_1 + x_2 y_2)_1 + (x_1 y_2 - x_2 y_1)_{1'} + \begin{pmatrix} x_2 y_2 - x_1 y_1 \\ x_1 y_2 + x_2 y_1 \end{pmatrix}_2$$



- The model framework involves lepton doublets (L), lepton singlets (E_L^c) and right handed neutrinos (N_R^c) with two Higgs doublets $H_{u,d}$ to facilitate supersymmetry. Below I present the table for these particles under $SU(2)_L \times U(1)_Y \times S_3$ with k_l being the modular weight.

Fields	E_1^c	E_2^c	E_3^c	L_l	L_3	N_l^c	N_3^c	H_u	H_d
$SU(2)_L$	1	1	1	2	2	1	1	2	2
$U(1)_Y$	1	1	1	-1/2	-1/2	0	0	1/2	-1/2
S_3	1'	1'	1	2	1	2	1'	1	1
k_l	2	4	2	2	2	2	4	0	0

SUPERPOTENTIAL

- The superpotential for the charged lepton sector
$$W_\ell = \alpha_\ell \left[(LE_1^c) Y_2^{(c)} \right] H_d + \alpha_{\ell_1} \left[(LE_2^c) Y_2^{(c)} \right] H_d + \beta_\ell \left[(LE_3^c) Y_2^{(c)} \right] H_d + \gamma_\ell \left[(L_3 E_3^c) Y_2^{(c)} \right] H_d + \chi_\ell \left[(L_3 E_2^c) Y_1^{(c)} \right] H_d$$
- The superpotential for the neutrino sector
$$W_\nu = \alpha_D \left[(LN^c) Y_2^{(c)} \right] H_u + \alpha_{D'} \left[(LN^c) Y_1^{(c)} \right] H_u + \gamma_D \left[(L_3 N_3^c) Y_1^{(c)} \right] H_u + \beta_D \left[(LN_3^c) Y_2^{(c)} \right] H_u + \chi_D \left[(L_3 N^c) Y_2^{(c)} \right] H_u + M \left[(\alpha_R N^c N^c) Y_2^{(c)} + \alpha_R' (N^c N^c) Y_1^{(c)} + \gamma_R (N_3^c N_3^c) Y_1^{(c)} + \beta_R (N^c N_3^c) Y_1^{(c)} \right]$$

MASS MATRICES

$$M_\ell = \frac{v_B}{\sqrt{2}} Y_\ell \begin{pmatrix} \alpha'_\ell \left(Y_2^{(4)} \right)_2 & \alpha'_{\ell_1} \left(Y_2^{(6)} \right)_2 & \beta'_\ell \left(Y_2^{(4)} \right)_1 \\ -\alpha'_\ell \left(Y_2^{(4)} \right)_1 & -\alpha'_{\ell_1} \left(Y_2^{(6)} \right)_2 & \beta'_\ell \left(Y_2^{(4)} \right)_2 \\ 0 & \chi'_\ell Y_{1'}^{(6)} & Y_1^{(4)} \end{pmatrix} \quad M_D = \frac{v_B}{\sqrt{2}} Y_D \begin{pmatrix} -\alpha'_D \left[\left(Y_2^{(4)} \right)_1 \right] + \alpha''_D \left[Y_1^{(4)} \right] & \alpha'_D \left(Y_2^{(4)} \right)_2 & \beta'_D \left(Y_2^{(6)} \right)_2 \\ \alpha'_D \left(Y_2^{(4)} \right)_2 & \alpha'_D \left[\left(Y_2^{(4)} \right)_1 \right] + \alpha''_D \left[Y_1^{(4)} \right] & -\beta'_D \left(Y_2^{(6)} \right)_1 \\ \chi'_D \left(Y_2^{(4)} \right)_1 & \chi'_D \left(Y_2^{(6)} \right)_2 & Y_{1'}^{(6)} \end{pmatrix}$$

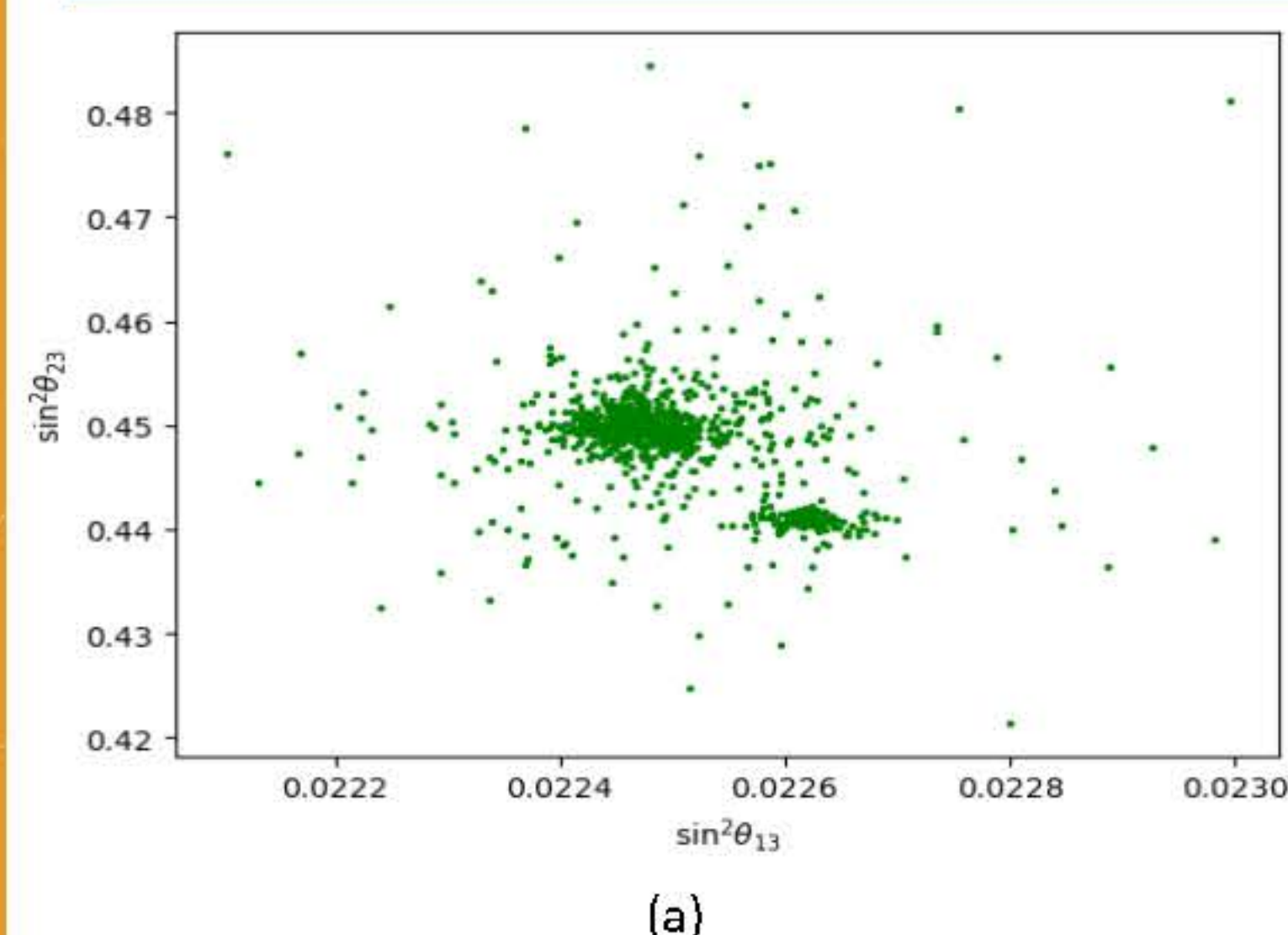
- So the neutrino mass formula for the type-I seesaw is given by

$$m_{\gamma} = M_D^T M_P^{-1} M_F$$

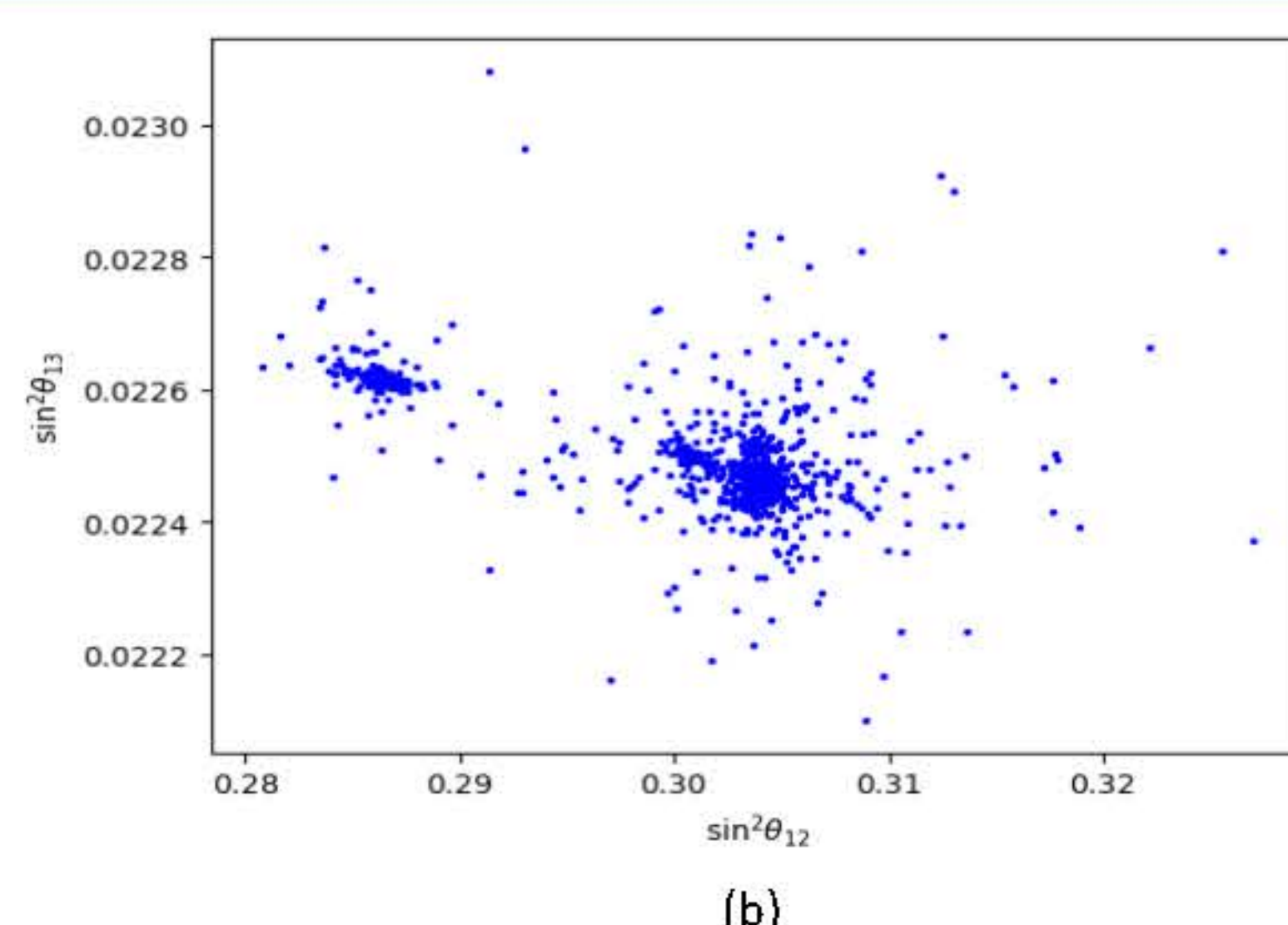
- We numerically diagonalize the neutrino mass matrix through the relation $U^\dagger M U = \text{diag}(m_1^2, m_2^2, m_3^2)$ where, $M = m_\nu m_\nu^\dagger$ and U being the model PMNS $U = U_l^\dagger U_\nu$ from which the neutrino mixing angles can be extracted.
- For numerical analysis we consider the NuFIT 5.2 neutrino oscillation data at 3σ interval as follows:

$$\text{NH} : \Delta m_{atm}^2 = [2.428, 2.597] \times 10^{-3} eV^2, \Delta m_{sol}^2 = [6.82, 8.03] \times 10^{-5} eV^2, \sin^2 \theta_{13} = [0.02029, 0.02391], \sin^2 \theta_{12} = [0.270, 0.341], \sin^2 \theta_{23} = [0.406, 0.620].$$
- The below figures are described as follows :

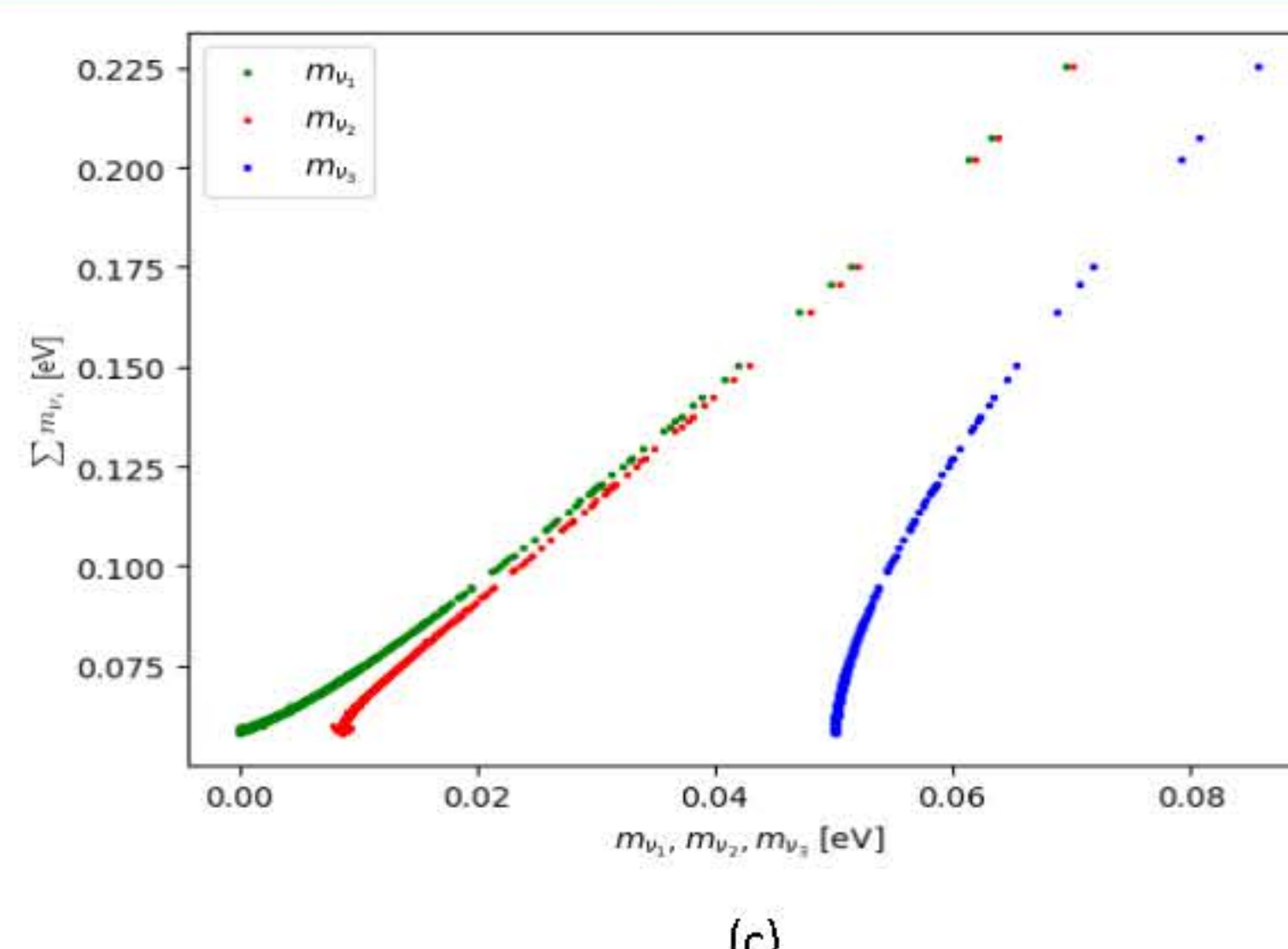
- a. This figure establishes the correlation between $\sin^2 \theta_{13}$ and $\sin^2 \theta_{23}$ and it is evident that they satisfy their respective 3σ ranges.
- b. This figure establishes the correlation between $\sin^2 \theta_{13}$ and $\sin^2 \theta_{23}$ and it is evident that they satisfy their respective 3σ ranges.
- c. This figure establishes the correlation between the Σm_{ν_i} [eV] and the active neutrino masses ($m_{\nu_1}, m_{\nu_2}, m_{\nu_3}$) [eV] and it is evident that it satisfies the normal hierarchy.
- d. This figure shows the correlation between the Jarlskog invariant J_{CP} and mixing angle $\sin^2 \theta_{13}$ within their 3σ ranges.



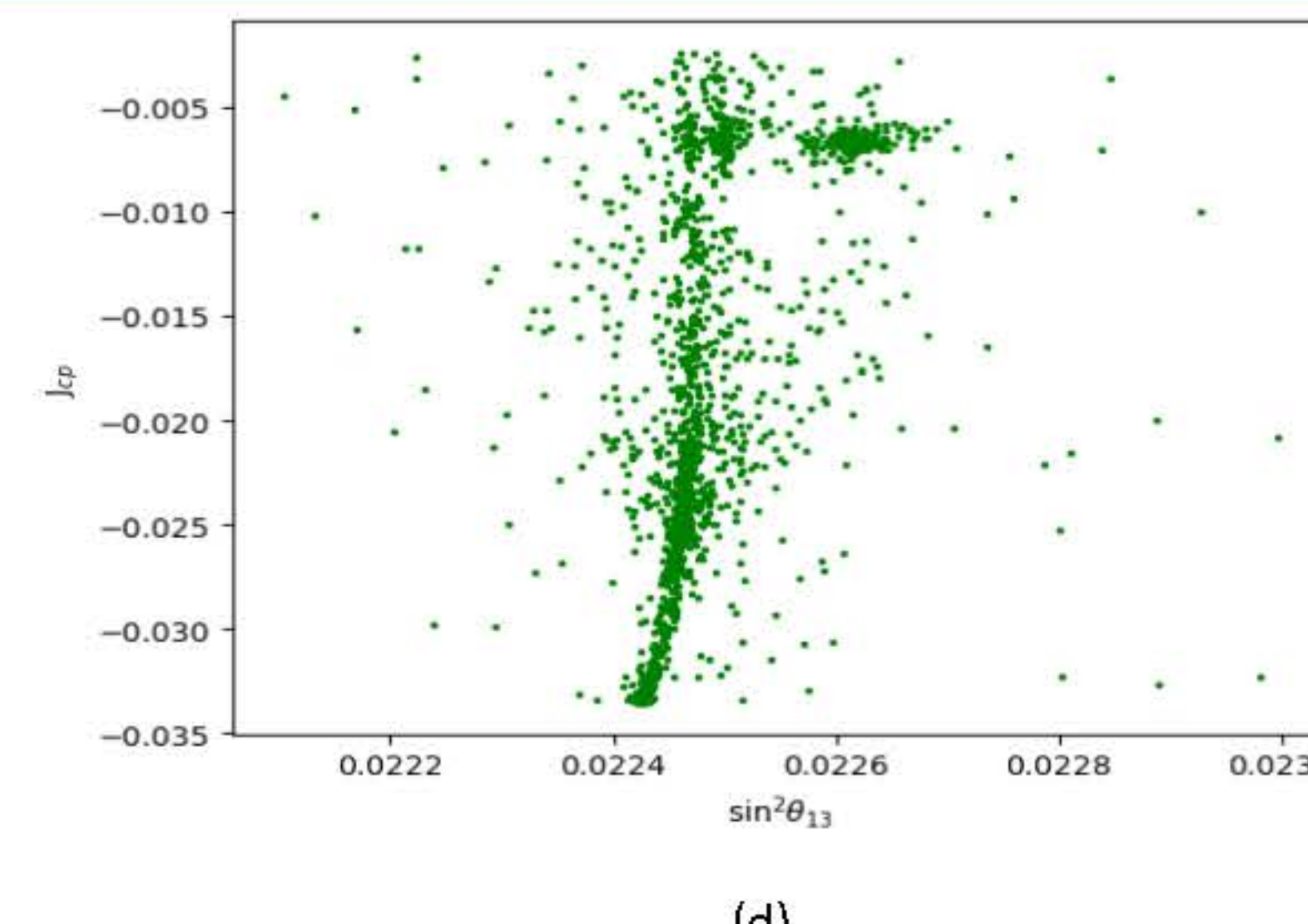
(a)



(b)



(c)



[d]

- We investigated the type-I seesaw mechanism under modular S_3 symmetry which has only singlets and a doublet representation making it the simplest permutation group to examine the neutrino phenomenology. Hence, the mass matrices of the model so represented acquire a unique structure because of the S_3 charge assignments and modular weights k_i .
- As the Yukawa couplings have modular forms expressed in-terms of the Dedekind eta function, hence, we only have the free parameters which when calibrated by involving chi-square minimization technique gives the results for the physical observables in the range that satisfies the experimental data, which makes our model testable in the experiments.

1. Are neutrino masses modular forms?,” doi:10.1142/9789813238053_0012 [arXiv:1706.08749 [hep-ph]].
2. Modular S_3 symmetric radiative seesaw model,” Phys. Rev. D 100, no.11, 115037 (2019) doi:10.1103/PhysRevD.100.115037 [arXiv:1907.04716 [hep-ph]].
3. A simplest modular S_3 model for leptons,” JHEP 09, 043 (2023) doi:10.1007/JHEP09(2023)043 [arXiv:2306.09028 [hep-ph]].

- This research has received funding support from the NSRF via the Program Management Unit for Human Resources & Institutional Development, Research and Innovation [grant number B13F660066].
- I also acknowledges the National Science and Technology Development Agency, National e-Science Infrastructure Consortium, Chulalongkorn University, and the Chulalongkorn Academic Advancement into its 2nd Century Project, NSRF via the Program Management Unit for Human Resources & Institutional Development, Research, and Innovation (Thailand) for providing computing infrastructure that has contributed to the research results reported within this paper.

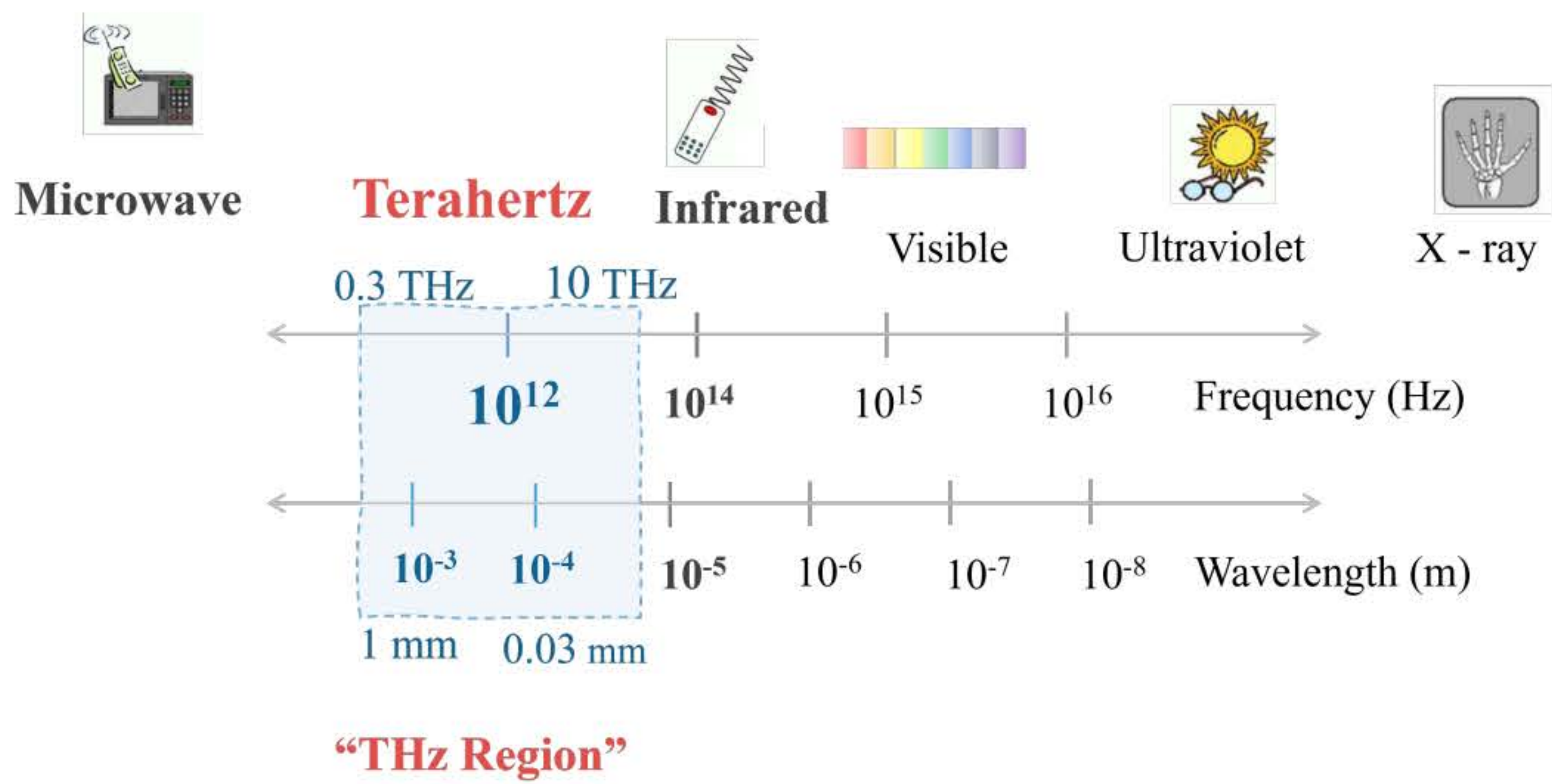
Development of a Super-radiant THz FEL Beamline at Chiang Mai University

K. Damminsek, N. Chaisueb, W. Jaikla, W. Jaipang,
N. Khangrang, E. Kongmon, J. Saisut, C. Thongbai, S. Rimjaem*

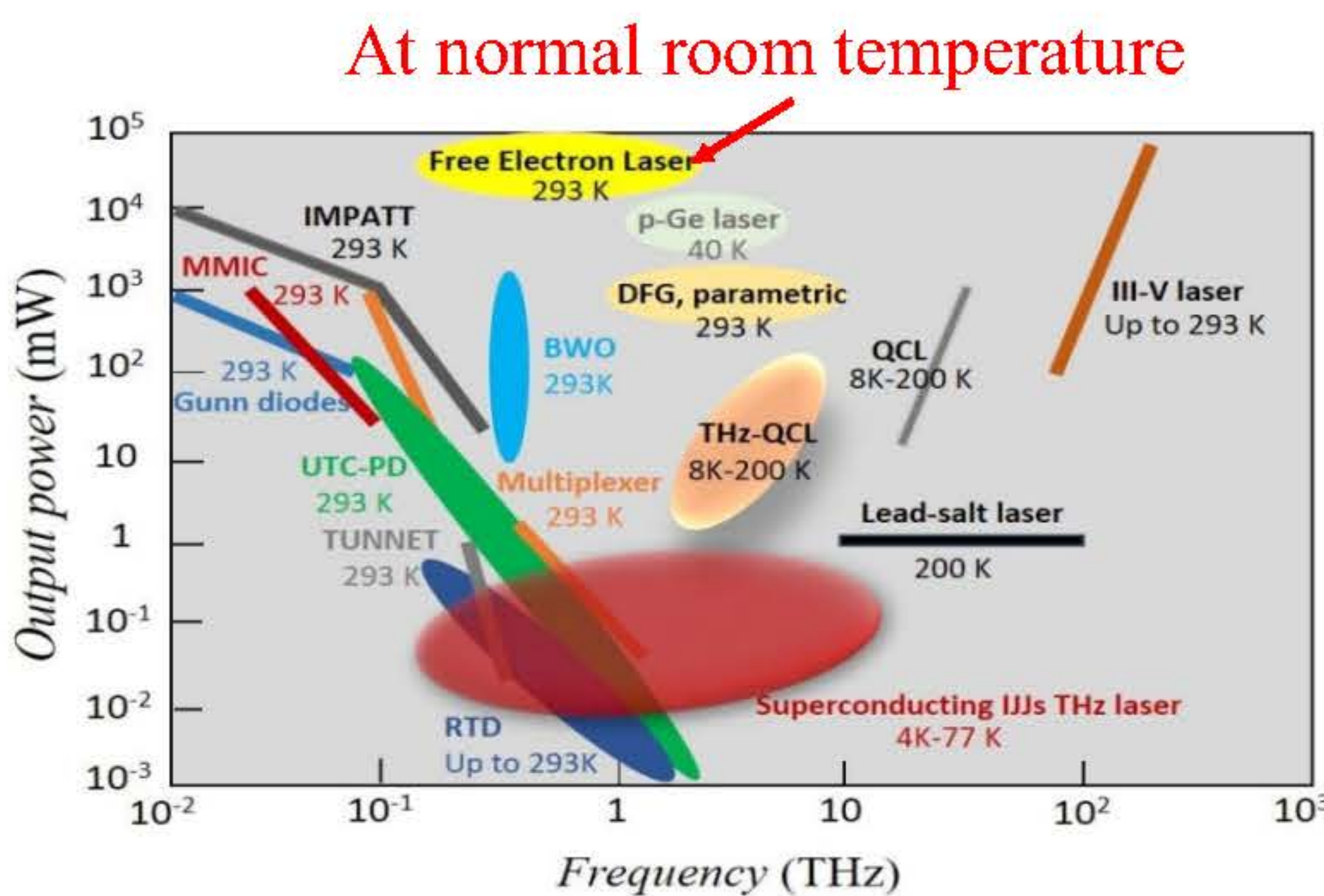
Department of Physics and Material Science, Faculty of Science, Chiang Mai University

Head of the project: Asst. Prof. Dr. Norraphat Srimanobhas

THz radiation in the EM spectrum



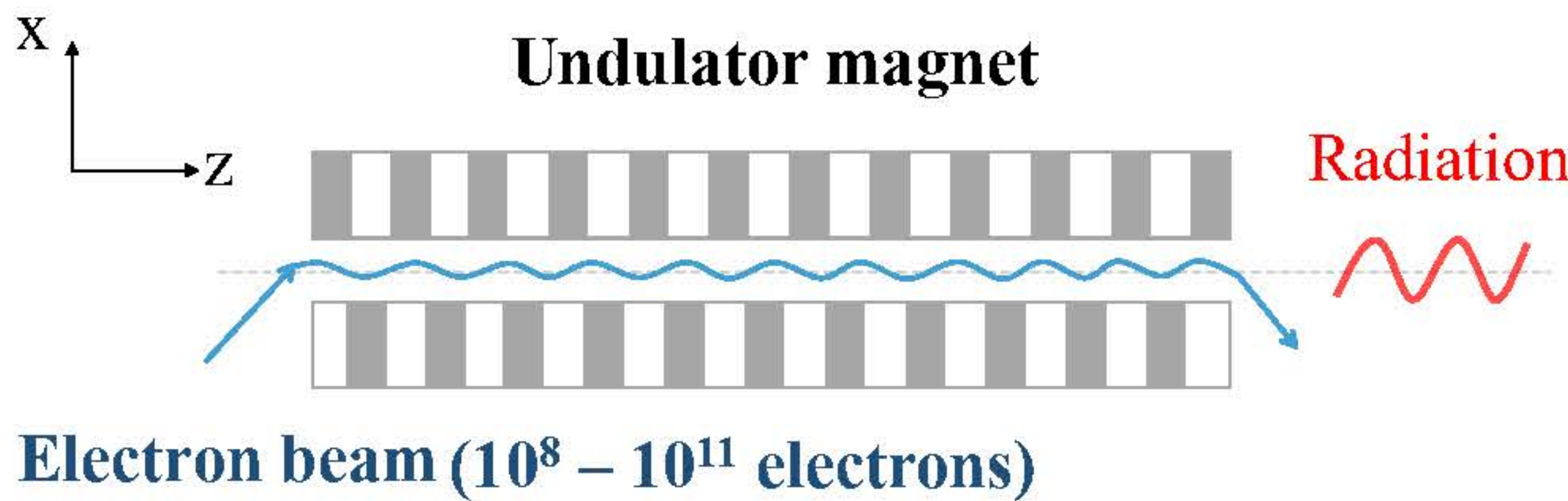
Advantages of Super-radiant FEL



- Coherent radiation
- High brightness
- Short pulse
- High peak power
- Tunable wavelength

FEL vs. Non-accelerator based lasers

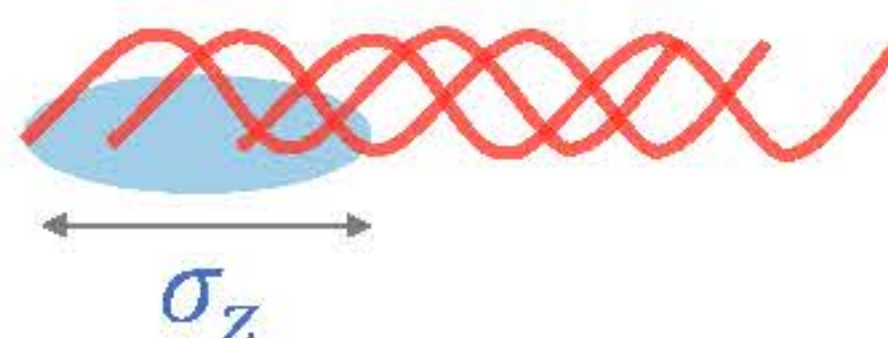
Super-radiant radiation



$$\lambda = \frac{\lambda_u}{2\gamma^2} \left(1 + \frac{K^2}{2} + \theta^2 \gamma^2 \right)$$

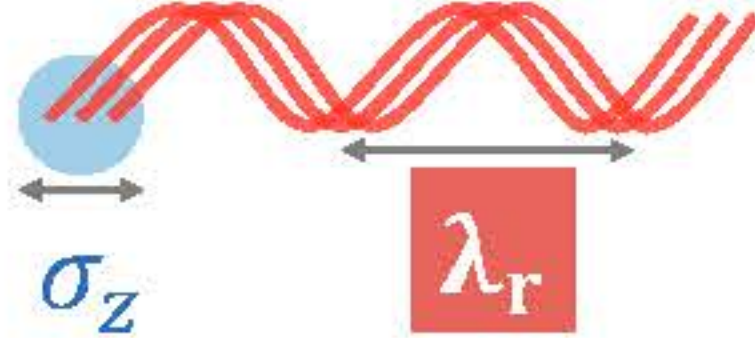
$$K = \frac{eB_0\lambda_u}{2\pi m_e c} = 0.934 B_0 [Tesla] \lambda_u [cm]$$

Incoherent radiation



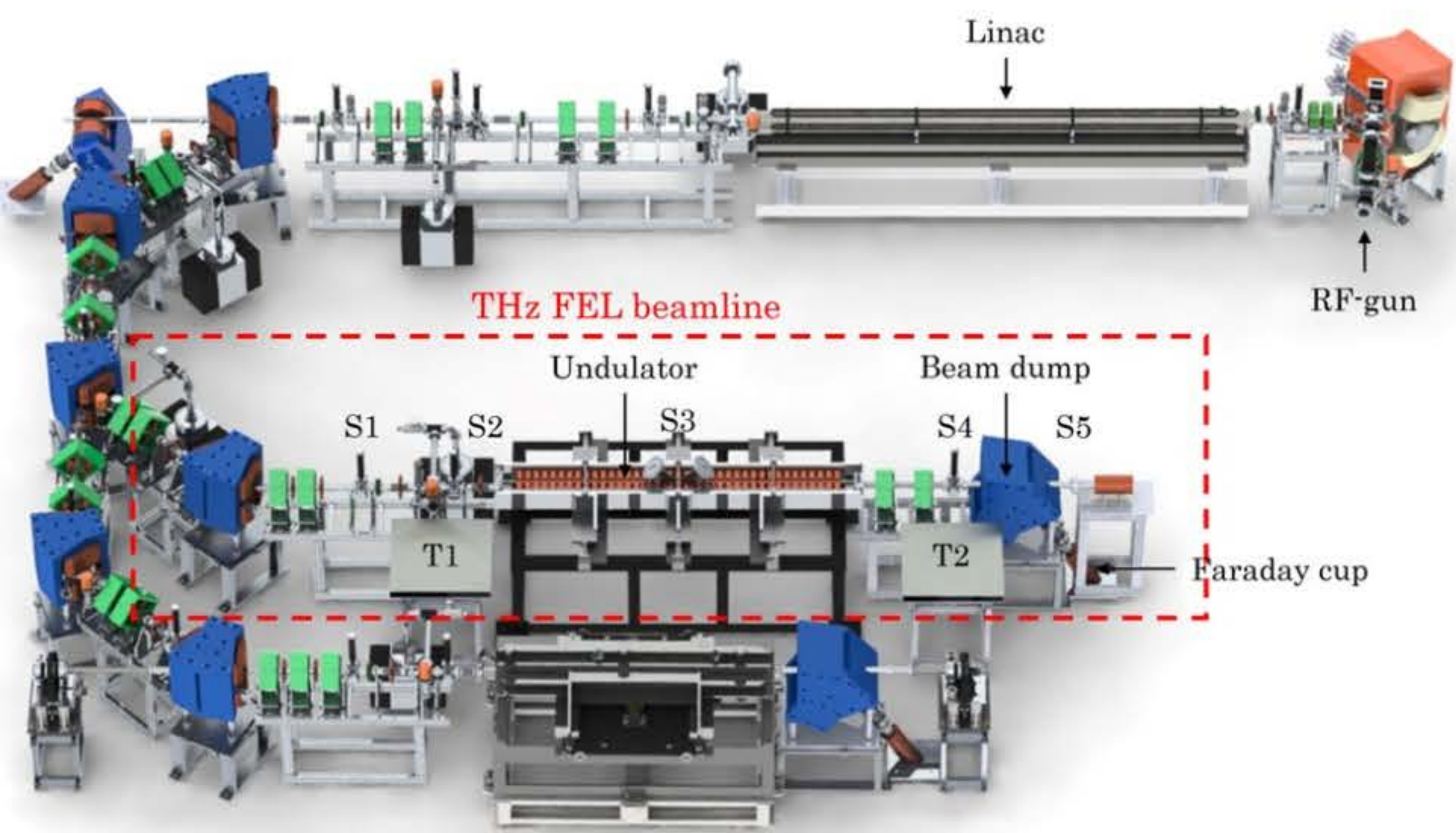
$$\text{Intensity} \propto N_e$$

Coherent radiation



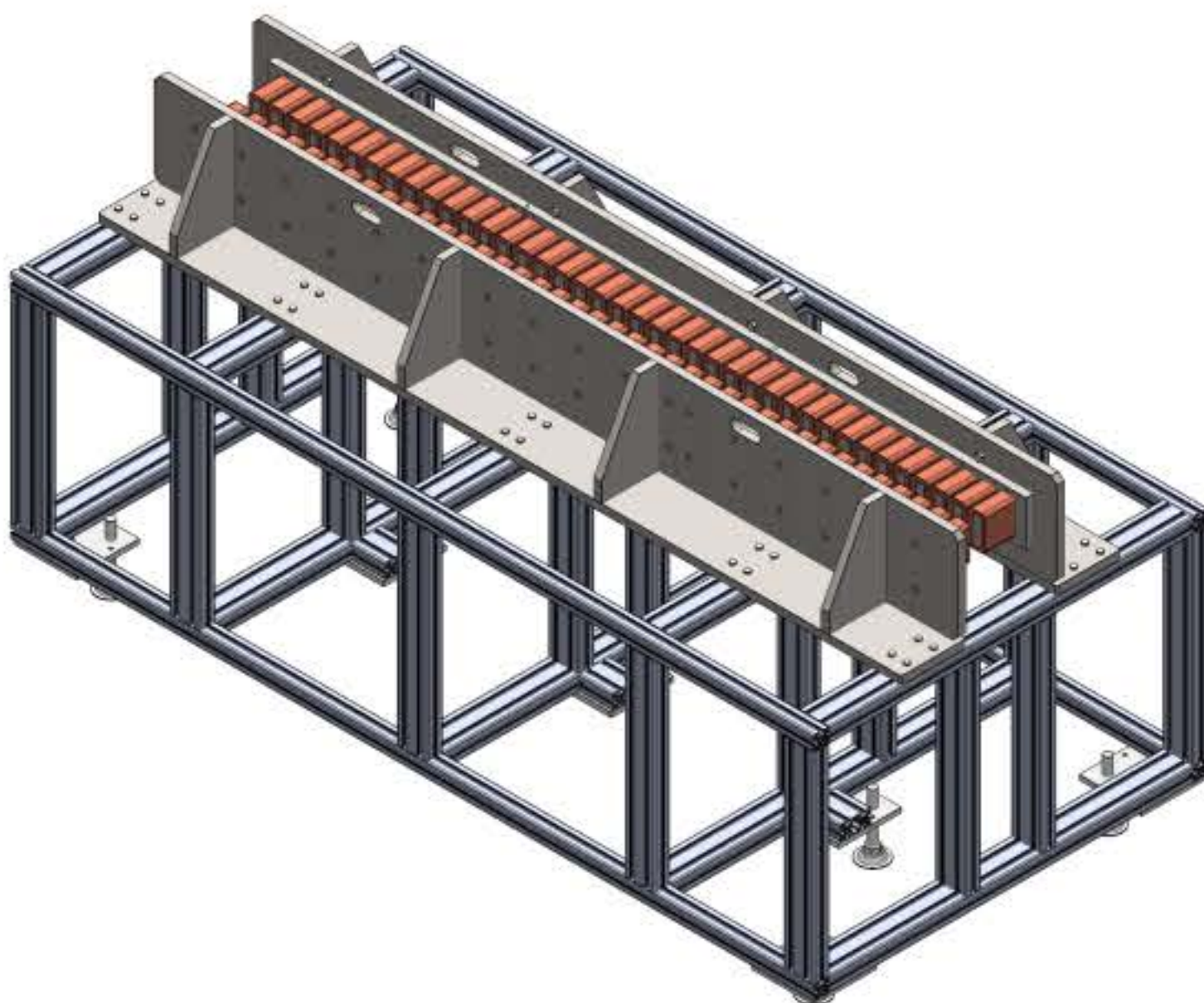
$$\text{Intensity} \propto N_e^2$$

THz FEL beamline at PCELL accelerator



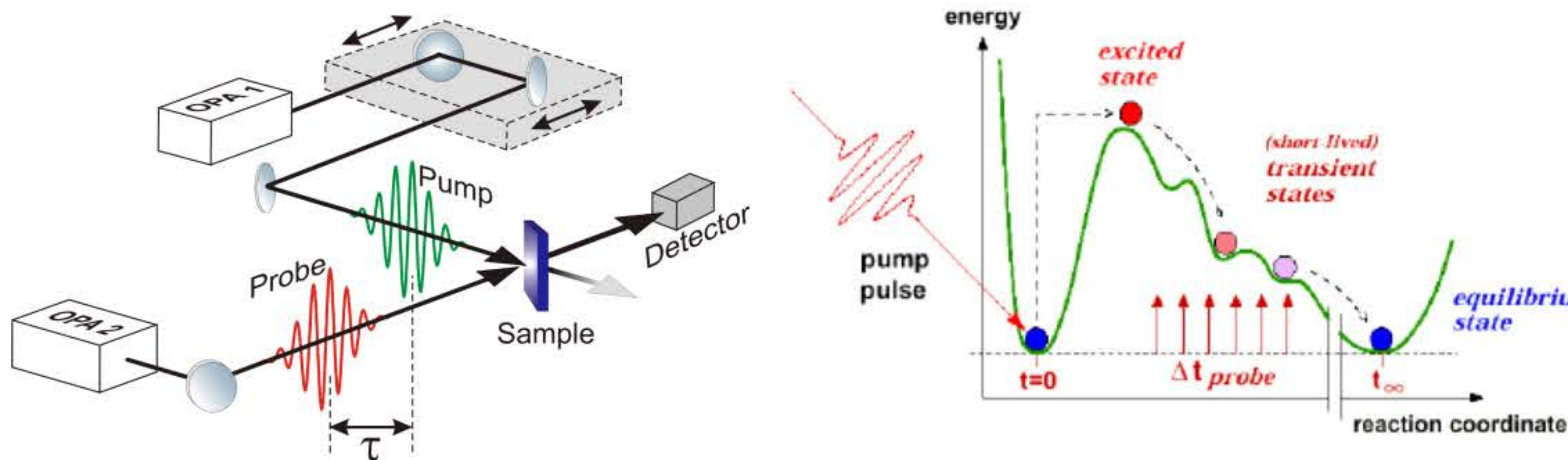
PCELL accelerator including THz FEL beamline

Parameter	Value	Unit
Number of periods	19.5	
Period length (λ_u)	100	mm
Gap width (g)	15	mm
Max. applied current	6	A
K parameter	0.1 - 2	
Radiation frequency	0.1 - 3	THz



Optimized parameters and the 3-D diagram of THz undulator

Applications for THz radiation



The pump pulse initially interacts with a sample response, and a probe pulse monitors the short-term interaction with the sample.

Optimum Electron Beam Properties

Electron beam properties	10 MeV	16 MeV
Bunch charge (pC)	50	50
RMS bunch length (fs)	304.3	203.4
Peak current (A)	165.7	245.7
Transverse emittance (mm.mrad)	0.42	0.34
Energy spread (%)	0.23	0.16

Start-to-end computer simulations of an electron beam along the PCELL THz-FEL beamline by using ASTRA code

Conclusion and Outlook

- Start-to-end computer simulations of an electron beam along the PCELL THz-FEL beamline were performed using ASTRA code
- Properties of the coherence radiation at the undulator exit evaluated using the SPECTRA code: tunable between 0.1 – 3 THz, 0.1 – 100 nJ
- Specifications of the undulator for THz-FEL amplification were investigated
- Additional components have been constructed and installed in the PCELL accelerator
- THz-FEL undulator is under construction and the optical equipment for THz radiation/FEL characterization is under discussion

Acknowledgment

This research has received funding support from the NSRF via the Program Management Unit for Human Resources & Institutional Development, Research and Innovation [grant number B13F660066]

Cosmological Model from Non-extensive Properties of Black Hole

Ratchaphat Nakarachinda^{†,1,2}, Chakrit Pongkitivanichkul³, Daris Samart³, Lunchakorn Tannukij², and Pitayuth Wongjun^{§,1}

¹ The Institute for Fundamental Study (IF), Naresuan University, 99 Moo 9, Tah Poe, Mueang Phitsanulok, Phitsanulok, 65000, Thailand

² Department of Physics, School of Science, King Mongkut's Institute of Technology Ladkrabang, 1 Chalong Krung 1 Alley, Lat Krabang, Bangkok 10520, Thailand

³ Khon Kaen Particle Physics and Cosmology Theory Group (KKPaCT), Department of Physics, Faculty of Science, Khon Kaen University, 123 Mitraphap Rd., Khon Kaen, 40002, Thailand

[†] Postdoctoral Researcher

[§] Corresponding Author; Email: pitbaa@gmail.com

Head of Beyond Standard Model Physics Project: Norraphat Srimanobhas

Introduction & Motivation

A challenge remains to be overcome in the dark energy model that describes the accelerated expansion of the Universe during the late-time epoch. In this study, the authors are interested in one of the candidates called holographic dark energy (HDE). Let us consider the bound in energy of an ordinary quantum system: $L_{IR}^3 \Lambda_{UV}^4 \lesssim M_{bh} \sim L_{IR}/G$, where Λ_{UV} , M_{bh} and G are the UV cutoff of the quantum field theory described the system, black hole's mass and Newtonian gravitational constant, respectively. It is obvious that there exists a sufficiently large length L_{IR} which does not preserve the aforementioned bound. The energy density for HDE is defined as matter with saturated energy that does not collapse into a black hole [1]:

$$\rho_{HDE} \sim \frac{1}{GL_{IR}^2}. \quad (1)$$

In studying the dynamics of the Universe using HDE model, the length scale L_{IR} need to be specified. The first attempt is to choose it as the Hubble radius. Unfortunately, HDE cannot drive the accelerated expansion. It rather evolves as a non-relativistic matter. The successful choice is the future particle horizon. Even though the late-time dynamics of the Universe can be explained, the model suffers from a theoretical problem of causality. Information in the future is required in order to describe the present-time phenomena.

Remarkably, the same energy density in Eq. (1) can also be obtained from the thermodynamic properties of black hole:

$$\rho_{HDE} \sim \frac{dM_{bh}}{dV} = \frac{T_H dS_{BH}}{dV}, \quad (2)$$

Here, the first law of black hole thermodynamics is applied at the second equality. T_H ($\sim 1/L$), S_{BH} ($\sim L^2/G$) and V ($\sim L^3$) are the Hawking temperature, Bekenstein-Hawking entropy and volume. It is very important to note that the S_{BH} is constructed based on standard Gibbs-Boltzmann (GB) statistics. However, the non-extensive nature of the black hole's entropy is inconsistent with an extensive property GB entropy. The suitable entropic function of black hole's area has been debatable. This study focuses on an alternative Rényi entropy:

$$S_R = \frac{1}{\lambda} \ln(1 + \lambda S_{BH}), \quad (3)$$

where λ is the non-extensive parameter [2]. A significant effect due to the non-extensivity is to stabilize the black hole as shown in Fig. 1 which is the diagram between the Gibbs free energy $\mathcal{G}_R = M_{bh} - T_R S_R$ and temperature $T_R = (\partial M_{bh} / \partial S_R)_\lambda$. This motivates the authors to construct a dark energy via Rényi thermodynamics so-called Rényi Holographic dark energy (RHDE).

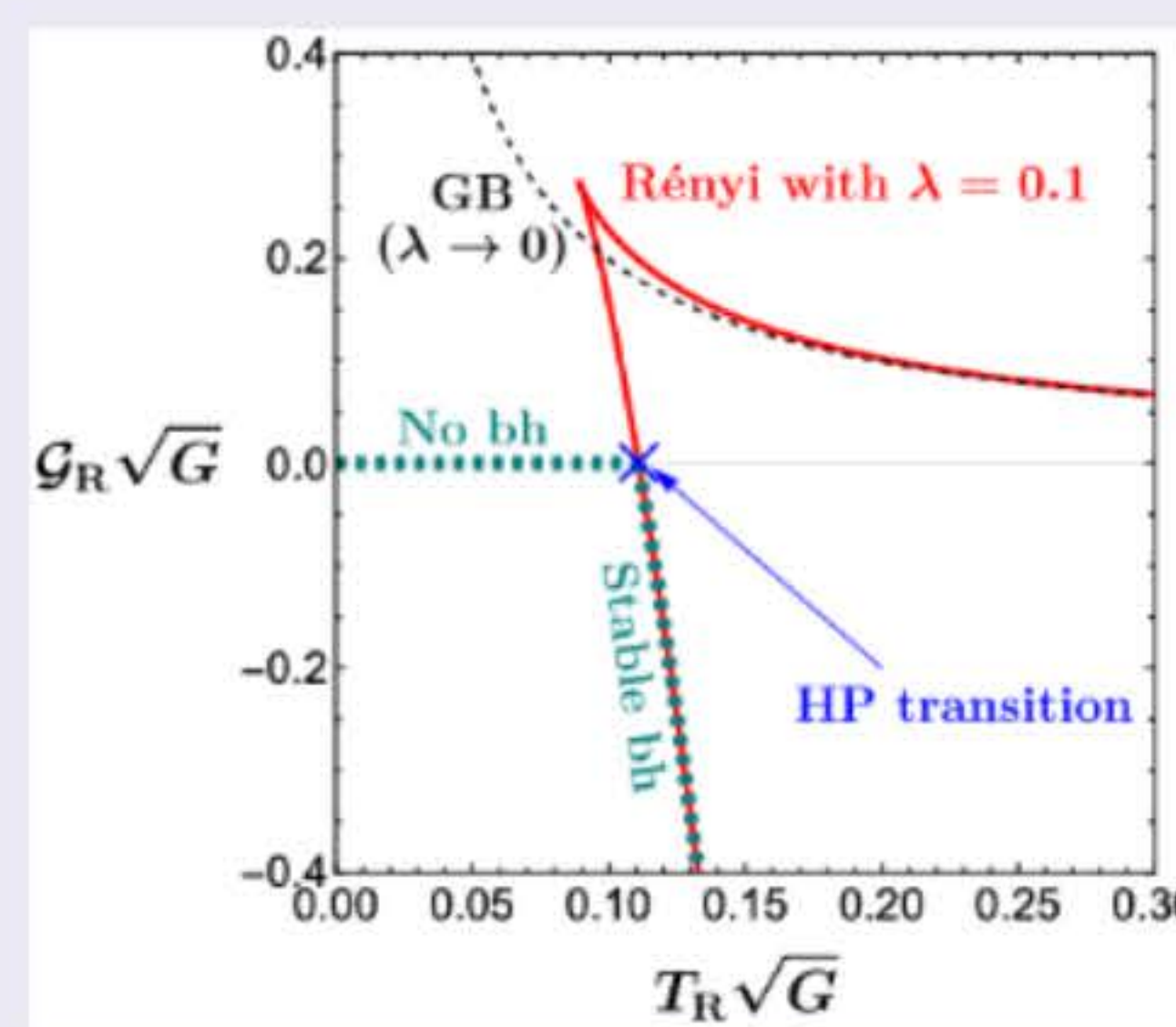


Figure 1: Phase structure of black hole

Methods

- Based on the Rényi description of black hole thermodynamics, the phase space of the black hole must be reconsidered. The thermodynamic quantities and relations are modified and the phase space is necessarily extended [3].

$$dM_{bh} = T_R dS_R + V_R dP_R, \quad M_{bh} = 2T_R S_R - 2V_R P_R. \quad (4)$$

In this consideration, the non-extensive parameter is interpreted as thermodynamic pressure: $P_R = 3\lambda/(32G^2)$. The volume V_R is proportional to the conjugate quantity of λ : $V_R = (\partial M_{bh} / \partial P_R)_{S_R}$.

- According to the stabilization of the Rényi black hole, the energy density is defined via the change under fixed- λ process. To avoid the causality problem, we construct the cosmological model by choosing the IR length scale as the Hubble radius

$$\rho_{RHDE} \sim \left(\frac{dM_{bh}}{dV_R} \right)_\lambda = \frac{9b^2}{16\pi G l_\lambda^2 \left[1 + \left(1 - \frac{l_\lambda^2}{l_H^2} \right) \ln \left(1 + \frac{l_\lambda^2}{l_H^2} \right) \right]}, \quad (5)$$

where b^2 , $l_H = H_0/H$ and $l_\lambda = H_0 \sqrt{G/(\pi\lambda)}$ are the conventional constant, dimensionless Hubble radius and non-extensive length, respectively. H_0 is the Hubble parameter at present.

- A code for cosmological parameter estimation called SimpleMC [4] is used in constraining the model parameter from various observational datasets.

Results

In a very small l_H limit, RHDE evolves identically to the dominant species in the Universe. The Universe in this scenario cannot be expanded with acceleration. On the other hand, the energy density of RHDE is approximately constant. It affects cosmic evolution in the same way as the cosmological constant does. By solving the Friedmann equation numerically, the dynamics of the Hubble horizon are illustrated in Fig. 2. This result means that RHDE behaves as a scaling solution at early-time epoch and becomes a dominated contribution in driving the accelerated expansion at late time.

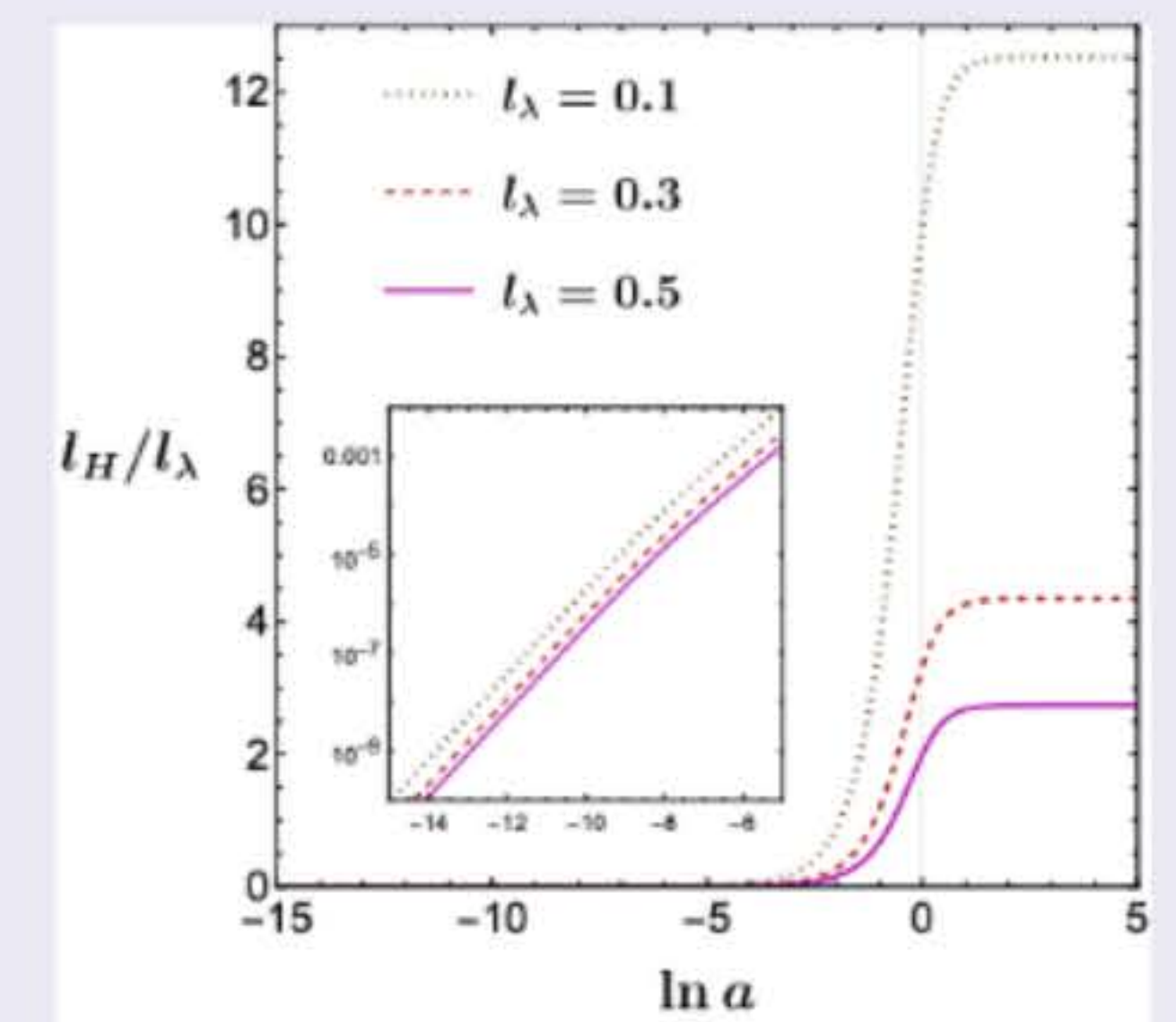


Figure 2: Evolution of Ratio l_H/l_λ

According to the observations at the early time and present [5], the ratio of the dark energy in the Universe is constrained corresponding to the viable range of parameter space: $0 < l_\lambda \lesssim 0.14$. We further determine the preferable value of l_λ using the likelihood analysis with the low-redshift datasets: Cosmic Chronometer (CC), Baryon Acoustic Oscillations (BAO), and Supernovae (SN) [6]. The quality in fitting the observational datasets is represented as the lower Akaike information criterion (AIC). From the results in Fig. 3, the best-fit

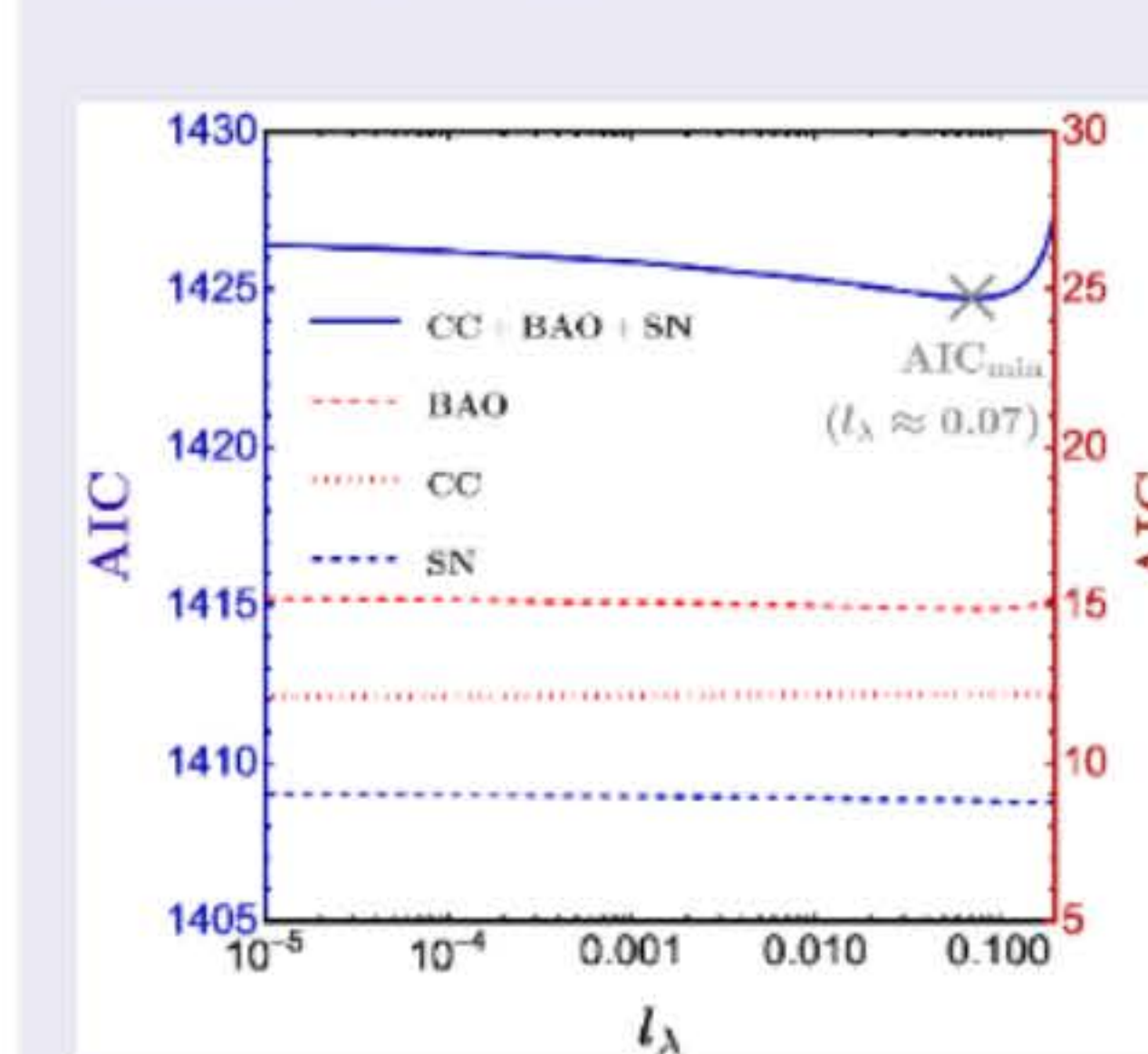


Figure 3: AIC of RHDE model with varying l_λ

cosmological model is obtained when the model parameter is set as $l_\lambda \approx 0.07$. In comparing RHDE to other models, it is slightly better than the standard Λ CDM model as seen in Tab. 1.

Table 1: Estimator of each model compared with Λ CDM

Models	AIC	Δ AIC
Λ CDM	1427.386	0
RHDE with $l_{\lambda, AIC_{min}}$	1424.754	-2.632
AdS-HDE: fixed b^2	1429.912	2.526
AdS-HDE	1431.910	4.524

Conclusion & Discussion

The accelerated expansion of the Universe nowadays can be explained using the proposed RHDE model without the causality problem. The effect of non-extensivity due to Rényi entropy can be thought of as the characteristic length in the context of cosmology (see Fig. 4).

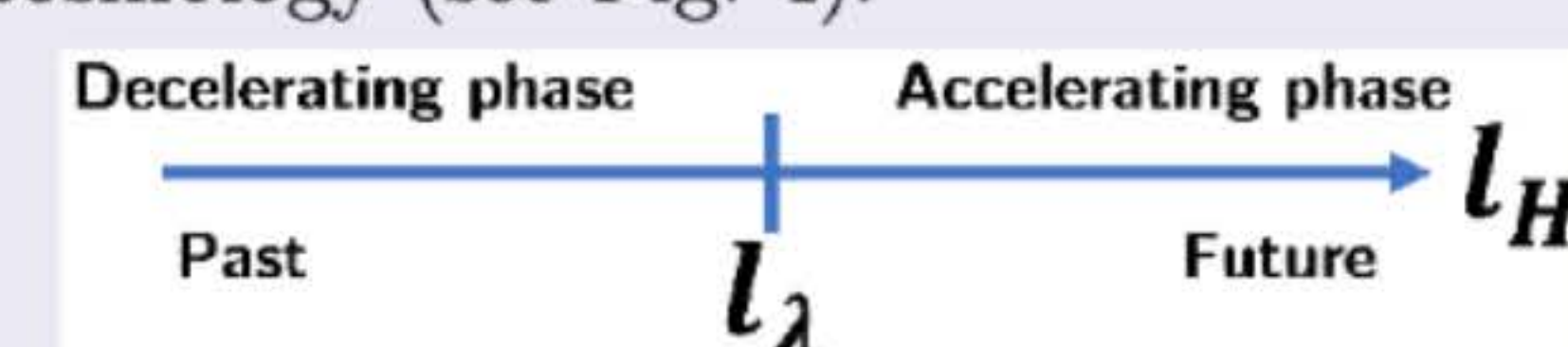


Figure 4: Regimes of l_H associated with dynamics of Universe

The Universe is affected by non-extensivity when its size is sufficiently large, and then transits from decelerating to accelerating phases. Note that it seems to be impossible in investigating the full perturbation analysis because the field description of HDE is still ambiguous.

Acknowledgements

This research has received funding support from the NSRF via the Program Management Unit for Human Resources & Institutional Development, Research and Innovation [grant number B13F660066].

References

- [1] S. D. H. Hsu, Phys. Lett. B **594**, 13–16 (2004); M. Li, Phys. Lett. B **603**, 1 (2004).
- [2] A. Rényi, Acta Mathematica Academiae Scientiarum Hungarica **10**, 193–215 (1959).
- [3] R. Nakarachinda, C. Promsiri, L. Tannukij and P. Wongjun, [arXiv:2211.05989 [gr-qc]].
- [4] J. A. Vazquez, I. Gómez-Vargas, and A. Slosar, Available in <https://igomezv.github.io/SimpleMC/index.html>
- [5] R. Bean, S. H. Hansen, and A. Melchiorri, Phys. Rev. D **64**, 103508 (2001); N. Aghanim et al. [Planck], Astron. Astrophys. **641**, A6 (2020) [erratum: Astron. Astrophys. **652**, C4 (2021)].
- [6] M. Moresco, R. Jimenez, L. Verde, A. Cimatti and L. Pozzetti, Astrophys. J. **898**, no.1, 82 (2020); S. Alam et al. [eBOSS], Phys. Rev. D **103**, no.8, 083533 (2021); D. Brout et al. Astrophys. J. **938**, no.2, 110 (2022).

Exploring Holographic Phase Transitions of Black Hole Through Lyapunov Exponent Probes

Chatchai Promsiri¹, Weerawat Horinouchi³, Ekapong Hirunsirisawat^{1,2} and Norraphat Srimanobhas³

¹Quantum Computing and Information Research Centre (QX), Faculty of Science, King Mongkut's University of Technology Thonburi, Bangkok, Thailand

²Learning Institute, King Mongkut's University of Technology Thonburi, Bangkok, Thailand

³Department of Physics, Faculty of Science, Chulalongkorn University, Bangkok, Thailand

Introduction

- In holography or AdS/CFT correspondence, the thermodynamic variables of black holes in the bulk Anti-de Sitter (AdS) space correspond to the thermal states of the conformal field theory (CFT) on its boundary. In this way, the Smarr formula that relates the thermal variables of black holes should be matching to the Euler relation in the dual CFT. However, it has found that the bulk pressure P which associate to the cosmological Λ term and its conjugate variable, namely the bulk volume V does not dual to the boundary pressure p and the spatial volume v of the field theories.

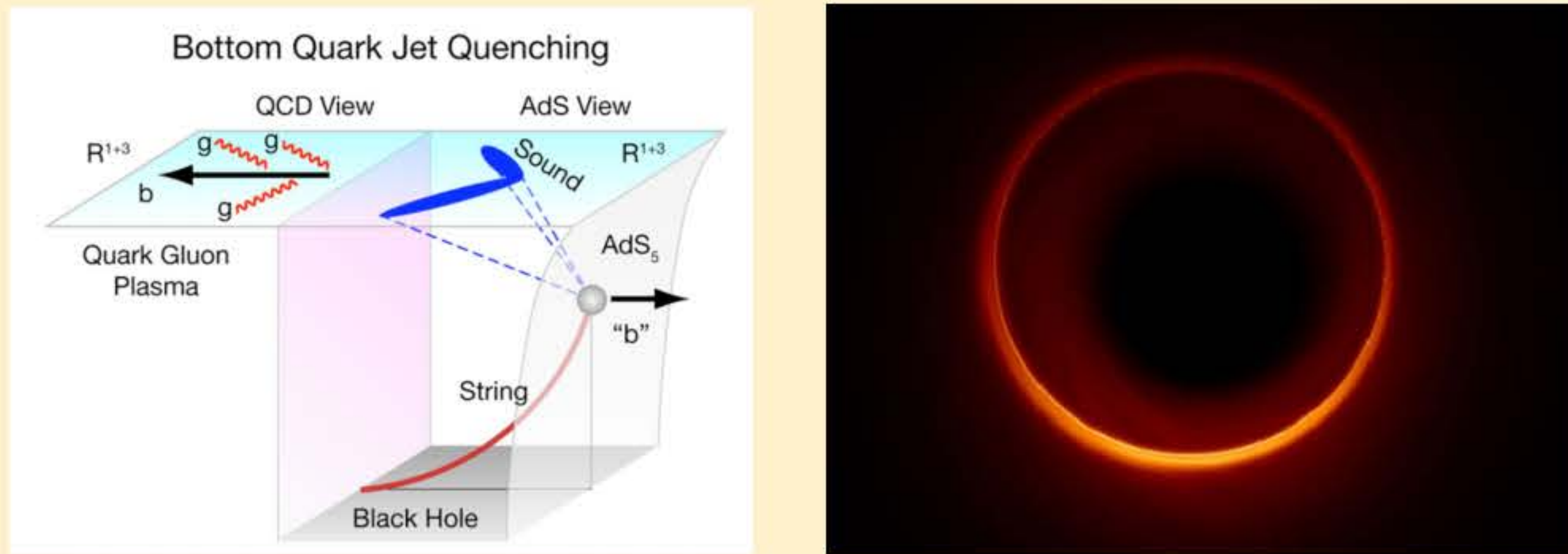


Figure 1 (Left) The energy loss in quark jet quenching in plasma that is holographic dual to a probing string drag in the background of AdS black hole. (Right) The photon ring of black hole.

- This problem can be resolved by assuming both the cosmological constant Λ and the Newton's constant G_N as the thermodynamic variable in the Smarr formula. From holography, variation of these variables lead to vary the central charge C of the dual CFT. The result indicates that all the terms in the first law of black hole and CFT thermodynamics are perfectly dual in the contexts of AdS/CFT correspondence.
- In seeking to determine the manifestation of thermal phase transitions in black holes, a common experimental approach involves the introduction of probes into a system, subsequently analyzing its response.
- In the context of this study, we employ this methodology to investigate the gravitational phase transition of charged AdS black holes that include the new pair of thermodynamic variable, i.e. C and its chemical potential μ_c , within the framework of holographic thermodynamics. This is achieved by adding probe particles into the bulk and examining their response, specifically focusing on the manifestation of geodesic instability.

Methods

- Holographic Thermodynamics of Charged AdS Black hole:
- The first law of black hole in the bulk

$$dM = \frac{\kappa}{2\pi} d\left(\frac{A}{4G_N}\right) + \frac{\Phi}{L} d(QL) - \frac{M}{n-1} \frac{dL^{n-1}}{L^{n-1}} + \left(M - \frac{\kappa A}{8\pi G_N} - \Phi Q\right) \frac{d(L^{n-1}/G_N)}{L^{n-1}/G_N}$$

- The CFT first law at the boundary

$$dE = TdS + \tilde{\Phi}d\tilde{Q} - pdv + \mu dC$$

with $\mu = \frac{1}{C}(E - TS - \tilde{\Phi}\tilde{Q})$ and $p = \frac{1}{n-1} \frac{E}{v}$.

- The first law of these two systems are equivalent when one identified the thermodynamic variables of CFT in terms of the gravitational theory as follow

$$E = M$$

$$\tilde{\Phi} = \frac{\Phi}{L}$$

$$\tilde{Q} = QL$$

$$v \sim L^{n-1}$$

$$C \sim \frac{L^{n-1}}{G_N}$$

Instability of circular geodesics:

- The Lyapunov exponent γ_L is a mathematical measure of sensitivity to initial conditions in a dynamic system.
- A positive Lyapunov exponent indicates chaotic behavior, meaning that small changes in initial conditions lead to unpredictable and divergent trajectories.
- In the context of particles motion near the black hole, it characterizes the rate at which nearby trajectories diverge from each other due to small perturbations in the initial conditions of the geodesics.
- The Lyapunov exponents for circular motion of massless particle near the black holes is given by

$$\gamma_L = \sqrt{-\frac{r_u^2 f'(r_u)}{2L^2} V''(r_u)}$$

In a case of massive particles, we have

$$\gamma_L = \frac{1}{2} \sqrt{[r_u f'(r_u) - 2f(r_u)] V''(r_u)}$$

Results & Discussion

- Extended canonical ensemble of CFT or fix (\tilde{Q}, v, C) ensemble

CFT phases	Black Hole phases	Color in the figures
Liquid (low entropy state)	Small black hole	Red
Mixed phases	Intermediate black hole	Green
Gas (high entropy state)	Large black hole	Blue

Table 1 The corresponding phases between the thermal states of CFT on the boundary and the charged AdS black holes in the bulk.

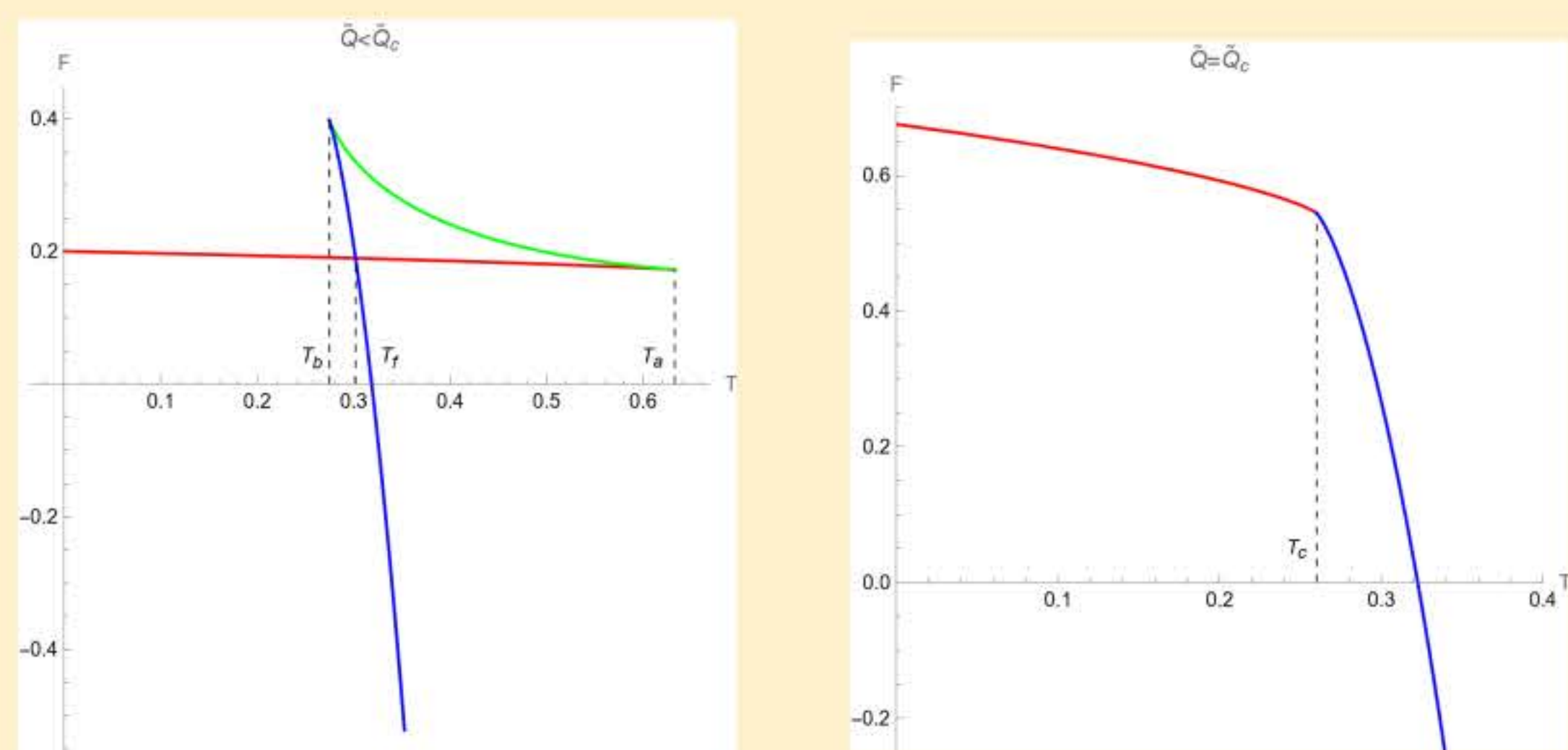


Figure 2 The free energy of CFT as a function of temperature with fix $C = 1$. (Left) For $\tilde{Q} < \tilde{Q}_c$, the free energy display the swallow tail shape. (Right) The swallow tail shape disappears when \tilde{Q} approach to the critical value.

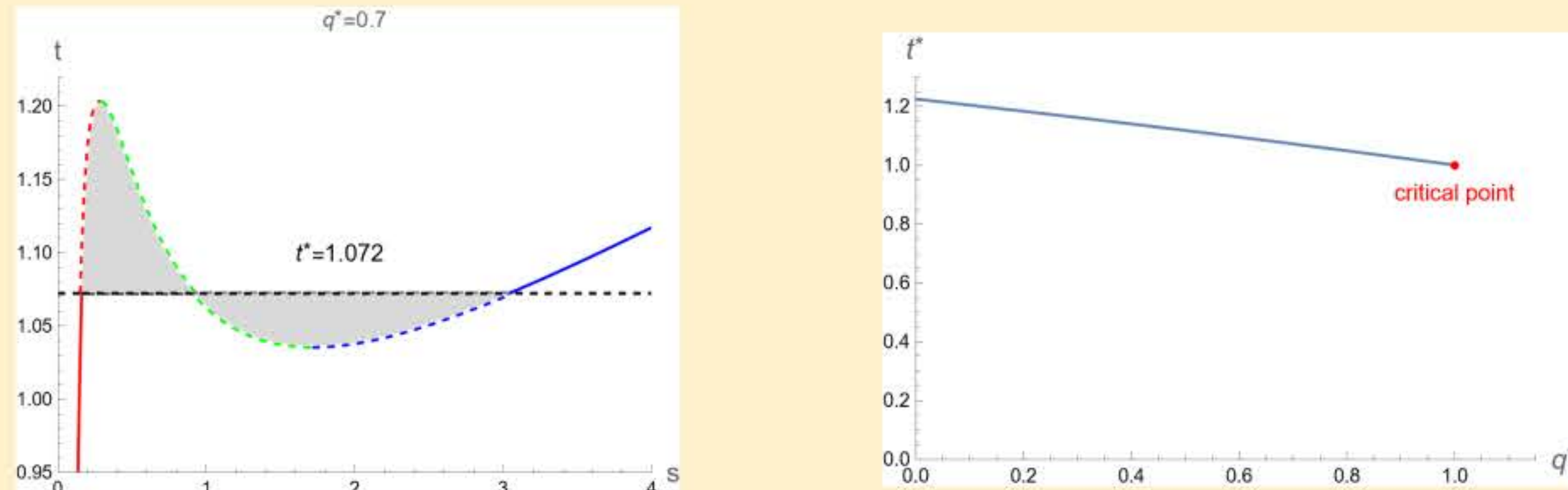


Figure 3 (Left) The rescaled $t - s$ graph of CFT with $q^* = 0.7$, the Maxwell equal area law indicate that the first-order phase transition occurs at $t^* = 1.072$. (Right) Plot t^* against q^* , the red point represents the critical point of the ensembles with fix $C = 1$.

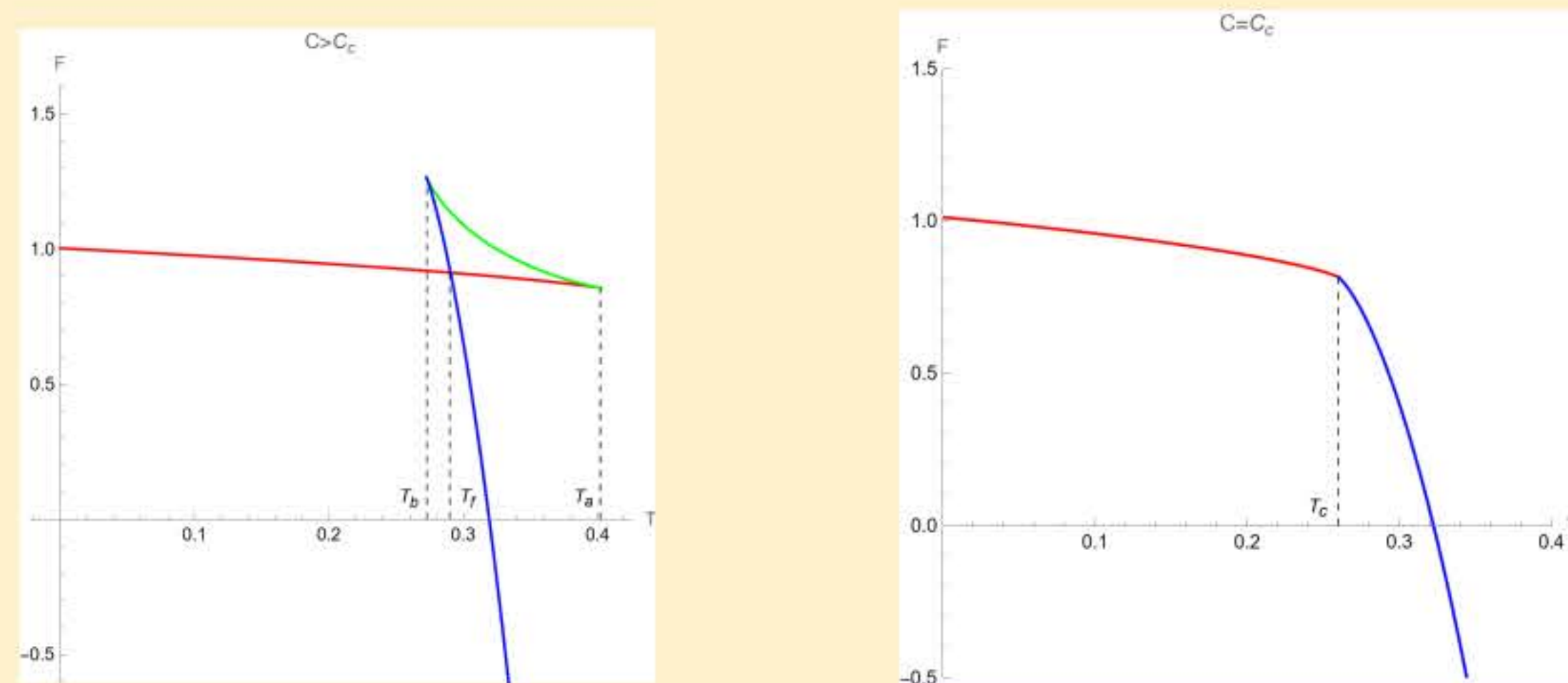


Figure 4 The free energy of CFT as a function of temperature with fix $\tilde{Q} = 1$. (Left) For $C > C_c$, the free energy display the swallow tail shape. (Right) The swallow tail shape disappears when the central charge approach to the critical value.

- Lyapunov exponents probe the dual black holes phase transition

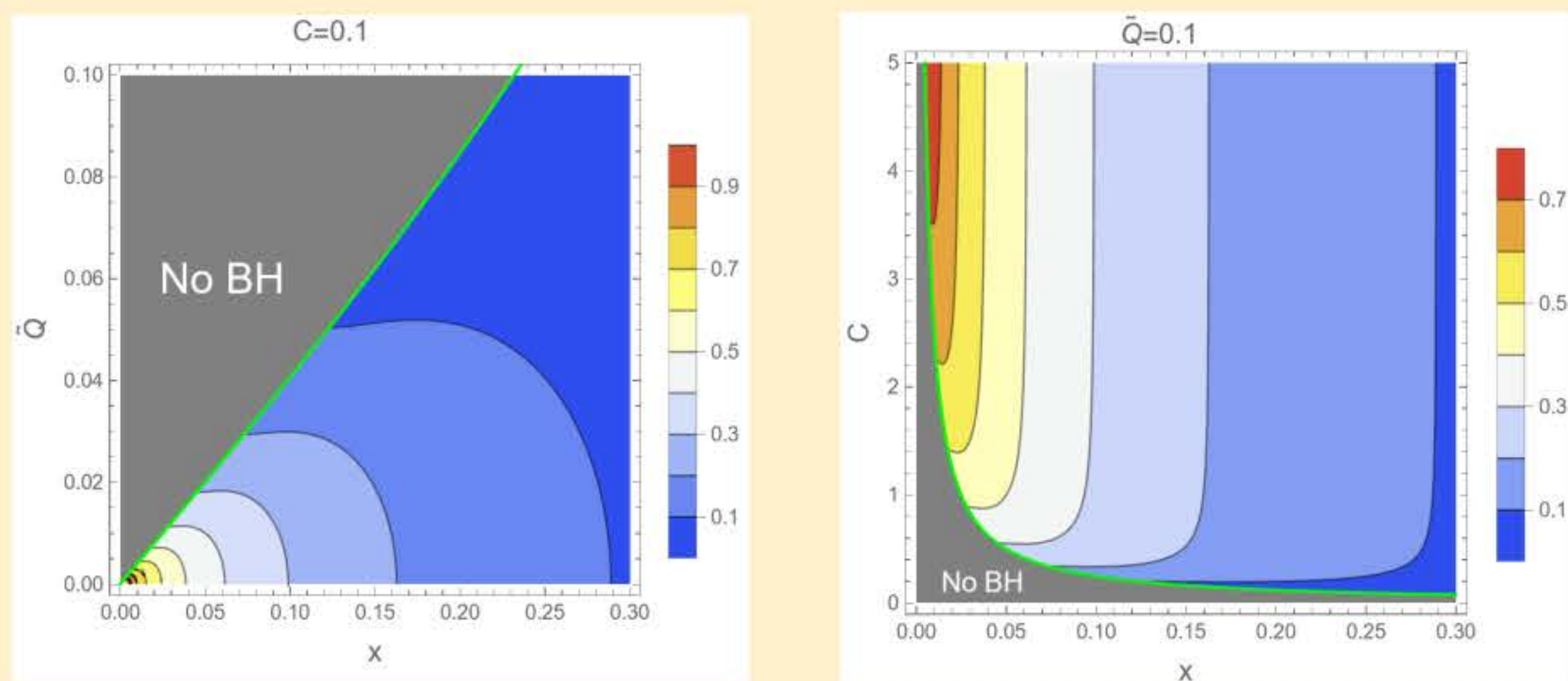


Figure 5 (Left) Contour plot of $\log_{10} \gamma_L$ for massless particle in $\tilde{Q} - x$ plane with fix C . (Right) Contour plot of $\log_{10} \gamma_L$ for massless particle in $C - x$ plane with fix \tilde{Q} .

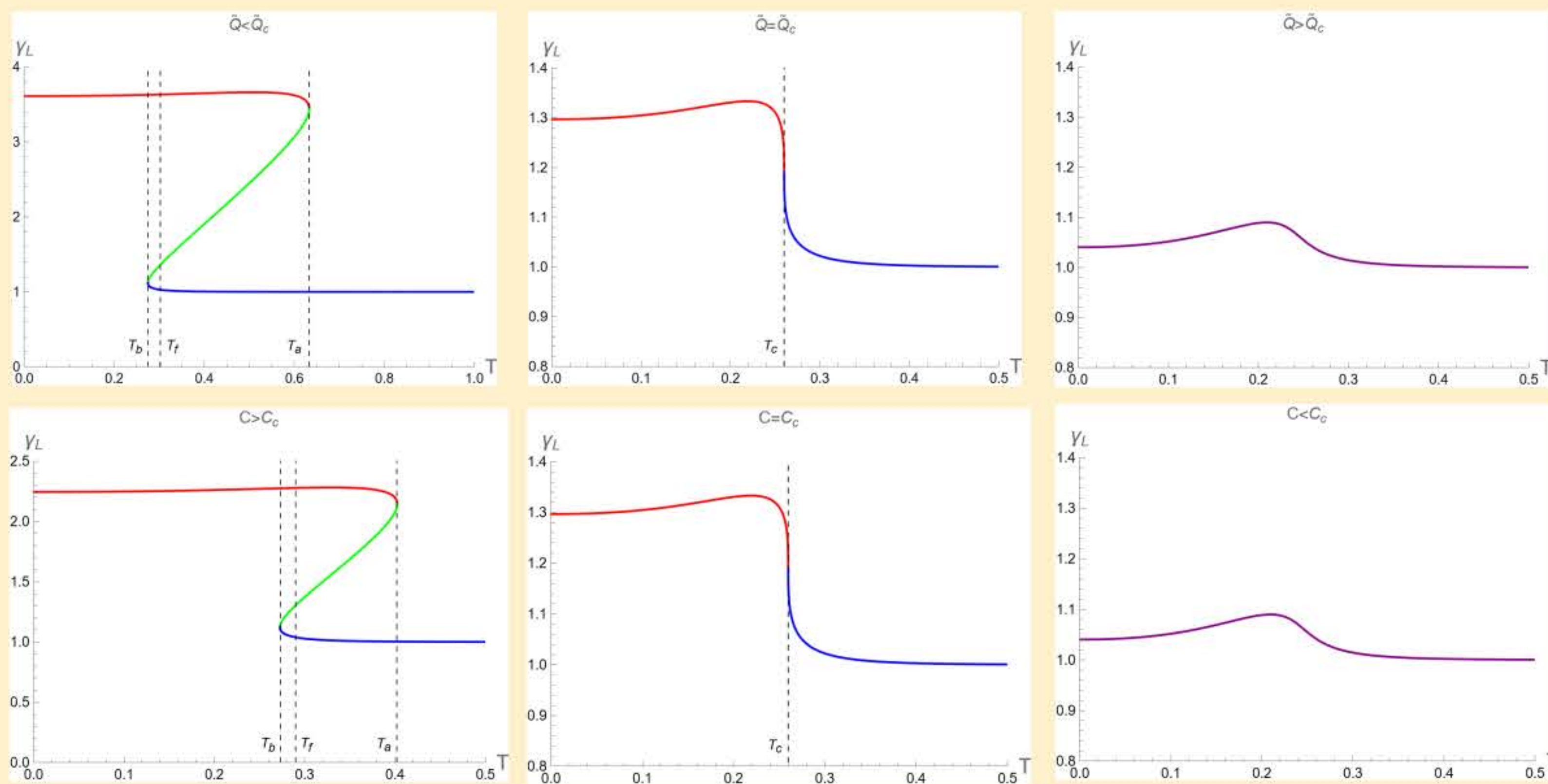


Figure 6 Plot Lyapunov exponent of null circular orbit against the temperature of black hole for fix C and \tilde{Q} in the first row and the second row, respectively.

Conclusion

- The concept of black hole thermodynamics has been theorized for an extended period, yet it has not been practically connected to astronomical observations.
- This study explores the holographic thermodynamics of charged black holes by using the distinctive characteristics of photon rings encircling black holes.
- Our results exhibits many aspects consistent with those from conventional black hole thermodynamics.
- Analyzing through Maxwell's equal area construction, the results show that the first order phase transition temperature decreases as the black hole charge is larger.
- Intriguingly, the black hole phase transition is investigated using Lyapunov exponent, which is a measure of sensitivity to initial condition of photon trajectories.
- This work is in progress and will be extended with further calculations on trajectories of massive particles around black holes. The holographic phase transition could be discussed more from the upcoming results.

Acknowledgements

This research has received funding support from the NSRF via the Program Management Unit for Human Resources & Institutional Development, Research and Innovation [grant number B13F660066]

References

- Aharony O., Gubser S., Maldacena J., Ooguri H. and Oz Y. Large N field theories, string theory and gravity, Phys.Rept. 323 (2000) 183-386.
- Gyulassy M. Getting to the bottom of the heavy quark jet puzzle, Physics 2, 107 (2009).
- Johnson M., et al. Universal interferometric signatures of a black hole's photon ring, Sci. Adv. 2020, 6, eaaz, 1310.
- Visser M. Holographic thermodynamics requires a chemical potential for color, Phys. Rev. D 105 (2022) 106014.
- Cong W., Kubiznak D., Mann R. and Visser M. Holographic CFT phase transitions and criticality for charged AdS black holes, JHEP 08 (2022) 174.
- Xiaobo Guo, Yuhang Lu and Peng Wang. Probing phase structure of black holes with Lyapunov exponents, JHEP 08 (2022) 153.



BRAINPOWER
CONGRESS 2023

ร่วมกันสร้างและขับเคลื่อนงานวิจัยขั้นแนวหน้า
สู่อุตสาหกรรมแห่งอนาคต



NANOTEC
a member of NSTDA

Development of biphenylene as two-dimensional material for hydrogen storage: A first-principles computational approach

Maneerat Chotsawat^a, Lappawat Ngamwongwan^b, Sirichok Jungthawan^b, Anchalee Junkaew^{c,*}, Suwit Suthirakun^{a,*}

^a School of Chemistry, Institute of Science, Suranaree University of Technology, Nakhon Ratchasima 30000, Thailand

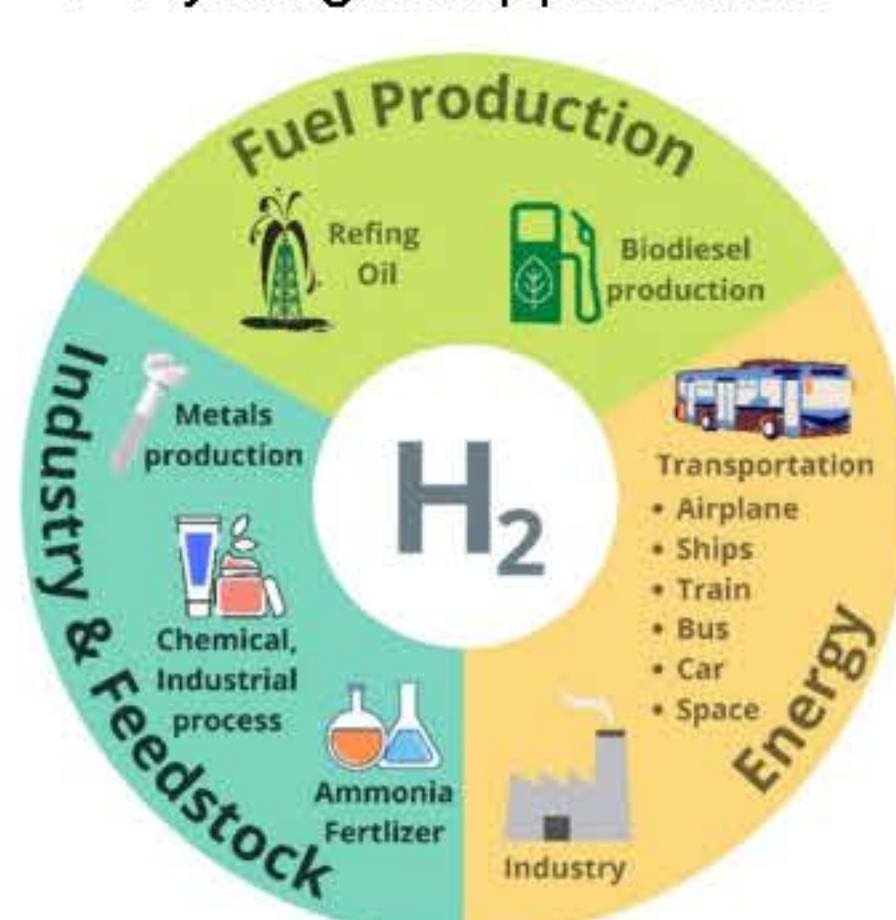
^b School of Physics, Institute of Science, Suranaree University of Technology, Nakhon Ratchasima 30000, Thailand

^c National Nanotechnology Center (NANOTEC), National Science and Technology Development Agency (NSTDA), 111 Thailand Science Park, Pathum Thani, 12120, Thailand

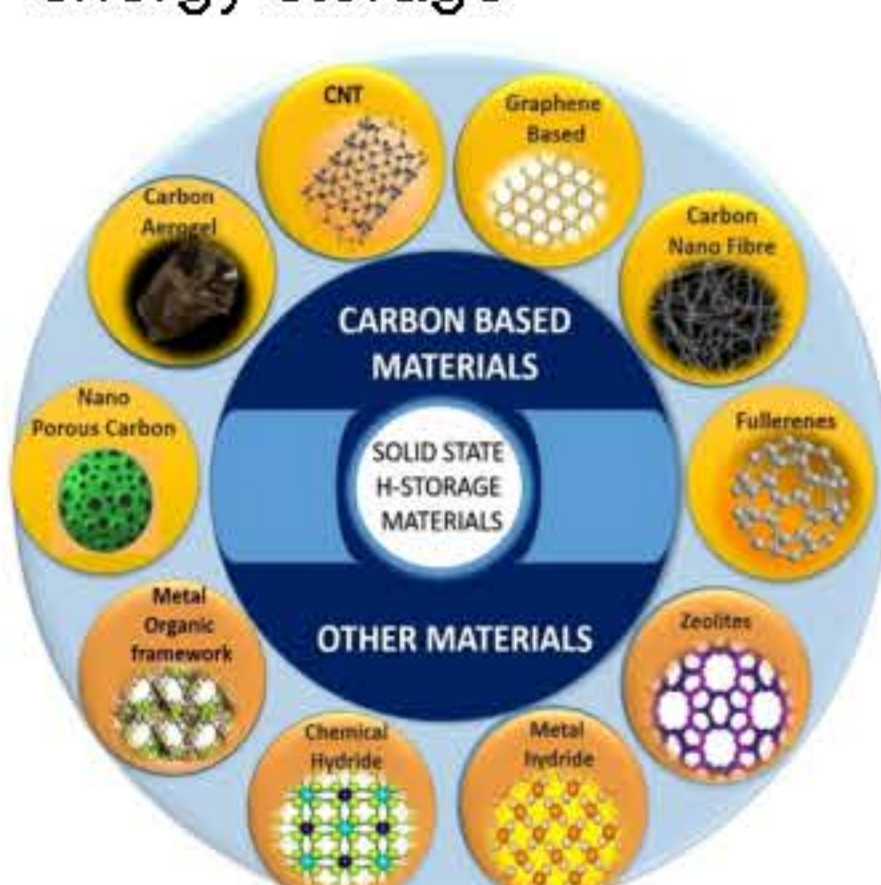
* Corresponding author: anchalee@nanotec.or.th (A. Junkaew); suthirak@sut.ac.th (S. Suthirakun)

Introduction

❖ Hydrogen applications



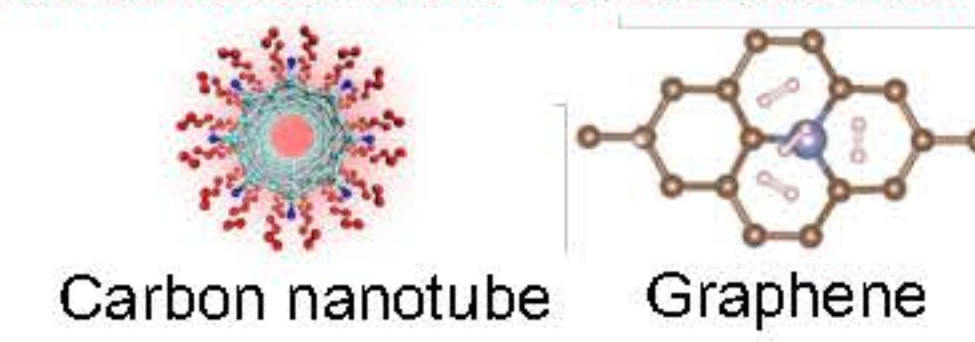
❖ Materials for hydrogen-based energy storage



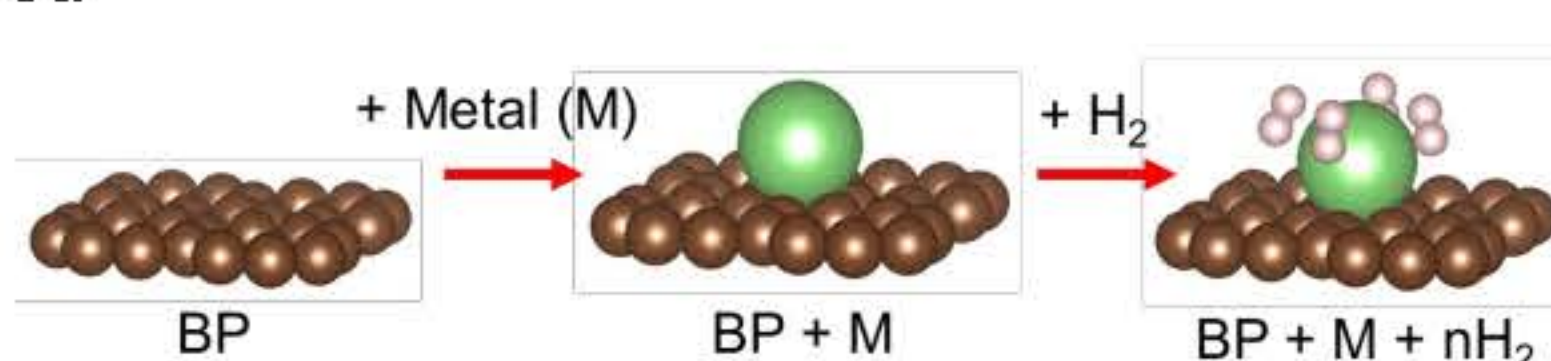
❖ Limitations of pristine nanomaterials

- High desorption temperatures
- High metal clustering
- Instability at higher temperatures

❖ Metal decorated nanomaterials



- Can improve H₂ adsorption
- Enhances the hydrogen storage capacity



❖ Advantages of Hydrogen

- Clean fuel
- Sustainable
- Eco-friendly
- High energy density
- Better safety

❖ Advantages of biphenylene (BP)

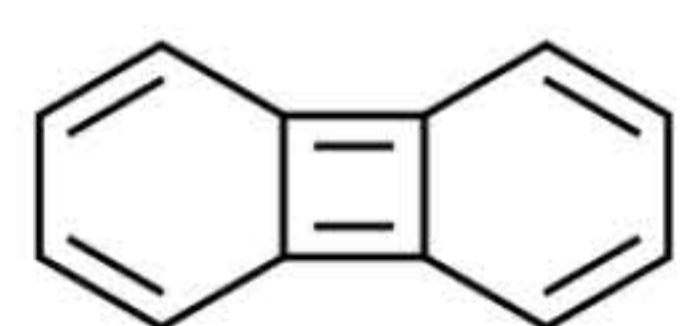
- Metallic
- Large surface area
- Abundance
- Low cost
- Light weight

Objective

- To study and develop the efficiency of two-dimensional materials in the biphenylene (BP) group for hydrogen storage using computer simulation based on the theory of density functional theory (DFT).
- To investigate the mechanism of hydrogen adsorption on two-dimensional materials in the biphenylene group with different types of decorated metals.

Computational details

- DFT calculations: VASP 6
- PAW and PBE functional
- Van der waal correlation: DFT-D3
- Energy and force convergence criterion: 1x10⁻⁶ eV and 0.01 eV/Å
- 2 x 2 biphenylene monolayer model: 7 x 7 x 1 k-points; 500 eV cutoff
- Calculation of adsorption energy for BP + M :



Biphenylene structure

$$E_{ads} = E_{tot(BP+M)} - E_{tot(BP)} - E_{tot(M)}$$

- Calculation of charge density difference for BP + M :

$$\Delta\rho = \rho(BP + M) - \rho(BP) - \rho(M)$$

- Calculation of average adsorption energy for BP + M + H₂ :

$$E_{ads} = \frac{E_{tot(BP+M+nH_2)} - E_{tot(BP+M)} - (nE_{tot(H_2)})}{n}$$

- Calculation of charge density difference for BP + M :

$$\Delta\rho = \rho(BP + M + nH_2) - \rho(BP + M) - \rho(nH_2)$$

- Calculation of gravimetric hydrogen wt% for BP + M + H₂ :

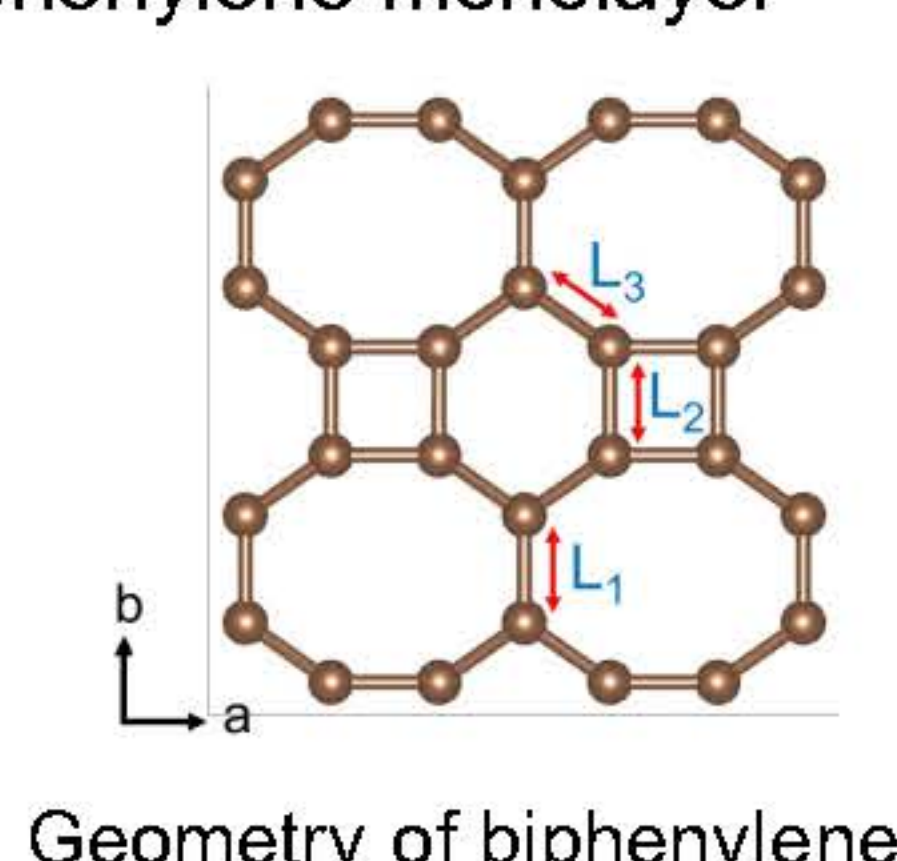
$$H_2(\text{wt}\%) = \left[\frac{(n_{H_2} \times W_{H_2})}{(n_C \times W_C) + (n_M \times W_M) + (n_{H_2} \times W_{H_2})} \right] \times 100\%$$

Acknowledgements

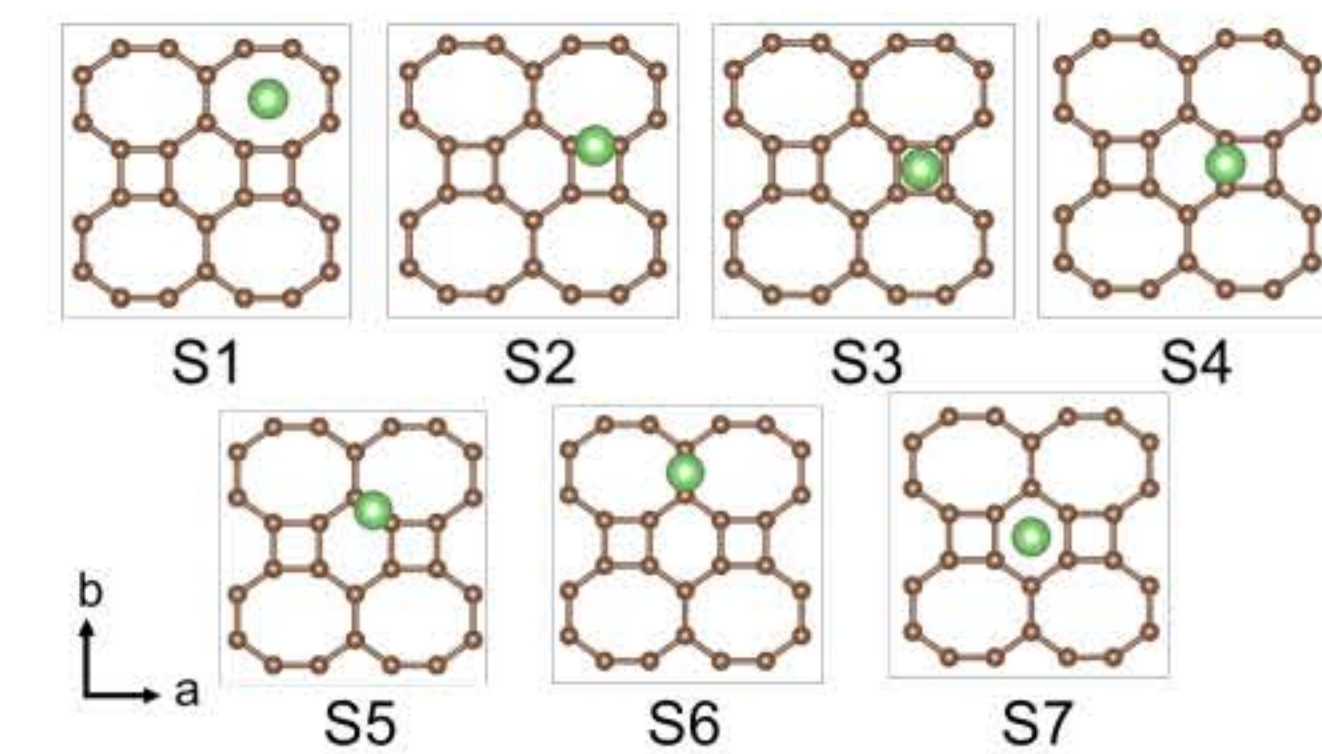
This research has received funding support from (i) Suranaree University of Technology (SUT) and (ii) the NSRF via the Program Management Unit for Human Resources & Institutional Development, Research and Innovation (PMU-B) [grant number B13F660067]

Results and discussion

❖ Biphenylene monolayer

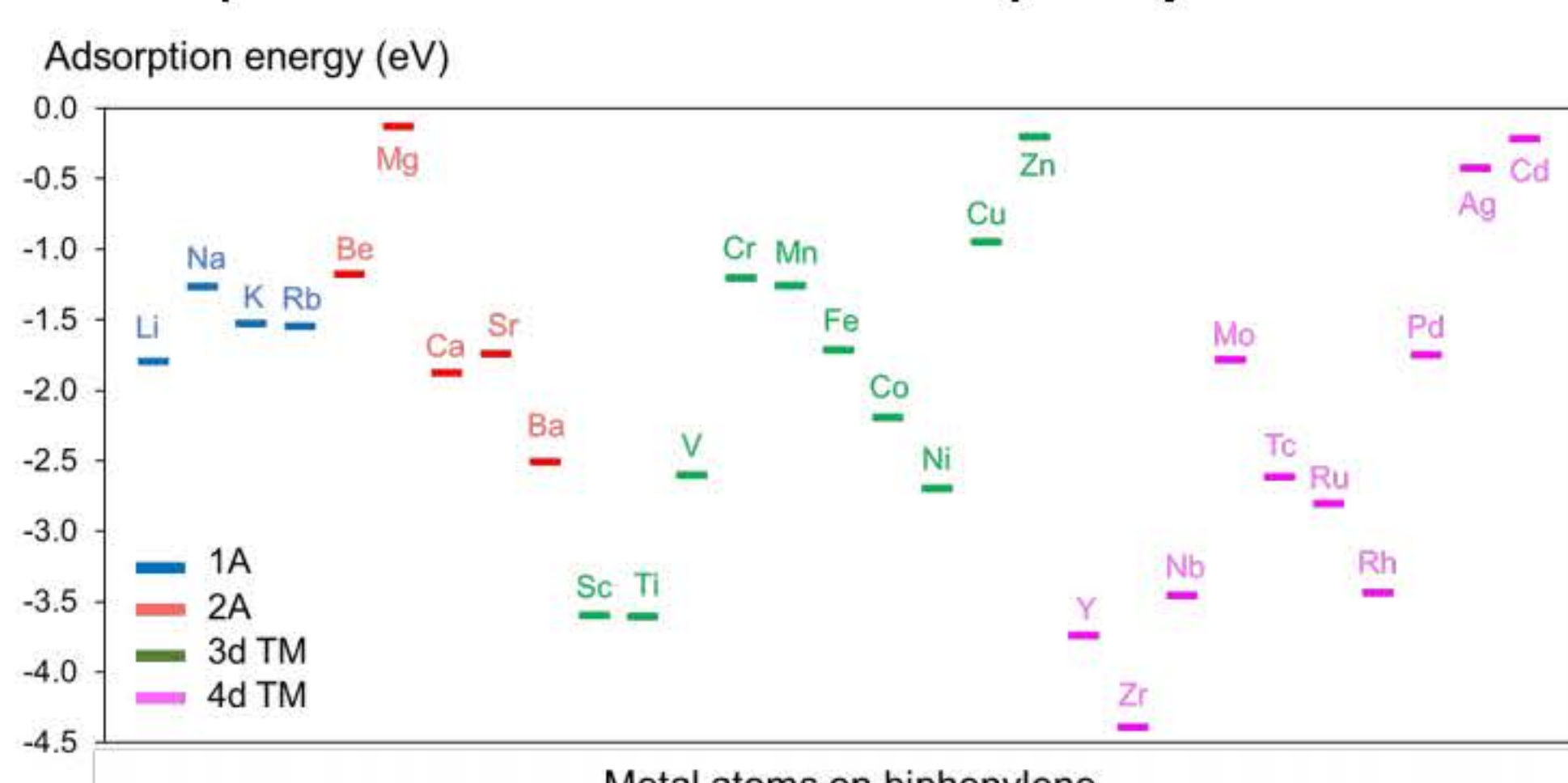


Geometry of biphenylene



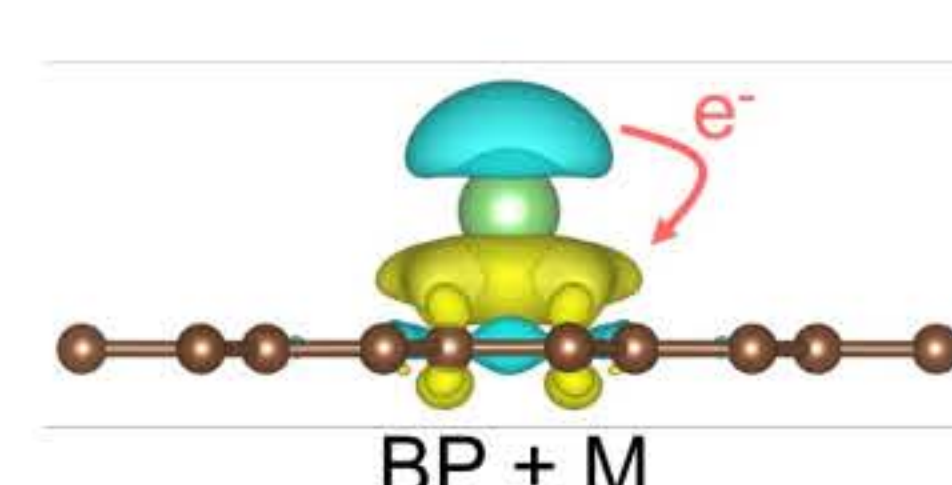
Possible adsorption sites for metal on BP

❖ Adsorption of metal atoms on biphenylene sheet



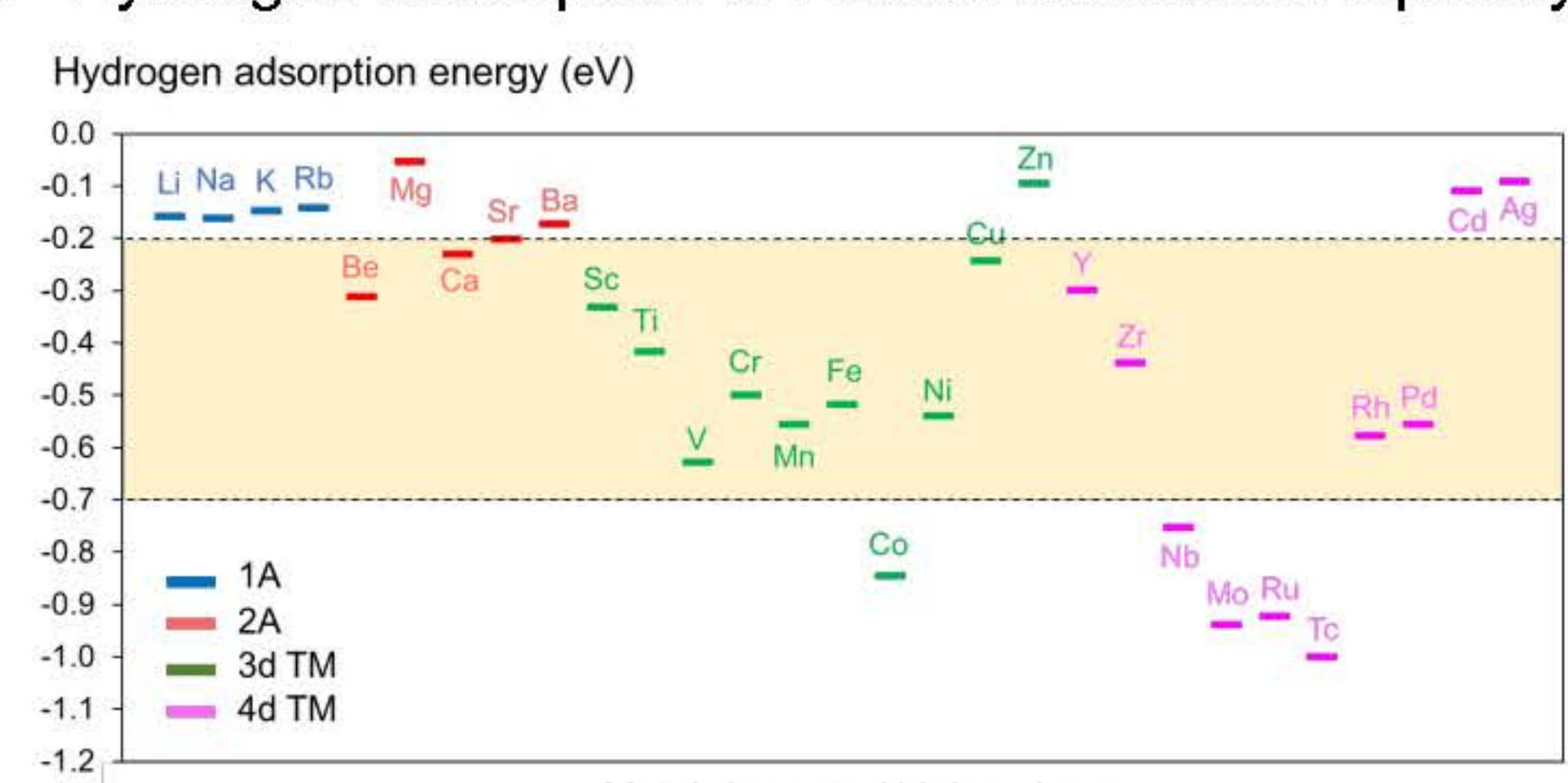
Adsorption energies of metal atoms on BP

- The stronger binding interaction of BP + M is the charge transfer from metal to C-2p orbital of biphenylene.



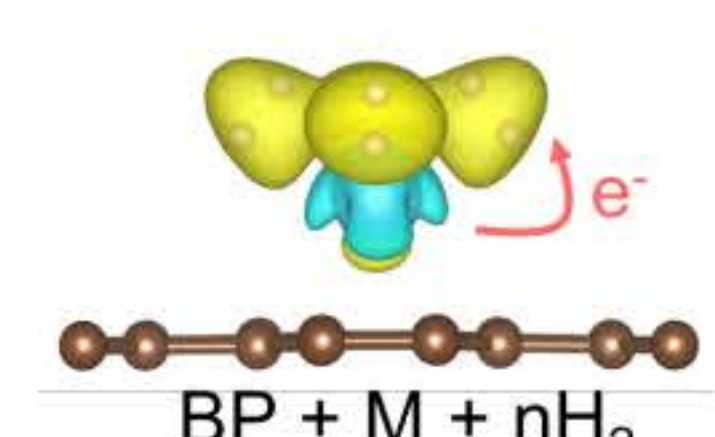
Charge density difference plot

❖ Hydrogen adsorption on metal-decorated biphenylene structures



Adsorption energies of H₂ on BP + M

- The 3d TM-decorated biphenylene shows strong hydrogen adsorption energies in the range of -0.2 to -0.7 eV and charge transfers from metal to H₂.



Charge density difference plot

The maximum number of H₂ molecules and gravimetric hydrogen wt% on BP + M

Group	Metals on BP	Adsorbed H ₂ molecules	Average adsorption energy (eV)	Gravimetric hydrogen wt%
1A	Li	4	-0.16	9.20
	Na	4	-0.16	7.77
	K	4	-0.15	6.72
	Rb	4	-0.14	4.83
2A	Be	2	-0.31	4.71
	Mg	4	-0.05	7.67
	Ca	4	-0.23	6.66
	Sr	4	-0.20	4.77
	Ba	4	-0.17	3.68

Group	Metals on BP	Adsorbed H ₂ molecules	Average adsorption energy (eV)	Gravimetric hydrogen wt%
3d TM	Sc	4	-0.33	6.40
	Ti	4	-0.42	6.26
	V	3	-0.63	4.65
	Cr	3	-0.50	4.62
4d TM	Mn	3	-0.56	4.51
	Fe	3	-0.52	4.48
	Co	3	-0.84	4.38
	Ni	3	-0.54	4.39
	Cu	2	-0.24	2.87
	Zn	4	-0.09	5.50

- The maximum number of adsorbed H₂ molecules on metal-decorated biphenylene is 4H₂.
- BP + Sc and BP + Ti nanomaterial could perform as superior hydrogen storage material.

Conclusions

- The metal-decorated biphenylene shows stronger binding interaction and high gravimetric hydrogen capacity.
- The 3d TM-decorated biphenylene could perform as superior hydrogen storage material.



3 BRAINPOWER
CONGRESS 2023

ร่วมกันสร้างและขับเคลื่อนงานวิจัยขั้นแนวหน้า
สู่อุตสาหกรรมแห่งอนาคต



BIOTEC
a member of NSTDA



GISTDA



สร้างคน
ข้ามพรมแดน

Multi-omics Analysis for Space Agriculture: Investigation of Biochemical Pathway in Seed Germination Processes in Different Rice Varieties Using TMT-Based Proteomics

Succheewin Krobthong¹, Yodying Yingchutrakul², Chanat Aonbangkhen³, Sithiporn Channumsin⁴, Narit Boonhaijaroen⁵, Tatpong Tulyananda^{1,*}

¹ School of Bioinnovation and Bio-Based Product Intelligence, Faculty of Science, Mahidol University, Bangkok, Thailand,

² National Center for Genetic Engineering and Biotechnology (BIOTEC), National Science and Technology Development Agency (NSTDA), Pathum Thani, Thailand

³ Center of Excellence in Natural Products Chemistry (CENP), Department of Chemistry, Faculty of Science, Chulalongkorn University, Bangkok, Thailand

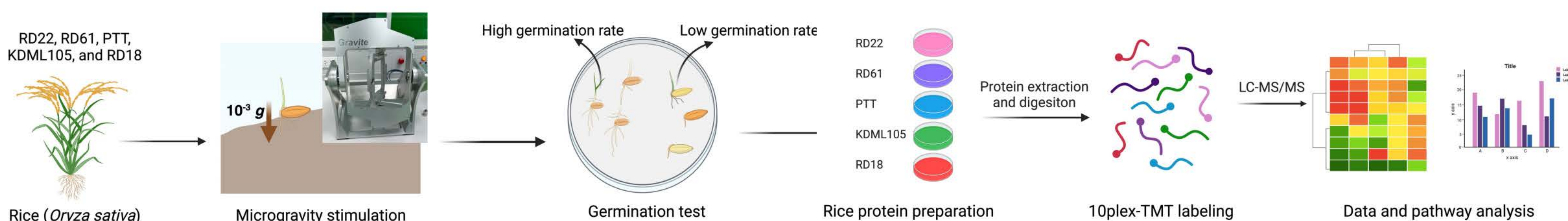
⁴ Space Technology Research Center, Geo-Informatics and Space Technology Development Agency (GISTDA), Chonburi, Thailand

⁵ Vaam Company Limited, Samut Sakhon, Thailand

Introduction

Understanding how to grow crops in space is crucial for long-term human survival there. Astronauts depend on freeze-dried food, which may be inadequate for longer missions, leading to expensive resupply trips and health risks due to nutrient loss over time. Therefore, growing fresh crops is a sustainable alternative. Rice, a nutritious staple for many, is a good candidate for space farming due to its essential nutrients and bioactive compounds. This study examines how simulated microgravity affects rice seed germination, utilizing proteomics and metabolomics to analyze the influence on proteins and plant hormones. The results offer insights into selecting rice varieties that can thrive in space's unique conditions.

Methods

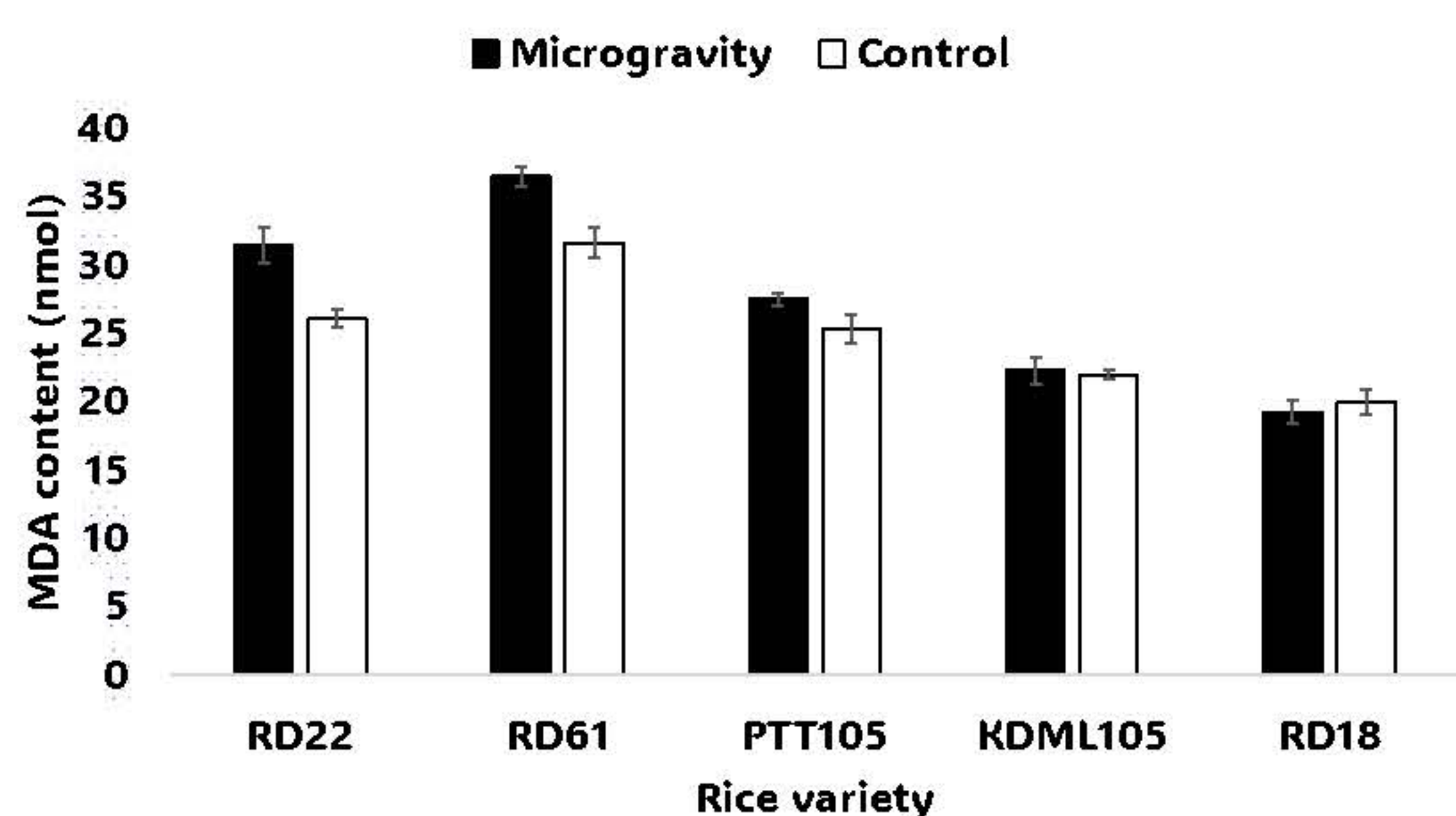


Results & Discussion

Effect of microgravity on germination rate in different rice varieties

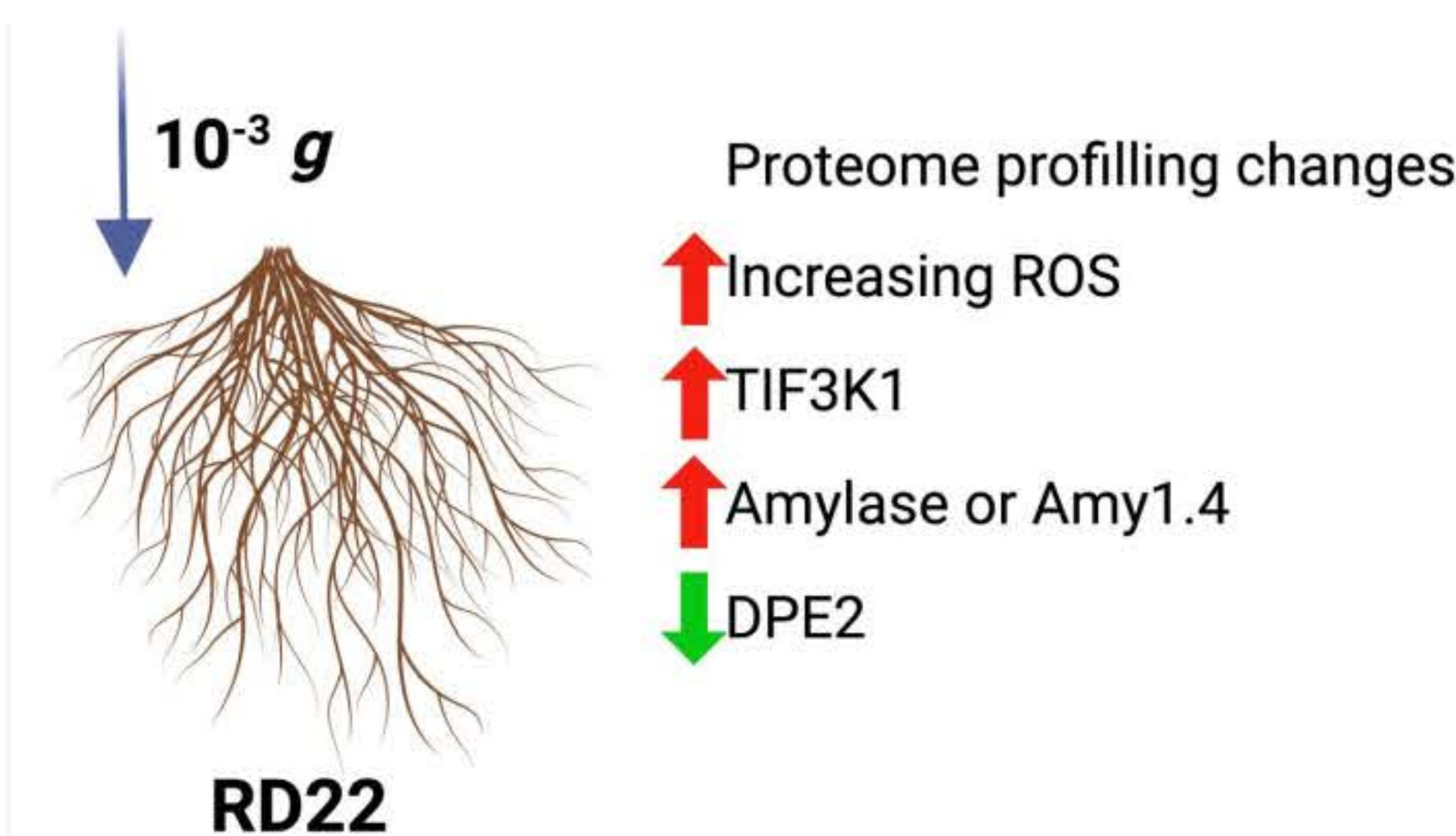
There was **no significant** difference in %GP between microgravity and normal gravity conditions across all rice varieties. In terms of the quantity of germination rate, RD22 exhibited the highest %GP, followed by RD61. Three rice varieties, namely PTT105, KDML105, and RD18, displayed %GP values below 50%.

Comparative MDA level in rice seedling between micro- and normal-gravity condition



It was observed that different rice varieties responded variably to microgravity. Specifically, varieties RD22 and RD61 exhibited significantly higher MDA levels when grown in microgravity than under normal gravity conditions. Our proteomic analysis revealed that **Catalase isozyme A** had a significant 2.036-fold increase (p-value < 0.01) under microgravity compared to normal gravity conditions. This suggests an enhanced antioxidant capacity in the seeds to manage ROS in these challenging conditions.

Conclusion

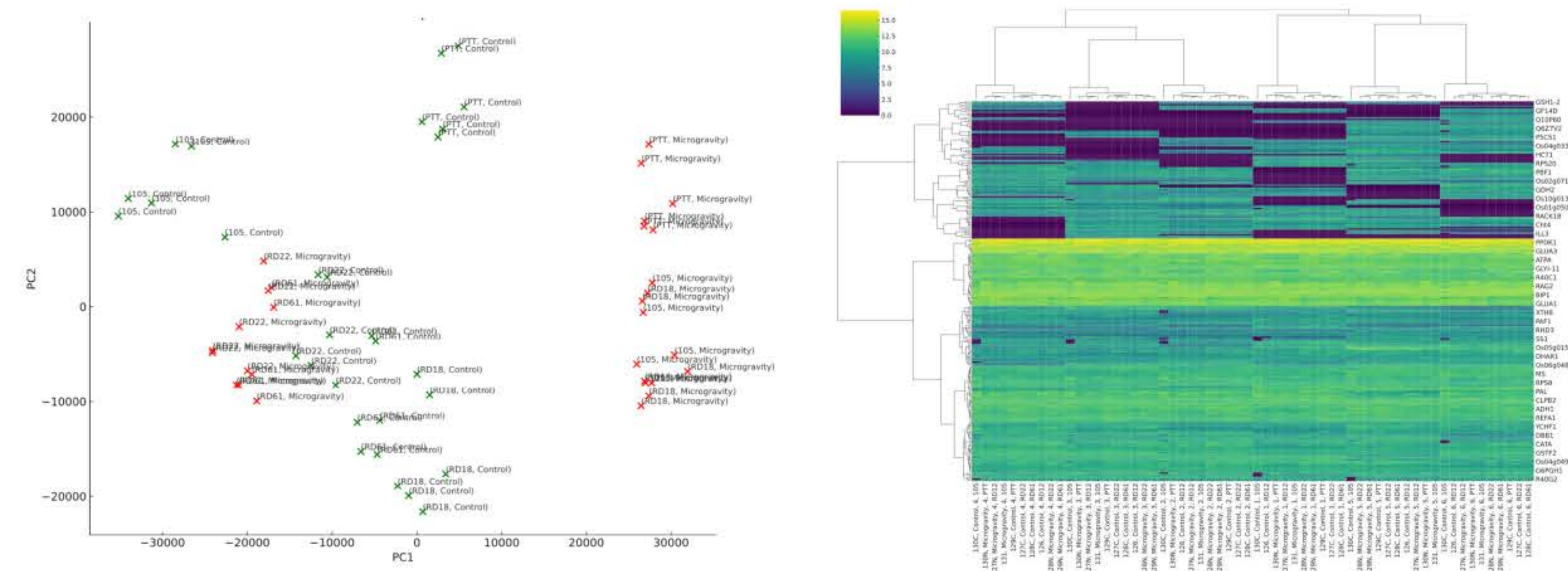


The study investigated rice germination under microgravity using a 3D-clinostat. RD22 showed the highest germination rate and adaptability, with changes in protein regulation and elevated gibberellic acid or GA3 levels under microgravity. This suggests RD22's potential for space agriculture, warranting further research into its cultivation in extraterrestrial farming systems.

Acknowledgements

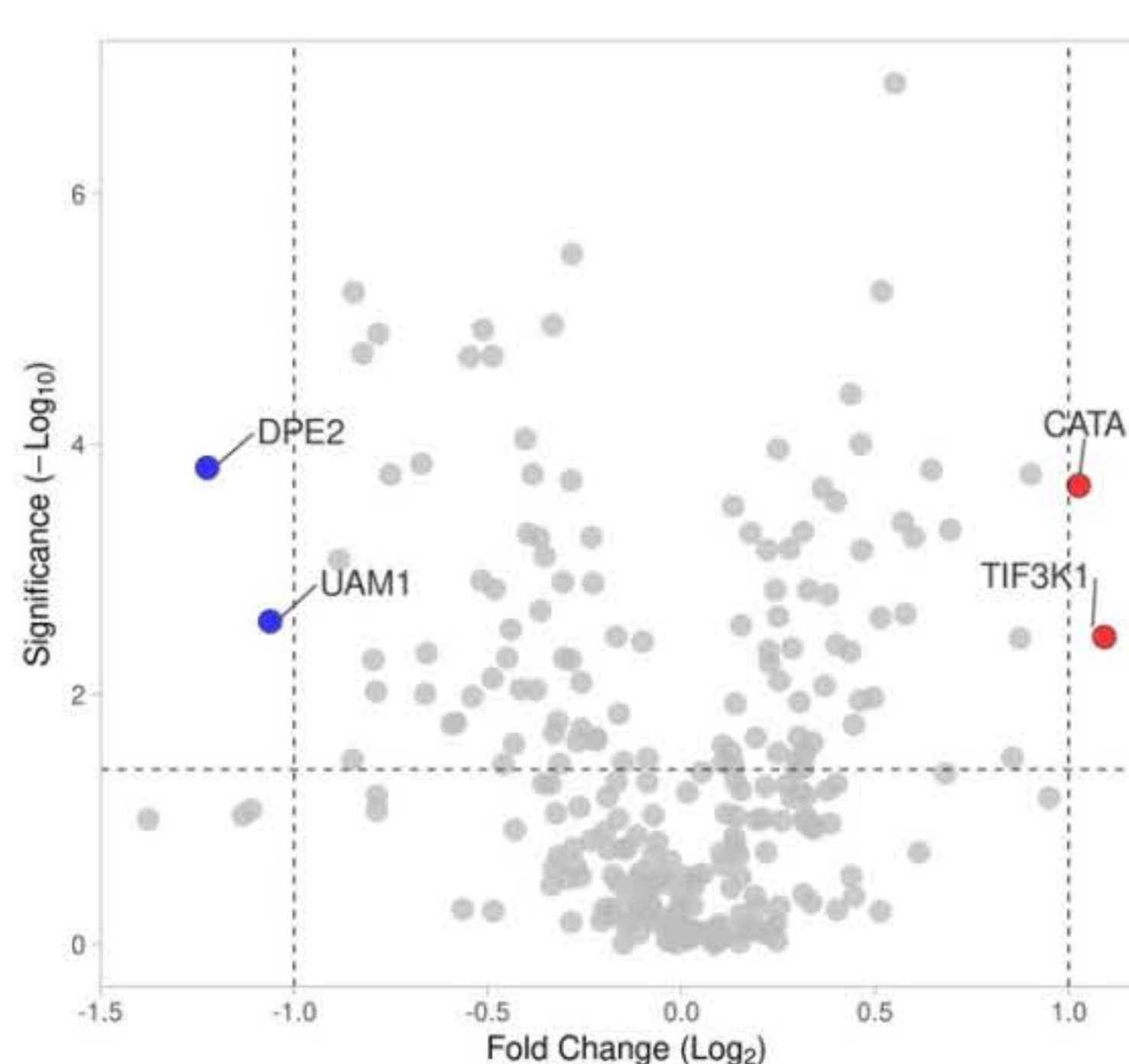
This research has received funding support from the NSRF via the Program Management Unit for Human Resources & Institutional Development, Research and Innovation [grant number B13F660122]

Investigating the effect of microgravity on rice seed germination



(A) PCA of the proteome profiling. (B) The heatmap depicts log2-transformed expression levels of various proteins (y-axis) across different experimental conditions (x-axis).

The analysis revealed distinct clusters of proteins, indicating similarities and differences in their expression profiles across the samples.



The protein expression levels in microgravity conditions were compared with those in normal gravity conditions across all rice varieties examined. An analysis of proteomic data across all rice varieties revealed two proteins, **TIF3K1** and **DPE2**, present in two out of five rice varieties studied.

Tif3k1 protein was significantly up-regulated in the RD22 variety yet down-regulated in RD18.

Modeling Airborne Virus Transmission Under Microgravity Conditions

Chayanin Sararat¹, Nattaporn Chattham², and Charin Modchang¹

¹ Biophysics Group, Department of Physics, Faculty of Science, Mahidol University, Bangkok, 10240, Thailand
² Department of Physics, Faculty of Science, Kasetsart University, Bangkok, 10900, Thailand

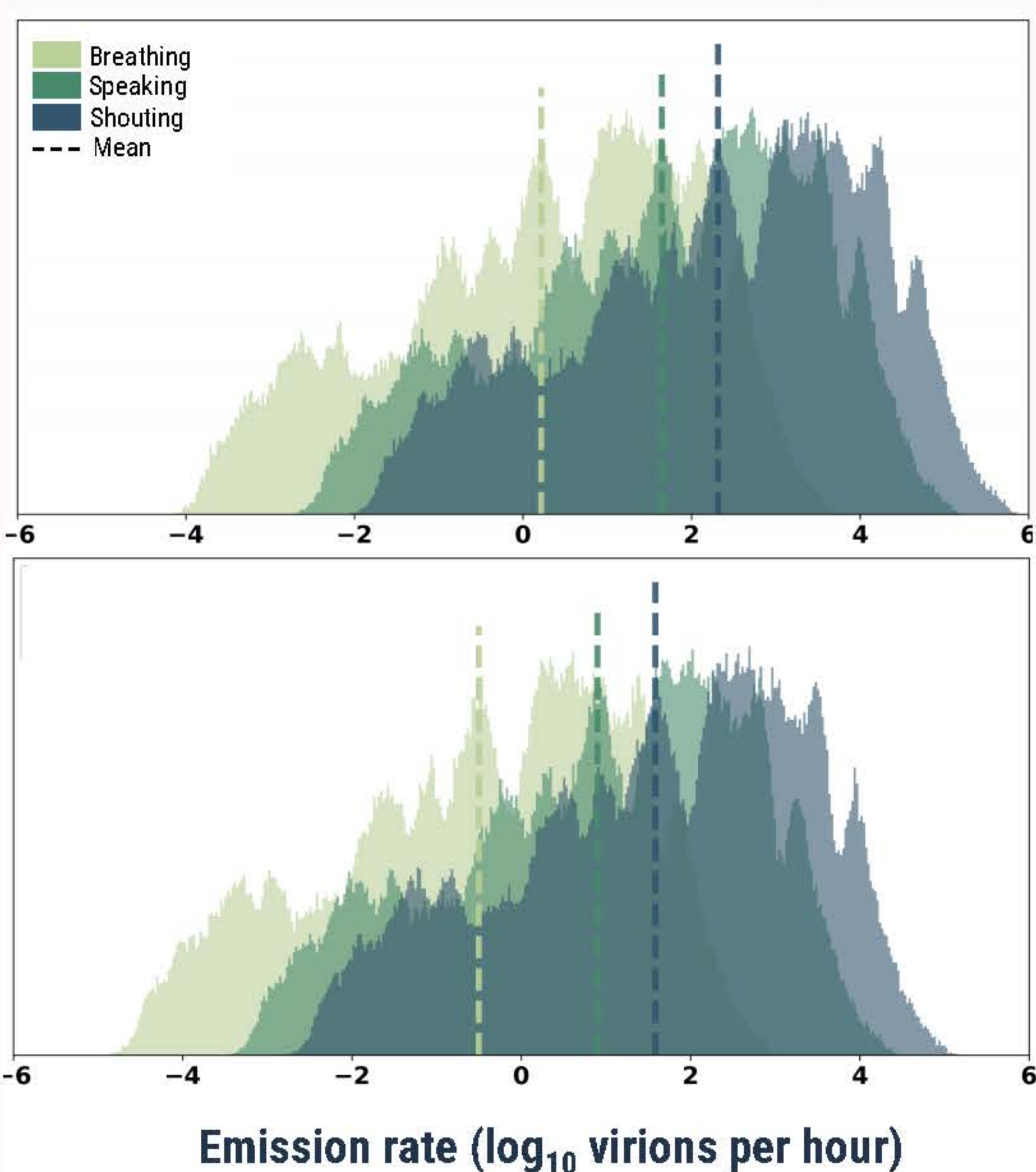


Introduction

Airborne transmission refers to the spread of infectious agents through the air via small respiratory droplets or aerosols. These airborne particles can travel varying distances and remain for extended periods, posing a unique challenge for disease control and prevention. In microgravity conditions, the traditional understanding of airborne transmission may be altered. Modeling airborne transmission under microgravity conditions is crucial for ensuring the health and safety of astronauts and contributes to our broader understanding of disease transmission in unique environments. In this study, we adapt the COVID Airborne Risk Assessment (CARA) framework [1] to model the airborne transmission of the virus from the point of emission until deposition in the respiratory tract of exposed hosts and eventually evaluate the risk of infection.

Results & Discussion

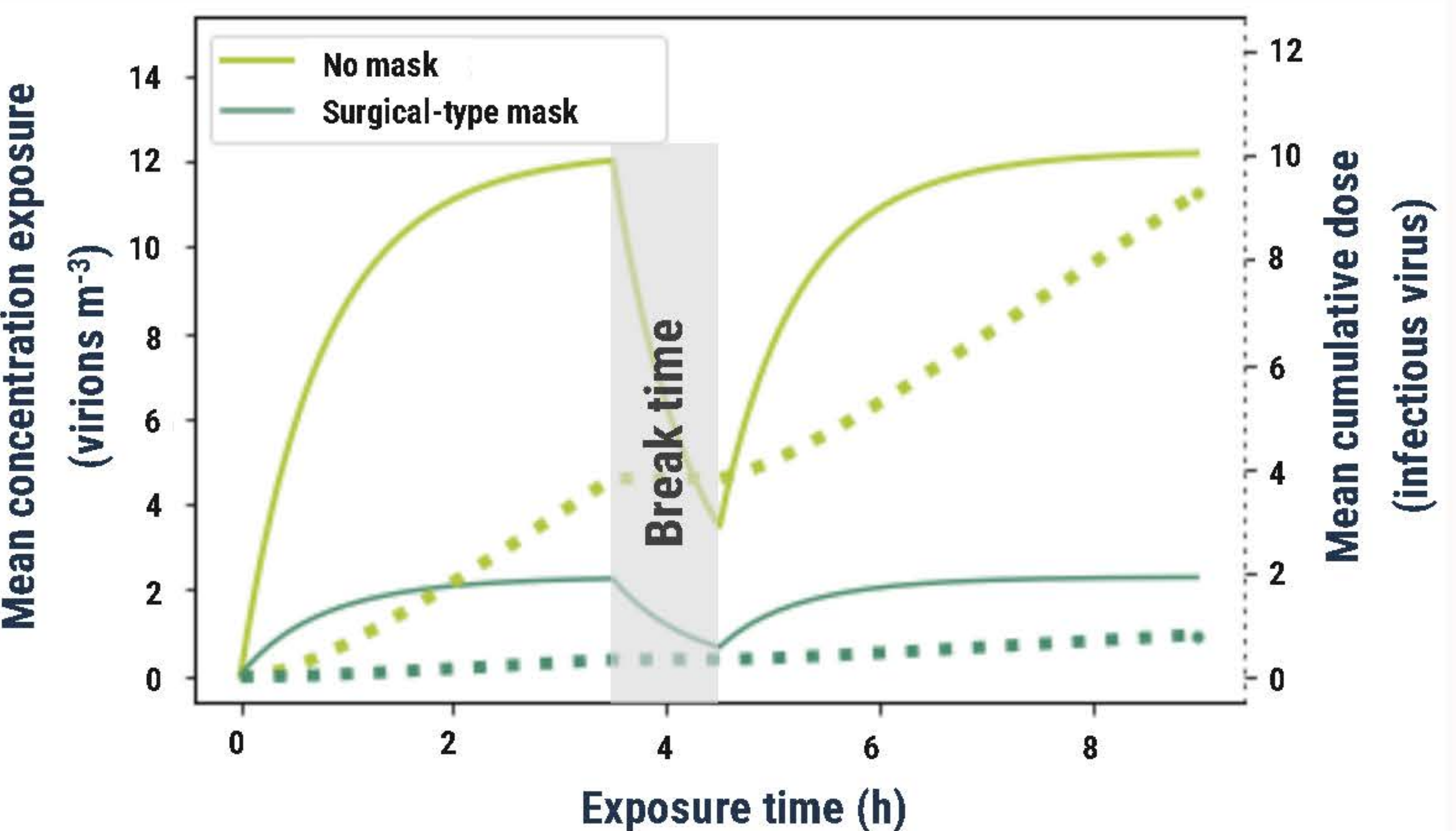
Emission rates from an infected host engaged in breathing, speaking, and shouting while seated



Mean emission rates
Without mask
89 virions per hour
2384 virions per hour
11242 virions per hour

With mask
17 virions per hour
425 virions per hour
2060 virions per hour

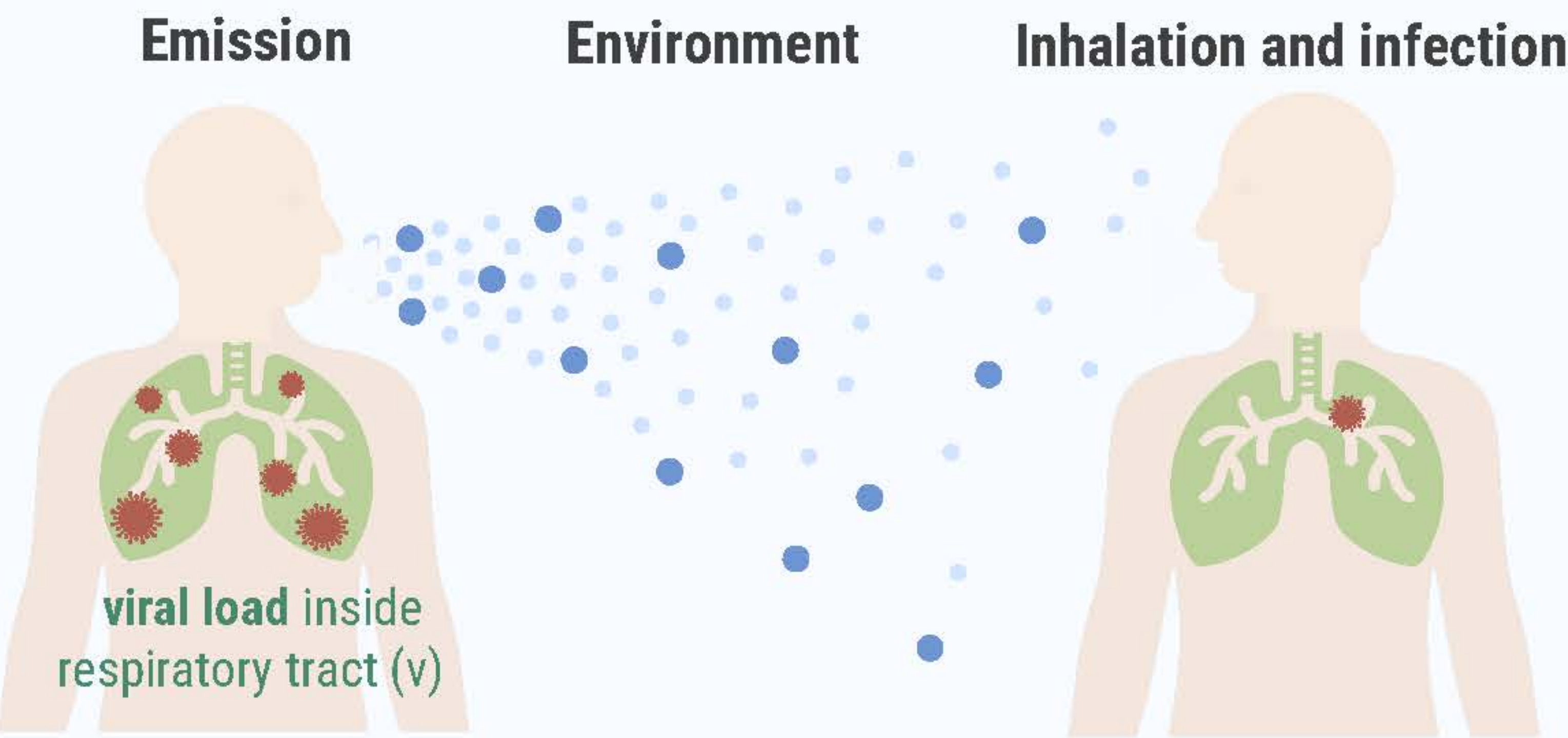
Viral concentration profile over the exposure time and the cumulative absorbed dose



Conclusion

According to our initial research, we have identified the potential adaptability of the CARA framework for exploring the impact of microgravity on the transmission of airborne viruses. Our early findings highlight the crucial role of face masks and viral removal methods in mitigating the risk of infection."

Methods



1. Emission rate (E_v)
$$E_v = v E_p(D, f_{amp}, \eta_{out}) B$$

particle emission concentration breathing rate

2. Viral removal rates (λ_{vRR})
$$\lambda_{vRR} = \lambda_{ACH} + \lambda_g + \lambda_{bio} + \lambda_{filt}$$

ventilation gravitational settlement biological decay filtration

Gravitational settlement
$$\lambda_g = v_g/h \quad v_g = \frac{(\rho_p - \rho_{air})(D)^2 g_{eff}}{18\mu_{air}}$$

3. Viral concentration ($C(t)$)
$$\frac{\partial C(t)}{\partial t} = \frac{E_v N_{inf}}{V} - \lambda_{vRR} C(t)$$

number of infected hosts room volume removal rate

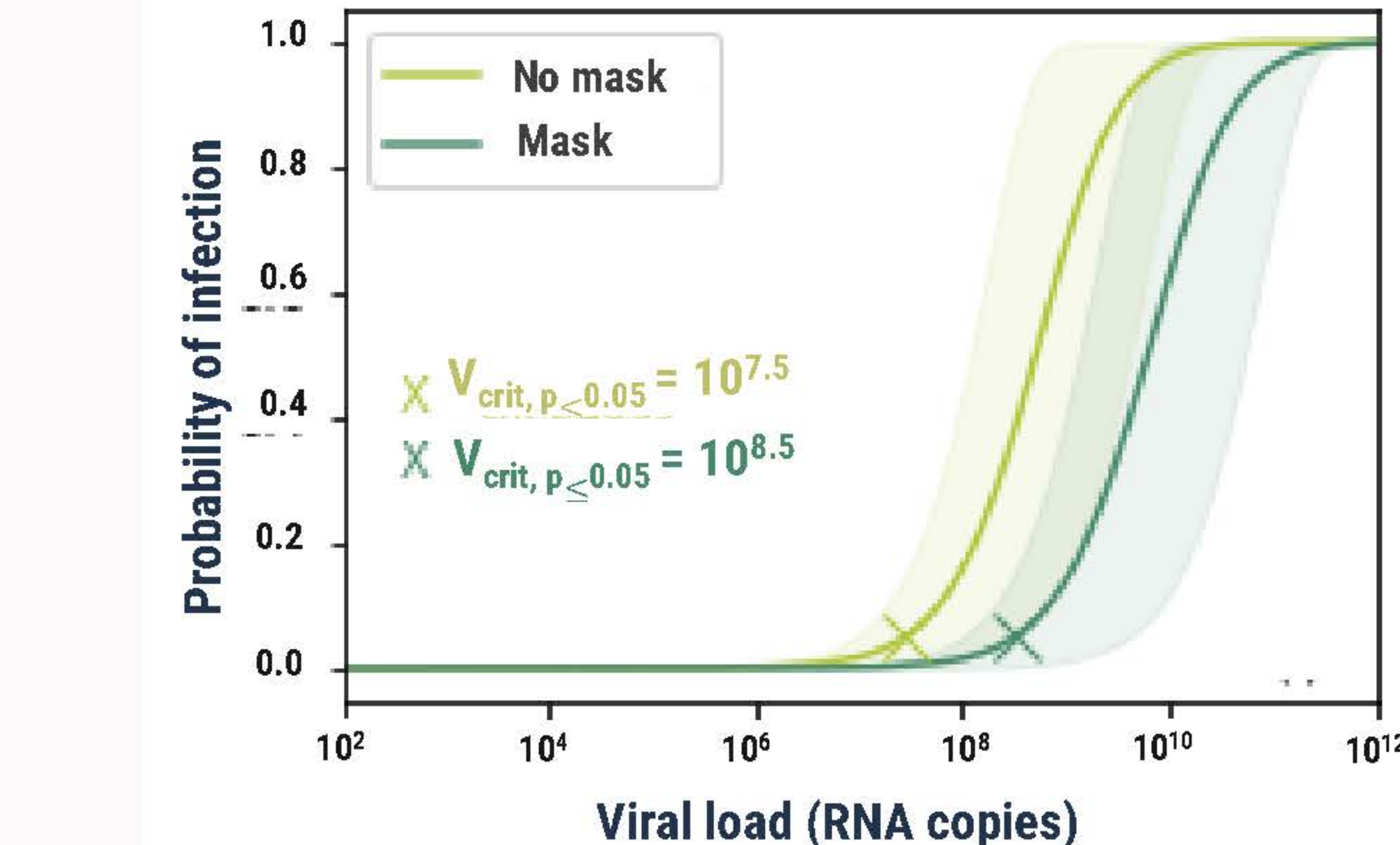
4. Depositing Dose (D_v)
$$D_v = \int_0^{D_{max}} \int_{t_i}^{t_{i+1}} C(t) dt f_{inf} B f_{dep} (1 - \eta_{in}) dD$$

breathing rate inward efficiency of face mask fraction of infectious virus deposition fraction in the respiratory tract

5. Infection probability
$$P = 1 - \exp\left(-\frac{D_v (1 - M)}{ID_{50}/\ln 2}\right)$$

host immunity infectious dose corresponds to a dose required to cause infection in 50%

Probability of infection as a function of viral load



Acknowledgements

This research has received funding support from the NSRF via the Program Management Unit for Human Resources & Institutional Development, Research and Innovation [grant number B13F660102]

Effects of microgravity on biological features and virulence of the fungal pathogen *Cryptococcus neoformans*

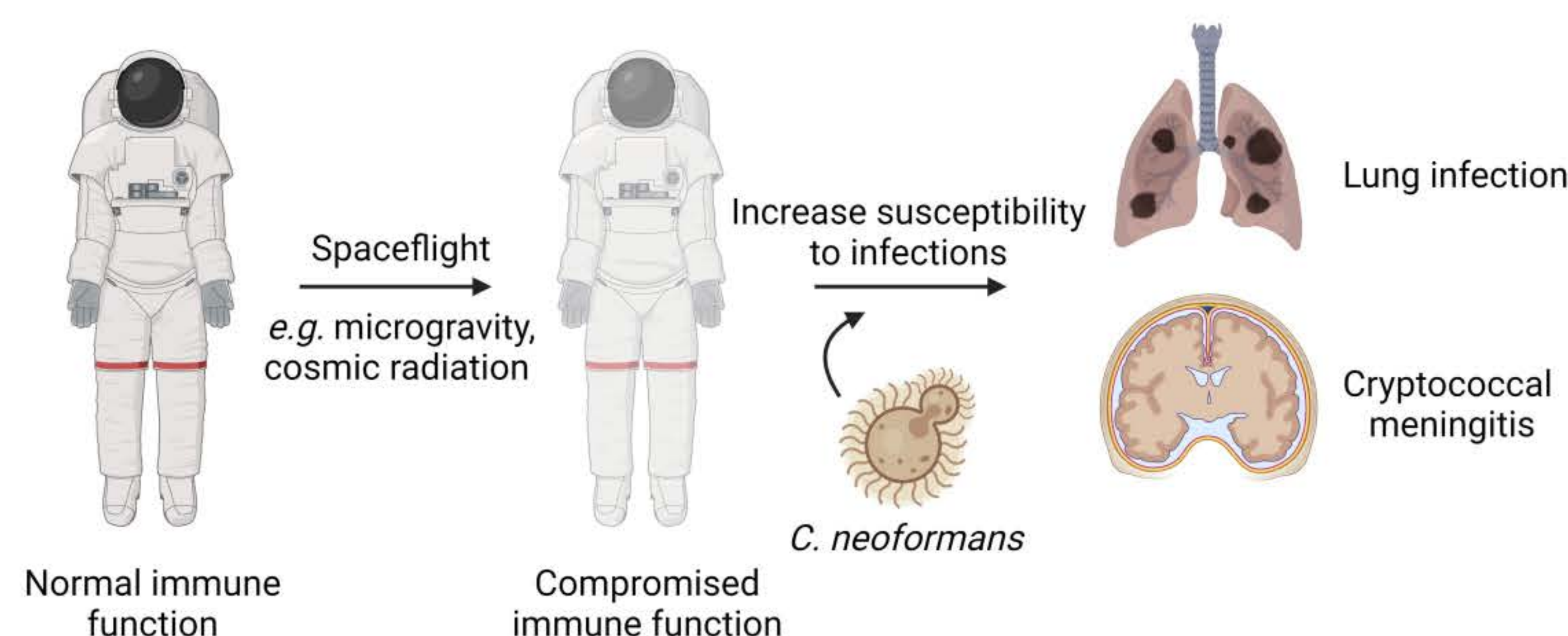
Tanaporn Phetruen¹, Muthita Khongthongdam¹, Tatpong Tulyananda², Sittiporn Channumsin³, Nattaporn Chattham⁴, Sittinan Chanarat^{1,*}

¹ Laboratory of Molecular Cell Biology, Department of Biochemistry and Center for Excellence in Protein and Enzyme Technology, Faculty of Science, Mahidol University, Bangkok, Thailand, ² School of Bioinnovation and Bio-based Product Intelligence, Faculty of Science, Mahidol University, Bangkok, Thailand, ³ Geo-Informatics and Space Technology Development Agency (GISTDA), Bangkok, Thailand, ⁴ Department of Physics, Faculty of Science, Kasetsart University, Bangkok, Thailand
* Email: sittinan.cha@mahidol.edu

Rationale and Significance

Cryptococcus neoformans is a fungus that causes cryptococcosis. It is an infection of the lungs and central nervous system known as cryptococcal meningitis. This type of fungus is commonly found in nature, including on the surface of soil, trees, and is often found in the droppings of birds such as pigeons. In people who are immunocompromised, for example HIV-infected individuals and organ transplanted patients, the risk and rate of *C. neoformans* infection often greatly increases. It has been reported that the condition in spaceflight when human are under microgravity or cosmic radiation, the human bodies may undergo the imbalance stage of microbiota and may induce the immunocompromised or immunosuppressed state and therefore increase this risk of the opportunistic infections.

One of the factors that increase the severity of cryptococcosis is ability of *C. neoformans* to change the morphology under different environmental conditions. The morphological diversity ranging from normal cells, giant or titan cells, microcells, cells with clustered-capsules, and released capsules. In this study, the effects of microgravity on biological feature and virulence of *C. neoformans* will be investigated for understanding and improving the biological safety of human in spaceflight.



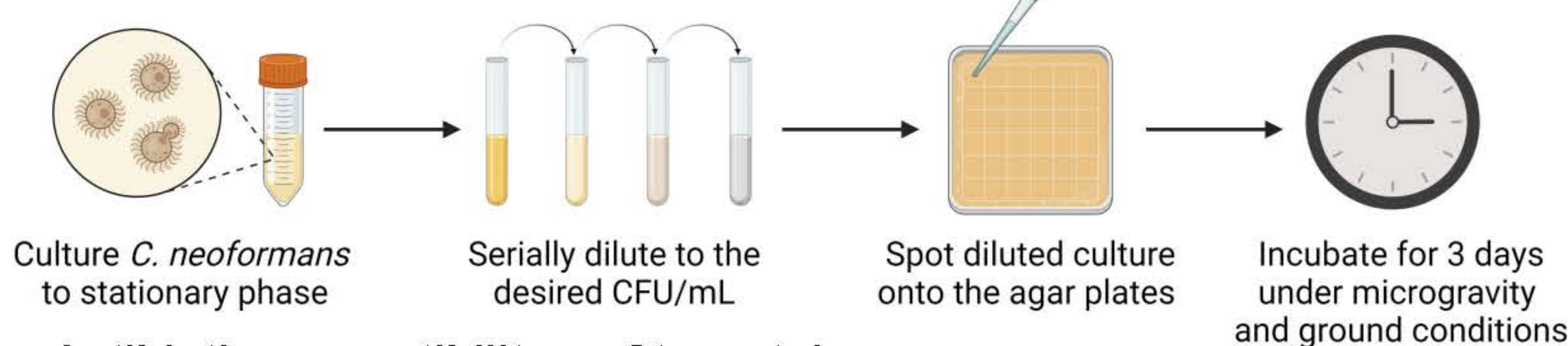
Methods

1. Strains and culture conditions: H99C, H99O, and KN99 representing low, intermediate and hypervirulent strains of *C. neoformans*, respectively, are used in this study. Cells are cultured in yeast extract peptone dextrose (YPD), synthetic complete (SC), or minimal media (MM) where appropriate.

	Less virulent	Intermediate virulent	Hypervirulent
	H99C	H99O	KN99α
Giant Cells	—	+	—
Micro Cells	—	+	+++
Released Capsules	—	+	+++
Clustered Capsules	+	+	++

Modified from Fernandes et al., 2022

2. Growth phenotype, antibiotic susceptibility, and stress tolerance:



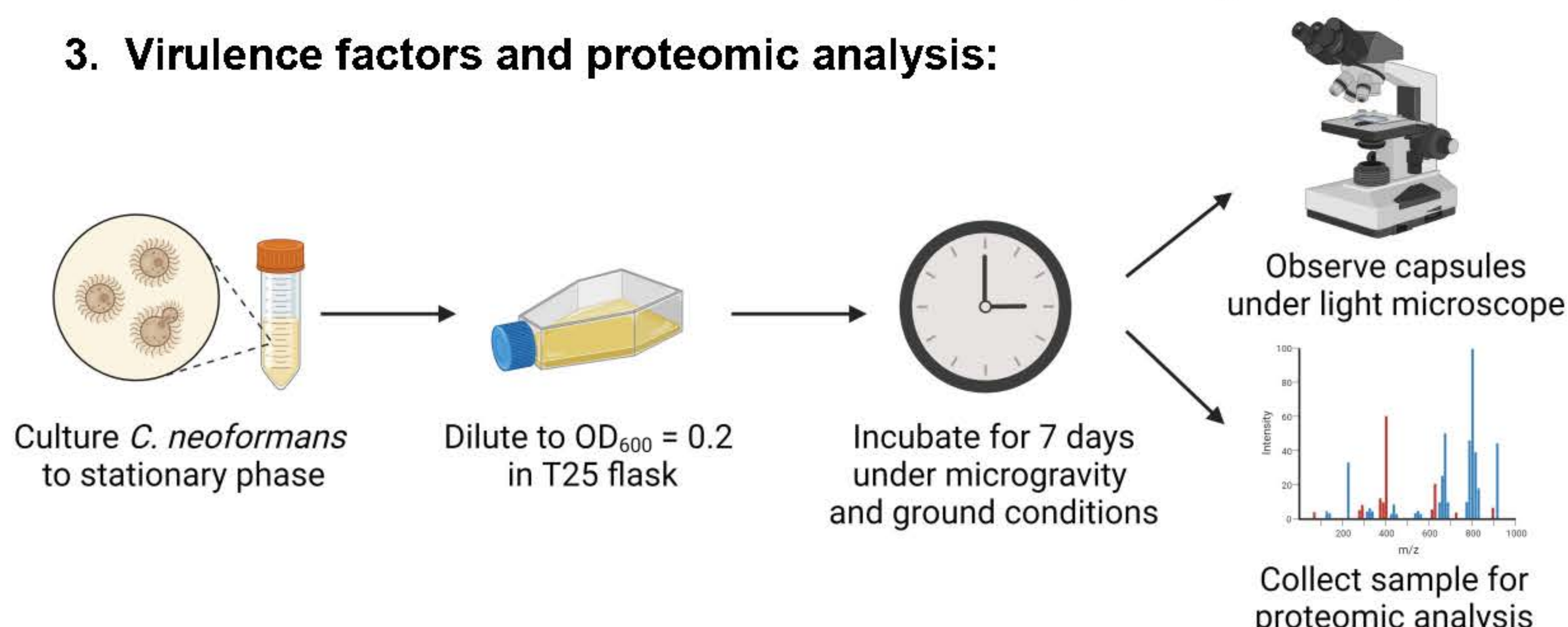
Antibiotic susceptibility

- Fluconazole (FLZ)
- Amphotericin B (AmB)
- Flucytosine (5FC)

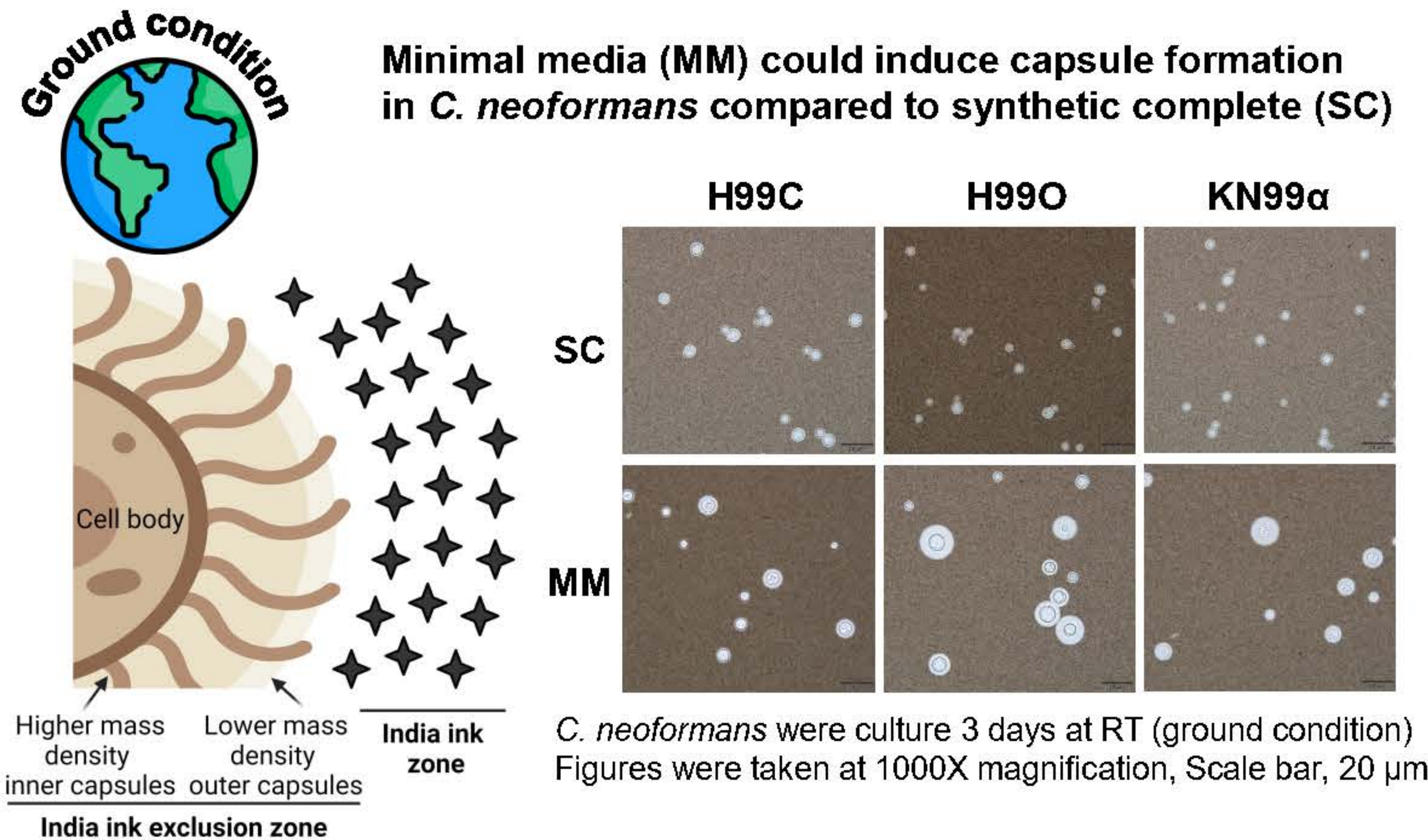
Stress tolerance

- Osmotic stress: 0.9, 1.2, 1.5 M NaCl
- ROS stress: 1, 2, 3 mM H₂O₂
- pH stress: pH 5.5, 7, 8
- Membrane stress: 0.01, 0.02, 0.03% SDS
- Cell wall stress: 0.5, 1, 2 mg/ml Congo red

3. Virulence factors and proteomic analysis:

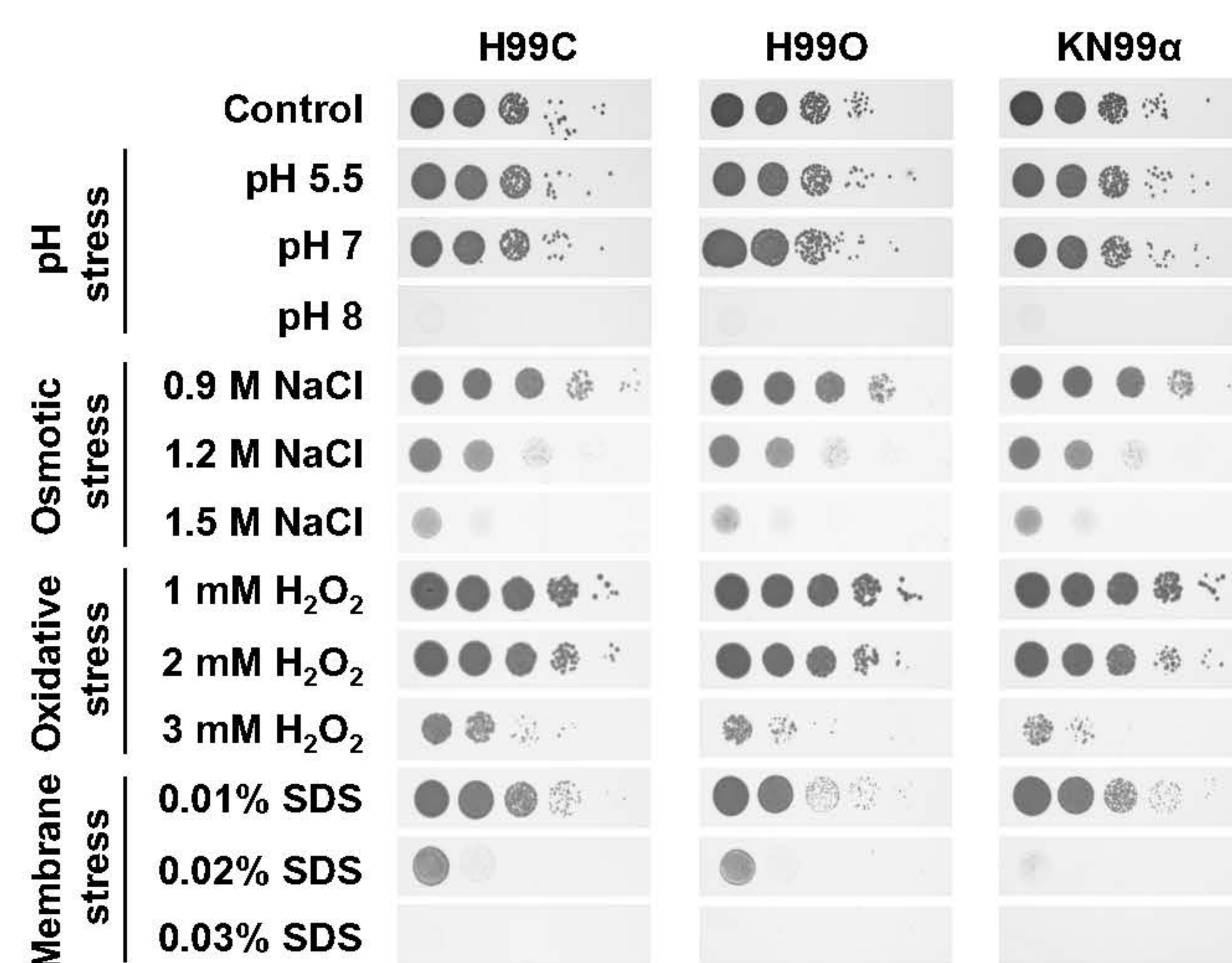


Results and Discussion



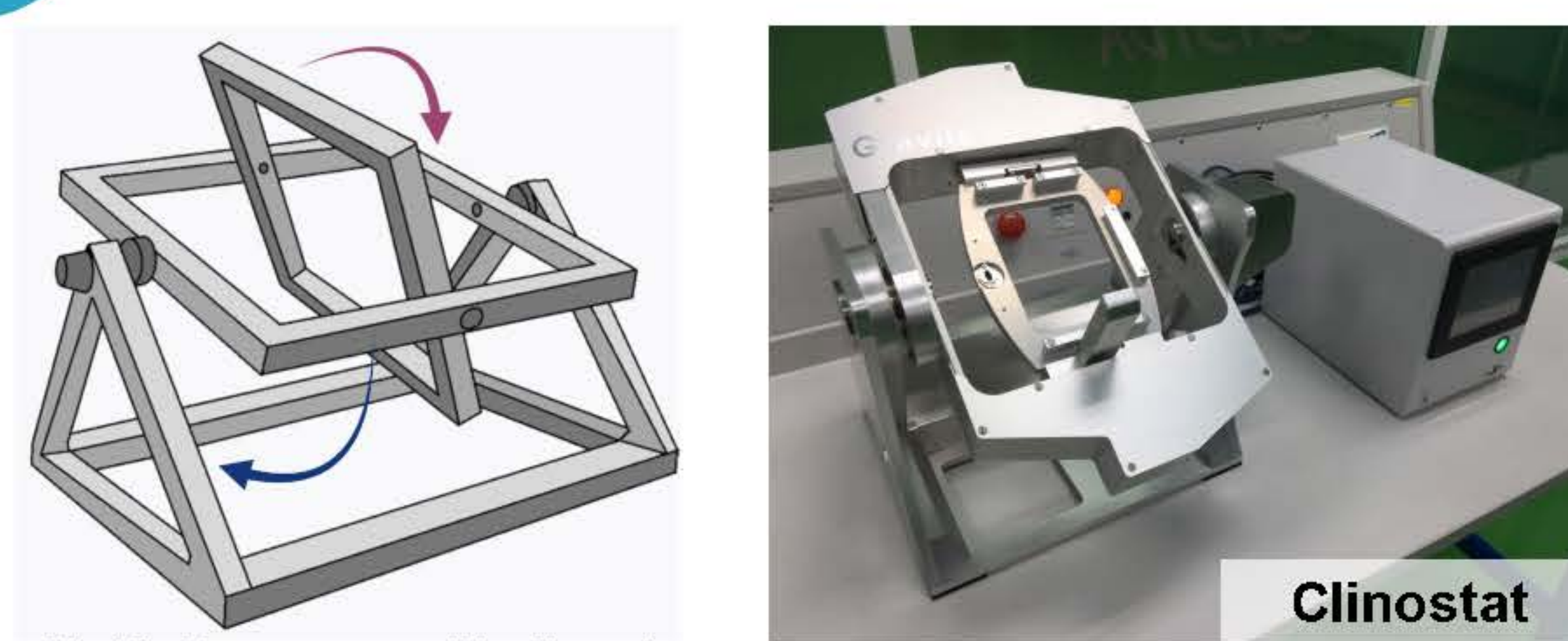
Growth, antibiotic susceptibility, and stress tolerance of *C. neoformans*

- Minimal inhibitory concentration (MIC) of antifungal agents against three strains of *C. neoformans* are 32 μg/mL for fluconazole, 0.25-0.5 μg/mL for amphotericin B, and 32-64 μg/mL for flucytosine.
- Examples of stress tolerance in *C. neoformans* at ground condition



Microgravity condition

The microgravity conditions are simulated using a 3D-clinostat, which continuously rotates both axes in the same direction to minimize the cumulative gravity vector at the center of the device



Conclusion and Future Plans

- Assays are verified for both ground and microgravity conditions including growth phenotype, antibiotic susceptibility, capsule formation, melanin synthesis, and different stress tolerance.
- Experiments related to clinostat and microgravity conditions will be performed at GISTDA, Sriracha District, Chonburi. The experiments in this research are expected to be carried out within February 2024.

Acknowledgements

- This research has received funding support from the NSRF via the Program Management Unit for Human Resources & Institutional Development, Research and Innovation [grant number B13F660122]
- Figures in this presentation are created with BioRender.com

Mechanism and dynamics of defects generated by air interruption on liquid crystal films

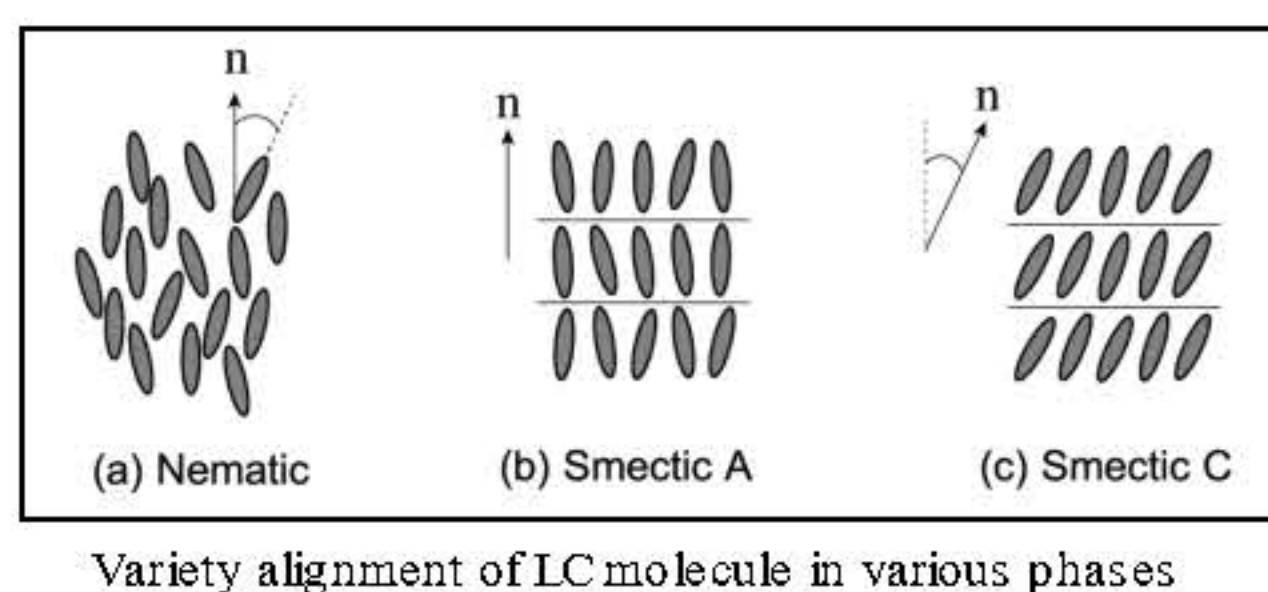
Gunganist Kongklad¹, Tanawut Rittidetch¹, Jutarat Kaewthong¹, Apichart Pattanaporkratana¹, Nattaporn Chattham^{1*}
¹ Department of Physics, Faculty of Science, Kasetsart University, Bangkok, Thailand, 10900
Project leader: Assoc.Prof.Dr. Nattaporn Chattam

Introduction:

Liquid crystal (LC) is a state of matter that exhibits properties that lie intermediate between regular liquids and solid crystals. Liquid crystal possesses the ability to exhibit fluid-like behavior, while simultaneously maintaining a molecular arrangement that resembles a crystal lattice. There exists an extensive variety of liquid crystal (LC) phases that can be differentiated based on their optical characteristics, specifically their textures.



LC film captured with a bright field microscope

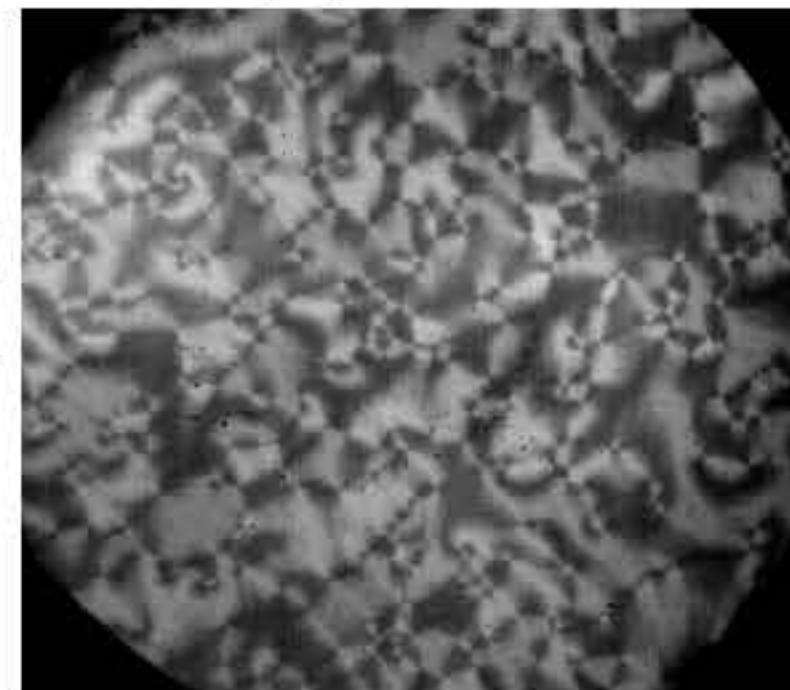


Variety alignment of LC molecule in various phases

The experimental setup involved the combination of air shear and pressure quenching methodologies. The task at hand involves the optimization of the mechanism responsible for generating pairs of point defects. The results of this study will provide the basis for the development of a component within the "payload", with the aim of future installation on the International Space Station (ISS).

Thermotropic LC, its order parameter is determined by temperature. Many thermotropic LCs exhibit a variety of phases as temperature changes. The investigation focused on the smectic C phase. It presents various advantages over nematic in terms of facilitating a quantitative analysis of defect interactions, dynamics, and annihilation processes[1]. The mechanism and dynamic of topology point defects generated by air interruption in LC film were studied.

The investigation of interactions between isolated point defects can be constrained to a quasi-two-dimensional (quasi-2D) system. Point defect study is the initial stage serves as a fundamental component in achieving the theoretical framework for elucidating intricate structures and various patterns of defects.



Topology defect pair[2]

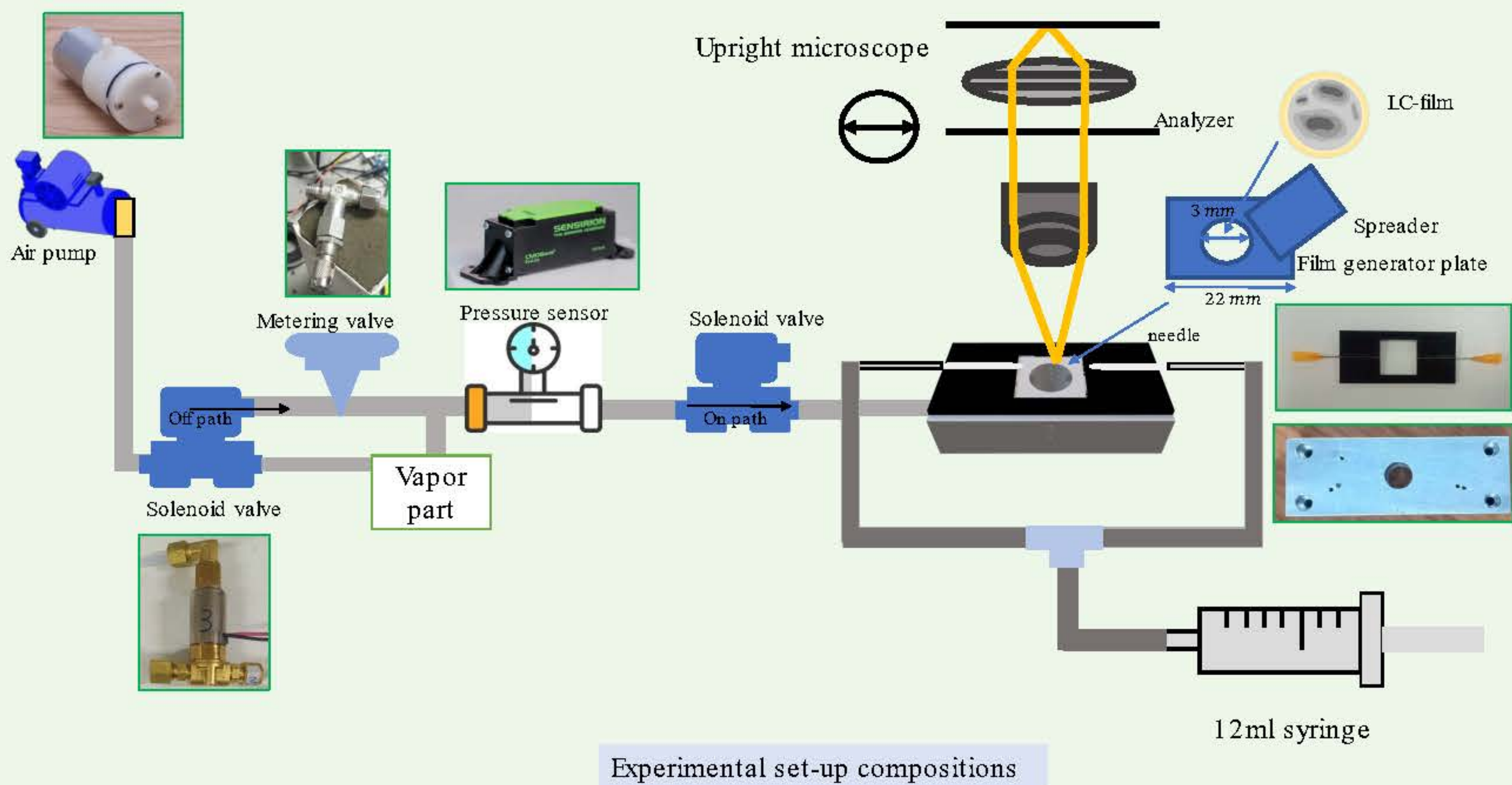
The rationale of this research:

A commonly employed application of liquid crystal (LC) technology is its utilization in liquid crystal displays (LCDs). Nowadays, liquid crystal display (LCD) panels have found widespread application in various electronic devices, including mobile phones, televisions, and laptops. The consideration of LC technology applications in space is a subject of great fascination. The "OASIS" project is a pioneering initiative aimed at conducting research and analysis on LC. The collaboration known as the Thailand Liquid Crystal in Space (TLC) project emerged from a Memorandum of Understanding (MOU) signed between a United States space team and Kasetsart University. The TLC project is primarily managed by the liquid crystal laboratory team, which is affiliated with the Department of Physics in the Faculty of Science at Kasetsart University. Collaboration has been established with institutes such as the Geo-Informatics and Space Technology Development Agency (GISTDA) to facilitate the development of the payload. The term "payload" refers to the collection of experimental gadgets that are intended for launch to the International Space Station (ISS). This study was conducted as a terrestrial investigation to fulfill a component of the experiment within the payload. The considerations for the design of the set-up will be included. Moreover, testing in a micro-gravity environment also was planned.



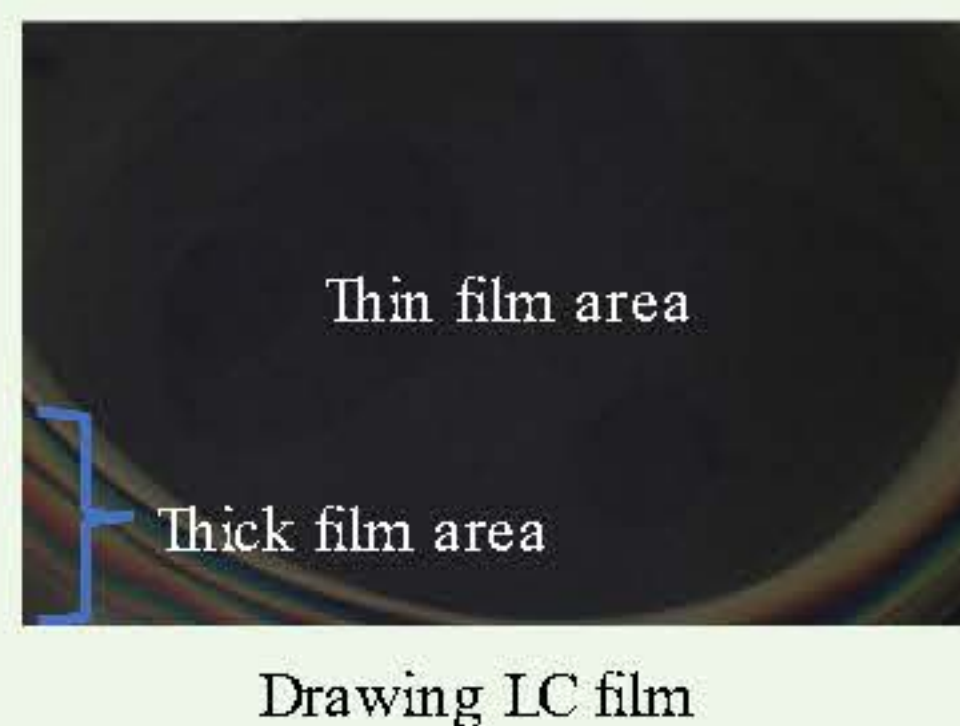
Material and designed set-up:

In this research, the liquid crystal film was drawn across the film holder. MXI 2805 liquid crystal was used to make up the film with phase transition as follows: Iso – 84.7 °C – N* – 81.4 °C – SmA* – 66.1 °C – SmC*[3]. All experiment was set up at room temperature (24-27 °C). A glass coverslip with a 3 mm hole drilled on it with a smooth surface was used as a film holder. The observation results were taken under a reflected light microscope with a de-crossing polarizer and analyzer.

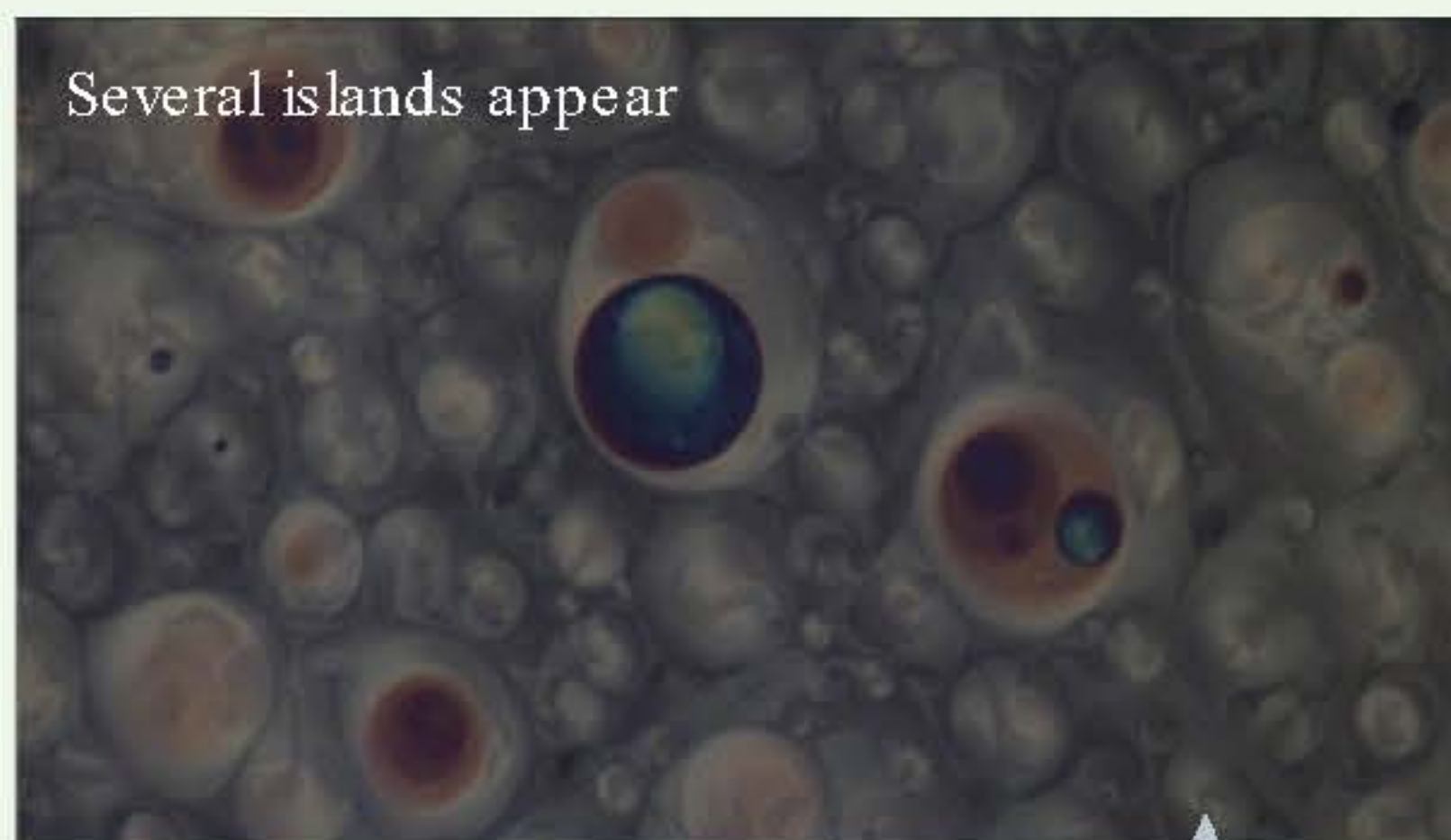


Experimental set-up compositions

Preliminary results:

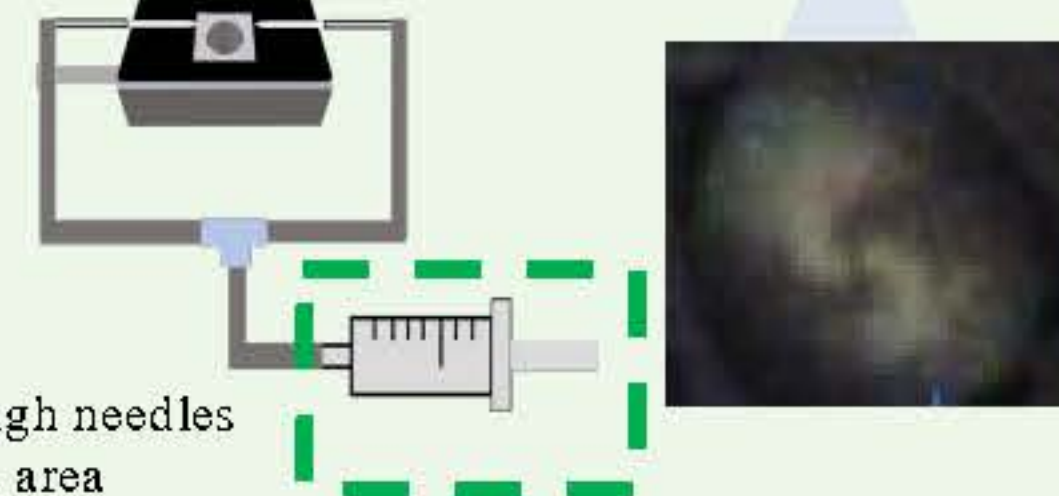


Drawing LC film



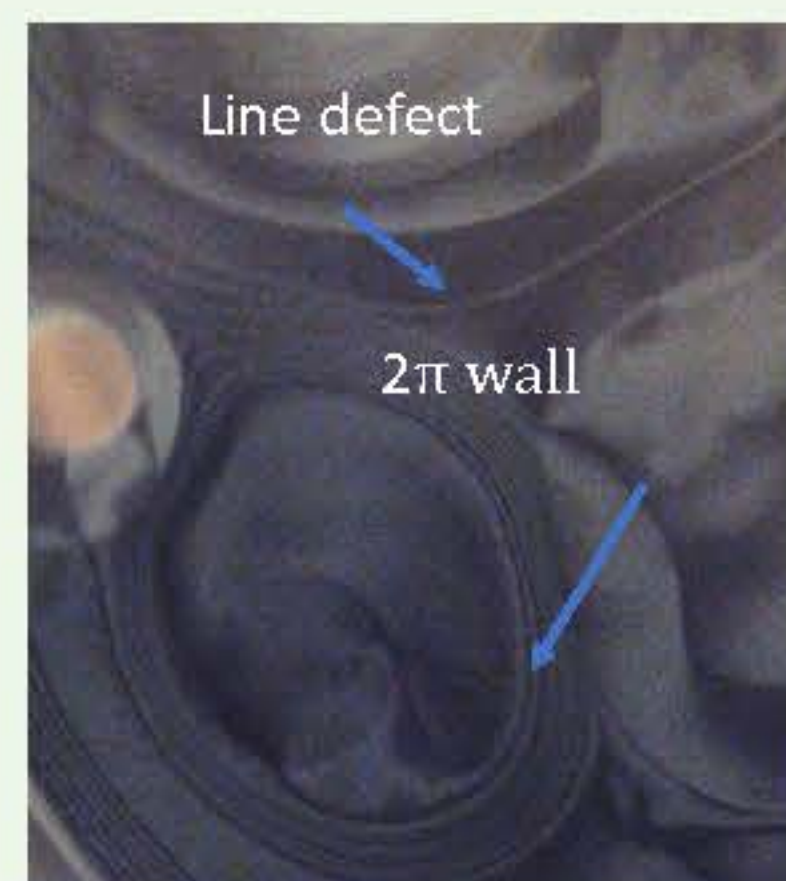
Several islands appear

Upon the initial creation of a film, it exhibits that its thickness is greatest at the outer edge and gradually decreases towards the center of the film.

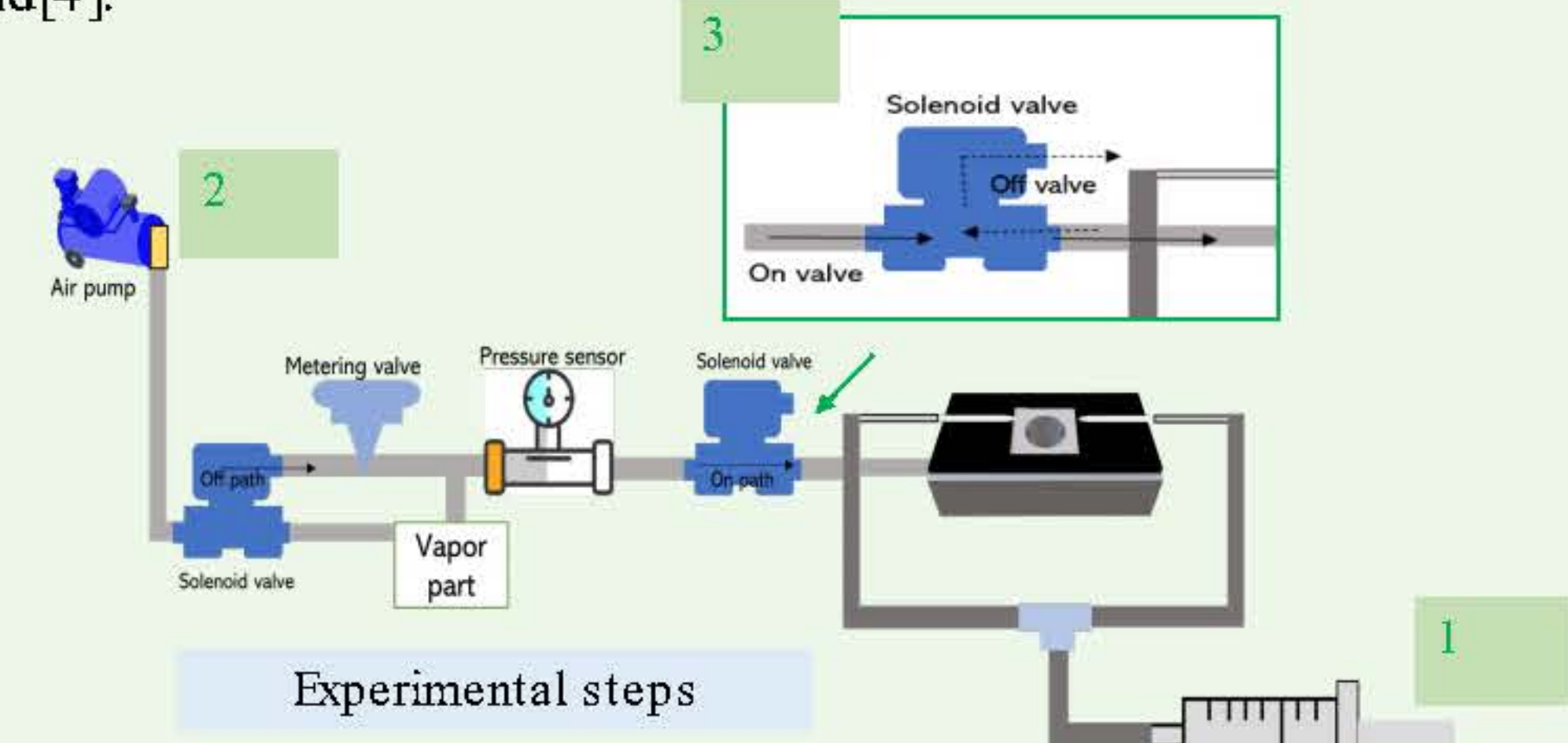


Topology defect(S=+1)in island

Two needles, each with a diameter of 0.5 mm, were positioned approximately 3 mm above the film (on each side of the film). After air was injected into the film by the needles, the airflow from each tip of the needle was sheared due to their arrangement causing several islands to happen. The interior of each island is found to typically contain a +1 topological defect in the c-director field. This occurrence arises due to the presence of strong orientational anchoring conditions at the boundaries of the island[4].



However, line defects always formed in the film after air injection. Moreover, 2π wall can be found occasionally as well.



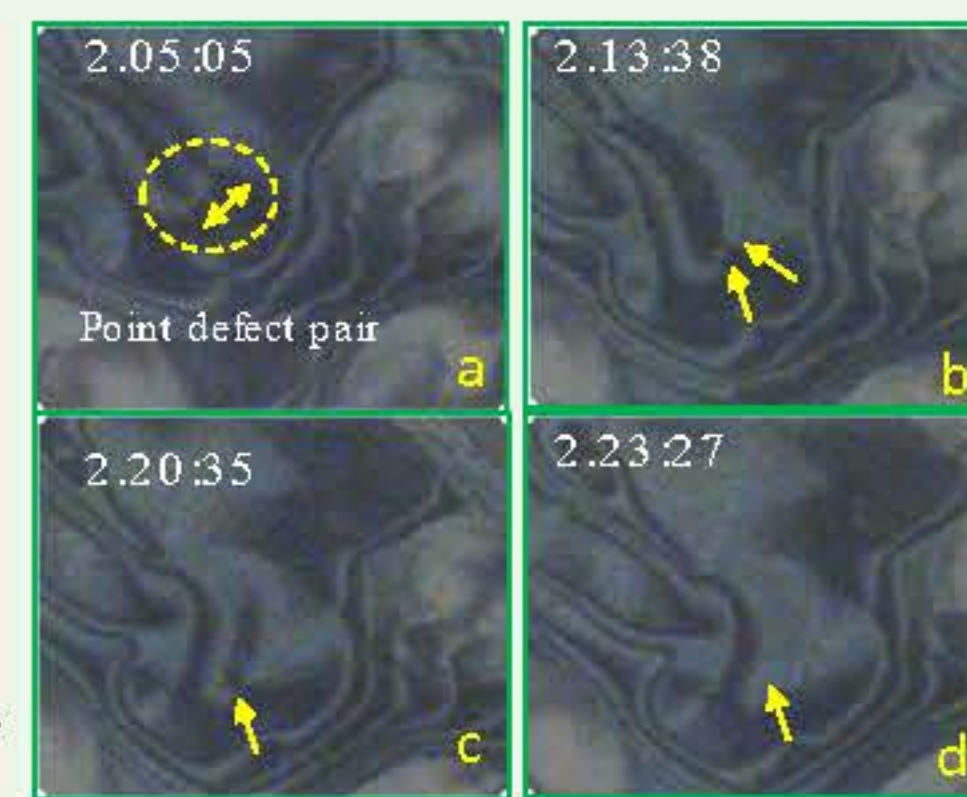
The application of air pumping causes an increase in pressure beneath the film, leading to the film in the form of bulging. The abrupt reduction in pressure thereafter induces the film to swiftly revert back to its initial planar configuration. In general, there is -1 defect outside the island[4]. Once subjected to quick quenching under pressure, the boundaries of the island were relaxed. Defect +1 will be retained.

3 Switch the solenoid valve off



Several points defect

An output way of the solenoid valve opens to the atmosphere with the off path. By switching the solenoid valve off, quenching of pressure occurs. Several defect points were observed. The annihilation of point defect paired with opposite charge will be taken into account in this study.



This outcome was extracted from a video displaying with modified speed x0.5.

Conclusion and Plan:

Conclusion	Further work			
❖ What I have done so far: ✓ Literature Review of LC and defect in LC ✓ Experimental design with air interruption to film system ❖ What I have found: ▪ Air blowing created islands with +1 defect ▪ Pressure quenching caused the boundary of the island to relax. ▪ Point defect pairs were found	❖ Ground-based examination	Plan	Detail	❖ Microgravity environment examination Plan and Detail ❑ How to collect data (design set-up) ❑ Test in clino stat at GISTDA ❑ Compare with ground-based results
		➢ Improvement set-up	❑ Use a motor drive syringe/use another pump instead syringe ❑ Film illumination by laser	
		➢ Data analysis	❑ Measure the distance between point defect vs time ❑ Free energy model	
		➢ Experimental factor	❑ Flow rate and pressure measurement	

References:

- [1] S. P. Radzihovsky *et al.*, "Two-dimensional island emulsions in ultrathin, freely-suspended smectic liquid crystal films," *Soft Matter*, vol. 13, no. 37, pp. 6314–6321, 2017, doi: 10.1039/C7SM01584D.
- [2] R. A. Chowdhury, A. A. S. Green, C. S. Park, J. E. Mckennan, and N. A. Clark, "Topological defect coarsening in quenched smectic-C films analyzed using artificial neural networks," *J. Phys. Rev. E*, vol. 107, no. 4, p. 044701, Apr. 2023, doi: 10.1103/PhysRevE.107.044701.
- [3] K. Harth and R. Stannarius, "Topological Point Defects of Liquid Crystals in Quasi-Two-Dimensional Geometries," *Front. Phys.*, vol. 8, May 2020, doi: 10.3389/fphys.2020.00112.
- [4] D. Pettit, T. C. Lubensky, and D. R. Link, "Topological inclusions in 2D smectic C films," *Liq. Cryst.*, vol. 25, p. 579, 1998.

Acknowledgment:

Authors would like to thank Prof. Noel Clark and Prof. Joseph MacLennan from University of Colorado, Boulder for fruitful discussions. The funding support has been received from the NSRF via the Program Management Unit for Human Resources & Institutional Development, Research and Innovation [grant number B13F660122].

Experiment and Simulation on Azo-based Nematic Liquid Crystal droplets under photoactive and optical tweezers



Worawat Traiwattanapong¹, Suchapan Makaew¹, Jarinee Kiang-ia¹, Pongthep Prajongtat², Papichaya Chaisakul¹, Gurumurthy Hegde^{3,4}, Nattaporn Chattham¹

¹Department of Physics, Faculty of Science, Kasetsart University, Bangkok 10900, Thailand.

²Department of Materials Science, Faculty of Science, Kasetsart University, Bangkok 10900, Thailand

³Department of Chemistry, CHRIST (Deemed to be University), Bangalore 560029, India.

⁴Centre for Advanced Research and Development (CARD), CHRIST (Deemed to be University), Bangalore 560029, India.

1. Introduction

Liquid crystal (LC) materials have been increasingly studied and developed in both university and industrial marketing such as Samsung Electronics Co, Ltd, Apple inc, Canon Kk, etc, as shown in Fig. 1. Because LC materials are high in refractive index and optical anisotropy, hence, they can be used for many applications such as liquid crystal displays (LCD), optical modulator, and optical sensor [1-3]. There are many commercial products of LC materials available such as 5CB, E7, and 8CB. One of the most studied materials is 5CB (4-cyano-4'-pentylbiphenyl) nematic liquid crystal (NLC). Hence, the behavior of 5CB liquid crystal materials have been widely studied such as photoactive, optical tweezers, and defects. The azo groups are chemical compounds with N=N linkage that can be applied to other materials to transform them into mechanically active materials under ultraviolet (UV) light irradiation. We are thus focusing on applied azo linkage to NLC so that mechanical response and optical response can be studied together. Here, we investigate the behavior of NLC droplets based on azo compounds, exhibiting photoactive characteristics when manipulated with optical tweezers.

Additionally, we examine the behavior of electric field (E-field) directions in circularly polarized light after its interaction with the NLC droplets, utilizing a 3D Finite-Difference Time-Domain (3D-FDTD) simulation. Our findings indicated a notable alteration in the E-field directions of the LC in radial structure compared to the original light source. This change is attributed to the interplay between LC orientation and defect positioning.



Fig.1. (a) Patent documents in liquid crystals increases significantly over time (b) top applicants of liquid crystals [4].

2. Methods

2.1 Experimental part

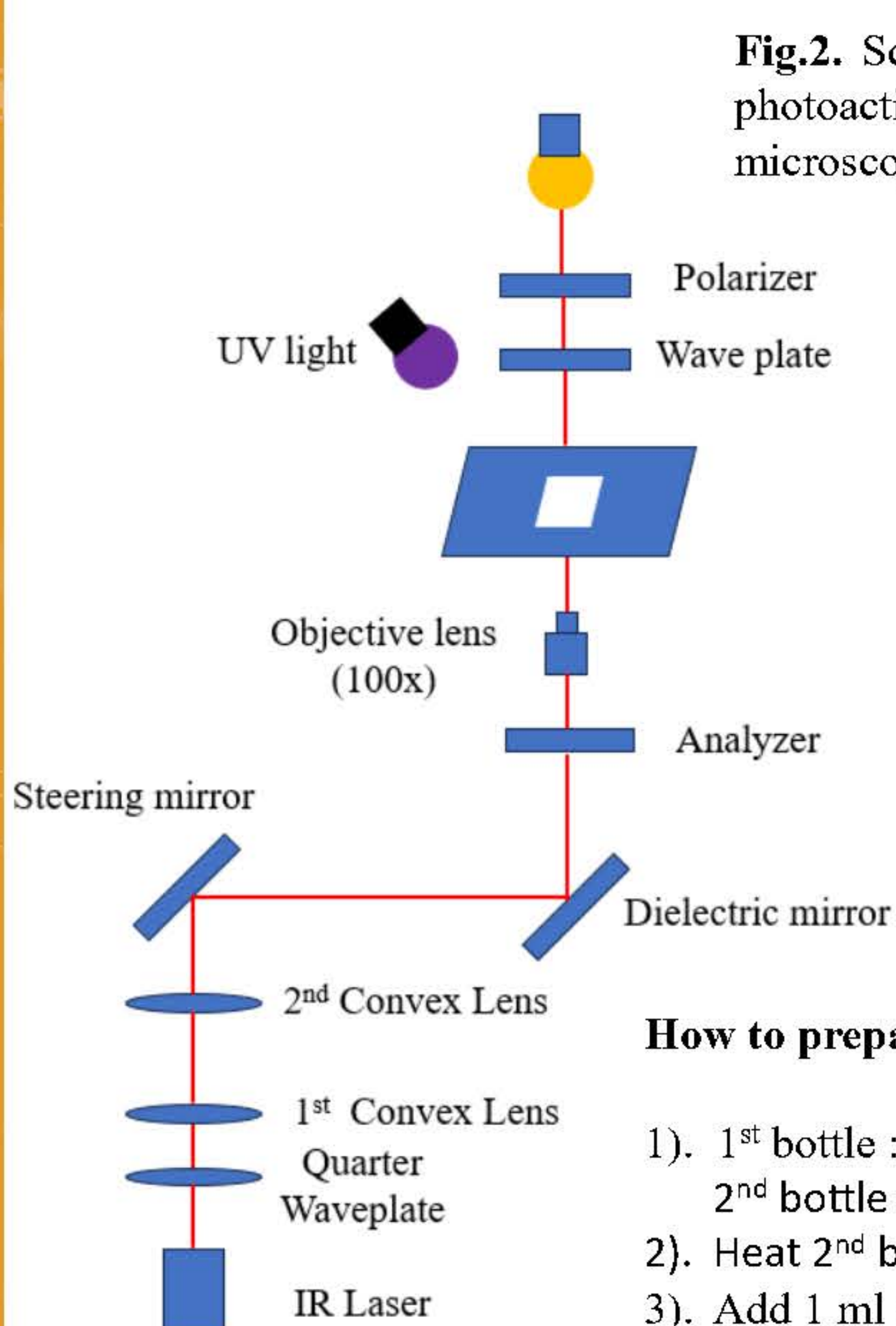


Fig.2. Schematic illustration of the optical tweezers and photoactive behavior setup on a Nikon Eclipse Ti inverted microscope.

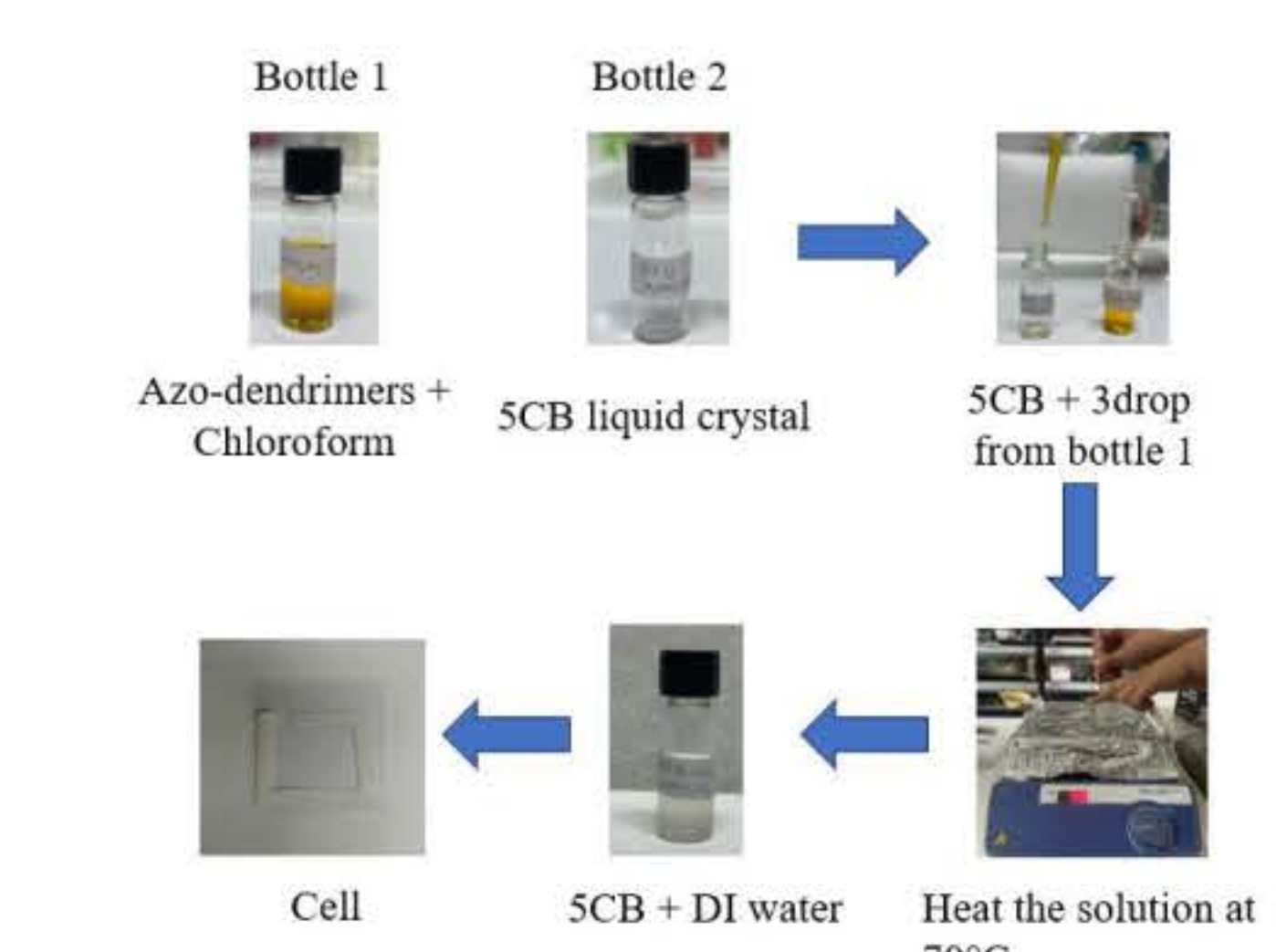


Fig.3. Schematic diagram showing the steps for Azo-based NLC droplets

How to prepare the NLC droplets based on azo compounds

- 1st bottle : 1500 µg of azo compounds + 0.5 ml of chloroform
- 2nd bottle : 4500 µg of 5CB + 3 drop of 1st bottle
- Heat 2nd bottle for 4 mins at 70 °C
- Add 1 ml of DI water to 2nd bottle
- Insert the solution in 2nd bottle into a cell

4. Conclusion

We investigated the behavior of NLC droplets based on azo compound exhibiting photoactive characteristics when manipulated with optical tweezers under UV light and circularly polarized light at the wavelength of 1064 nm. These droplets generate inner topological point defects, which we thoroughly examined. Our experimental observations revealed two types of topological points defects within the NLC droplets consisting of the hedgehog defect (NLC adopting a radial structure) and the boojum defect (NLC displaying a bipolar structure). The emergence of both structures is dependent on UV light irradiation and termination. Azo-based NLC droplets can change from radial structure to bipolar structure under UV light irradiation. We also treated them under low-intensity circularly polarized light optical tweezers and the hedgehog defect are found rotating and slowly decrease rotation speed and stop completely when the UV changes their structure to bipolar. Once the UV light is deactivated, the droplets revert from a bipolar to a radial structure and interestingly, they regain their initial behavior to rotate when subjected to circularly polarized light. Additionally, we demonstrated the E-field direction in circularly polarized light after its interaction with the NLC droplets using 3D-FDTD. We found that the E-field directions of the LC in radial structure is different from the original light source due to LC orientation and defect positioning.

5. Acknowledgement

This research has received funding support from the NSRF via the Program Management Unit for Human Resources & Institutional Development, Research and Innovation [grant number B13F660122]

2.2 Simulation setup

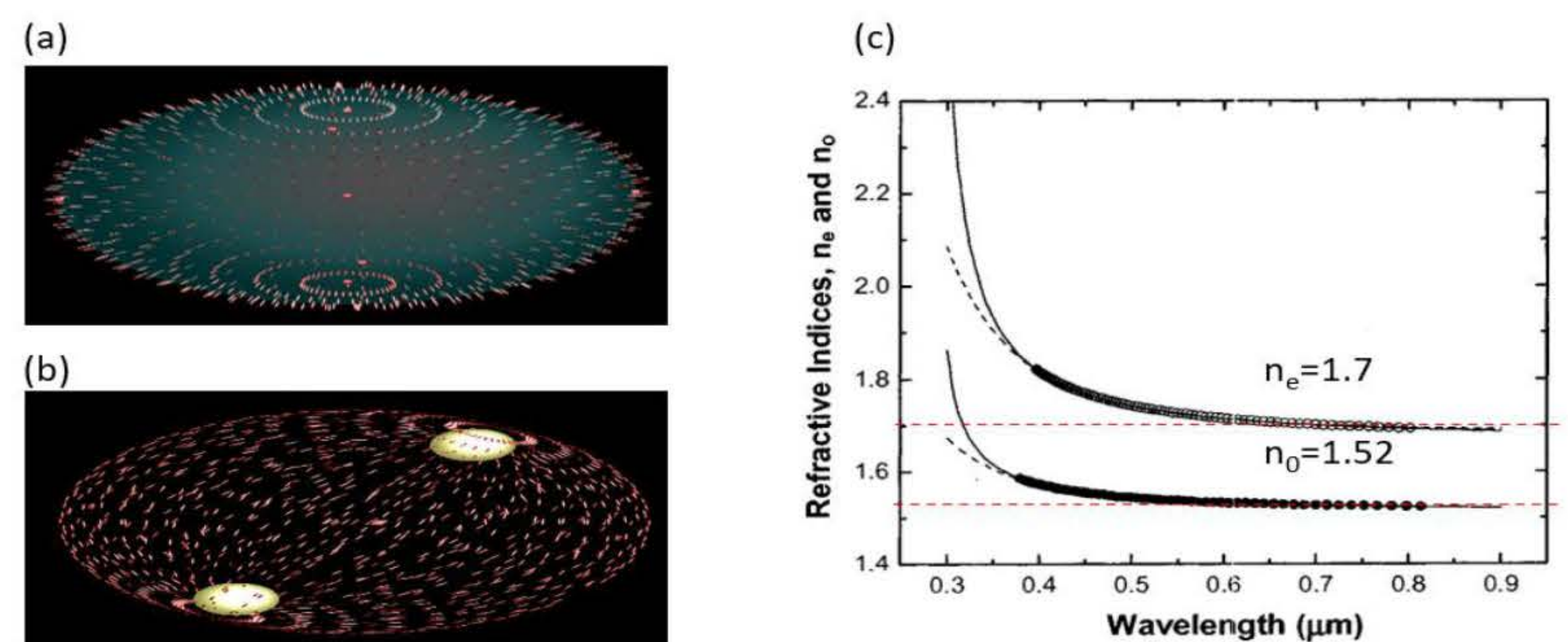
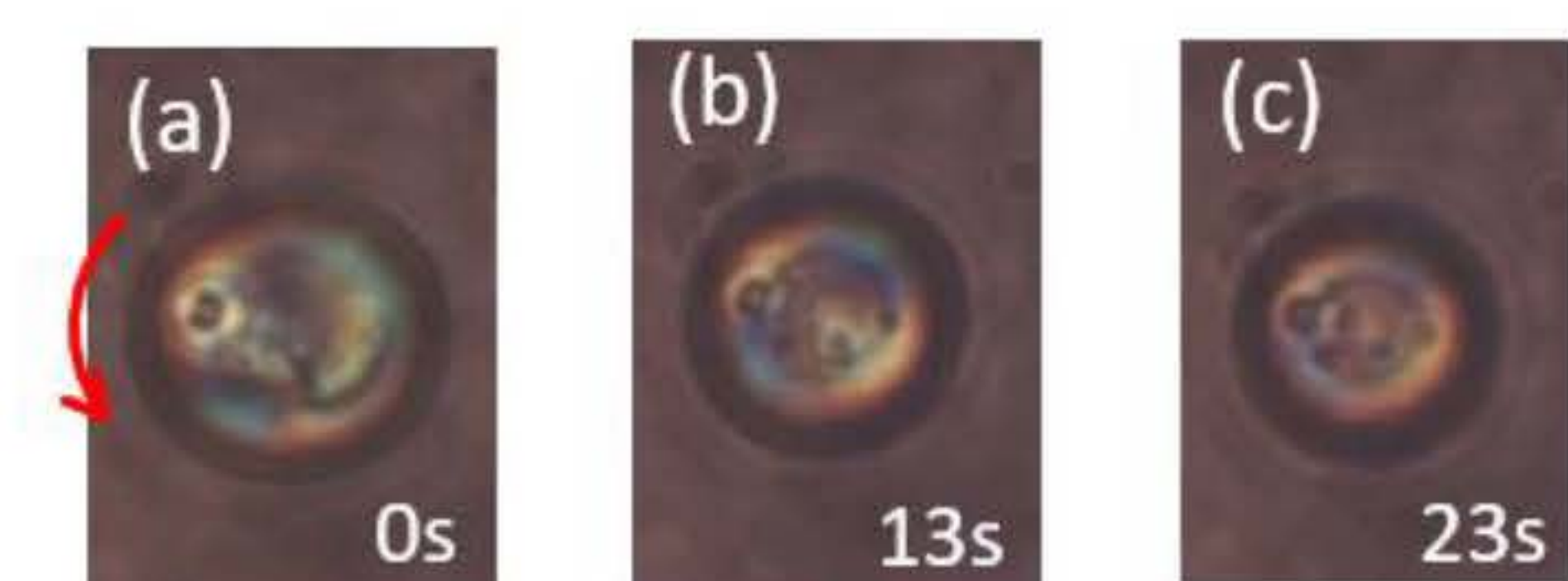


Fig. 4. Schematic of liquid crystal droplets in (a) radial structure, (b) bipolar structure. (c) Refractive indices versus wavelength of 5CB molecules.

We investigated the E-field directions in circularly polarized light after its interaction with the NLC droplets using a 3D Finite-Difference Time-Domain (3D-FDTD) simulation at the optical wavelength of 1064 nm. We first created two types of NLC droplets of radial and bipolar structures, as shown in Fig 4(a) and (b). The refractive indices of NLC molecule in z-direction (n_e) and xy-direction (n_o) are 1.7 and 1.52, respectively, as shown in Fig 4(c).

3. Results and Discussions

UV on (Radial → bipolar structure)



UV off (bipolar → Radial structure)

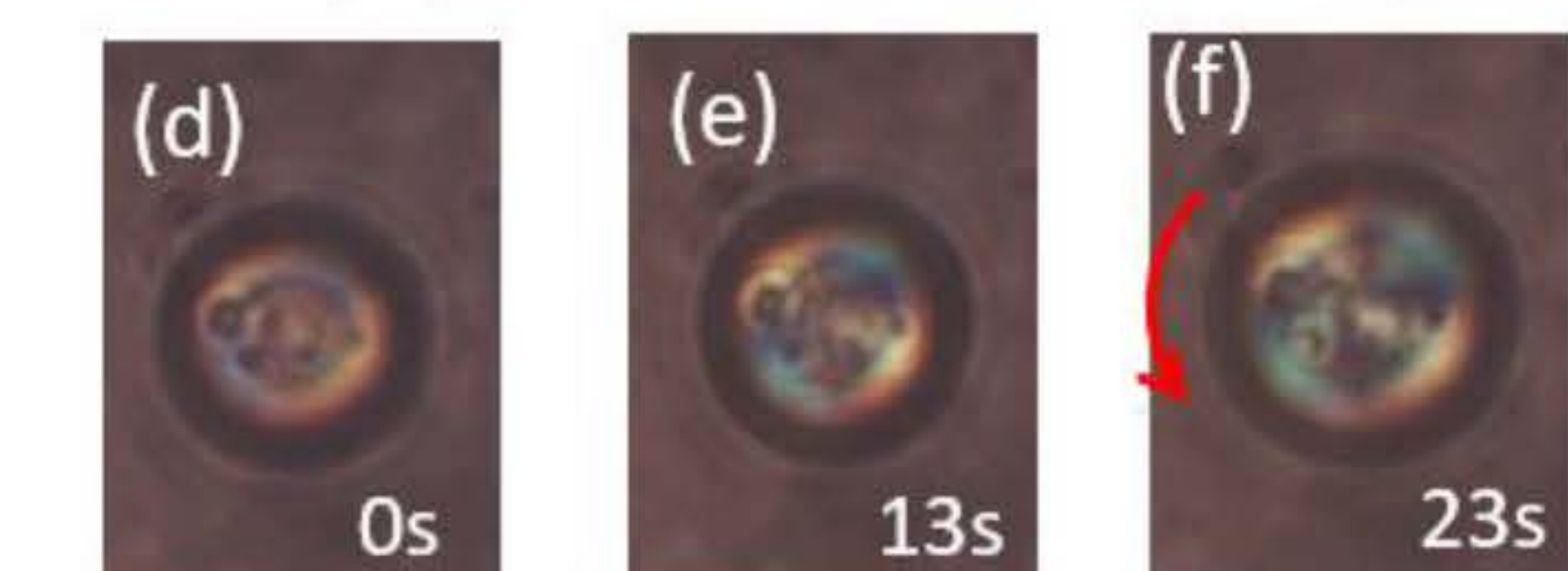


Fig. 5. Series of video frames in the transformation processes (a-c) from radial structure to bipolar structure under UV irradiation, (d-f) from bipolar structure to radial structure.

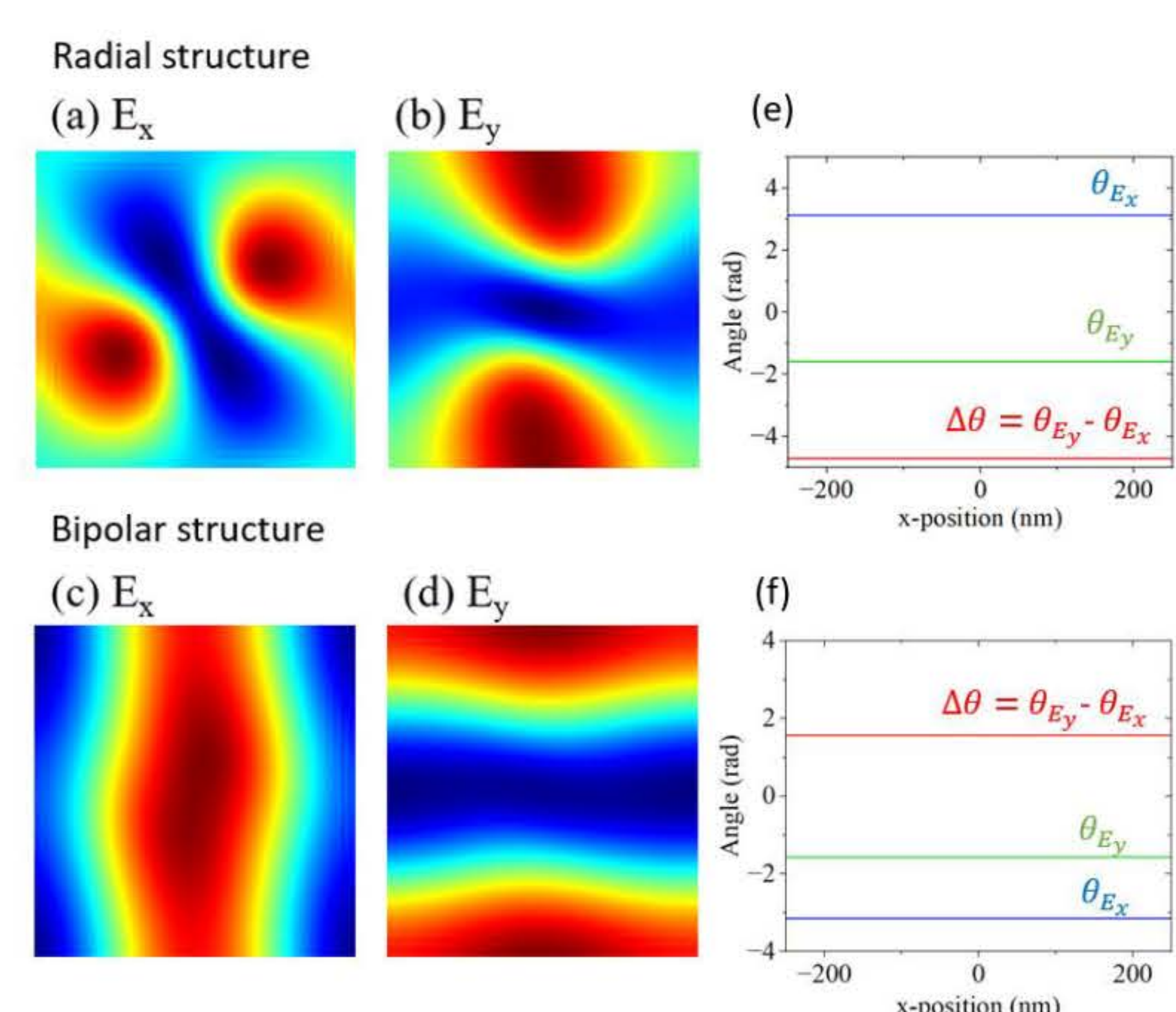


Fig. 6. E-field in x- and y-directions of (a-b) radial and (c-d) bipolar structures. Angle of E_x and E_y of (e) radial and (f) bipolar structures.

6. References

- T. Geelhaar, Liquid Crystals **24**, 91-98 (1998)
- R. J. Carlton, J. T. Hunter, D. S. Miller, R. Abbasi, P. C. Mushenheim, L. N. Tan, and N. L. Abbott, Liquid Crystals Reviews **1**, 29-51 (2013)
- K. M. Johnson, D. J. McKnight, and I. Underwood, IEEE Journal of Quantum Electronics **29**, 699-714 (1993)
- <https://www.lens.org>

An Atomic-Scale Investigation of Liquid Crystal Orientation in Different Solvents

Nililla Nisoh^{1,2}, Nathanon Kerdkaen^{1,2}, Nattaporn Chattham¹, Mikko Karttunen^{3,4,5} and Jirasak Wong-ekkabut^{1,2,*}

¹ Department of Physics, Faculty of Science, Kasetsart University, Bangkok 10900, Thailand; lilla.phys@gmail.com

² Computational Biomodelling Laboratory for Agricultural Science and Technology (CBLAST), Faculty of Science, Kasetsart University, Bangkok 10900, Thailand

³ Department of Chemistry, The University of Western Ontario, 1151 Richmond Street, London, ON N6A 3K7, Canada; mkarttu@uwo.ca

⁴ Department of Physics and Astronomy, The University of Western Ontario, 1151 Richmond Street, London, ON N6A 3K7, Canada

⁵ The Centre for Advanced Materials Research (CAMBR), The University of Western Ontario, 1151 Richmond Street, London, ON N6A 3K7, Canada

* Correspondence: jirasak.w@ku.ac.th

Introduction

Liquid crystals (LCs) are a distinct state of matter that exhibits properties of both liquids and solids. Their unique characteristics, such as molecular orientation, phase behavior, and conformational features, have led to their widespread application in the manufacturing process of Liquid Crystal Displays (LCDs), optical switches, and various optical devices. Of particular interest is the phenomenon of solute adsorption at the interface between a bulk LC and aqueous phases, potentially inducing orientational or anchoring transitions. The interaction of solutes at LC-aqueous interfaces is recognized as the mechanism that activates the reorientation of LC upon the addition of different solutes. However, the comprehensive of the physical principle behind this collective reorientation remains limited.

To address this gap, molecular dynamics (MD) simulation emerges as a highly effective method for studying the behavior of liquid crystals. In this work, we employed atomistic MD simulations to investigate the molecular organization of the most widely used nematic 4-pentyl-4'-cyanobiphenyl (5CB) and smectic 4-octyl-4'-cyanobiphenyl (8CB) in presence of solvents and alcohol. The primary focus is to comprehend how solvents affect the orientational order, molecular conformation, and dynamic diffusion behavior of 5CB and 8CB. This study is a part of the Thailand Liquid Crystals in Space project, which is investigating liquid crystals for space technologies. The findings of this research are poised to facilitate the development of innovative liquid crystal materials distinguished by unique features. This, in turn, is expected to broaden their application within the realm of space technologies.

Phase Behavior of Liquid Crystal in Different Solvents

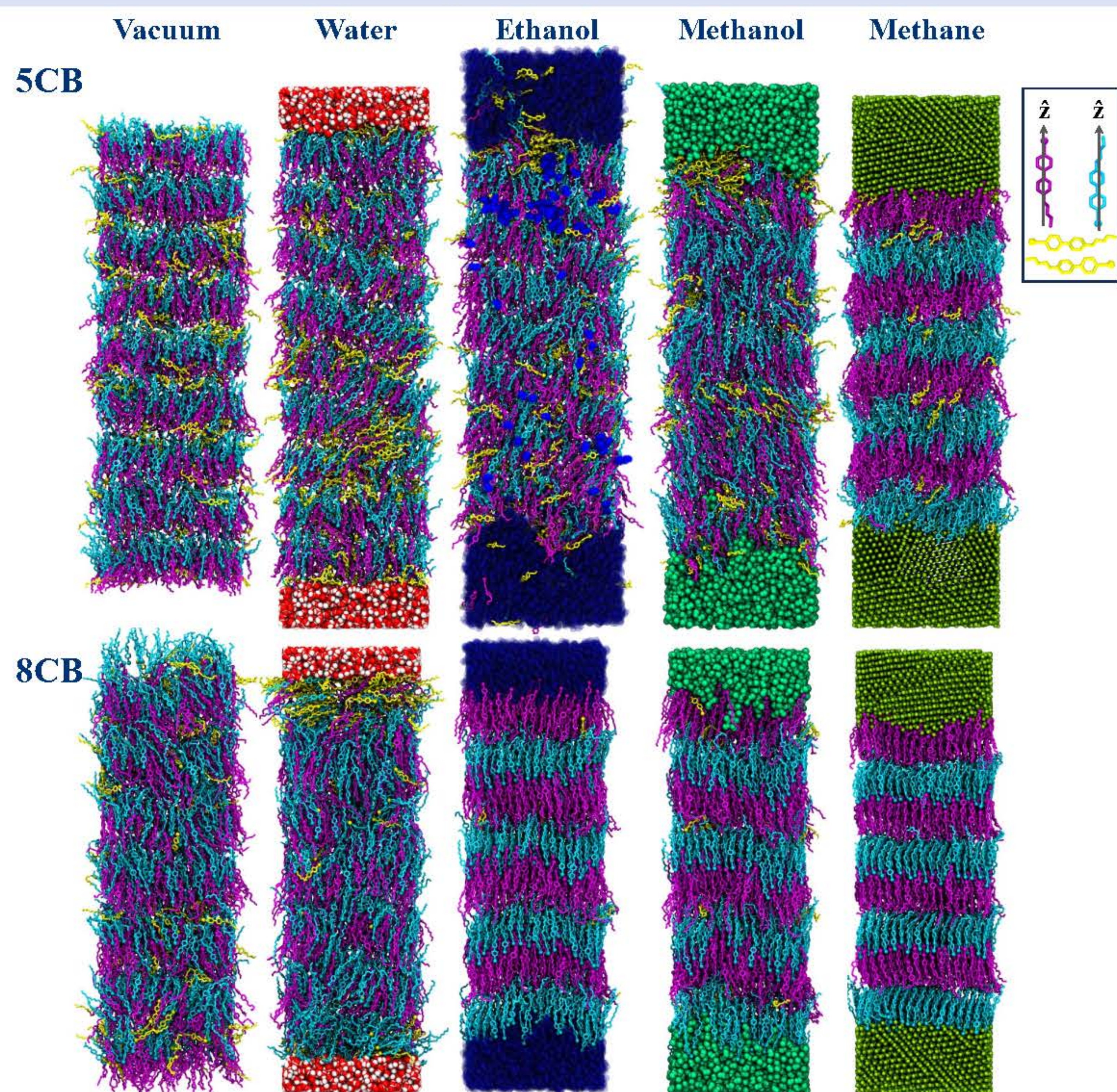


Figure 1 Molecular snapshot comparison of 5CB and 8CB in the presence of water, ethanol, methanol and methane after 100ns. Color-coding highlights variations in angle (θ) from the molecule long axes in the range: $0^\circ \leq \theta < 60^\circ$ (purple), $60^\circ \leq \theta < 120^\circ$ (yellow) and $120^\circ \leq \theta < 180^\circ$ (cyan).

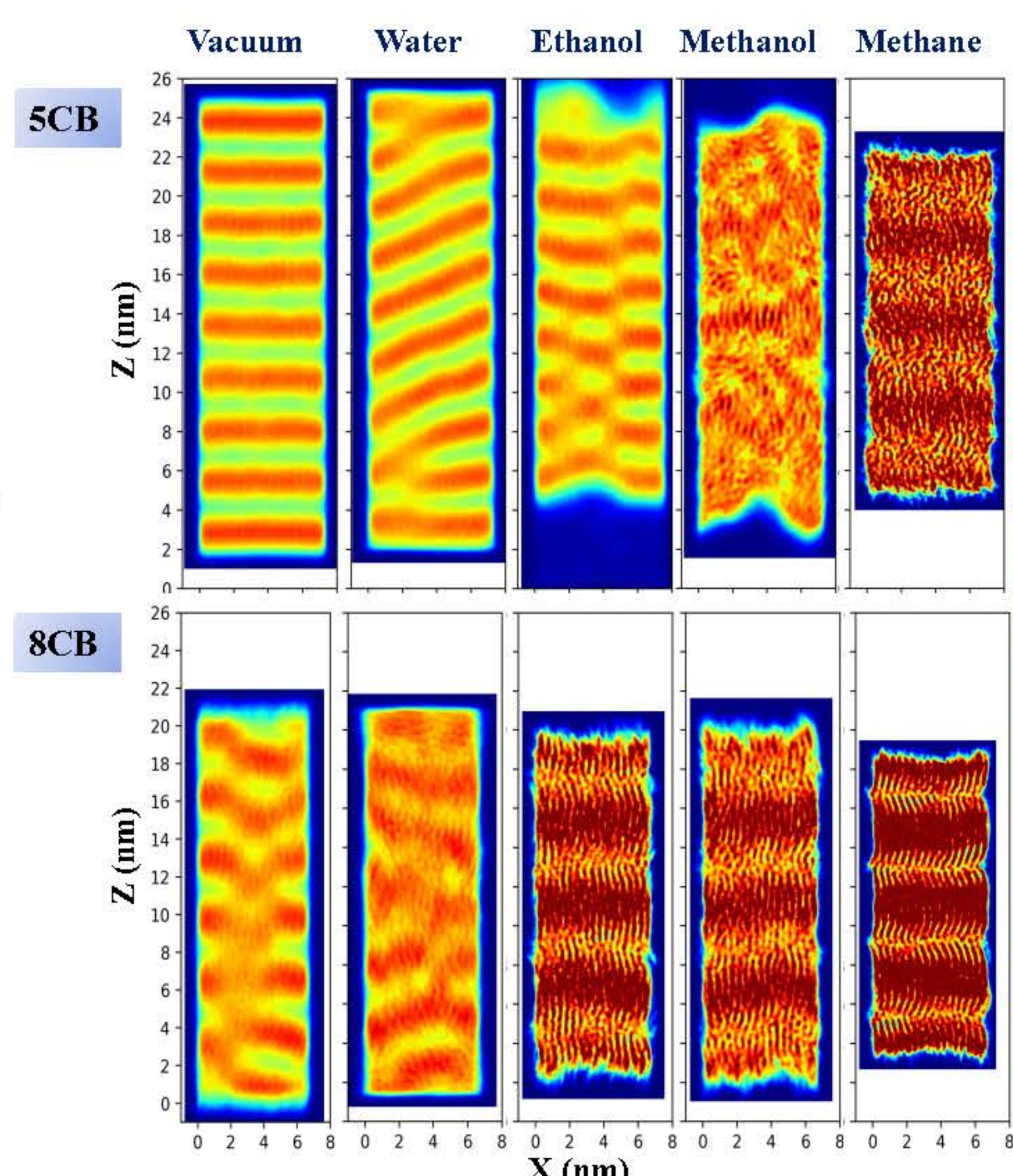


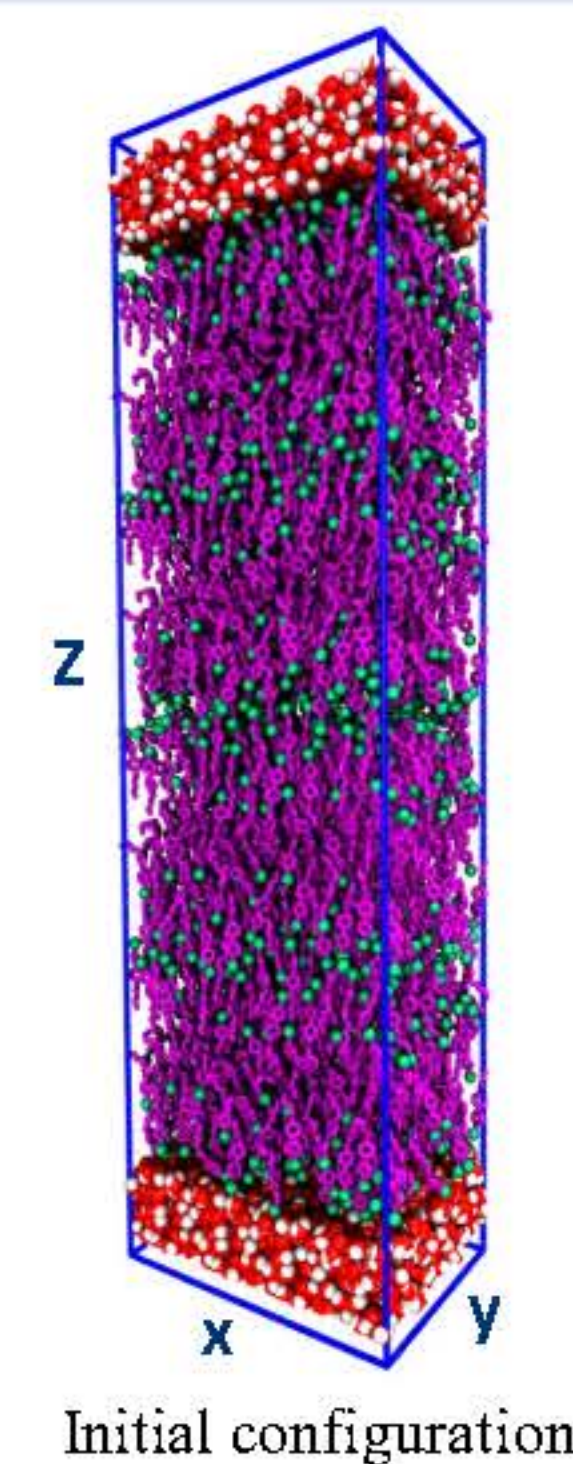
Figure 2 2D liquid crystal density map in the presence of different solvents

Acknowledgement

This research has received funding support from the NSRF via the Program Management Unit for Human Resources & Institutional Development, Research and Innovation [grant number B13F660122].

Methods

The United atom model



Simulation Conditions

- The united-atoms force fields developed by Zhang et al.
- NVT ensemble at 300 K
- 2,048 molecules for both 5CB or 8CB
- 4,474 molecules for water/methanol, 3,594 molecules for ethanol and 9,856 for methane
- A periodic simulation box with dimensions of $7.3 \times 5 \times 27$ nm³ for 5CB and $6.6 \times 7 \times 22$ nm³ for 8CB
- The GROMACS 5.1.2 program
- All system were subject to multiple intervals of 100 ns MD simulations ($10 \times 100 = 1000$ ns)

Solvents-induced Orientation

The orientational order of LC molecules can be characterized using the Second Legendre polynomial $P_2(z)$

$$\langle P_2(z) \rangle = \frac{1}{2} (3 \cos^2 \theta - 1)$$

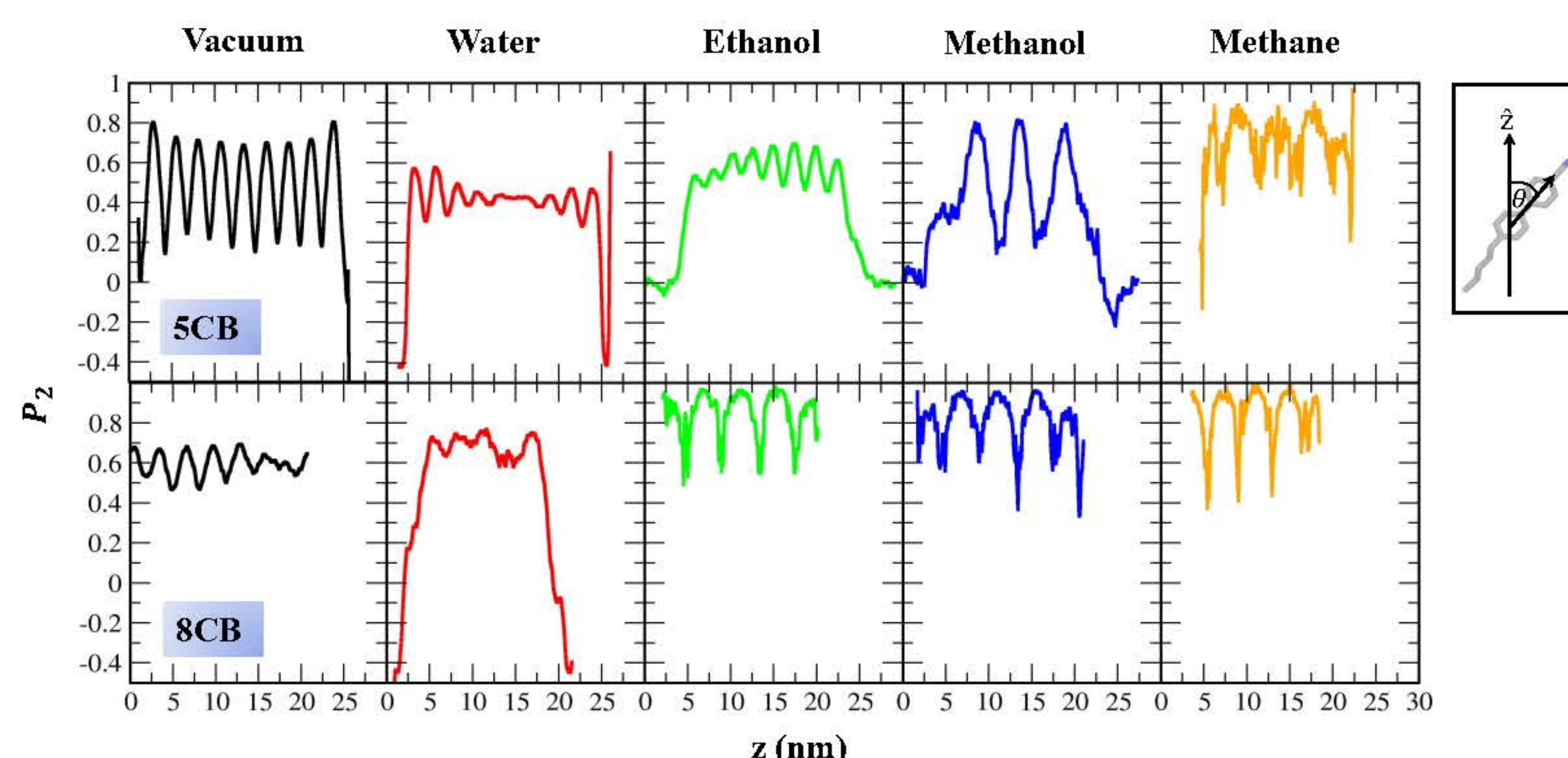


Figure 3 The orientation order parameter $\langle P_2(z) \rangle$ at 300K of 5CB and 8CB in different solvents.

Angle Distribution

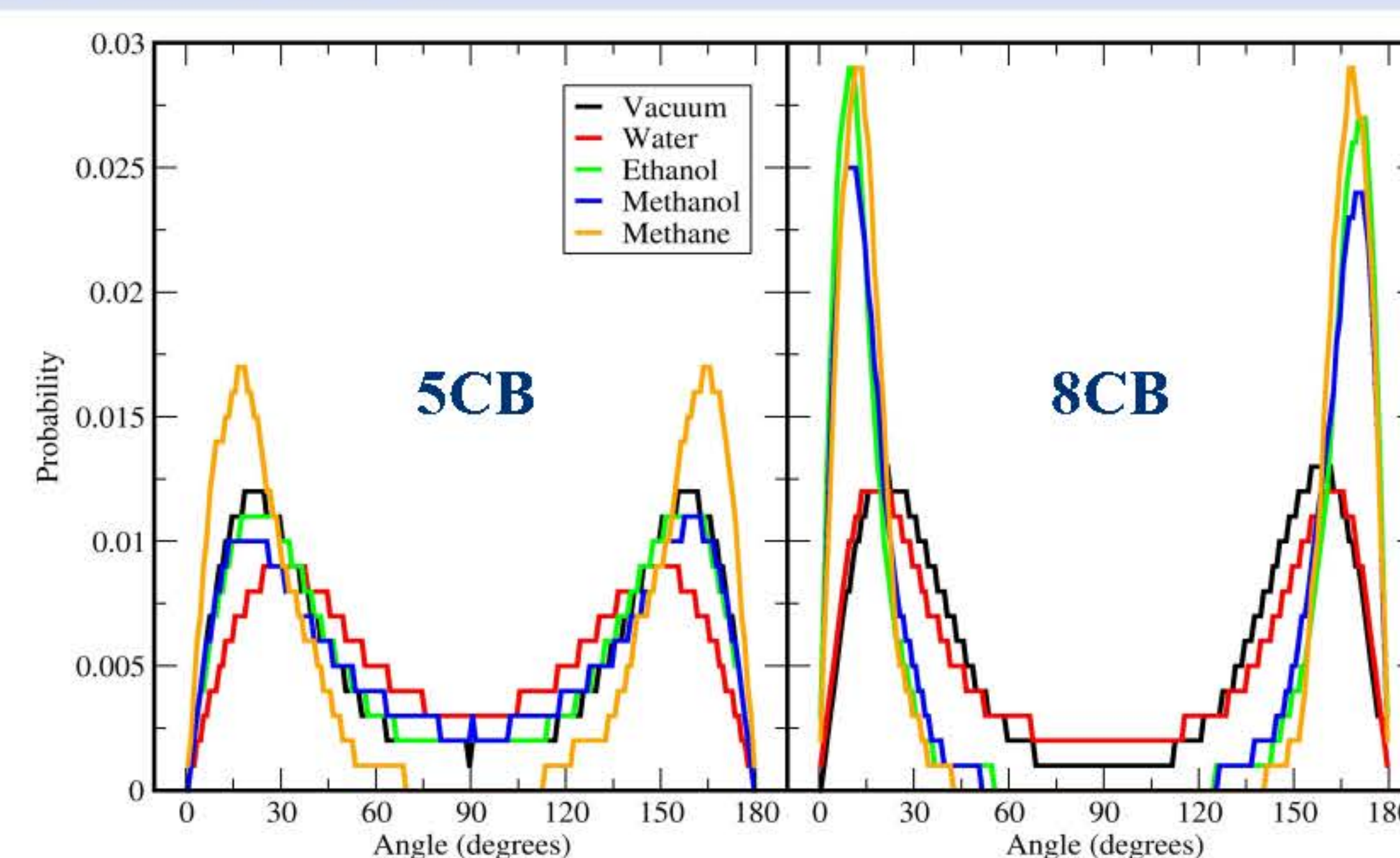


Figure 4 Angle distribution of θ for 5CB and 8CB at different solvents. All relative to z-axis.

Density Profiles of Liquid Crystal

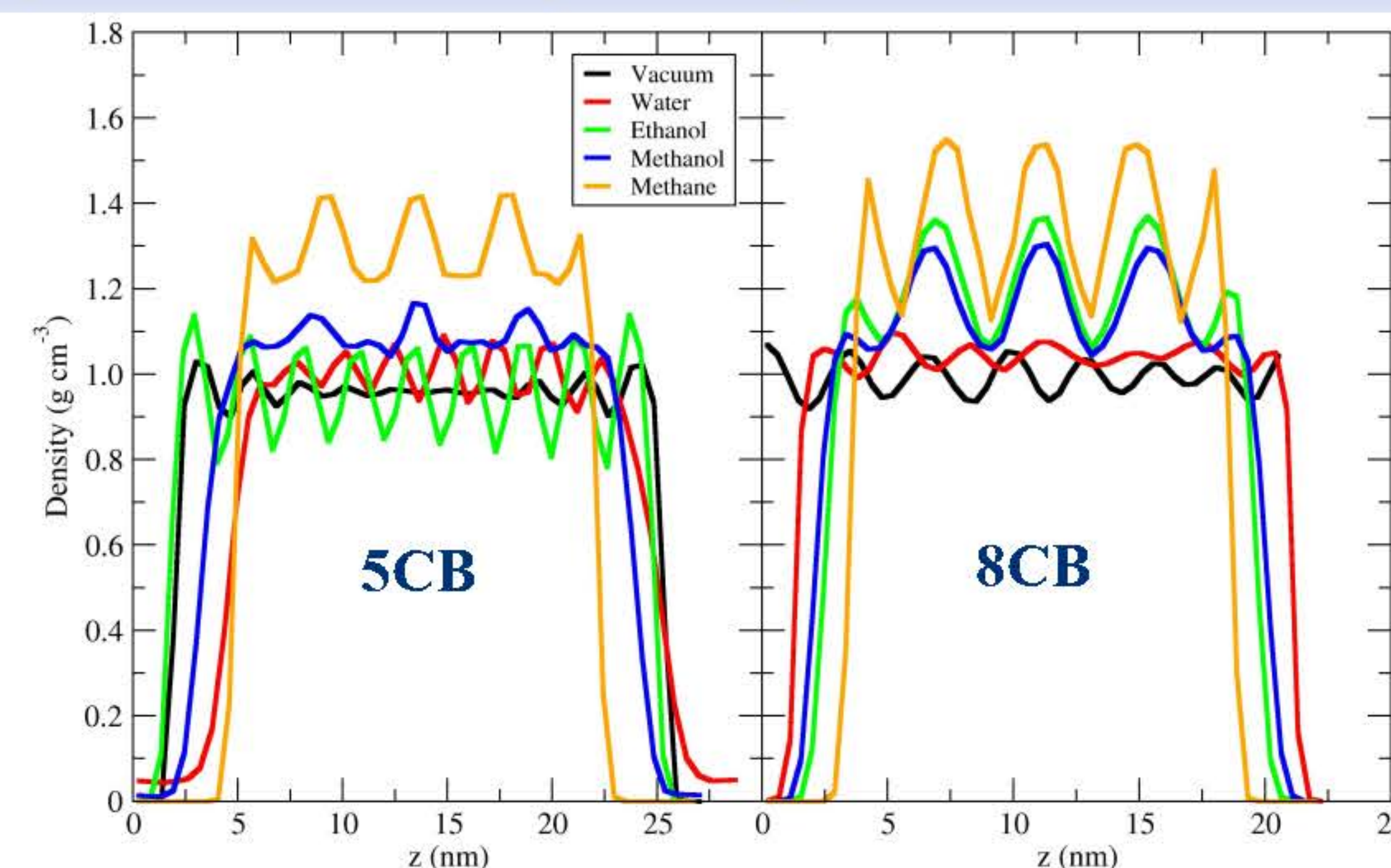


Figure 5 Mass density profiles along the z direction of 5CB (left) and 8CB (right) in the different solvents (water, ethanol, methanol, methane).

Future work

Future work may involve exploring solvent dynamics, especially variations in permeability among different solvents and the diffusion properties of 5CB in ethanol. Calculations for the local orientation order parameter within the interface of the liquid crystal and solvents are of interest. Additional simulation setups will involve 5CB and 8CB in diverse solvents at varying temperatures. There is also curiosity about the thermal behavior of the liquid crystal, prompting a study on the transition temperature (T_c) across different solvent conditions.

Reference

Jianguo Zhang, Jiaye Su, and Hongxia Guo
The Journal of Physical Chemistry B **2011** 115 (10), 2214-2227 DOI: 10.1021/jp111408n

Simulations of Interface between Azodendrimer and Liquid Crystal for Space Applications

Postdoctoral Researcher *Dr. Pornkamon Nalakarn*
Principle investigator *Assoc. Prof. Dr. Jirasak Wong-ekkabut*
Project Head *Assoc. Prof. Dr. Nattaporn Chattam*
Department of Physics, Faculty of Science, Kasetsart University
Bangkok, Thailand

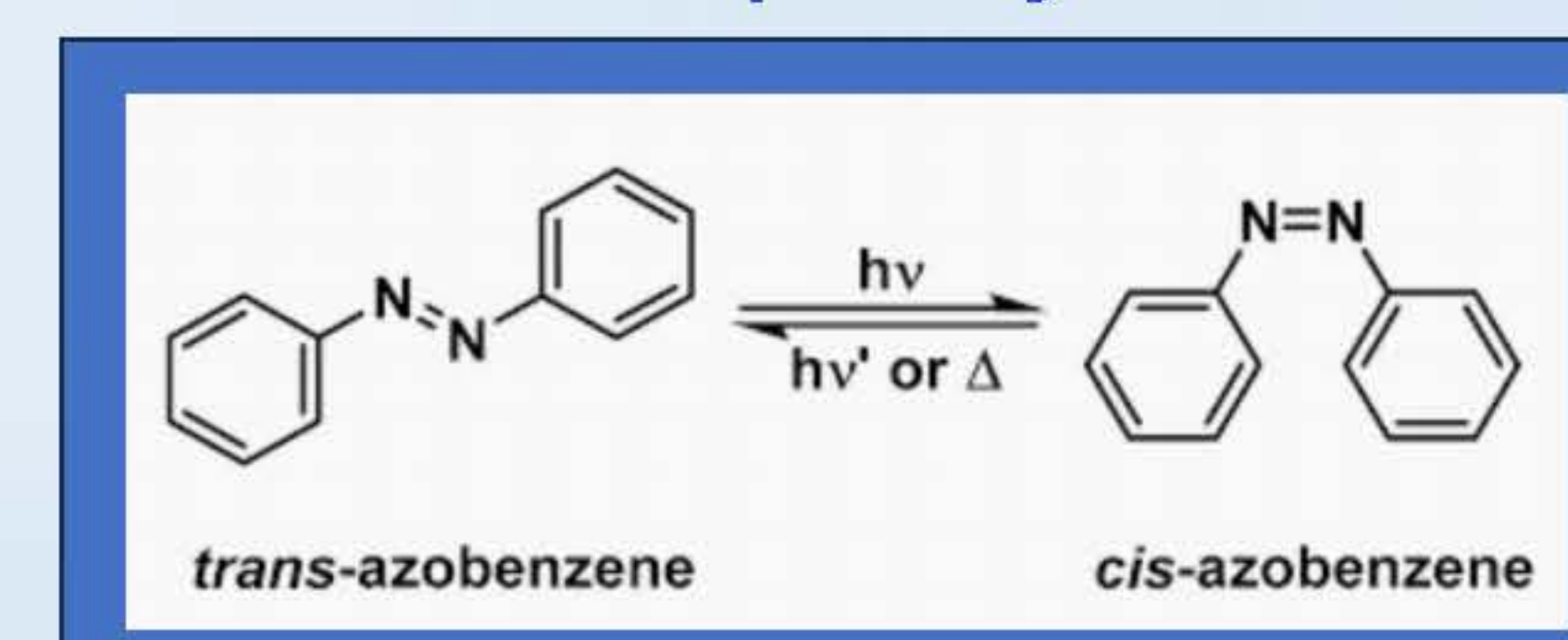


Introduction

Liquid Crystal (LC) is a fascinating materials with diverse applications, responding to external stimuli such as light, heat and electric fields. *Dendrimers* can act as active materials when azo groups are added to their ends. *Azodendrimer* is a special molecule that acts like a command surface. When exposed to Ultraviolet (UV) light, it change its phase. This molecule is significant as crucial interface carriers for liquid crystal, influencing the change mechanisms and directional characteristics of the liquid crystal.

Computer simulation is a useful tool for studying the interaction of Azodendrimer and Liquid Crystal, providing how molecules arrange and behave in different phases.

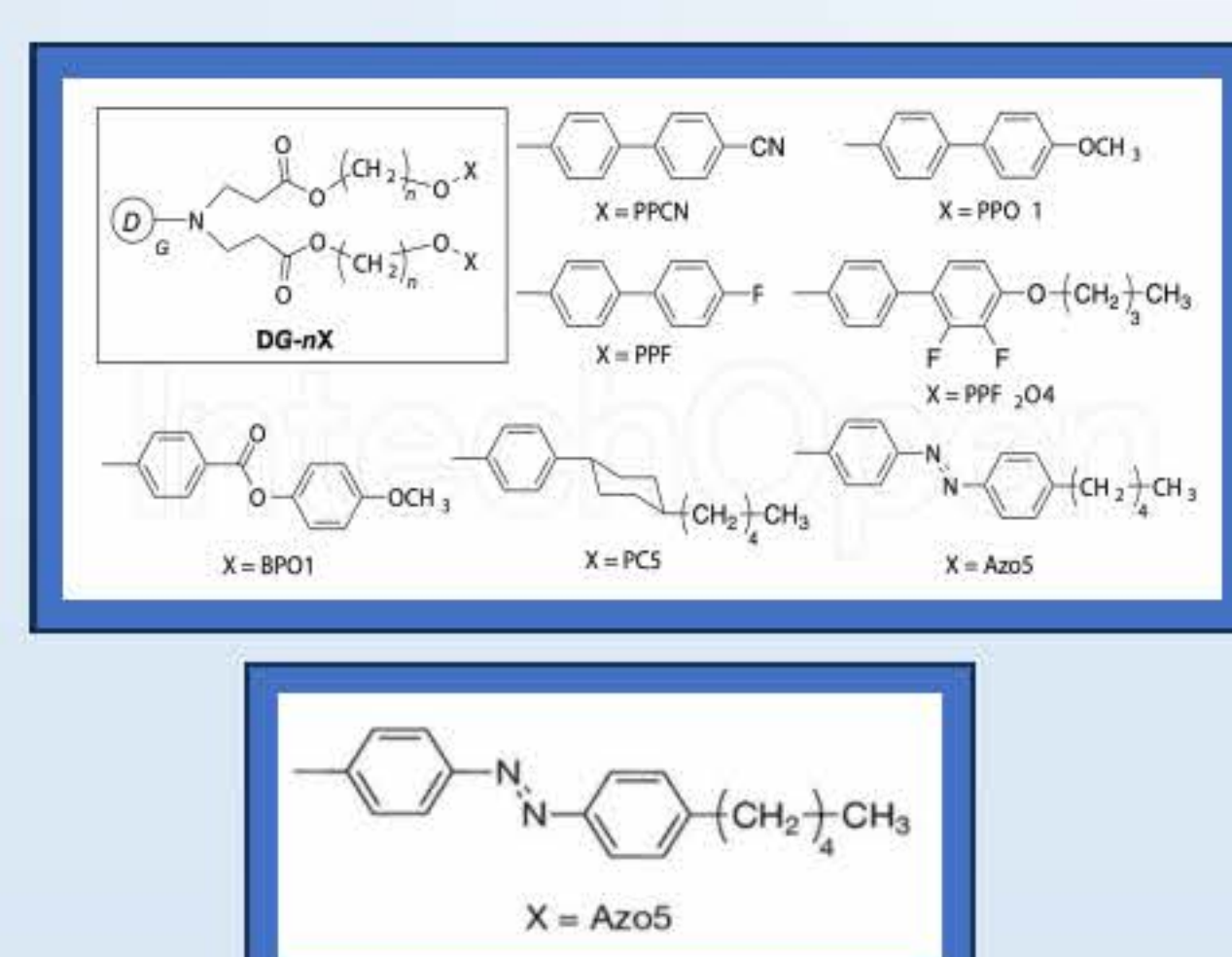
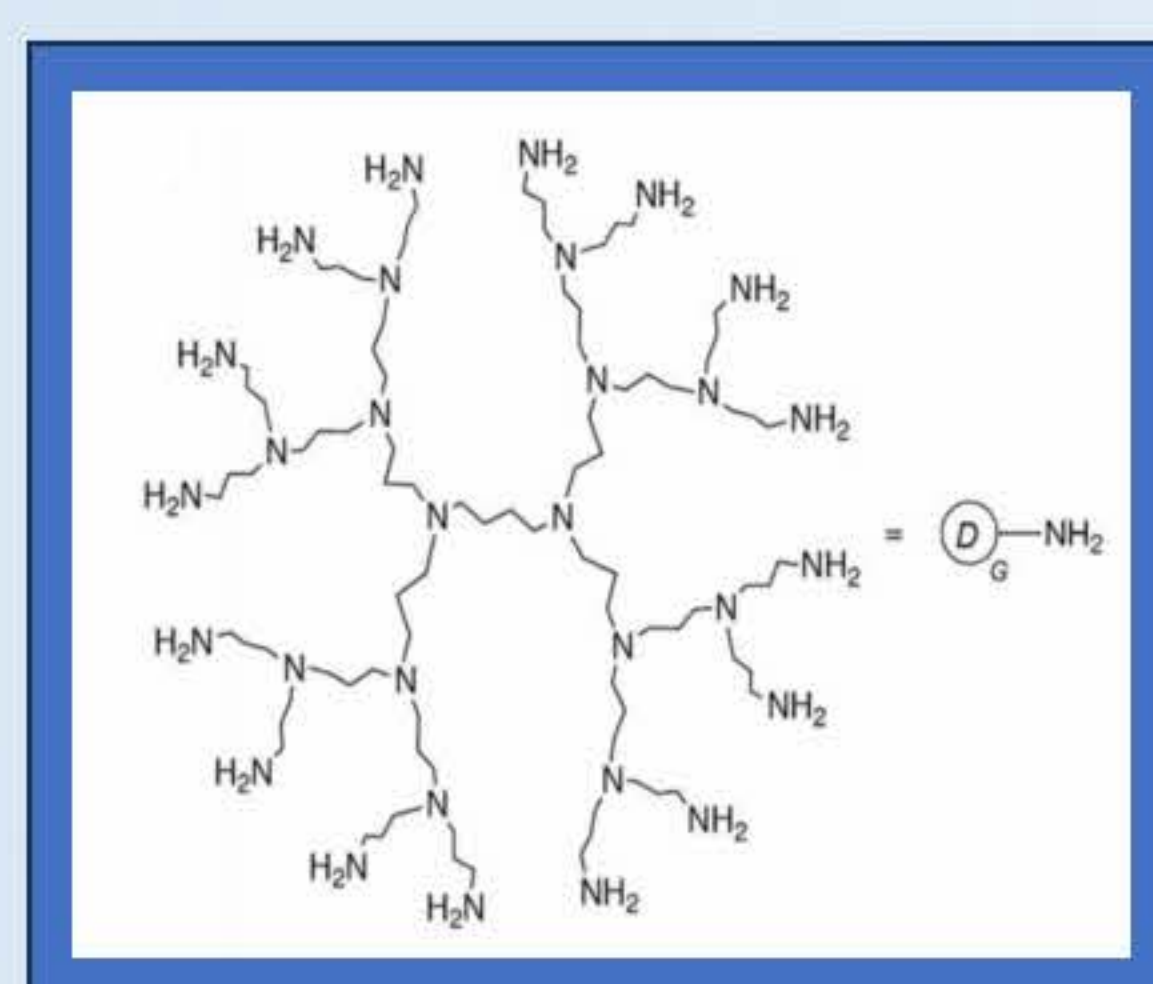
In the present study, we use Molecular Dynamics (MD) simulation to explore the mechanisms that alter the arrangement and direction of Azodendrimer and liquid crystal on an atomic scale when activate by UV light.



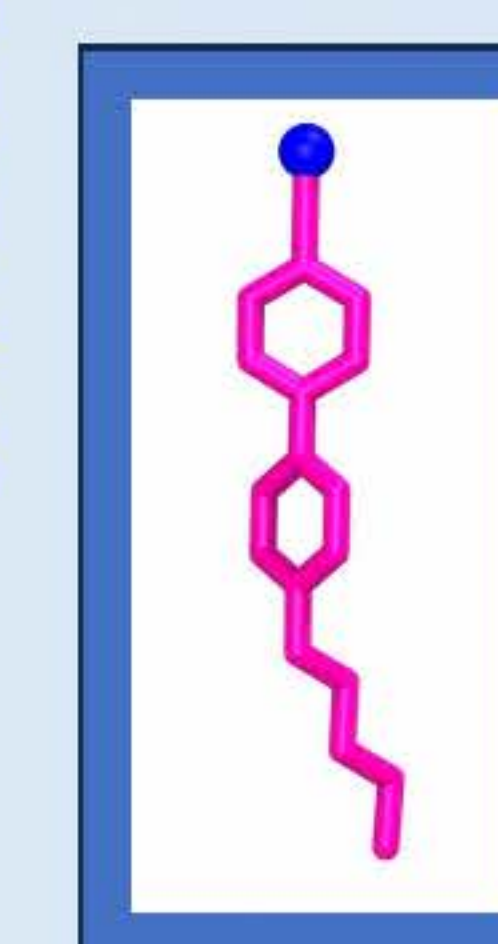
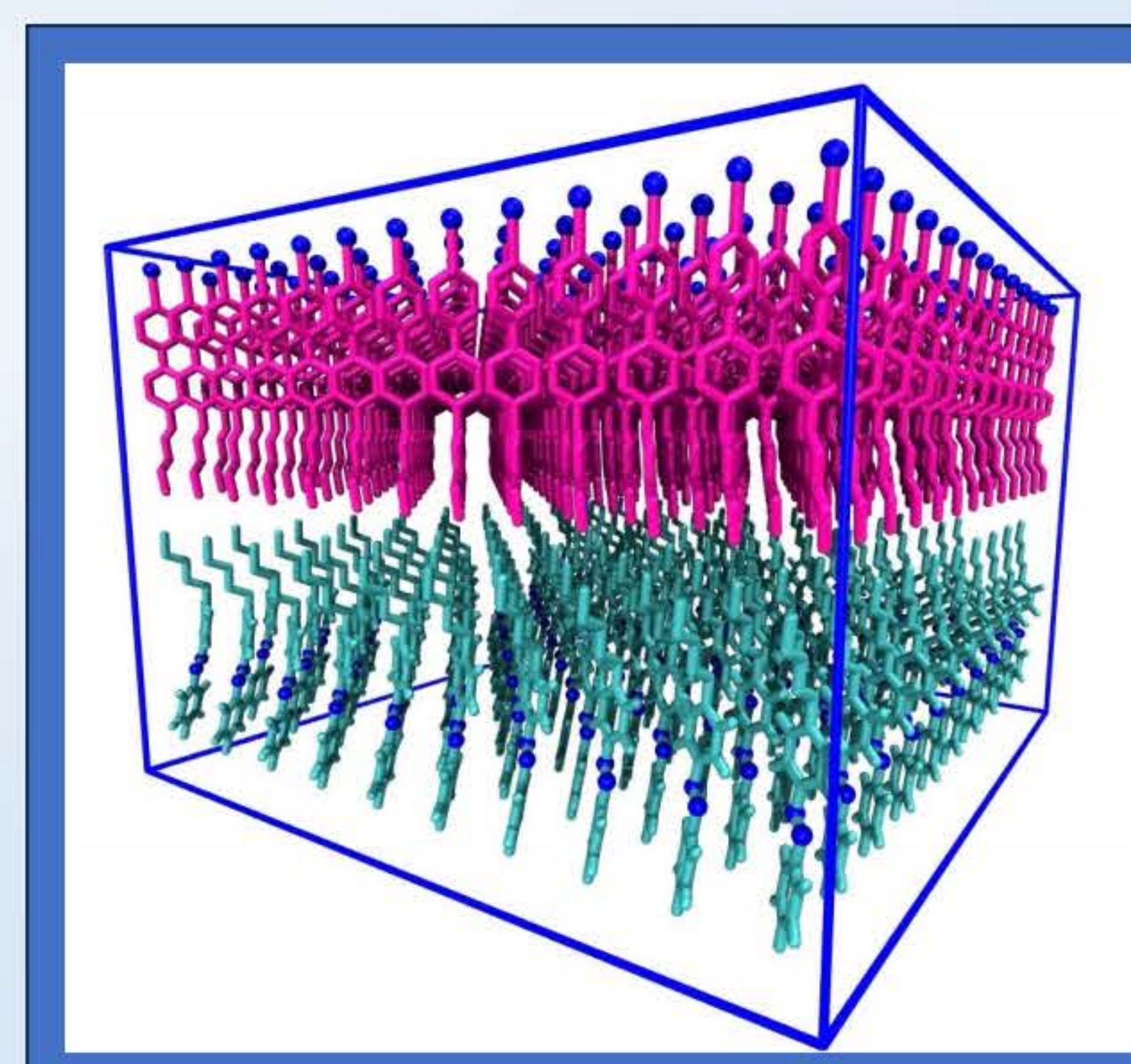
Methods

In this study, Molecular Dynamics (MD) simulation are employed to

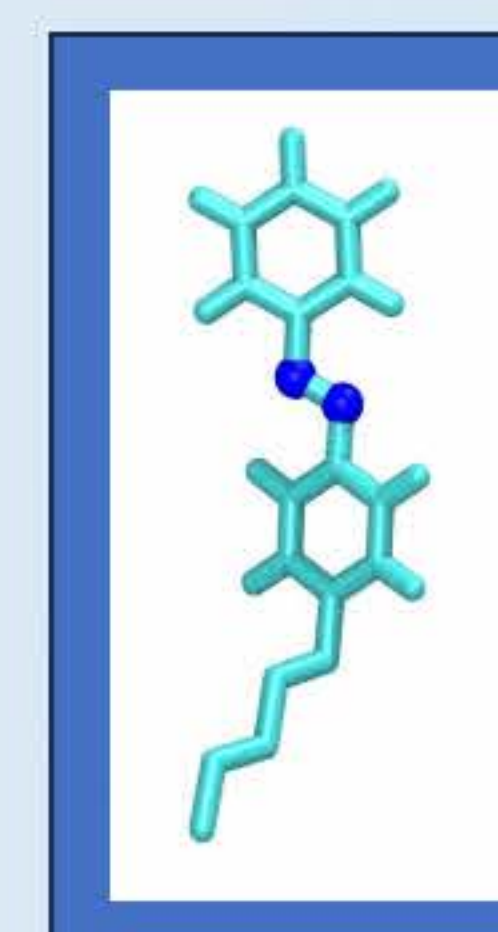
- ❑ Investigate the atomic-level structure of Azodendrimer and liquid crystal
- ❑ Analyze the interaction of Azodendrimer and Liquid Crystal through MD simulation
- ❑ Examine the mechanisms influencing the arrangement and direction of Azodendrimer
- ❑ Explore trans-cis photoisomerization in the context of Azodendrimer and liquid crystal study



Atomistic MD simulation were performed to explore the interaction of Azodendrimer and Liquid Crystal. The system preparations and simulations were done using the Gromacs software. The system comprises of liquid crystal (5CB), nematic liquid crystal (NLC), and Azodendrimer (D2-6Azo5).



5CB



D2-6Azo5

Results and Discussion

- Atomistic MD simulation is employed to investigate the atomic-level of Azodendrimer, liquid crystal and the interaction of Azodendrimer and nematic liquid crystal (5CB)
- The interaction of Azodendrimer and nematic liquid crystal (5CB) were analyzed.
- The mechanisms of phase transition and directional change of both Azodendrimer and nematic liquid crystal (5CB) were investigated.

Conclusion

Atomistic MD simulation is utilized to investigate the atomic-level characteristics of Azodendrimer, liquid crystal and their mutual interaction, specifically focusing on the nematic liquid crystal (5CB). In addition, the mechanisms governing the phase transition and directional changes of Azodendrimer and 5CB are comprehensively understood.

Future works

- ❑ Set up the simulation system for Azodendrimer, 5CB and other solvents, and investigate their interactions, phase transitions and directional characteristics
- ❑ Change liquid crystal 5CB to 8CB
- ❑ Explore trans-cis photoisomerization in the context of the arrangement of Azodendrimer and liquid crystal
- ❑ Study the physical properties of the system

References

1. Takezoe H, Haba O. Azodendrimers as a Functional Material [Internet]. Dendrimers - Fundamentals and Applications. InTech; 2018. Available from: <http://dx.doi.org/10.5772/intechopen.70715>
2. Malik M, Aamir Iqbal M, Shahid W, Zaheer Ud Din S, Ikram M, Anwar N, et al. Overview of Liquid Crystal Research: Computational Advancements, Challenges, Future Prospects and Applications [Internet]. Liquid Crystals. IntechOpen; 2022. Available from: <http://dx.doi.org/10.5772/intechopen.101417>

Acknowledgements

This research has received funding support from the NSRF via the Program Management Unit for Human Resources & Institutional Development, Research and Innovation [grant number B13F660122]

Therapeutic approach for osteopenia and fragility fracture during aberrant gravity: integrative effect of neuroendocrine, adipokine, myokine, and exercise

Wajathip Bulanawichi¹, Wanwisa Deenin¹, Panan Suntornsaratoon^{1,2}, Narattaphol Charoenphandhu^{1,2,3}

¹Center of Calcium and Bone Research (COCAB), Faculty of Science, Mahidol University, Bangkok, Thailand

²Department of Physiology, Faculty of Science, Mahidol University, Bangkok, Thailand

³Institute of Molecular Biosciences, Mahidol University, Nakhon Pathom, Thailand

Email: Wajathipb@gmail.com

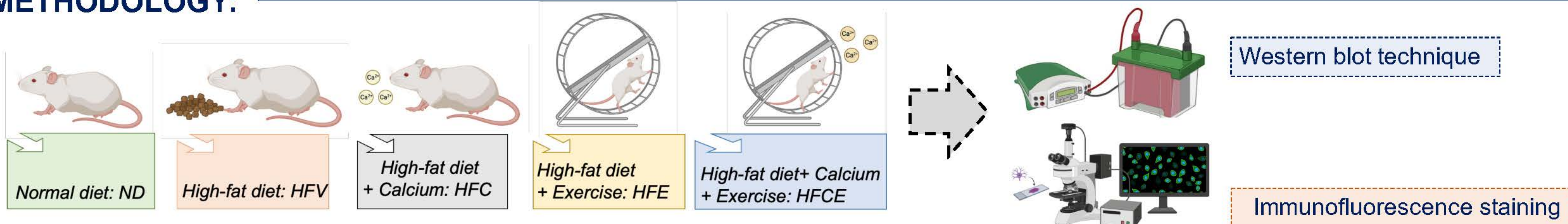
INTRODUCTION:

During gravitational conditions, osteoporosis can arise because of changes in the signal of mechanical receptors on bone cells, which can be caused by either increasing or decreasing gravity. Additionally, alterations in bone cell stem cells can contribute to osteoporosis because they also have mechanical receptors. Different tissue cells surrounding the bones or beyond may respond to changes in gravity through passing out signals in different forms. These signals could affect how bone cells function by affecting the release of cytokines, myokines, adipokines, and neuroendocrine.

There are numerous varieties of mechanical receptors found in tissues, including Piezo1/2, TRPV4, TRPC1, TRPC6, and pressure-sensitive connexin. The force and pressure occurring on all sides of the tissue are impacted by the change in gravity. Moreover, this causes changes to the volume, size, and form of the cells, which result in a range of responses. On the other hand, osteoporosis is present in several conditions, including thalassemia, diabetes, obesity, and hypertension

AIM: To study the effect of mechanical loading from impact exercise on mechanosensitive ion channels (Piezo1 and 2) in high-fat-fed rats

METHODOLOGY:



RESULTS:

❖ Specificity determination of Piezo1 and Piezo2 antibody

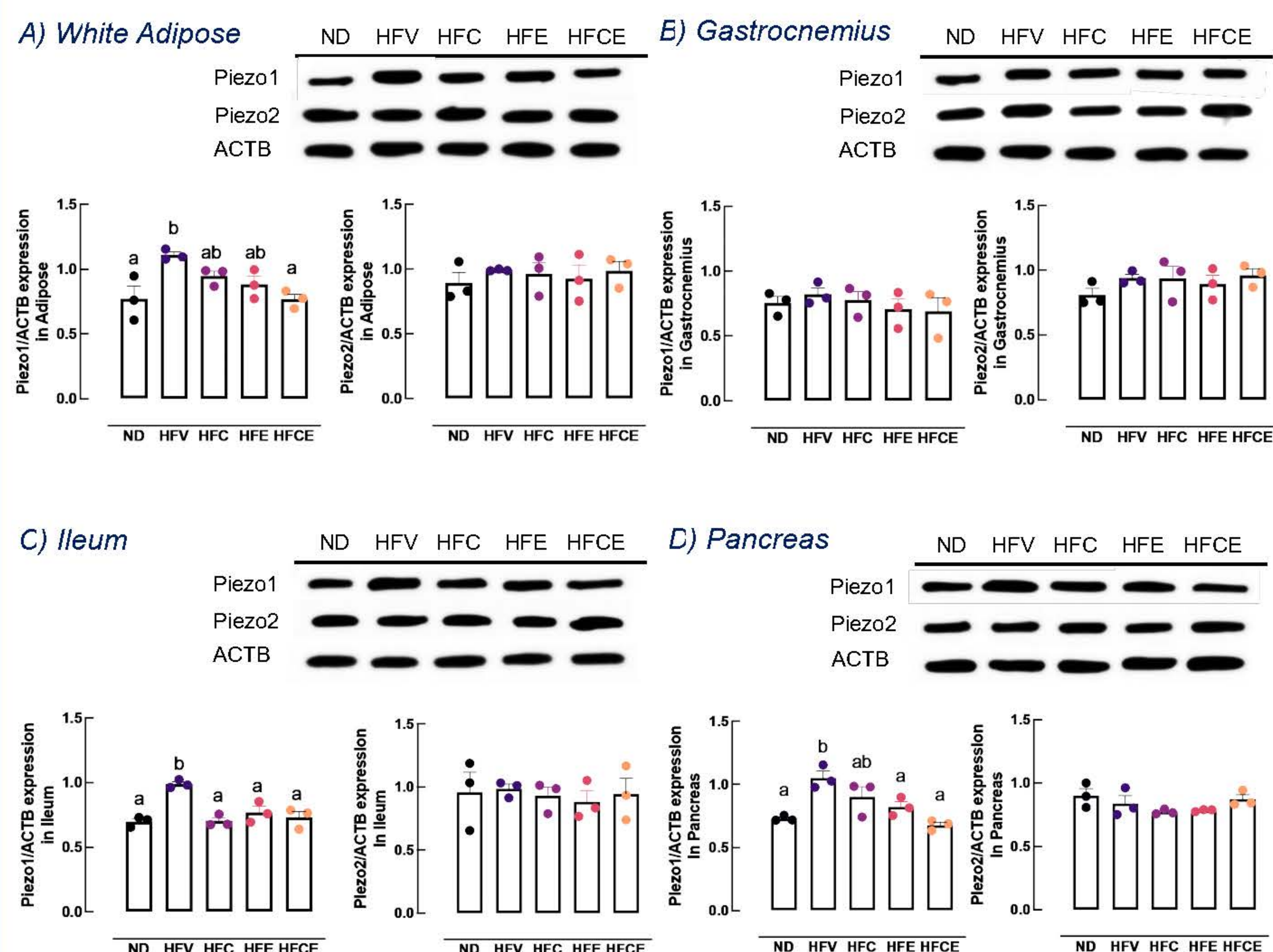


Fig1: Expression of mechanosensitive channels Piezo1 and 2 in each tissue by western blot technique. Results are expressed as means ± SE with individual values. The differences between experimental groups were determined by one-way ANOVA. The results not sharing a common superscript letter were significantly different at $P < 0.05$.

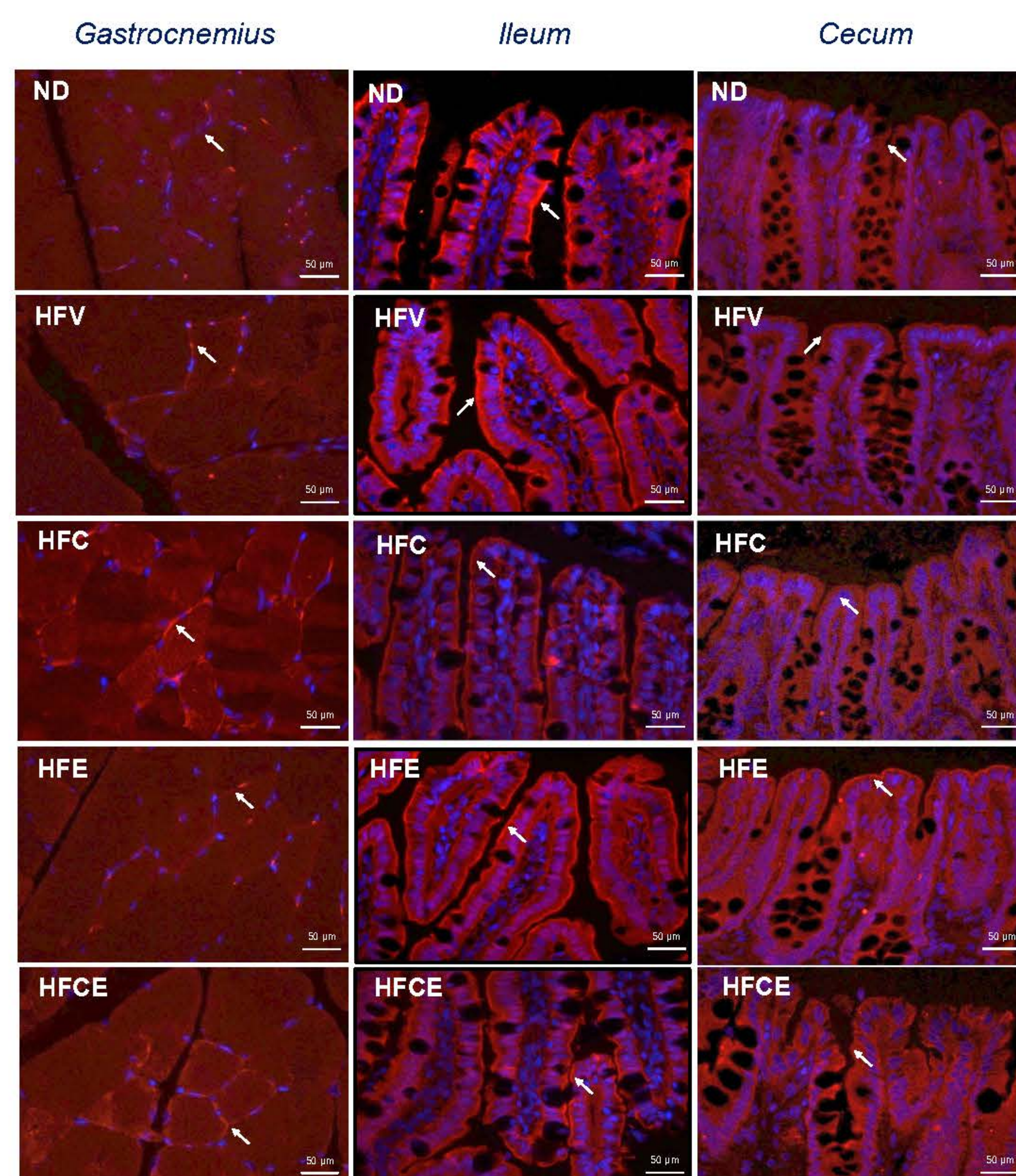


Fig2: Representative immunofluorescence staining of mechanosensitive channels Piezo1 of Gastrocnemius, Cecum, and Ileum.

DISCUSSION AND CONCLUSION:

- ❖ In this found that the HFV-induced protein expression on Piezo1 in White adipose, Intestine, and pancreas. Administration of calcium as well as exercise decreases Piezo1 expression in HFV conditions.
- ❖ Additionally, The expression of Piezo2 showed no significantly different level in all tissues.
- ❖ In conclusion, our study indicated that Piezo1 and Piezo2 play crucial roles in signal transduction and mechanosensation in various organs and tissues.

ACKNOWLEDGMENTS:

This research has received funding support from the NSRF via the Program Management Unit for Human Resources & Institutional Development, Research, and Innovation [grant number B13F660122]

Therapeutic approach for osteopenia and fragility fracture during aberrant gravity: integrative effect of neuroendocrine, adipokine, myokine and exercise

Wanwisa Deenina^{a,b}, Wajathip Bulanawichit^{a,b}, Panan Suntornsaratoon^{a,b}, Narattapon Charoenphandhu^{a,b,c,d}

^a Department of Physiology, Faculty of Science, Mahidol University, Bangkok, Thailand., ^b Center of Calcium and Bone Research (COCAB), Faculty of Science, Mahidol University, Rama VI Road, Bangkok 10400, Thailand., ^c Institute of Molecular Biosciences, Mahidol University, Nakhon Pathom, Thailand., ^d The Academy of Science, The Royal Society of Thailand, Dusit, Bangkok, Thailand.



INTRODUCTION

Hypertension is induced by the pressure exerted on blood vessels and is one of the most targeted diseases for mechanobiology research. Piezo acts as the long-sought baroreceptor mechanosensors which are critical for acute blood pressure control. Piezo was primarily examined mainly in hypertension, with a focus on **Piezo1**. This research focus on an important finding that links the **mechanosensitive ion channel** to hypertension.

Microgravity and partial gravity affect hydrostatic pressure and gravitational load, which may have an impact on tissues which regulate calcium homeostasis and bone density.

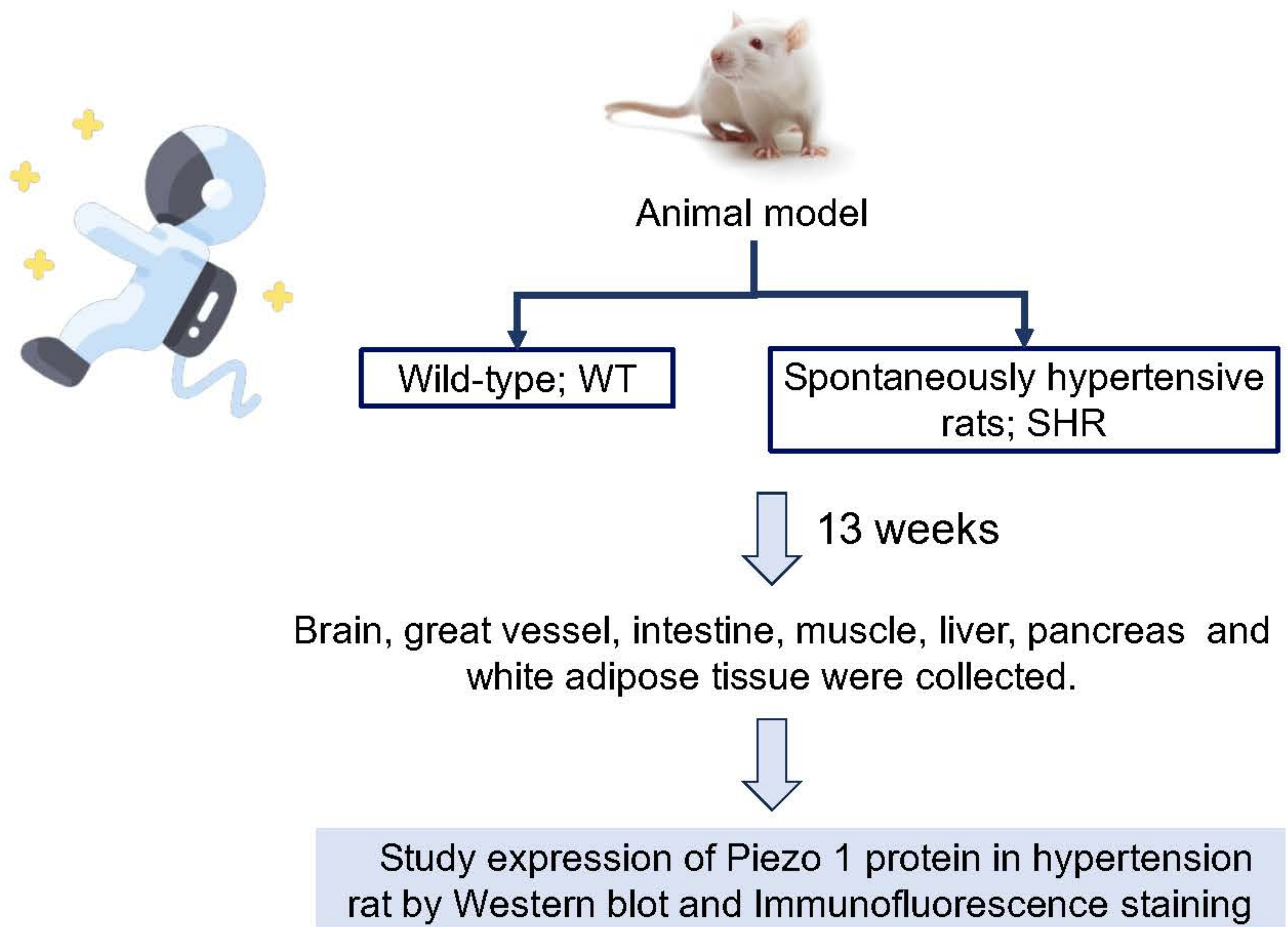
Objective:

To investigate the function of mechanosensory regulate the calcium and bone metabolism both normal and hypertension

Hypothesis:

The expression of mechanosensitive ion channel such as Piezo 1 proteins on tissues may change due to altered gravitational load during space flight.

METHODOLOGY



RESULTS & DISCUSSION

Effect of hypertension to expression of Piezo 1 protein by western blotting analysis

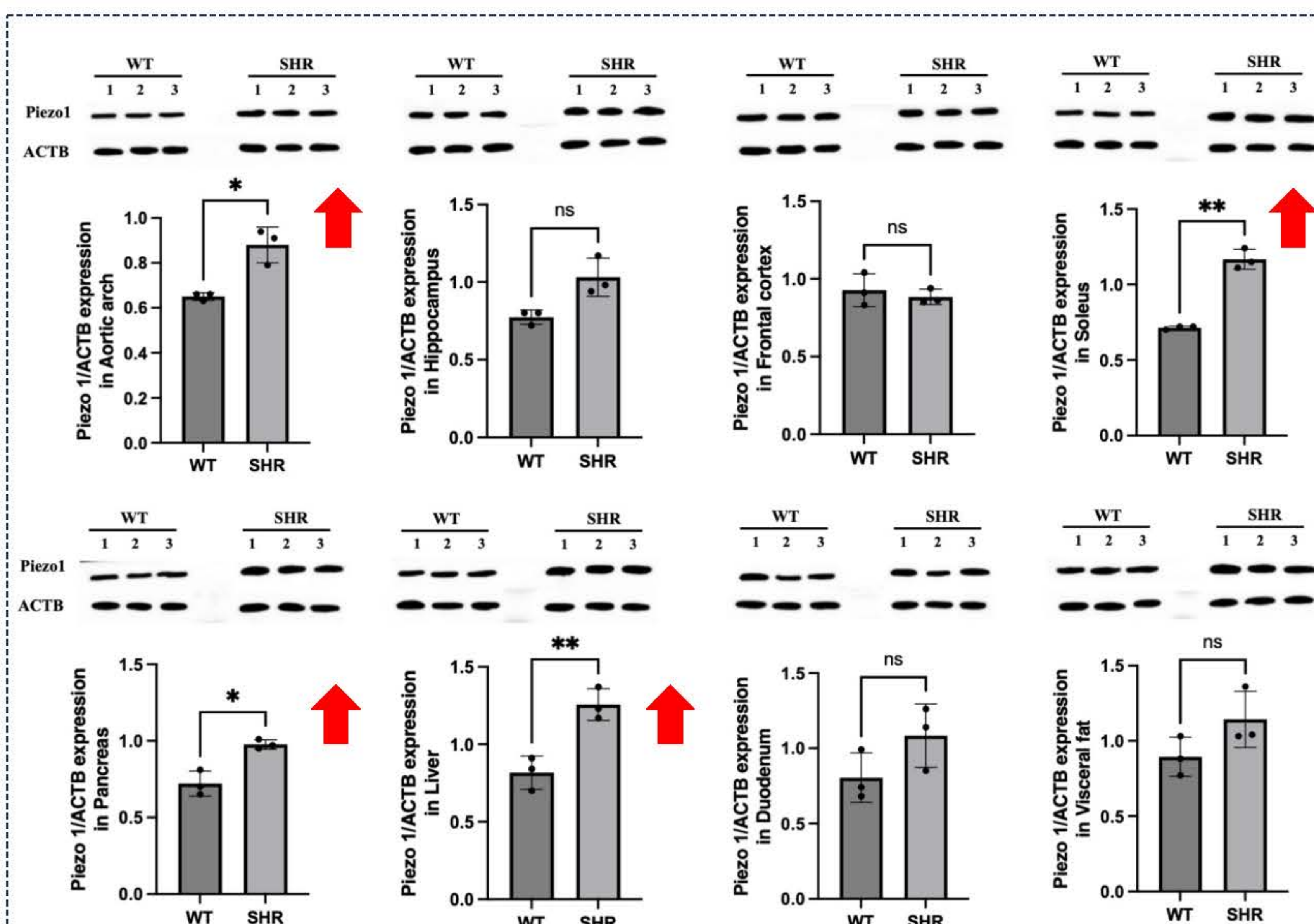


Figure 1. The expression of Piezo 1 protein in aortic arch, hippocampus, frontal cortex, soleus muscle, pancreas, liver, duodenum and visceral fat by Western blotting analysis

Effect of hypertension to expression of Piezo 1 protein by immunofluorescence staining

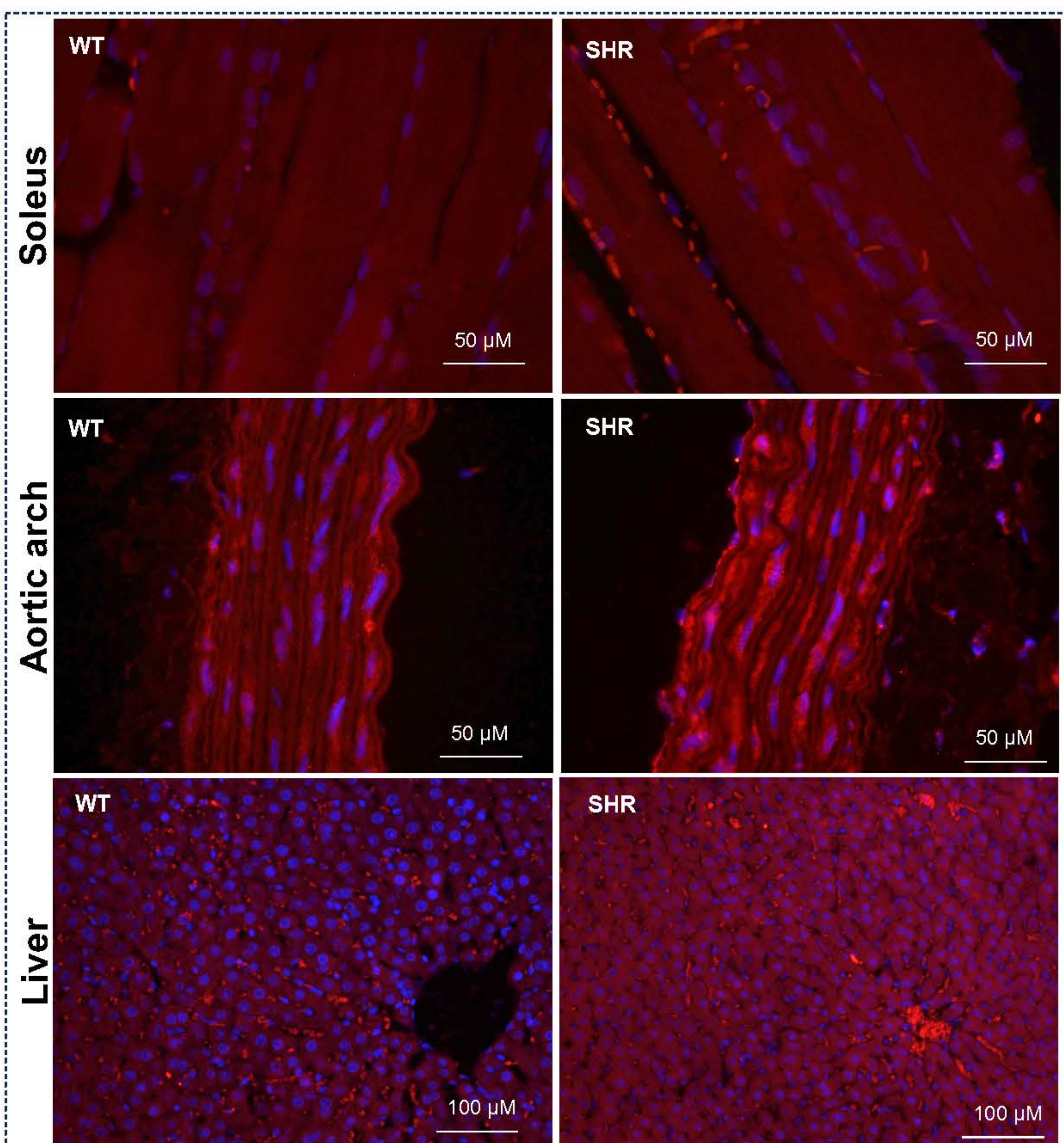
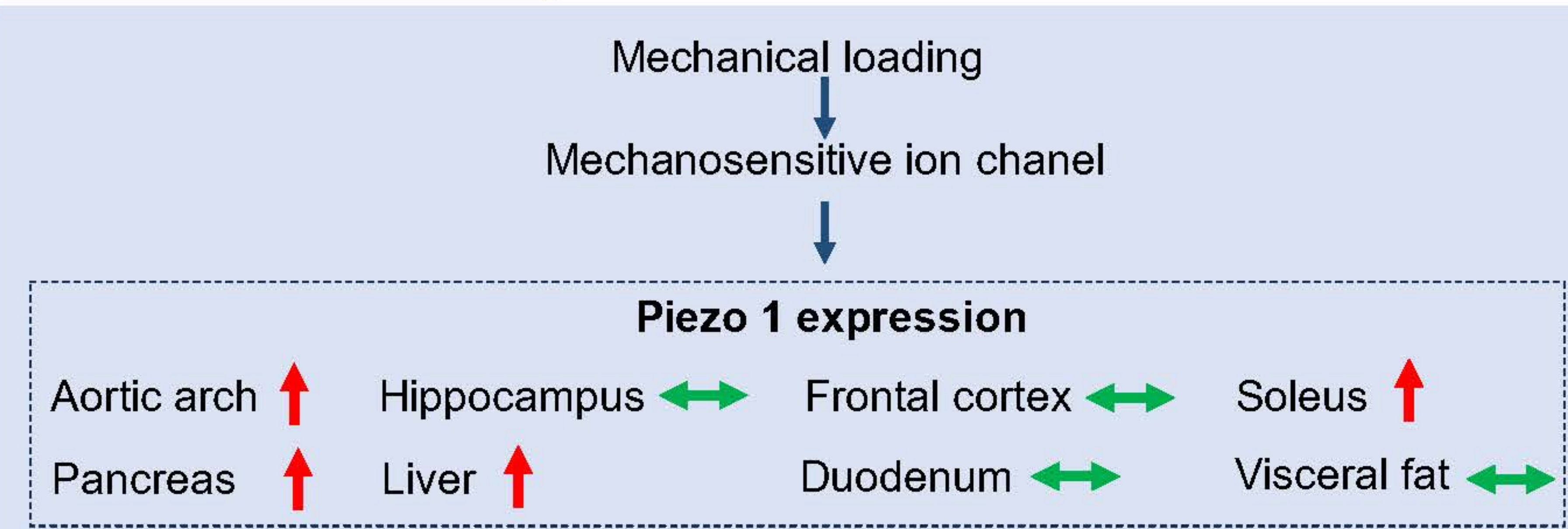


Figure 2. The expression of Piezo 1 protein in soleus muscle, aortic arch, and liver by immunofluorescence staining

In this study, we found that the Piezo1 channel detects mechanical loading. It is crucial to understand that mechanical loads promote the development of bone formation by activating on Piezo1 channels in bone cells. A lower level of Piezo1 was observed in the bone cells found in osteoporosis, and this was related to a decrease in bone mass. On the other hand, osteoporosis was associated with hypertension.

CONCLUSION



FUTURE WORK

We will study other mechanosensitive ion channels such as **Piezo 2**, **TRPV4** and **TRPC1**.

ACKNOWLEDGEMENT

This research has received funding support from the NSRF via the Program Management Unit for Human Resources & Institutional Development, Research and Innovation [grant number B13F660122]

Synergy of Inorganic Catalyst and Plasma-Assisted Catalytic CO₂ Conversion into Valuable Products

Pimchanok Tapangpan^{1,4}, Dheerawan Boonyawan³, Wassanai Wattanutchariya^{2,4}, Pornchai Rachtanapun^{2,5,6}, Choncharoen Sawangrat^{1,2,4*}

¹ Agriculture and Bio Plasma Technology Center, Science and Technology Park, Chiang Mai University, Thailand

² Research Center of Plasma Innovation for Sustainable Quality of Life, Chiang Mai University, Thailand

³ Department of Physic and Material Science, Faculty of Science, Chiang Mai University, Thailand

⁴ Department of Industrial Engineering, Faculty of Engineering, Chiang Mai University, Thailand

⁵ Division of Packaging Technology, Faculty of Agro-Industry, Chiang Mai University, Thailand

⁶ Center of Excellence in Agro Bio-Circular-Green Industry, Chiang Mai University, Thailand

* E-mail: choncharoen@step.cmu.ac.th and pimchanok_tap@cmu.ac.th

Turning global warming gas into value added products

Global warming is considered as an urgent environmental issue, and the major contributor of greenhouse gases is carbon dioxide (CO₂) which predominantly derives from the continuing consumption of fossil fuels worldwide.¹ Apart from the carbon capture and storage (CCS) that require a large space and increasing costs, CO₂ conversion and utilization (CCU) provides a more efficient process in terms of more energy efficient conversion of CO₂ into value-added products i.e., methane, carbon monoxide, alcohols, formic acid, and liquid hydrocarbons.²

Plasma technology currently appears as an effective route for CO₂ conversion due to the existence of high energetic electrons (1-10 eV) which can initiate the thermodynamically unfavorable CO₂ conversion at near ambient conditions.³ Particularly, microwave plasma has a high electric energy utilization efficiency up to the target efficiency of 60% easily under non-equilibrium conditions.⁴ However, plasma technology still suffered from low yield and selectivity of the desired products.¹ To overcome this limitation, the hybrid systems of plasma and appropriate catalysts were frequently observed (Fig. 1).⁵

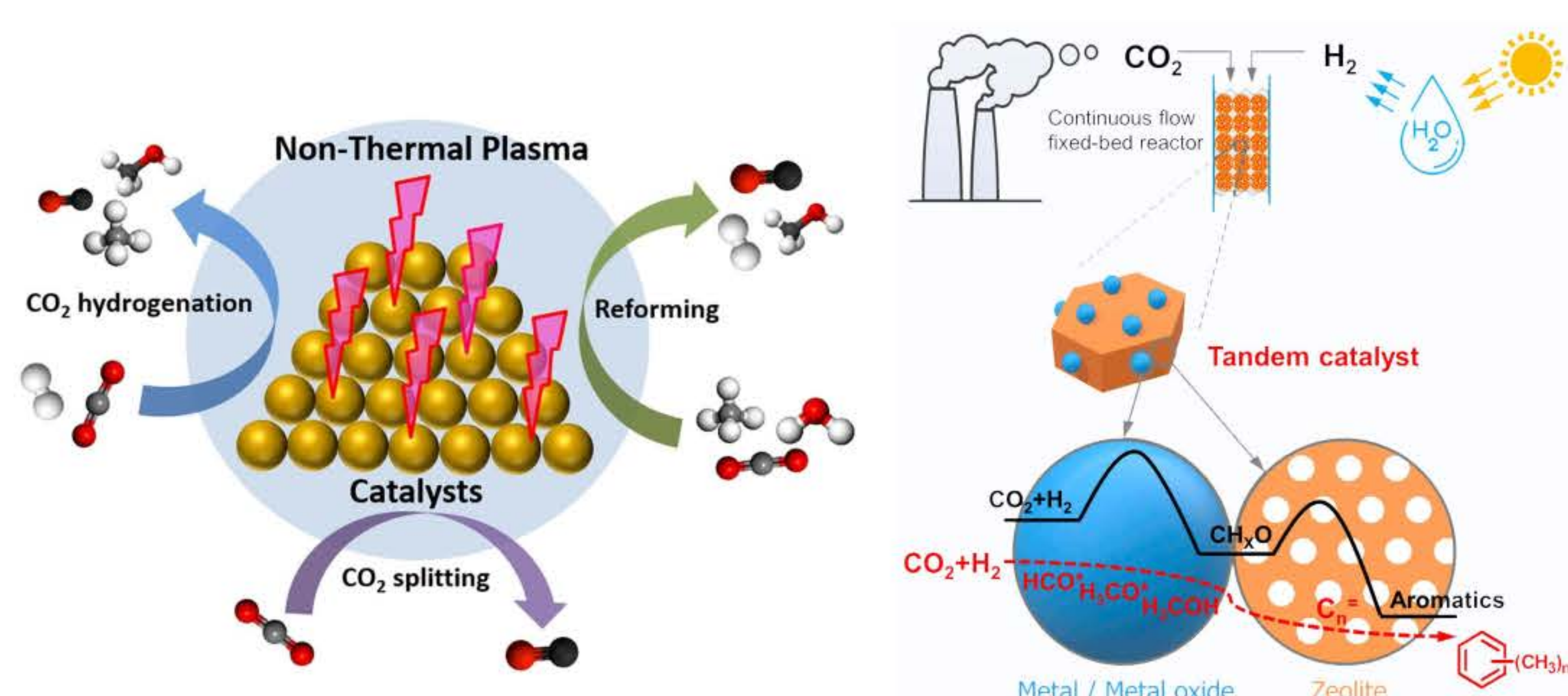
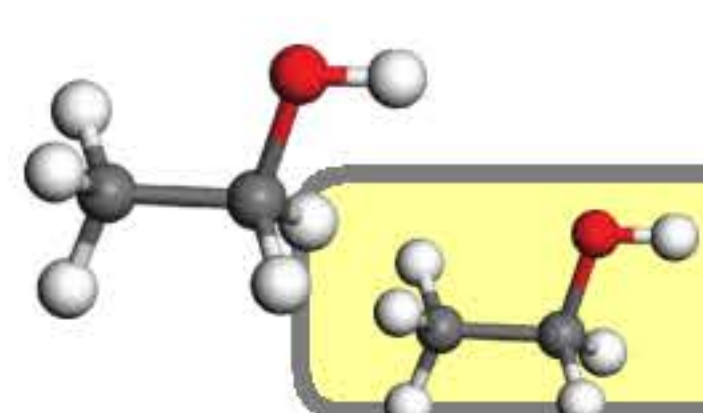


Fig. 1 An example of chemical reactions of plasma assisted catalyst for CO₂ conversion (left)⁶ and possible products generated from using metal/zeolite catalysts (right).⁷

Zeolite is a good catalyst candidate which is not only commercially available but also easy to tune to own properties of high stability under plasma condition.⁸ To composite the zeolite with metal / metal oxide especially copper (Cu)⁹, a feasibility of new catalyst for facile production of alcohols and aromatics is observed (Fig.1). An interesting target products are platform chemicals which an important feedstock used in the chemical and petrochemical industry e.g., methanol and ethanol. Generally, methanol is produced by the hydrogenation of CO₂ over industrial Cu/ZnO/Al₂O₃ catalysts under harsh conditions of 200-320 °C and 5-10 MPa.¹⁰ Consequently, to obtain milder condition and shorthorn reaction time of methanol synthesis, zeolite with tunable structure with Cu for CO₂ hydrogenation under synergy of plasma is suitable to fulfill the challenge interval of methanol synthesis.



Materials and Method

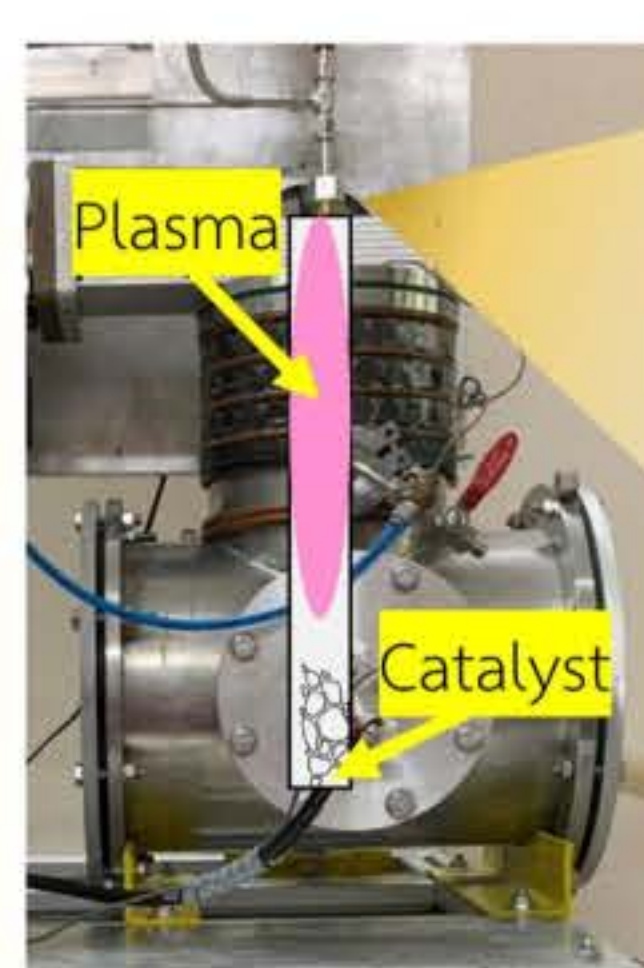
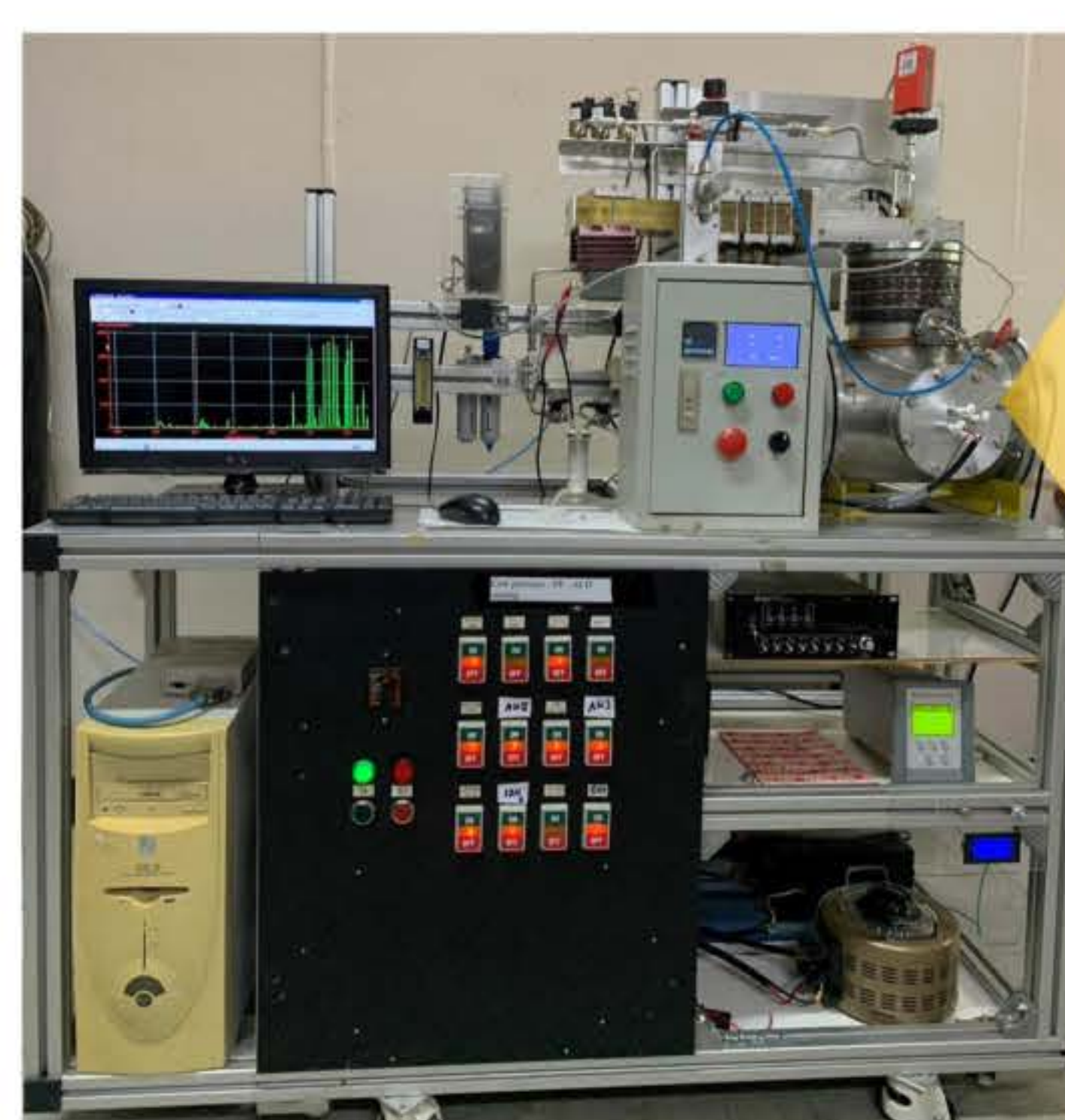
Synthesis and characterization of zeolite 13x from literature¹¹ and post-synthesis of Cu/zeolite13X composite via simple cation exchange

Optimization of reaction condition by measuring the product yields i.e., methanol and other products using microwave plasma-only

Applying plasma with synthesized catalysts to improve the reaction performance

Study the stability of synthesized catalysts after the reaction and their consecutive usage

Scaling up of the selected catalyst and fabrication of prototype to investigate the utilization of the system in industrial scale



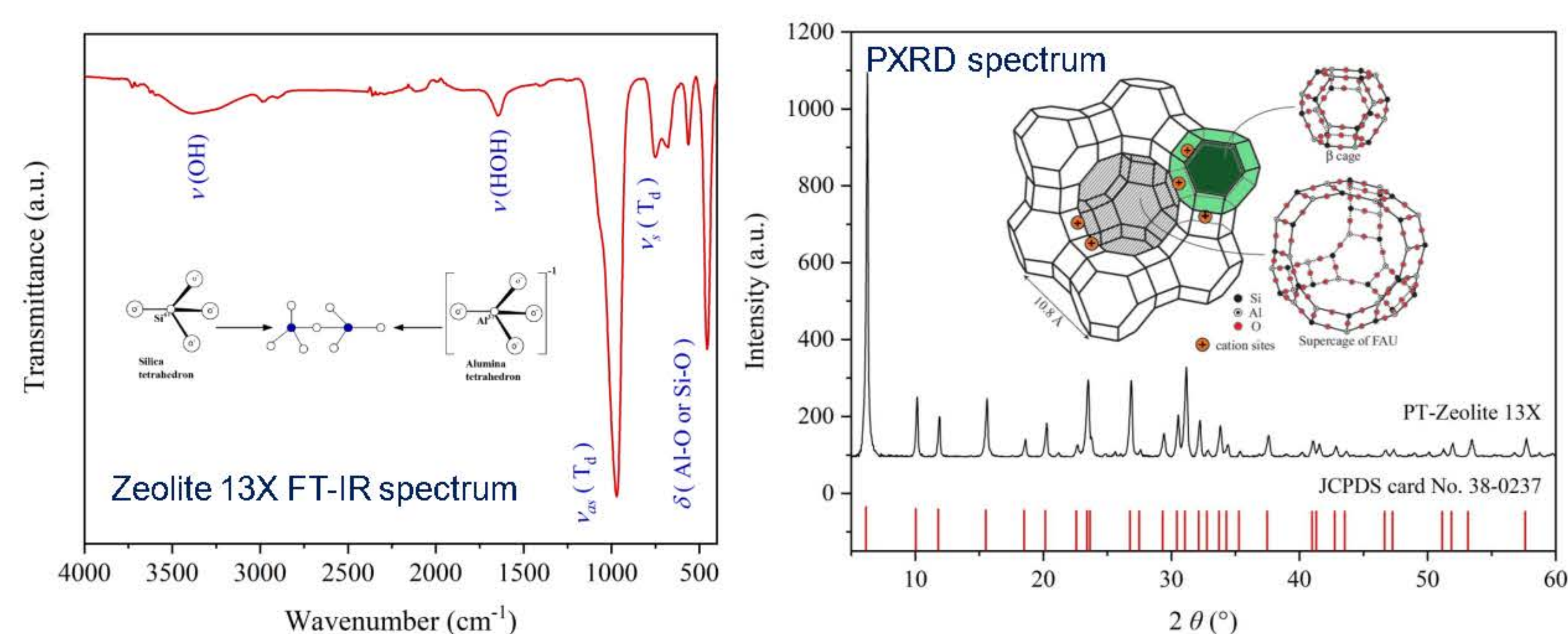
Catalyst column



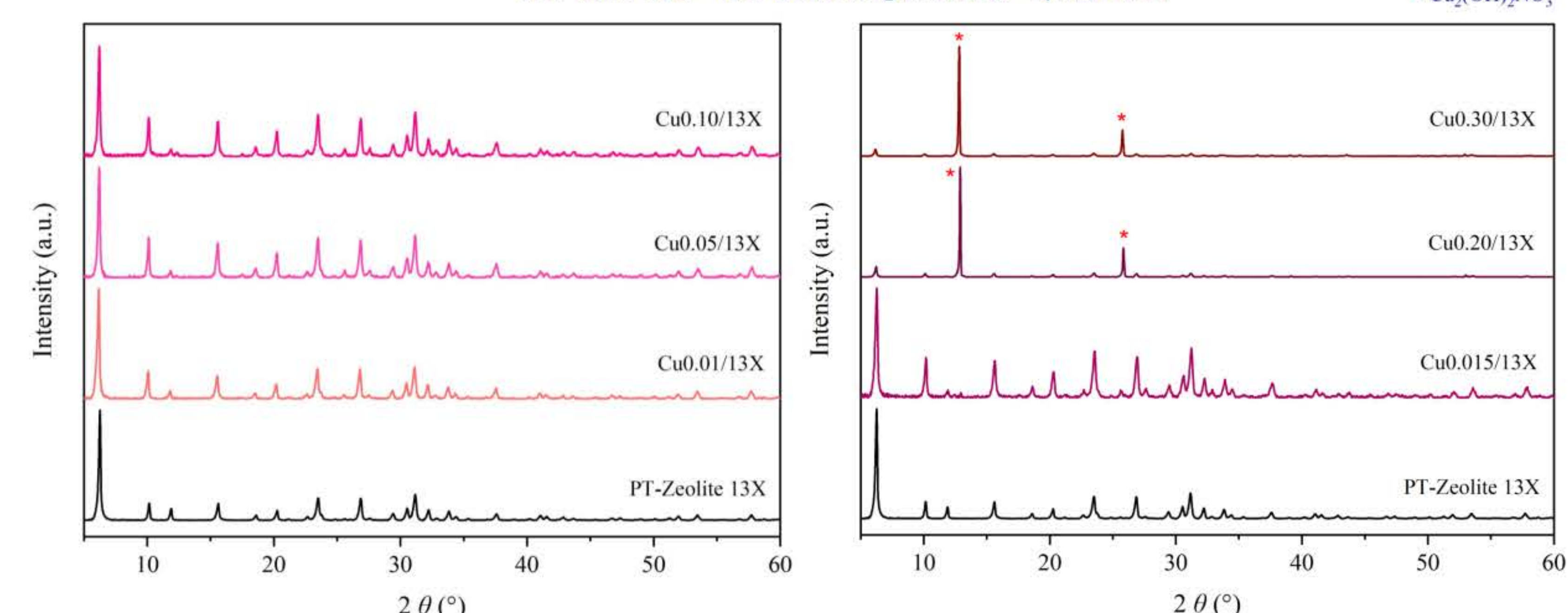
Plasma beam

Fig. 2 Setting of customized 2.4 GHz microwave plasma employed in this study

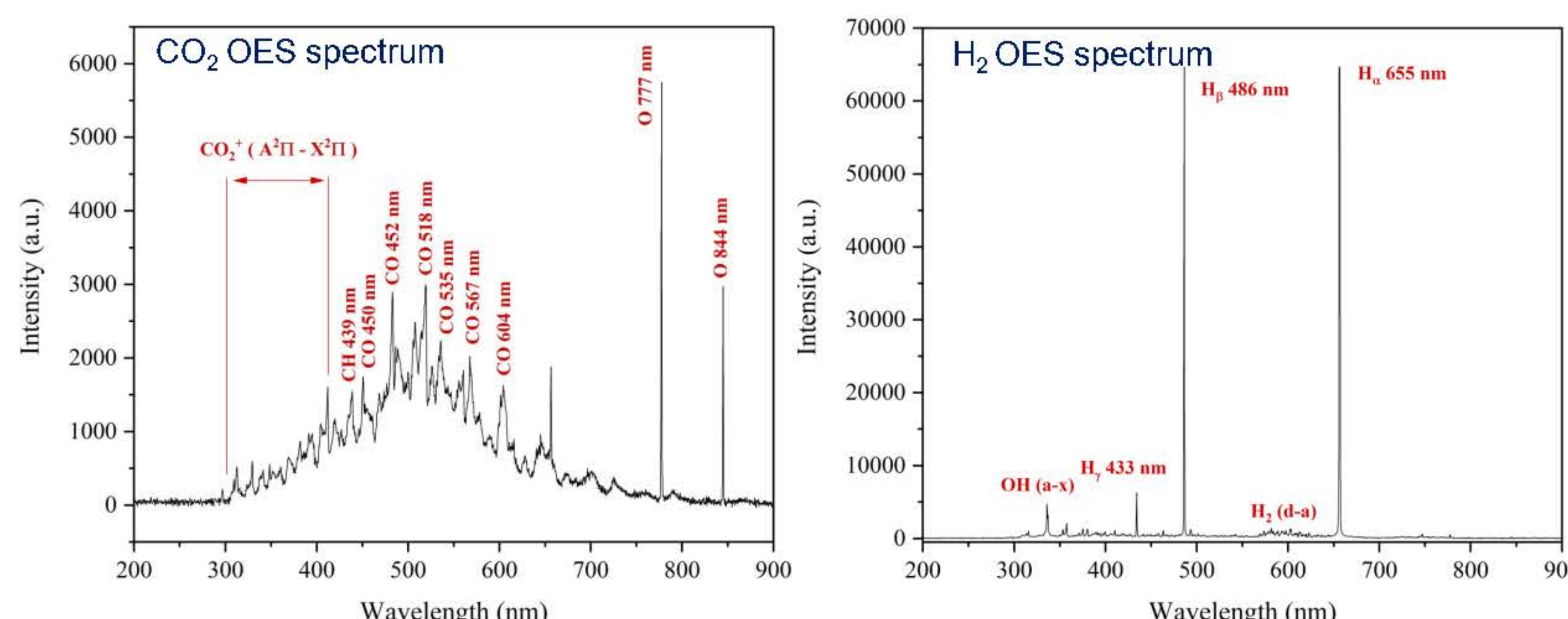
Results and Discussions



Na⁺ and Cu²⁺ ion exchange PXRD spectrum



The as-synthesized zeolite 13X was characterized by Fourier-transform infrared spectroscopy (FT-IR) and powder X-Ray diffraction analysis (PXRD). The FT-IR pattern indicated the symmetric and as-symmetric stretching modes (ν) of T₄O₄ (T₄ is tetrahedral of Si or Al) at 754 cm⁻¹ and 977 cm⁻¹. The bending modes of Al-O and Si-O were strongly appeared at 452 cm⁻¹. The existence of water molecules within product reflected through O-H stretching as labeled in FT-IR pattern. The PXRD pattern of obtained zeolite 13X suggested high crystallinity and purity of product which is well mated with JCPDS card no.38-0237. The post-synthetic cation exchange between Na⁺ and Cu²⁺ was saturated when soaked zeolite 13X in 0.15 M Cu(NO₃)₂ hydrate for 24h and this condition will be selected for further study.



The microwave plasma was employed to generate plasma beam of CO₂ (g), H₂ (g) and mixed CO₂/H₂ 1:1 (g). By using the frequency of 2.4 GHz with 150 V, the species in plasma beams were recorded by optical emission spectroscopy (OES). According to OES spectra, most of CO₂ (g) was mainly converted into CO (g) and almost of H₂ (g) was dissociated into H_{α,β,γ}. The plasma beam of mixed CO₂/H₂ 1:1 consisted all species from both plasma beam of CO₂ (g) and H₂ (g) in appropriate ratio.

Conclusions

- ❖ The high crystallinity and purity of zeolite 13X was successfully prepared via simple hydrothermal technique and characterized by FT-IR and PXRD techniques showing great quality which was suitable for further post-synthetic cation exchange between Na⁺ and Cu²⁺.
- ❖ The employed microwave plasma possessed great performance to generated necessary plasma species from CO₂ (g), H₂ (g) and mixed CO₂/H₂ 1:1 (g).

Acknowledgements

The study was conducted under the funding of Program Management Unit for Human Resources & Institutional Development, Research and Innovation (PMU-B) in the project of "Enhancing competency and capacity of high level manpower in plasma technology" (B13F660124) and Chiang Mai university. We thanks for supporting from Research Center of Plasma Innovation for Sustainable Quality of Life, Chiang Mai University and Plasma And Beam Physics Research Facility, Chiang Mai University .

Plasma-Based Technique and Related Disinfecting Techniques for Inactivation of Foodborne Pathogen and Residual

K. Moonsub^{1,2}, P. Seesuriyachan², D. Boonyawan³, P. Rachtanapun^{5,6,7}, C. Sawangrat^{2,6} and W. Wattanuchariya^{1,6,*}

¹Advanced Technology and Innovation Management for Creative Economy Research Group (AIMCE), Department of Industrial Engineering,

Faculty of Engineering, Chiang Mai University, Chiang Mai, Thailand.

²Department of Industrial Engineering, Faculty of Engineering, Chiang Mai University, Chiang Mai, Thailand.

³Division of Biotechnology, Faculty of Agro-Industry, Chiang Mai University, Chiang Mai, Thailand.

⁴Plasma and Beam Physics Research Facility, Department of Physics and Materials Science, Faculty of Science, Chiang Mai University, Chiang Mai, Thailand.

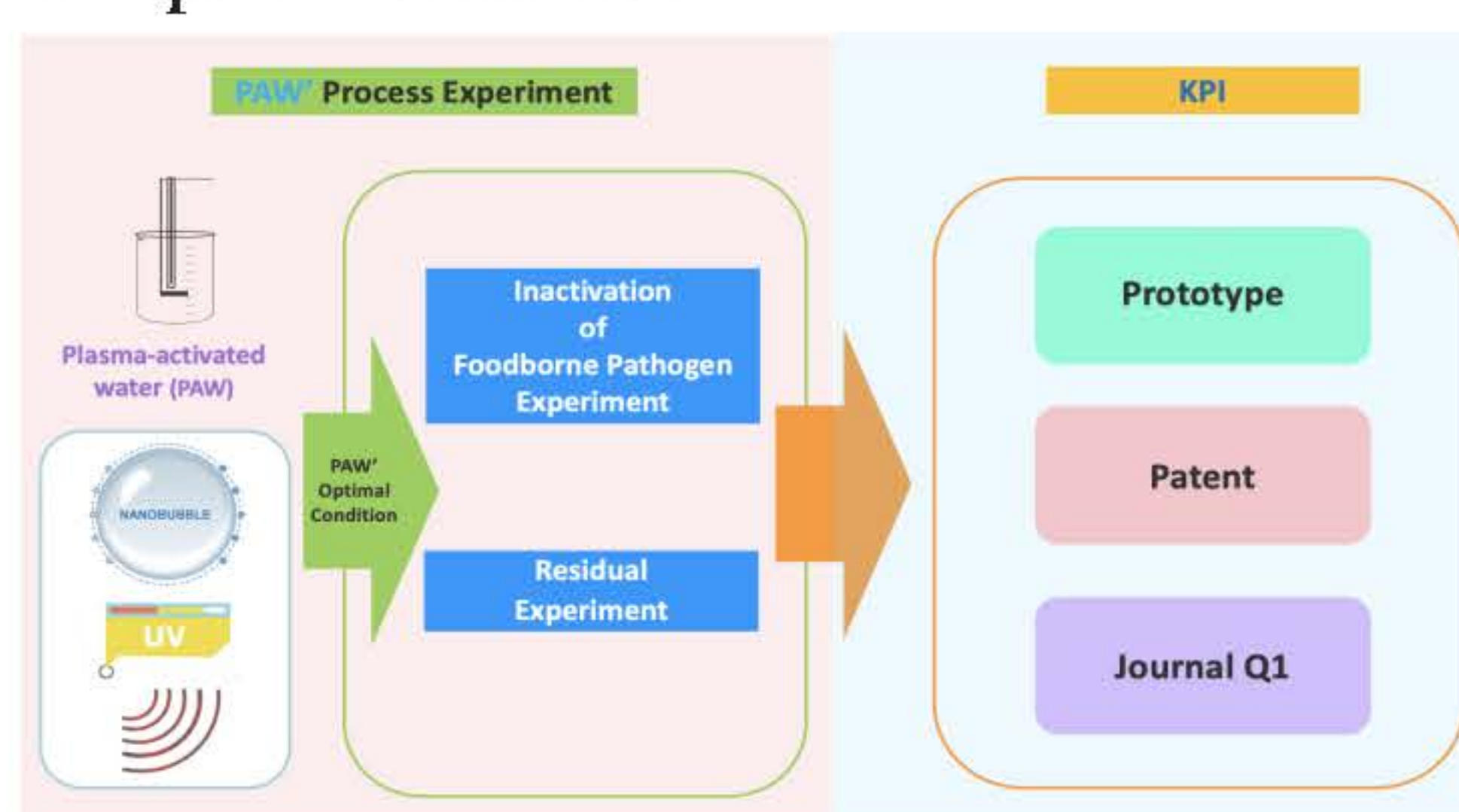
⁵Division of Packaging Technology, Faculty of Agro-Industry, Chiang Mai University, Chiang Mai, Thailand.

⁶Research Center of Plasma Innovation for Sustainable Quality of Life, Faculty of Engineering, Chiang Mai University, Chiang Mai, Thailand.

⁷Center of Excellence in Agro Bio-Circular-Green Industry (Agro BCG), Chiang Mai University, Chiang Mai, Thailand.

* Corresponding author: Wassana Wattanuchariya (Email: wassana@eng.cmu.ac.th)

Graphical Abstract



Introduction and Problem Statement

The food industry is a revenue-generating industry that continues to expand globally, according to the OECD-FAO Agricultural Outlook 2016–2025 report. The Food and Agriculture Organization of the United Nations (FAO) examines the future of the global livestock situation. Chemical disinfection and pesticide residue also causes residues in the production process that affect the health of consumers. Based on the problems mentioned above, researchers expect that plasma technology will reduce pathogens in food the action of reactive oxygen species (ROS) and reactive nitrogen species (RNS), as shown in Figure 1.. However, food is thick and complex which compromises its sterilization efficiency. Therefore, further research is needed to enhance the effectiveness of disinfection and decrease residual in food. To design systems that utilize PAW and supplementary disinfection techniques to reduce common foodborne pathogens, it is necessary to incorporate various aspects of knowledge, such as MNB (Micro/Nanobubble) technology, UV (Ultraviolet) light, and US (Ultrasonic) methods. This study proposes a method to increase sterilization efficiency using PAW and supplementary technologies such as MNB, UV, and US, in order to enhance the effectiveness of disinfecting food and decrease residual in the food industry.

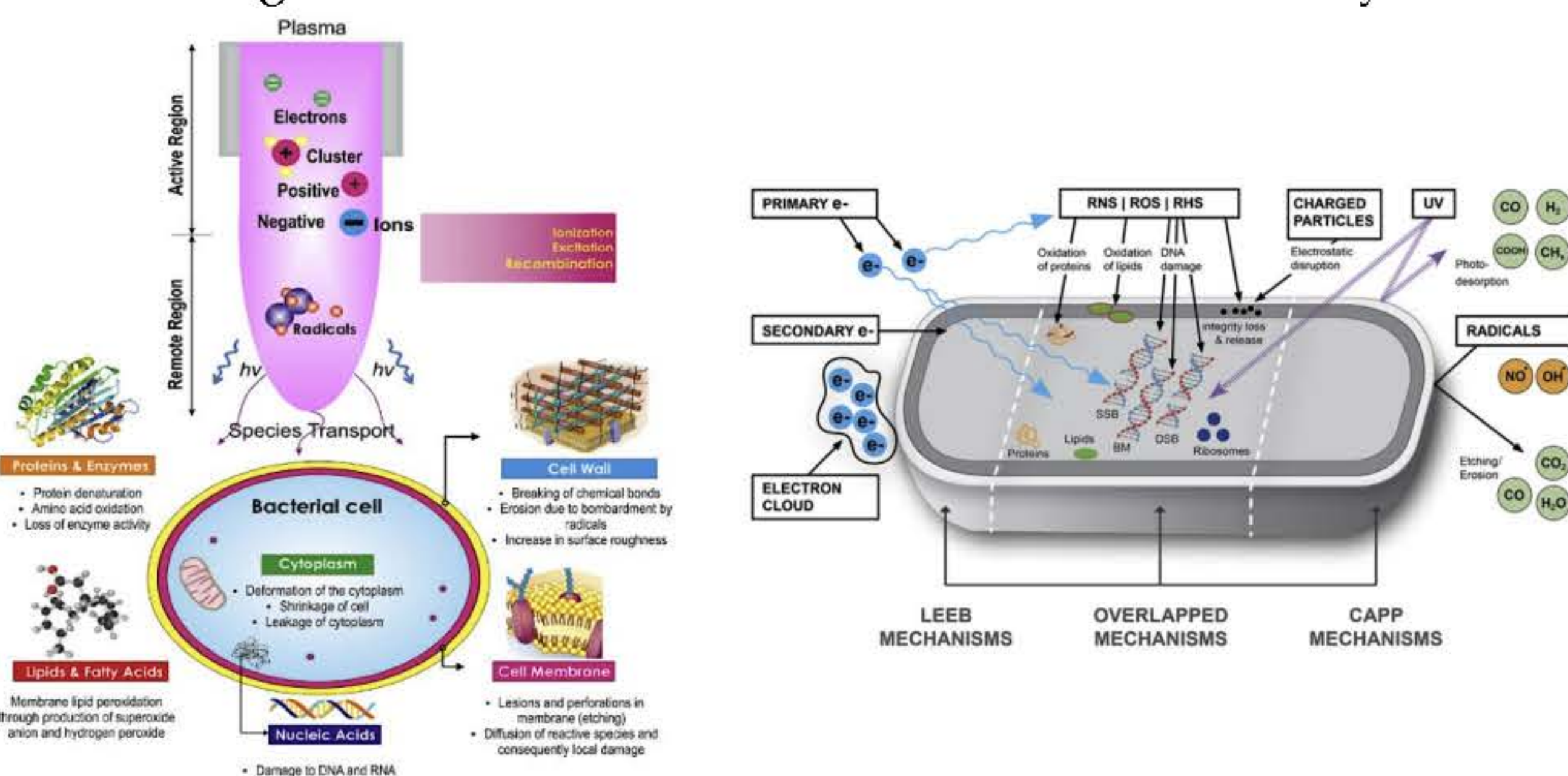


Figure 1. A schematic of the cold plasma on bacterial cell structure resulting in loss of functionality and sterilization

Methods

PAW generation

In this study, a PAW system was employed, with a Flyback Transformer (FBT) powered at 30 watts, operating for 20 minutes at 25° C. This PAW condition can produce the optimal concentration of H₂O₂, which can effectively deactivate common foodborne pathogens. To enhance sterilization efficiency, PAW is used in conjunction with MNB, UV, and US. Figure 2 shows a schematic and photographs of PAW combined with supplementary techniques.

Food-borne pathogens inactivation experiment

PAW MNB UV, and US technology, are required to study practical concerns for improving the effectiveness of plasma technology and supplemental disinfection procedures, as shown in Figure 2.

Pesticide residue experiment

Prepare a solution of Carbaryl in Methanol with a ratio of 1:1, mix carbaryl at a concentration of 10 µl/ml in PAW generation solution, then measure the amount of remaining residue using the GC-MS technique at a wavelength of 504-416 nm, as shown in Figure 2.

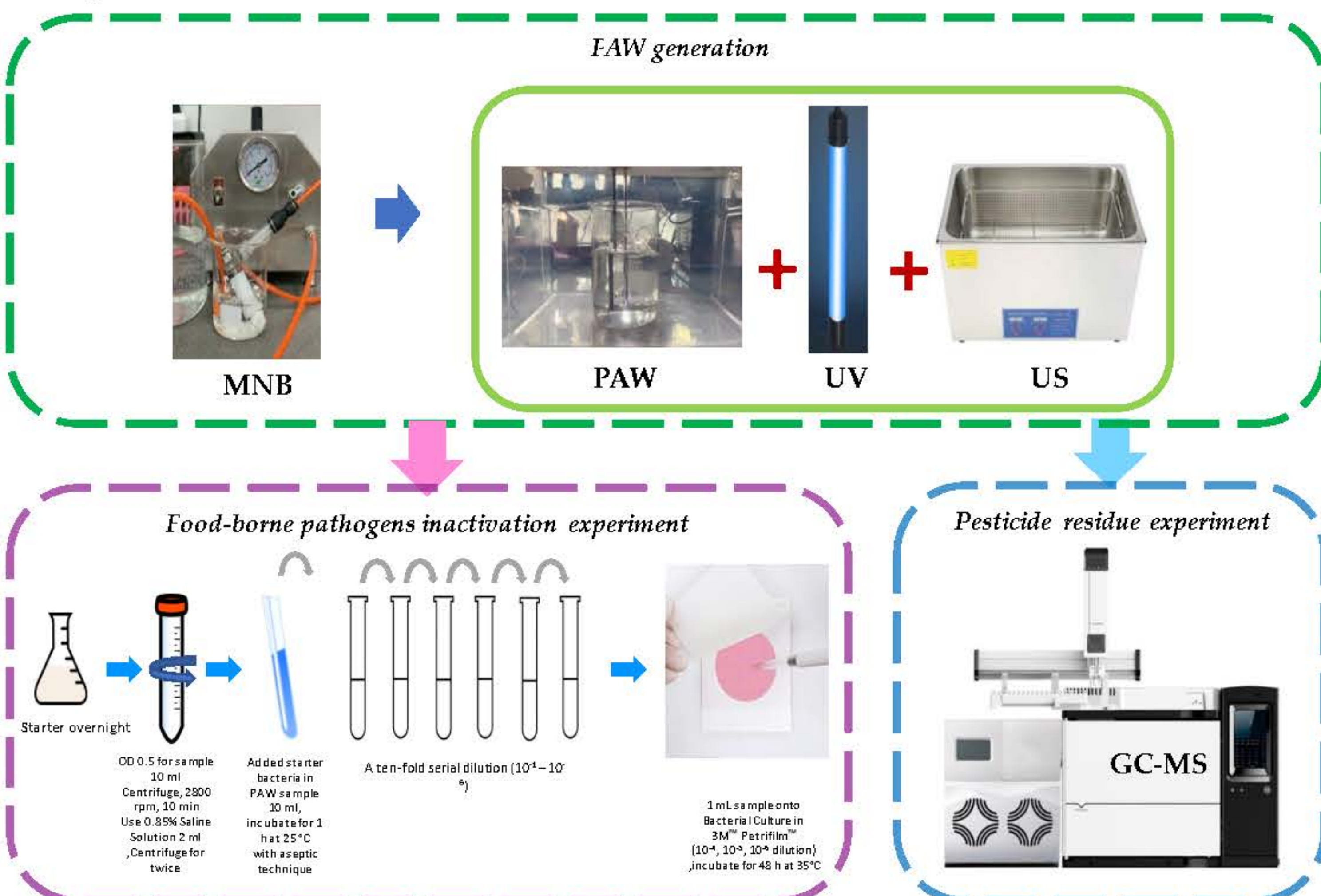


Figure 2. The experiment considered factor include PAW combine with MNB UV and US for the purpose of minimum Food-borne pathogens and Pesticide residue

Results and Discussion

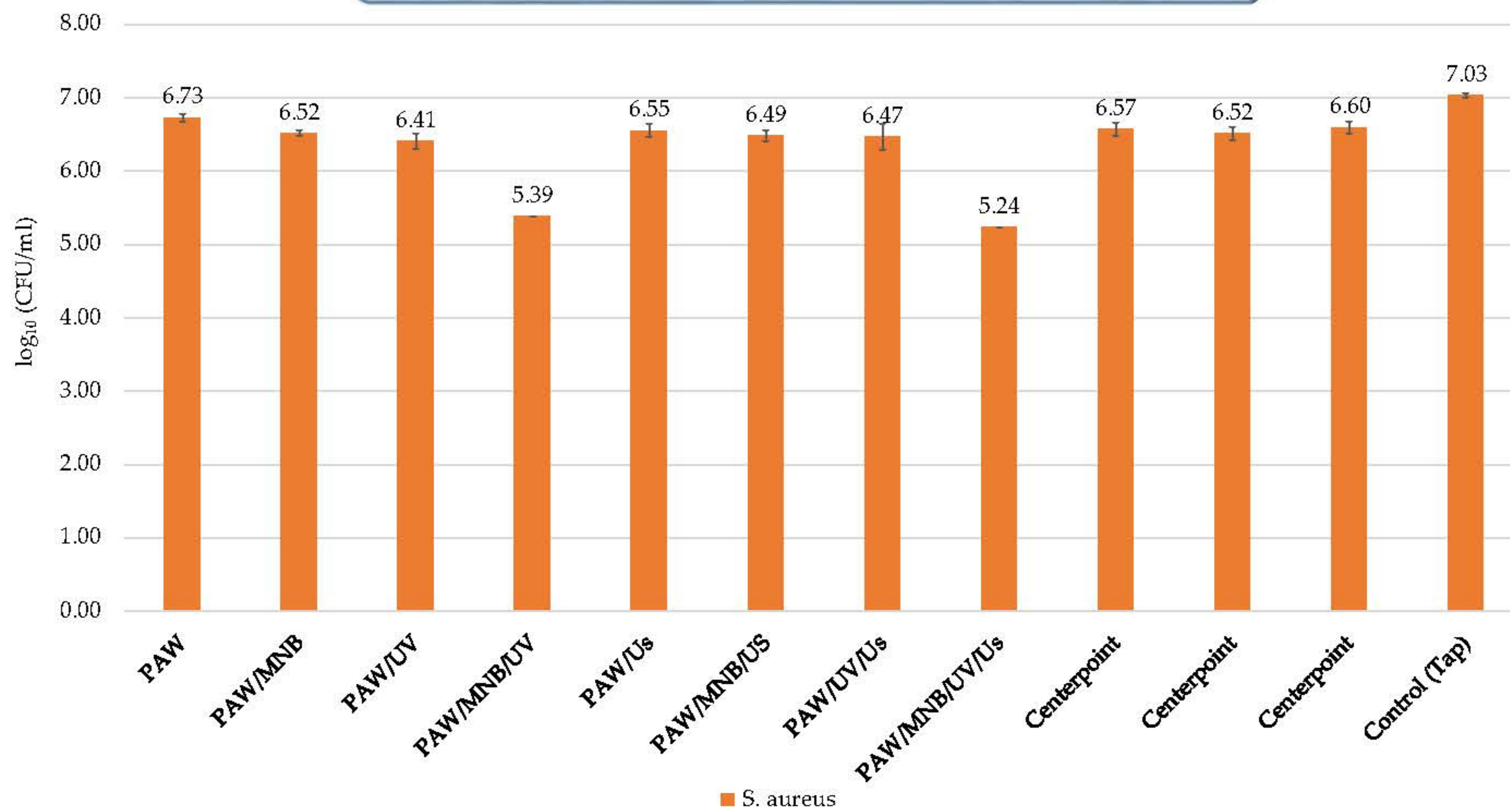


Figure 3. The result shows the surviving population of *S. aureus* after different plasma treatment conditions.

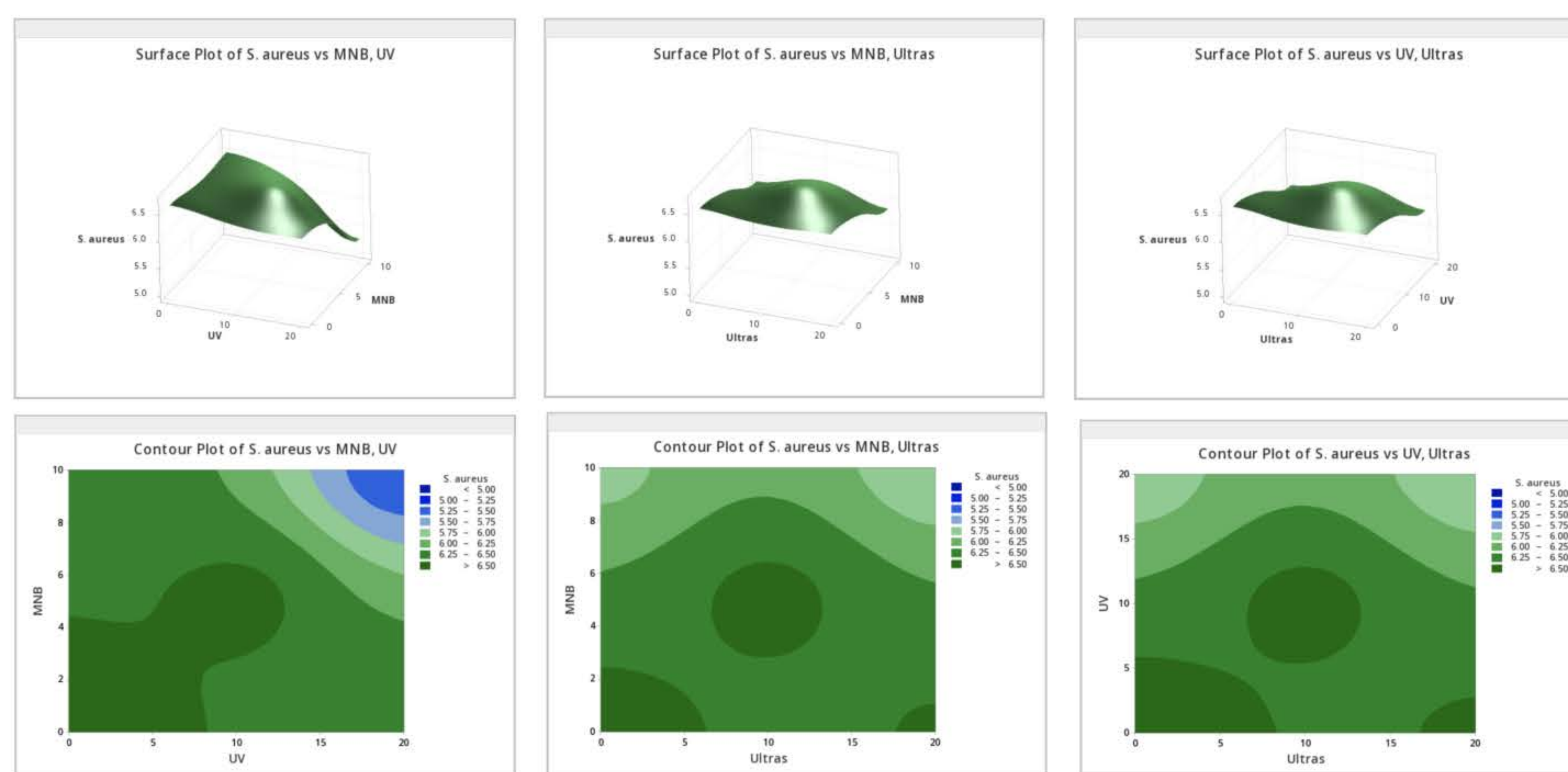


Figure 4. Schematic curve and Surface during plasma treatment at factor (A) and (B), (A) and (C), (B) and (C) to quantify *S. aureus*.

PAW' Generation Mechanism

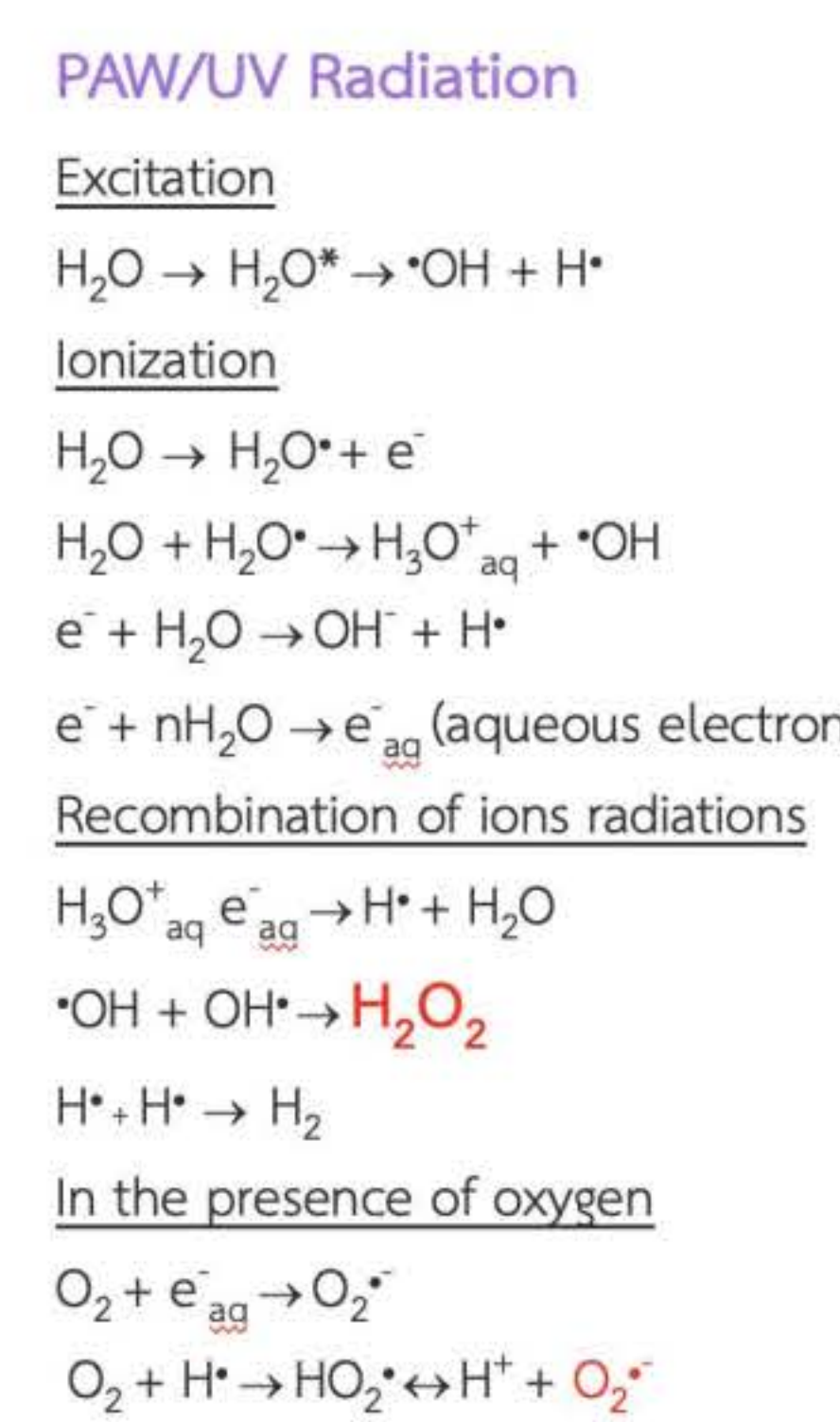
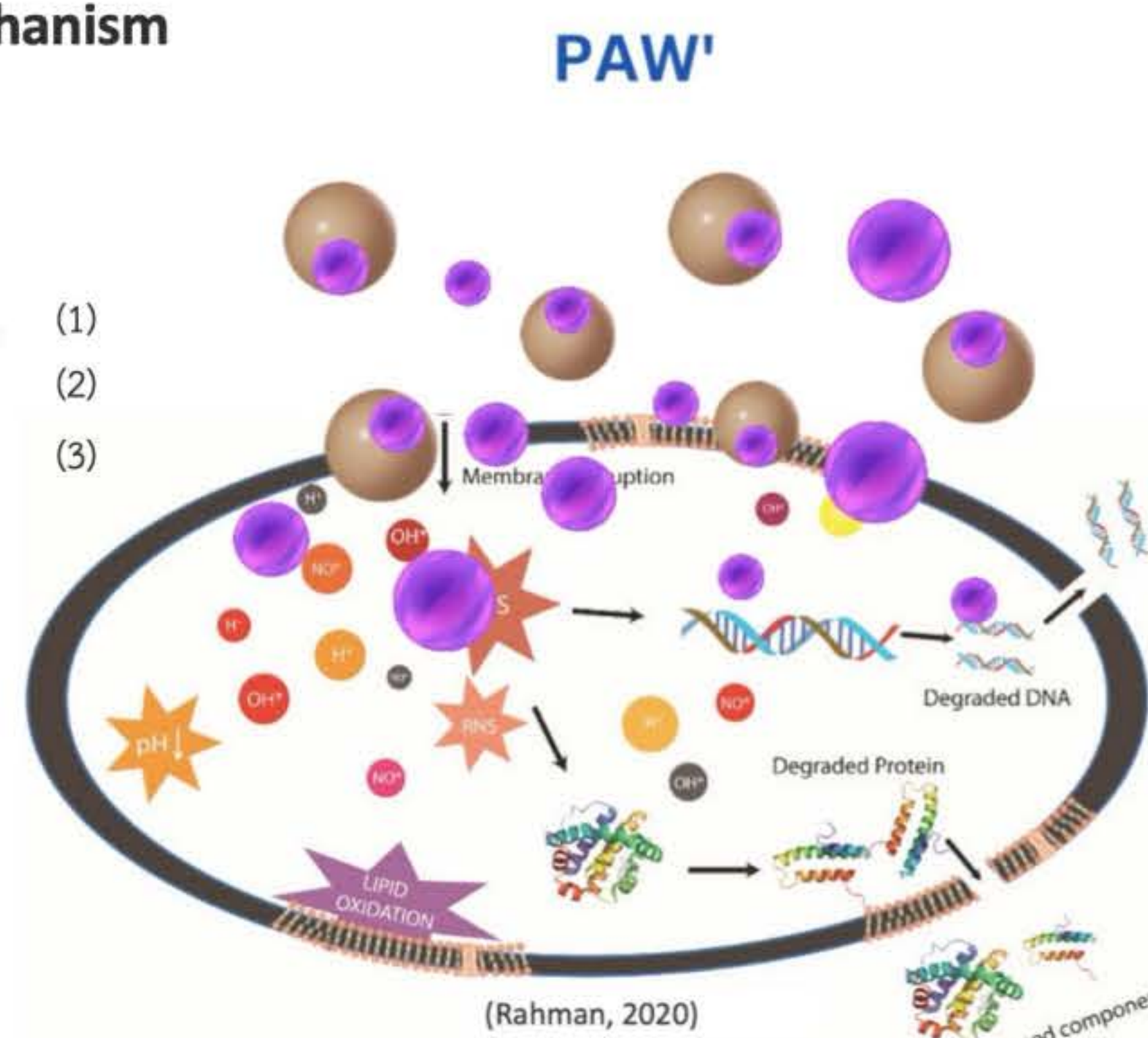
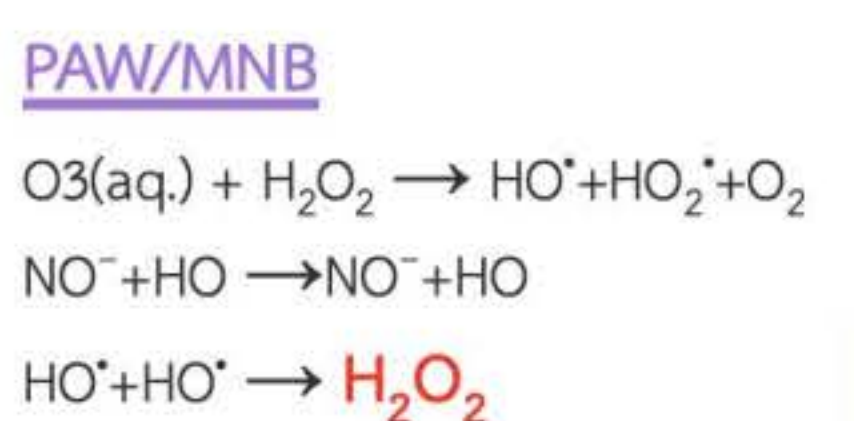


Figure 5. PAW' generation mechanism for bacterial inactivation

Conclusion

The researcher proposed a method to increase the efficiency of sterilization by using Plasma-activated water (PAW) together with supplementary technologies, including Micro/Nanobubbles (MNB), Ultraviolet (UV) Photolysis, and Ultrasonication (US). The parameters and optimal production contributing to the reduce residual were evaluated. This research focuses on creating a plasma system combined with related technology that can reduce residues in order to obtain an appropriate factor for reducing residues from the plasma system combined with related technology. This research has presented the efficiency of the plasma activated water generator together with related technology that is consistent with application in the food industry. From residues found in the food industry, a mechanism for reducing residues with this system has been developed.

Acknowledgements

This research has received funding support from the NSRF via the Program Management Unit for Human Resources & Institutional Development, Research and Innovation [grant number B13F660124] and Chiang Mai University. Researchers thank to Research Center of Plasma Innovation for Sustainable Quality of Life, Faculty of Engineering, Chiang Mai University.

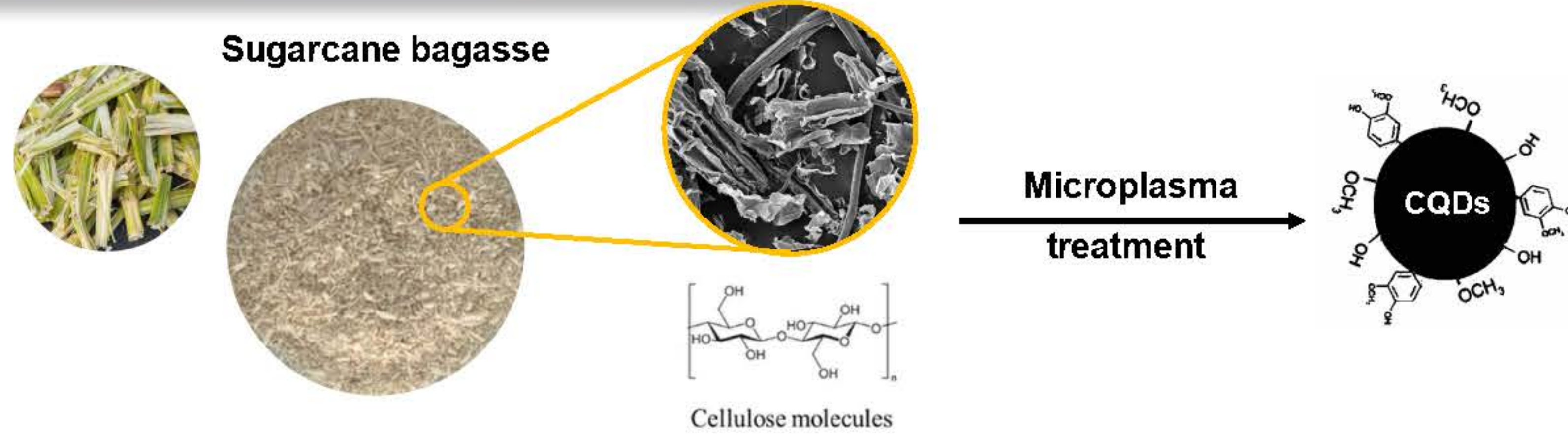
Plasma-Enhanced Synthesis of Carbon Quantum Dots (CQDs) Materials

J. Sukunta^a, C. Sawangrat^{b, c}, W. Wattanuchariya^{c, d}, K. Jantanasakulwong^{a, e, f}, S. Thanakkasaranee^{a, e, f},
N. Tanadchangsaeng^h, R. Panyathip^{a, e, g}, G. Kasi^a and P. Rachtanapun^{a, c, e, f, *}

^a Division of Packaging Technology, Faculty of Agro-Industry, Chiang Mai University, Chiang Mai 50100, Thailand.
^b Department of Industrial Engineering, Faculty of Engineering, Chiang Mai University, 239 Suthep, Mueang, Chiang Mai, 50200, Thailand.
^c Research Center of Plasma Innovation for Sustainable Quality of Life, Faculty of Engineering, Chiang Mai University, 239 Suthep, Mueang, Chiang Mai, 50200, Thailand.
^d Advanced Technology and Innovation Management for Creative Economy Research Group (AIMCE), Department of Industrial Engineering, Faculty of Engineering, Chiang Mai University, 239 Suthep, Mueang, Chiang Mai, 50200, Thailand.
^e Center of Excellence in Agro Bio-Circular-Green Industry (Agro BCG), Chiang Mai University, Chiang Mai 50100, Thailand.
^f Center of Excellence in Materials Science and Technology, Chiang Mai University, Chiang Mai 50200, Thailand.
^g Office of Research Administration, Chiang Mai University, Chiang Mai 50200, Thailand.
^h College of Biomedical Engineering, Rangsit University, Lak-Hok, Pathumthani, Thailand.
* Corresponding author: Pornchai Rachtanapun (Email: pornchai.r@cmu.ac.th)

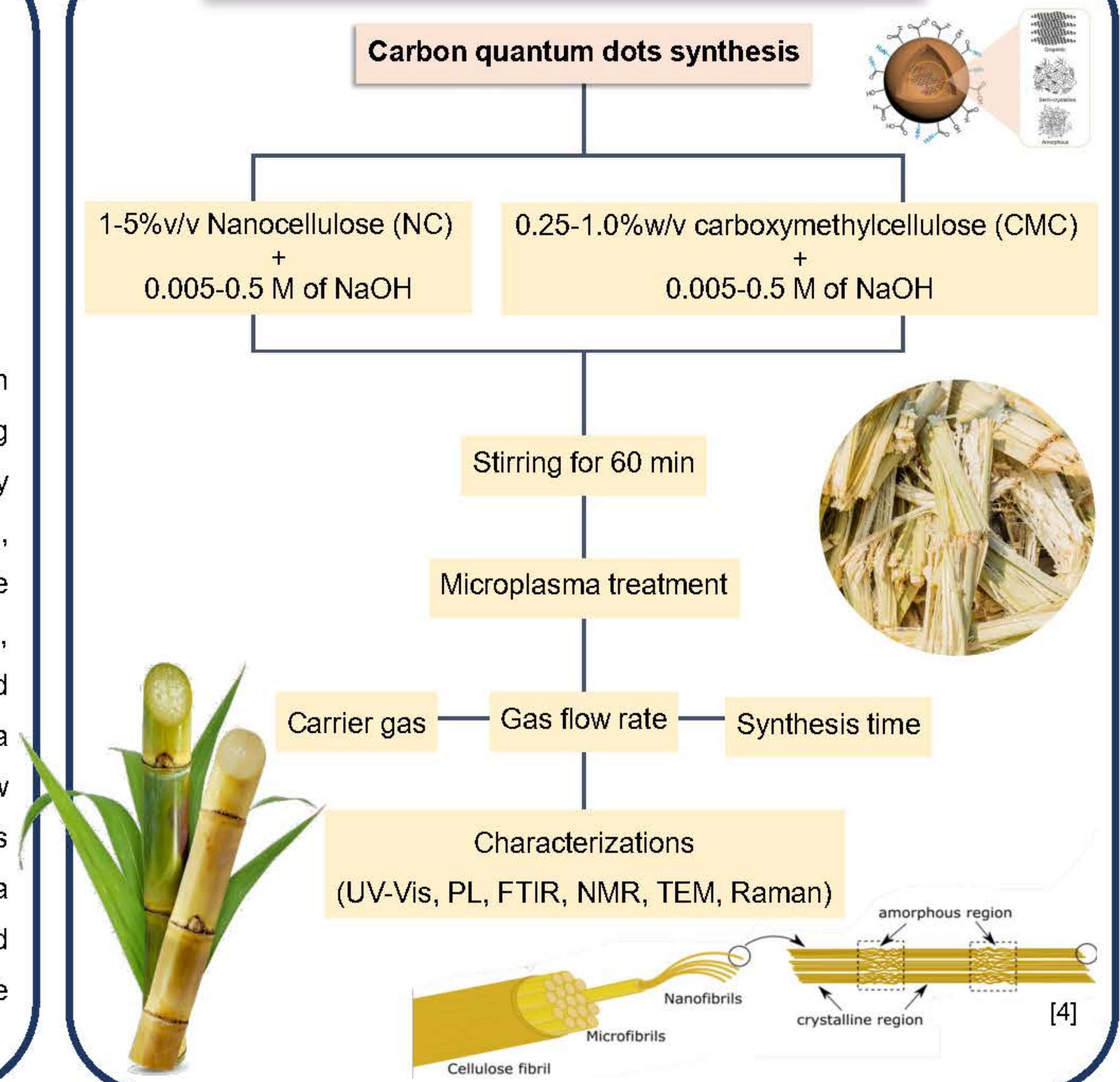


Introduction



Carbon quantum dots (CQDs) are a novel type of quantum dots that are composed of a carbon network with functional groups on the surface. CQDs possess several advantages such as low toxicity, biodegradability, strong fluorescence, tunable color emission, easy surface functionalization, low cost, high aqueous stability, and photostability [1]. CQDs have a wide range of potential applications in energy storage, environmental monitoring, catalysis, contaminants detection and complex environmental forensics, drug delivery, and other biomedical applications. There are numerous methods to synthesize CQDs such as laser ablation, arc discharge, electrochemical techniques, microwave-based methods, hydrothermal, and others [2]. These methods differ in terms of complexity, efficiency, and the quality of the resulting products. Plasma technology is one of the techniques that uses energetic species in plasma to initiate chemical reactions that can produce or modify nanomaterials. Moreover, plasma can operate at low temperatures and atmospheric pressure, making it suitable for large-scale manufacturing processes [3]. In this research, we study on the synthesis of carbon quantum dots (CQDs) using the microplasma technique which is a specific type of plasma with a small size and nonequilibrium features that are beneficial for CQDs and advanced nanomaterials synthesis. Furthermore, the agriculture wastes, the nanocellulose (NC-B) and carboxymethyl cellulose (CMC-B) from sugarcane bagasse have been used as carbon source for producing valuable CQDs materials.

Methods



Results & Discussion

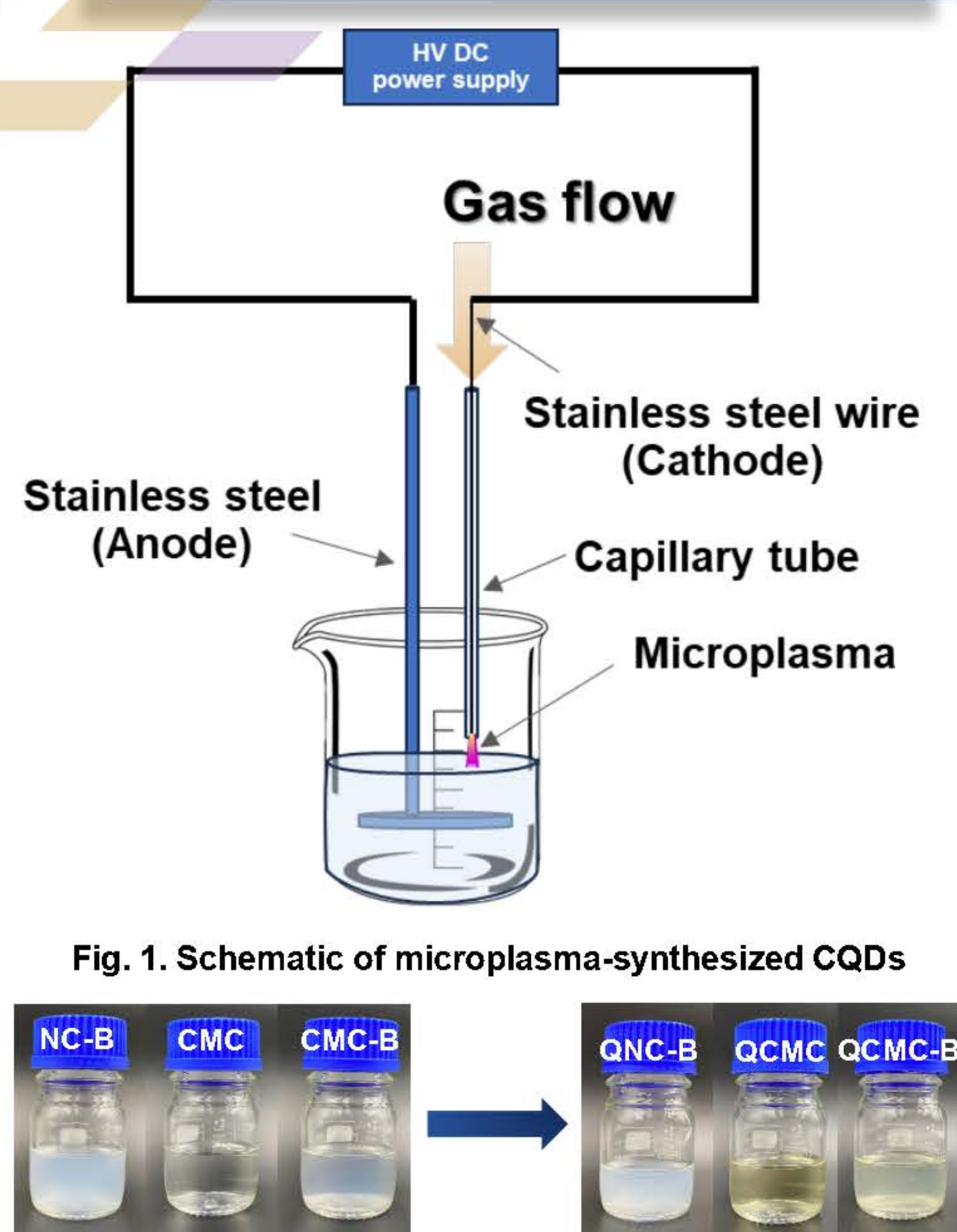


Fig. 2. The precursor solution before and after microplasma treatment

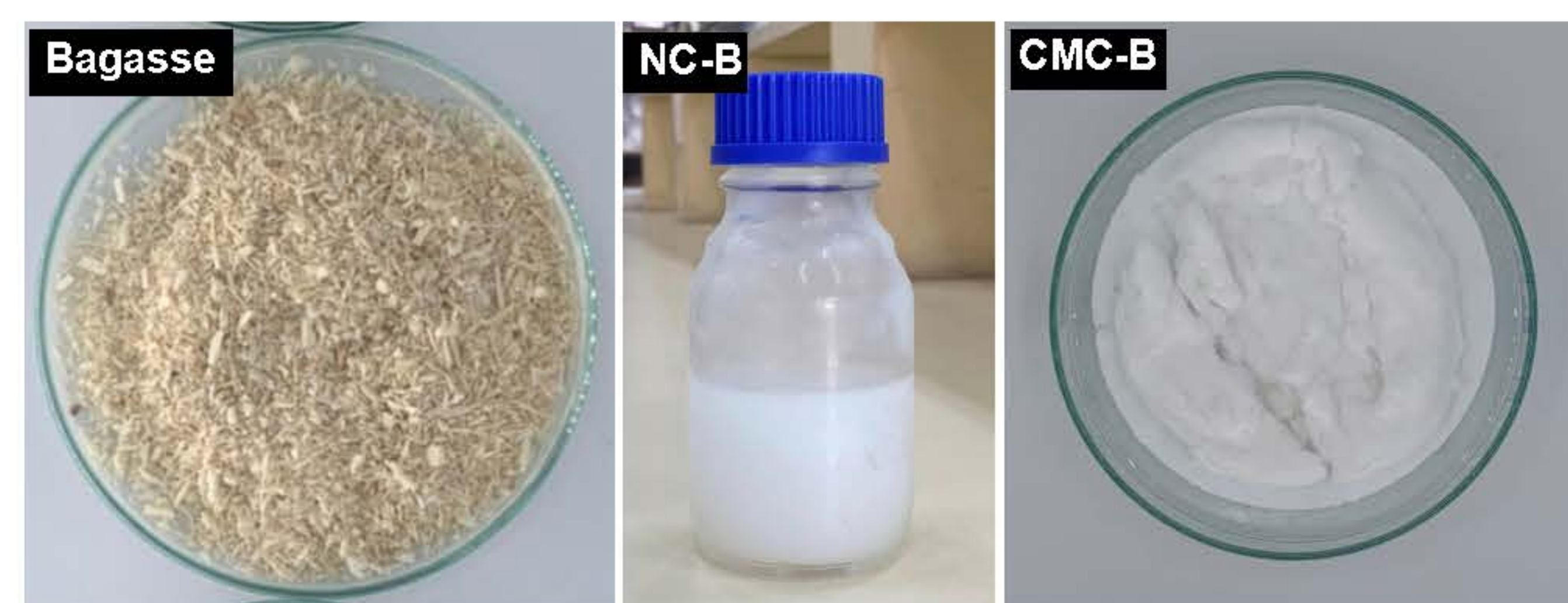


Fig. 3. The photographs of bagasse, nanocellulose (NC-B), and carboxymethyl cellulose from bagasse (CMC-B) as precursor materials.

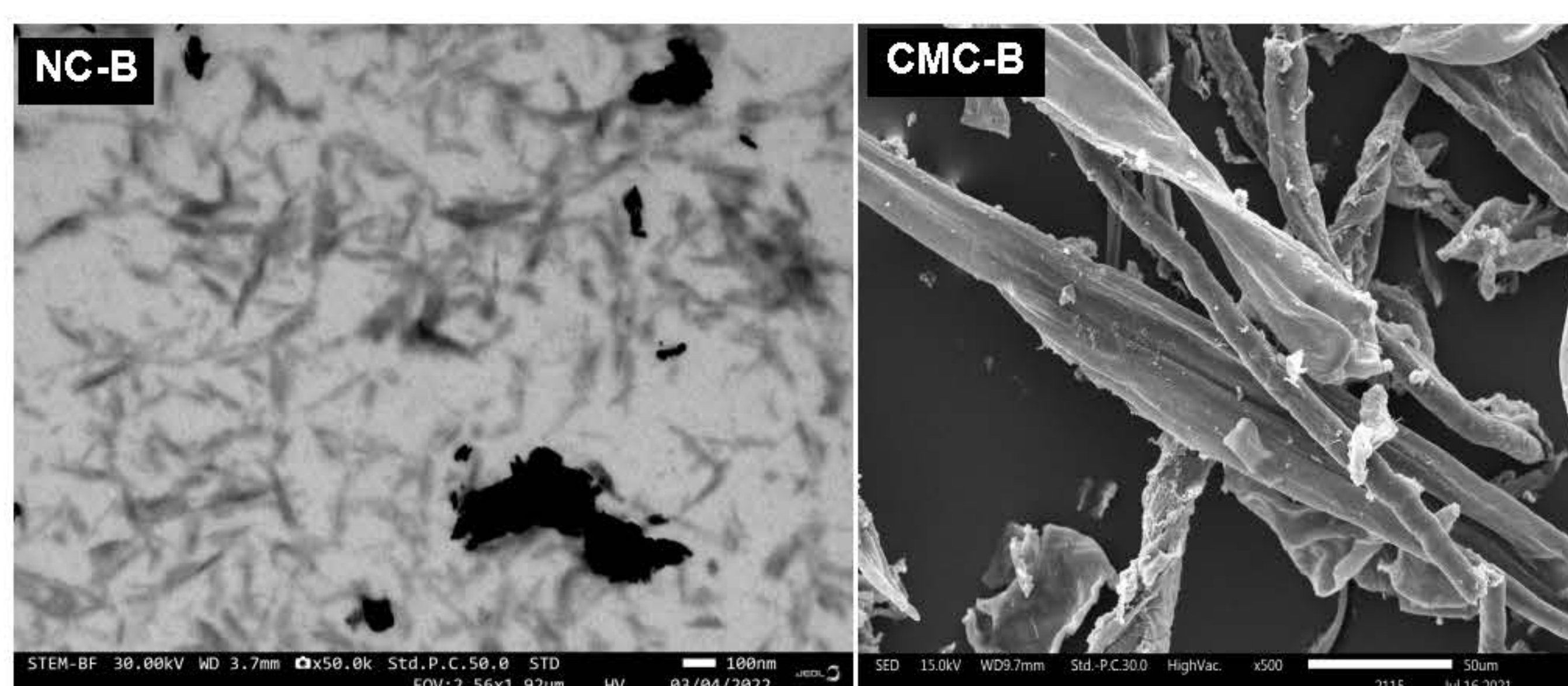


Fig. 4. STEM image of nanocellulose (NC-B), and SEM image of carboxymethyl cellulose (CMC-B) from bagasse as precursor materials.

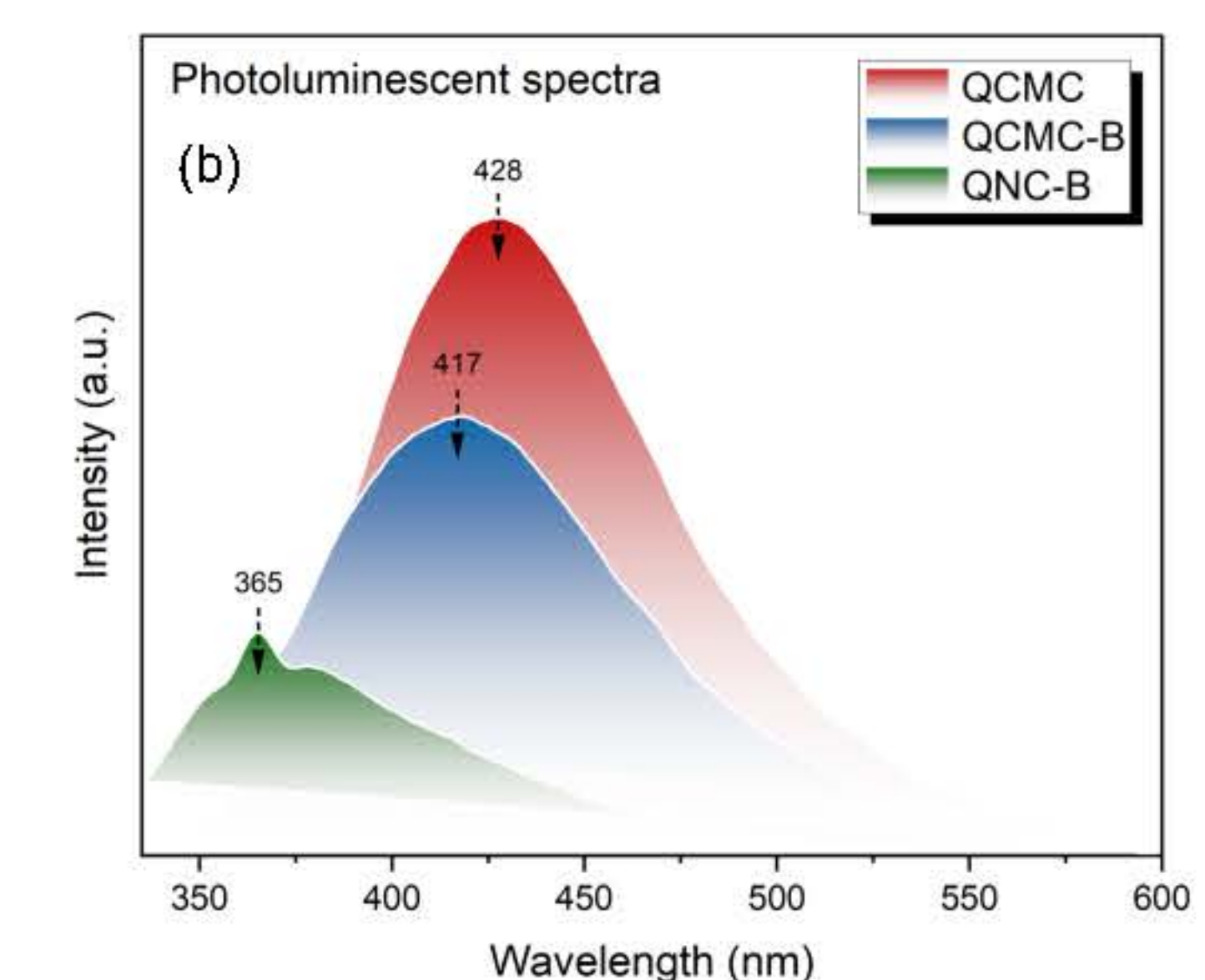
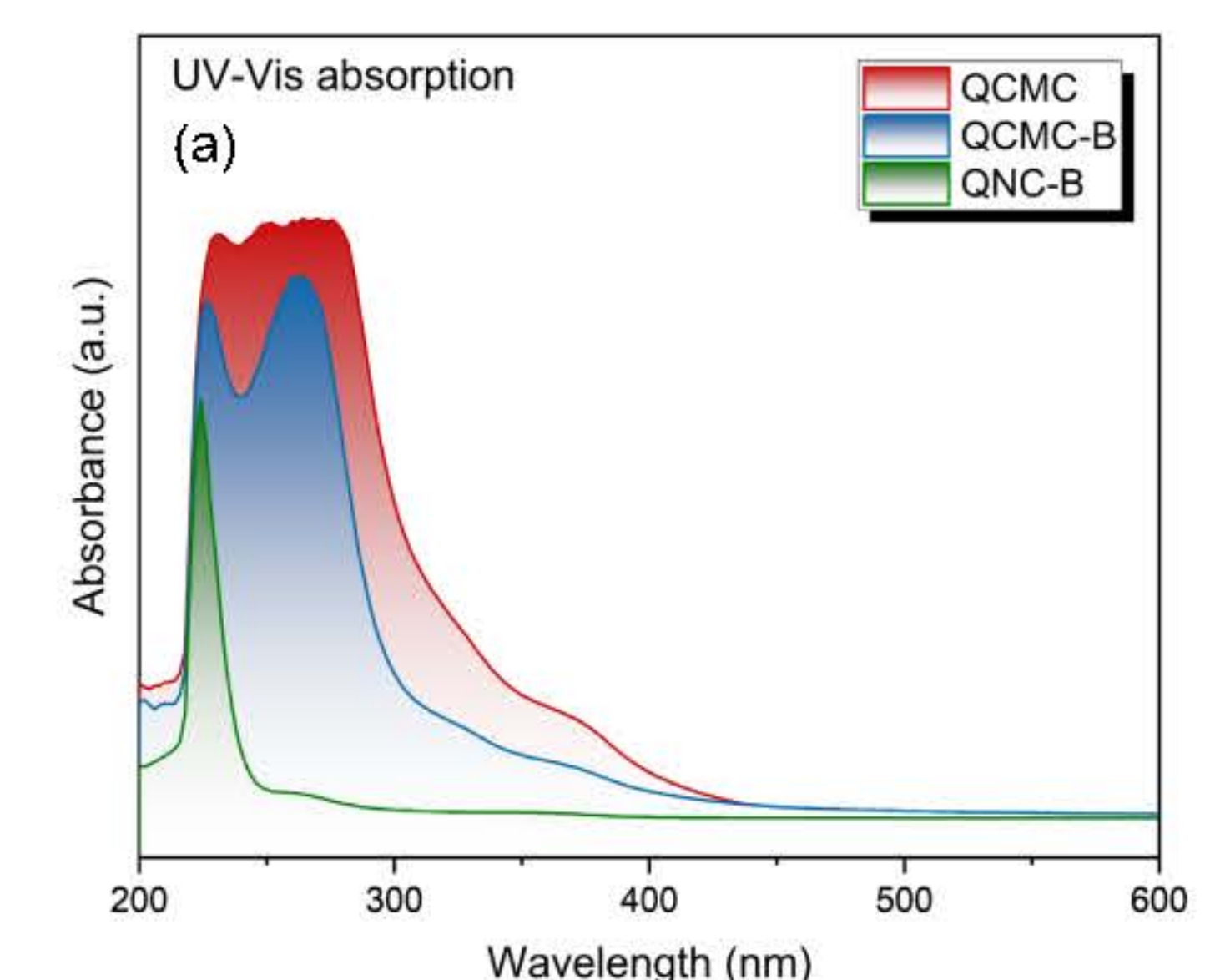


Fig. 5. UV-Vis absorption spectra (a) and photoluminescent spectra (b) of quantum dots from QNC-B, QCMC and QCMC-B with excitation wavelength at 325 nm.

Conclusions

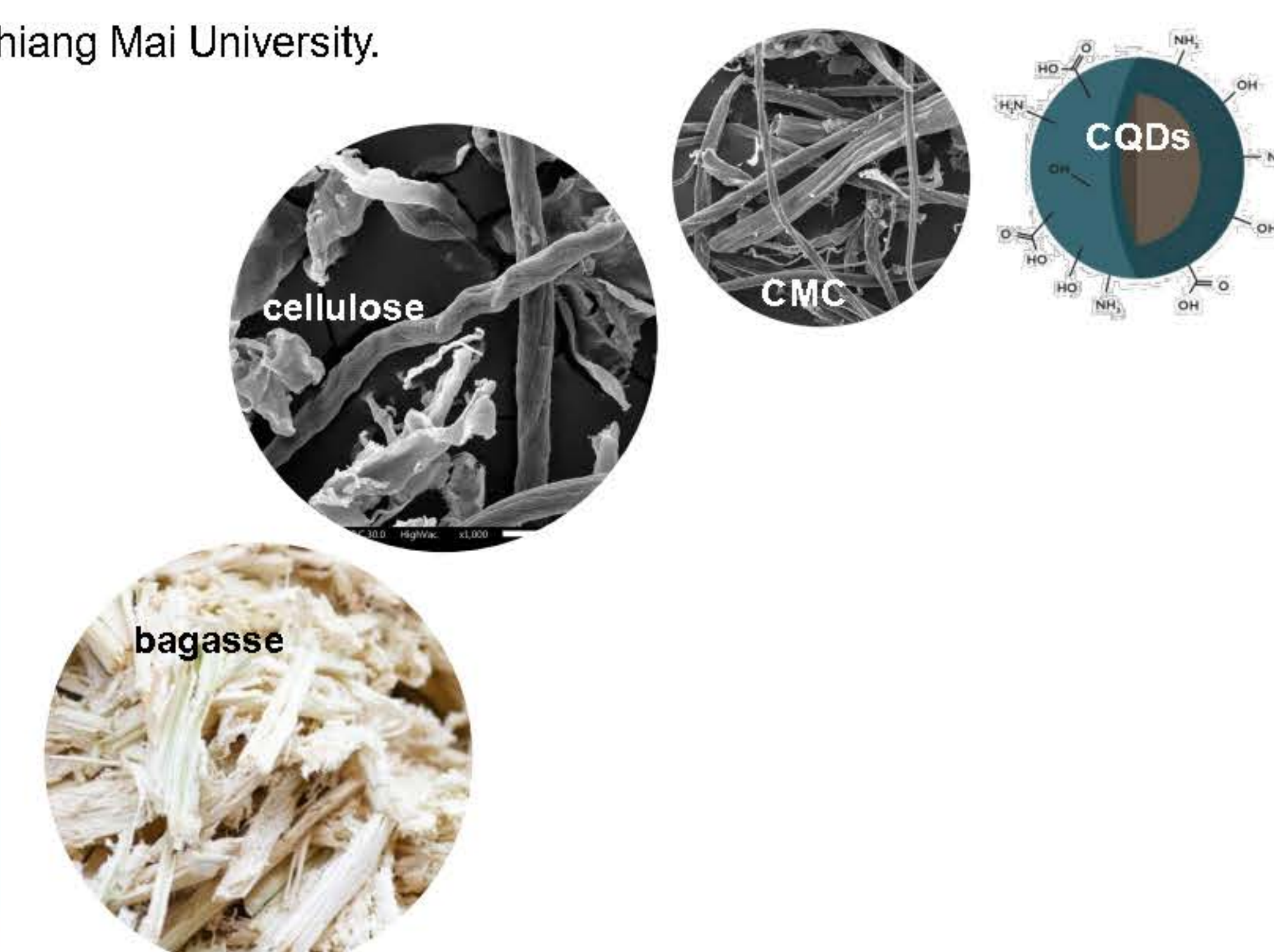
- ❖ Carbon quantum dots (CQDs) have been successfully synthesized by a facile microplasma treatment using carboxymethyl cellulose (CMC) as a precursor.
- ❖ As-synthesized CQDs exhibit absorption in the ultraviolet region caused by the $n \rightarrow \pi^*$ transition within the C=O in cellulose molecules.
- ❖ The as-synthesized CQDs samples were excited at 325 nm and showed the maximum emission wavelength of 365, 417, and 428 nm for QNC-B, QCMC-B, and QCMC, respectively.
- ❖ The study is an ongoing state that has been evaluating the optimal conditions for microplasma-synthesized CQDs from CMC-B and/or others agricultural waste.
- ❖ The CQDs will be characterized with advanced techniques to identify the structure and properties.

References

- [1] B. Gidwani, V. Sahu, S.S. Shukla, R. Pandey, V. Joshi, V.K. Jain, A. Vyas, Quantum dots: Prospectives, toxicity, advances and applications, *Journal of Drug Delivery Science and Technology*, 61 (2021) 102308.
- [2] S. Shabnam, S. Hajar, Applications of Quantum Dots in the Food Industry, in: T. Jagannathan (Ed.) *Quantum Dots*, IntechOpen, Rijeka, 2022, pp. Ch.10.
- [3] A. Khayal, V. Dawane, M.A. Amin, V. Tirth, V.K. Yadav, A. Algahtani, S.H. Khan, S. Islam, K.K. Yadav, B.-H. Jeon, Advances in the Methods for the Synthesis of Carbon Dots and Their Emerging Applications, *Polymers*, 2021.
- [4] Michelin M, Gomes DG, Romani A, Polizeli MdLTM, Teixeira JA. Nanocellulose Production: Exploring the Enzymatic Route and Residues of Pulp and Paper Industry. *Molecules*. 2020; 25(15):3411.

Acknowledgements

This research has received funding support from the NSRF via the Program Management Unit for Human Resources & Institutional Development, Research and Innovation [grant number B13F660124]. Special thanks should be given to Research Center of Plasma Innovation for Sustainable Quality of Life, Faculty of Engineering, Chiang Mai University, Agriculture and Bio Plasma Technology Center (ABPlas) for providing facilities and equipment in this work. This research work was partially supported by Chiang Mai University.



Plasma Catalytic CH₄ and CO₂ Conversion into Valuable Products over porous Ni/Al₂O₃ derived from MIL-53(Al) as Catalysts

Supaphorn Thammakan⁴, Dheerawan Boonyawan³, Wassanai Wattanutchariya^{2,4}, Pornchai Rachtanapun^{2,5,6}, Choncharoen Sawangrat^{1,2,4*}

¹Agriculture and Bio Plasma Technology Center, Science and Technology Park, Chiang Mai University, Thailand

²Research Center of Plasma Innovation for Sustainable Quality of Life, Chiang Mai University, Thailand

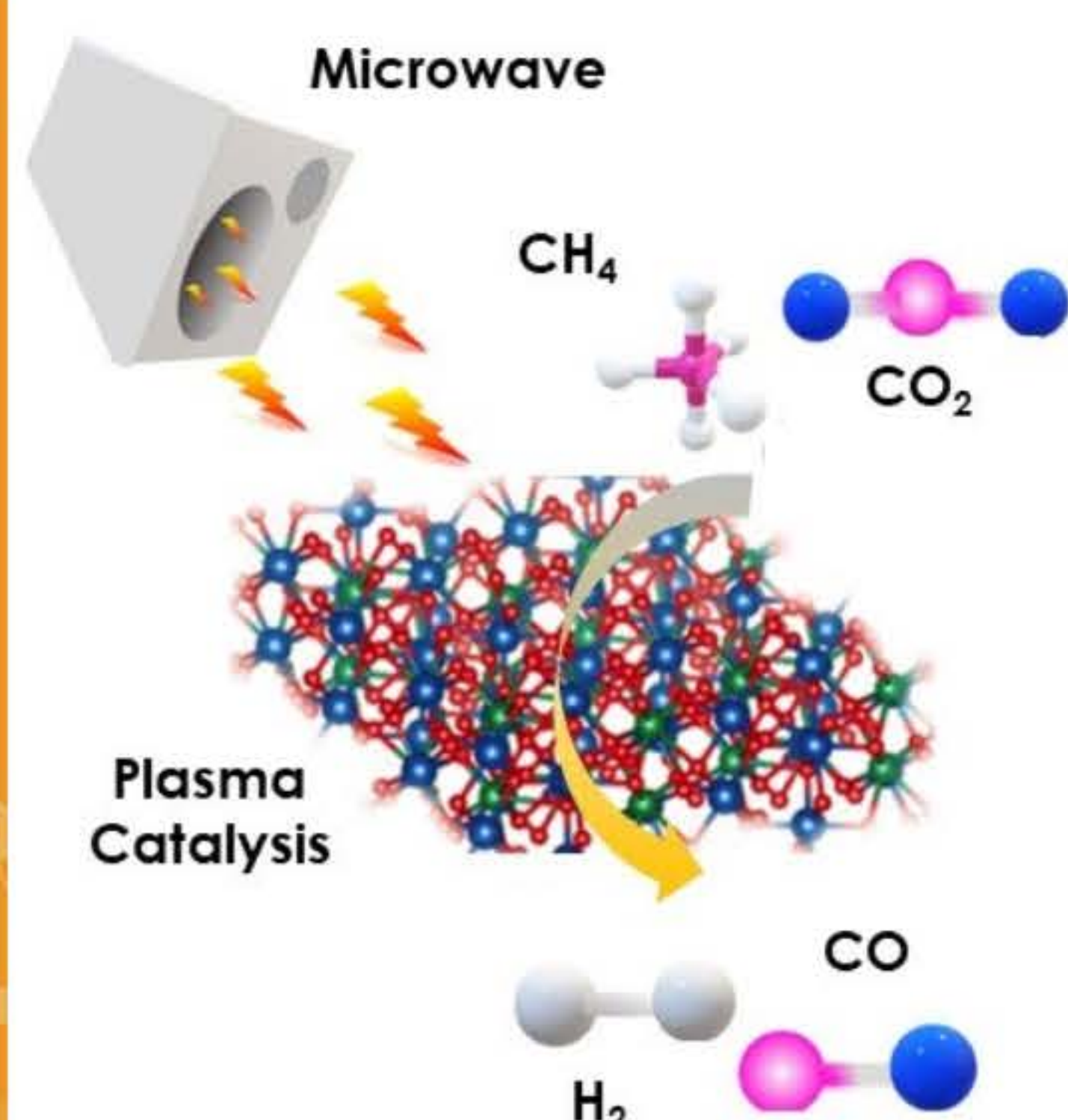
³Department of Physic and Material Science, Faculty of Science, Chiang Mai University, Thailand

⁴Department of Industrial Engineering, Faculty of Engineering, Chiang Mai University, Thailand

⁵Division of Packaging Technology, Faculty of Agro-Industry, Chiang Mai University, Thailand

⁶Center of Excellence in Agro Bio-Circular-Green Industry, Chiang Mai University, Thailand

*Email: Choncharoen@step.cmu.ac.th and Supaphorn_t@cmu.ac.th



The rising in atmospheric concentration of the two greenhouse gases (GHGs) of carbon dioxide (CO₂) and methane (CH₄), stemming primarily from anthropogenic activities, has drawn attention and earnest demand for sustainable technologies to mitigate its atmospheric accumulation. One of the most sustainable concepts is through the utilization of CO₂ and CH₄ as carbon sources for the preparation of high-economic products, e.g. syngas (H₂ and CO), to achieve a sustainable low-carbon economy and carbon-neutral ecosystem. Based on the conventional thermal catalysis of this CO₂ and CH₄ conversion reaction, it often suffers from high energy consumption, catalyst deactivation, and sintering at high temperatures. Recently, the combined non-thermal plasma (NTP), especially microwave plasma, with heterogeneous catalysts (plasma-catalysis) has attracted increasing interest as a promising way to overcome those barriers. The interaction of plasma with catalyst could generate a synergistic effect, which could decrease the activation energy barrier of catalysts, enhance the reaction performance, and energy efficiency. Therefore, highly efficient and stable catalysts are very critical for enhancement of the plasma-catalysis performance in CO₂ and CH₄ conversion reactions. Nickel-based catalysts on metal oxides as support materials have been extensively used in the NTP-catalytic CO₂ and CH₄ conversion due to the formation of the plasma-catalytic synergy at low temperature, high reactivity, and easy availability. Recently, porous materials, especially porous metal oxides derived from metal-organic frameworks (MOFs), was exploited as an ideal candidate for support materials in the CO₂ and CH₄ conversion due to their high surface area and great sacrificed template to well disperse active metal sites on it. In this research, we are interested in investigating the performance of Ni-based catalysts on the porous-Al₂O₃ support material especially Al₂O₃ derived from MOFs, i.e. MIL-53(Al), to enhance the microwave plasma-catalytic performance on the CO₂ and CH₄ conversion into desired products at mild conditions. Moreover, a deeper understanding of their role in plasma-catalytic CO₂ and CH₄ conversion reactions will be gained. This will provide important information for further guidance on the rational design of catalysts for the plasma-catalytic process, which is still critical and very challenging.

METHOD & EXPERIMENTAL

Synthesis of the porous Ni_{x%}/Al₂O₃ derived from MIL-53(Al)

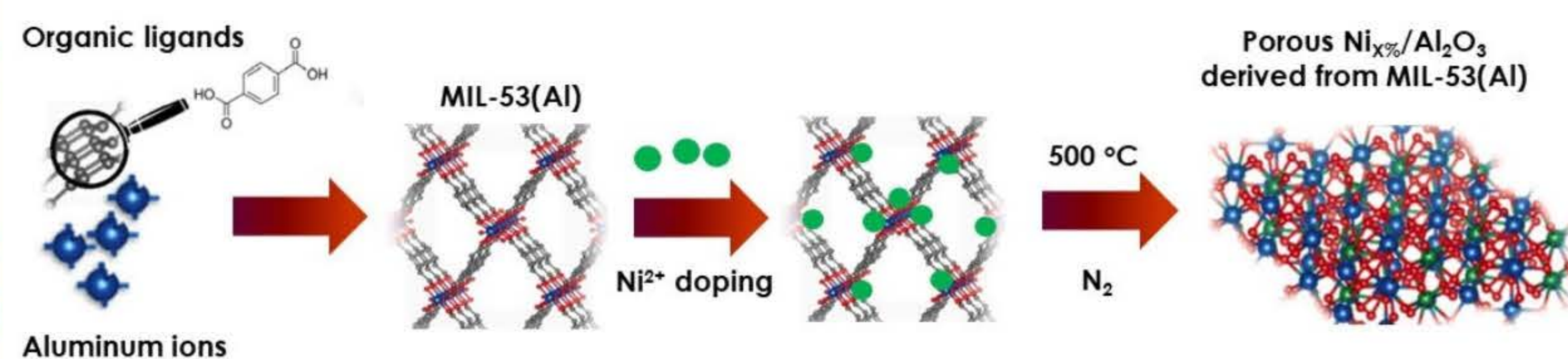


Fig. 1 Preparation process of porous Ni_{x%}/Al₂O₃ (X = 5-20 %wt) catalysts derived from MIL-53(Al)

Setting up the microwave plasma instrument & Study plasma of CH₄+CO₂

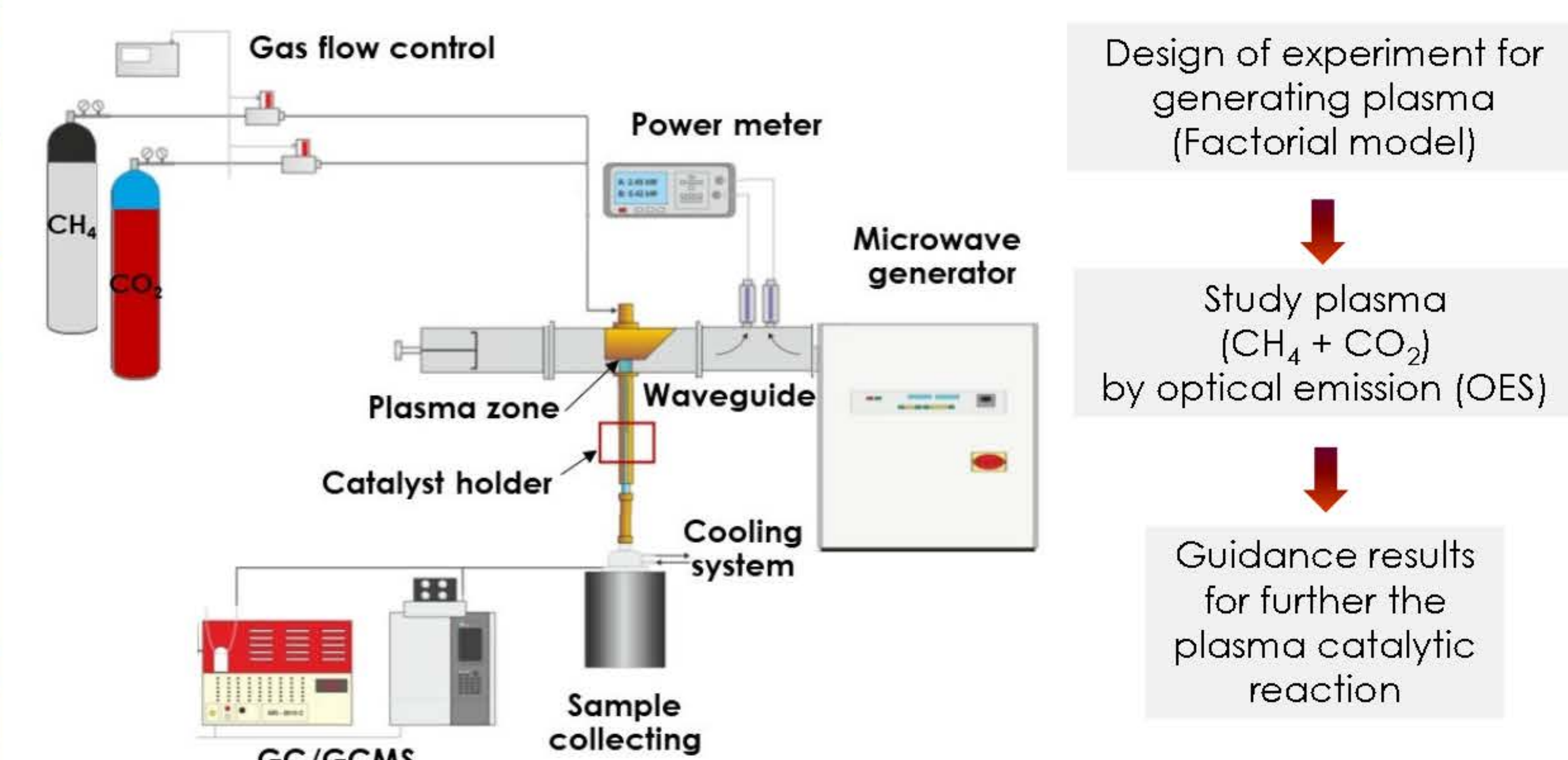


Fig. 2 A simplified diagram showing experimental setting used in plasma catalysis of CH₄ and CO₂ conversion experiments

PRELIMINARY RESULTS & DISCUSSION

Characterization of the catalysts

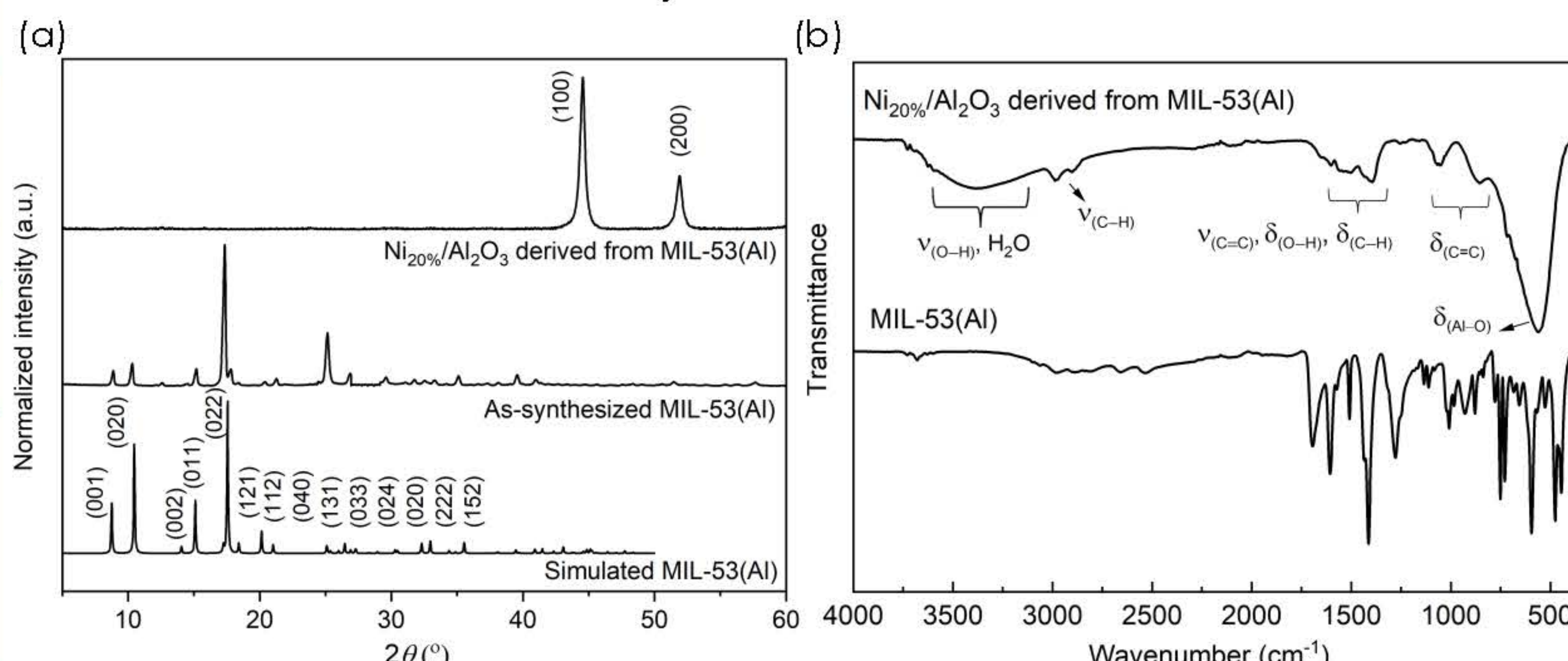


Fig. 3 (a) PXRD patterns of as-synthesized MIL-53(Al) compared to its simulated pattern, and porous Ni_{20%}/Al₂O₃ derived from MIL-53(Al), using to represent other %wt (5-20 %wt) of Ni particles and (b) IR spectrum of Ni_{20%}/Al₂O₃ compared to the pristine MIL-53(Al)

- Purity of the synthesized MIL-53(Al) and porous Ni_{20%}/Al₂O₃ catalysts derived from MIL-53(Al) were ensured by powder X-ray diffraction.
- The presence of Ni⁰ particles on the derived-Al₂O₃ was affirmed via the PXRD.
- FTIR confirmed the functional groups on the porous Ni_{20%}/Al₂O₃ catalyst, which derived from MIL-53(Al)

Optimization of generating plasma condition (CH₄ + CO₂)

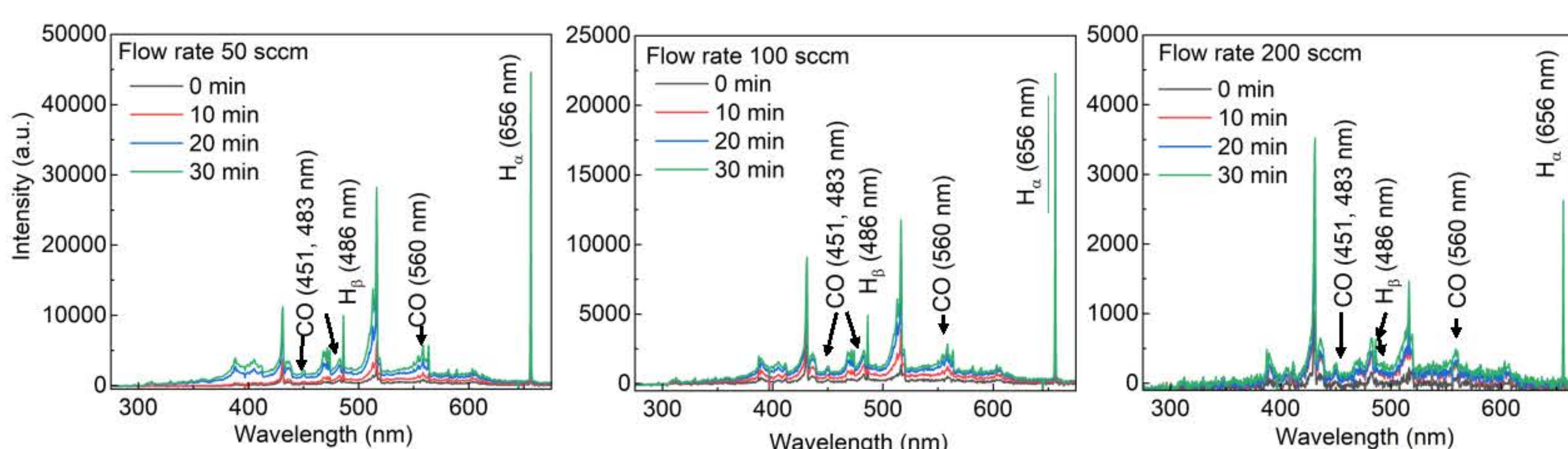


Fig. 4 OES spectra of plasma CH₄ + CO₂ with flow rate 50, 100, and 200 sccm, respectively at varied reaction time of 10-30 min (microwave power 150 applied Voltage, 2.4 GHz)

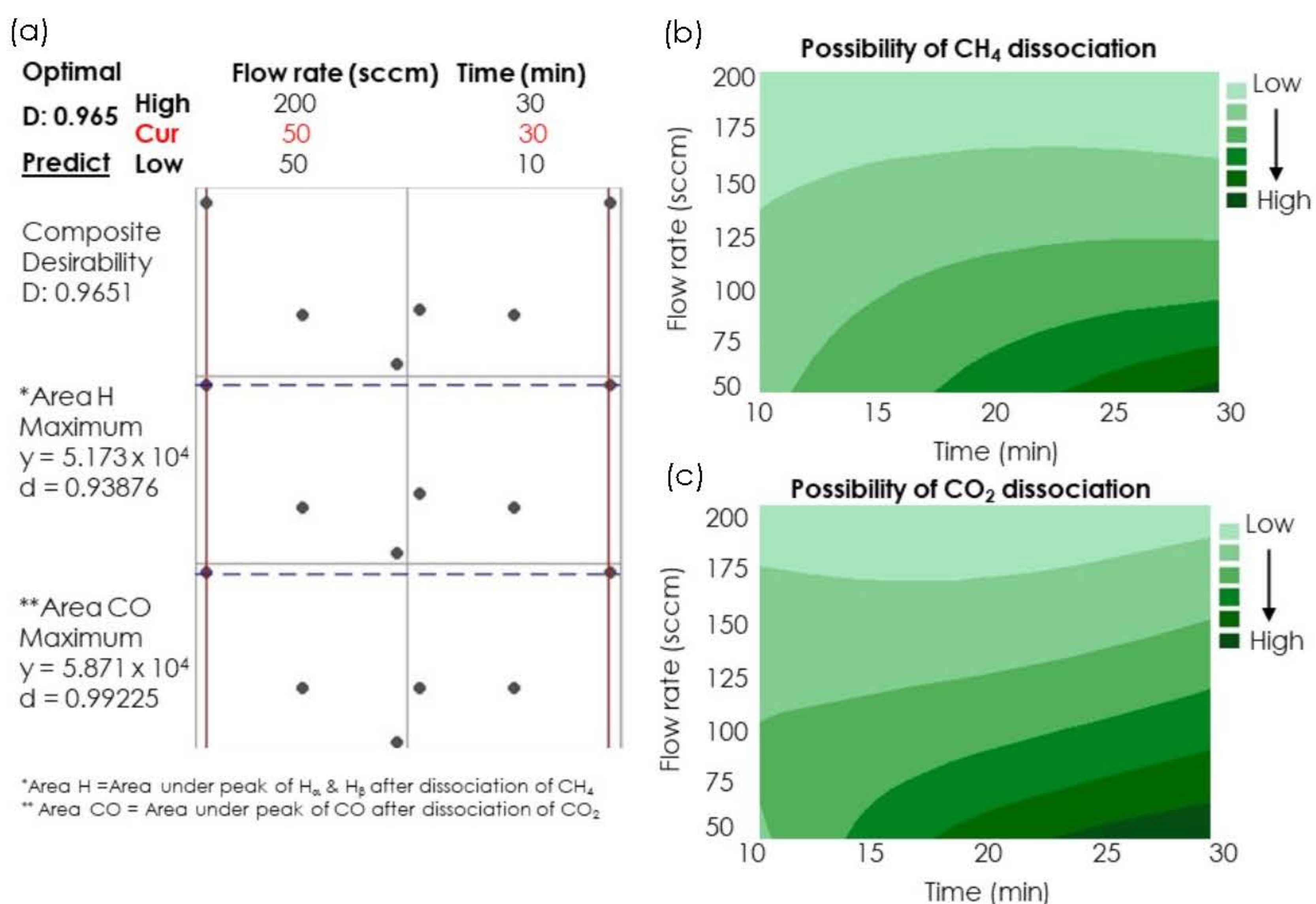


Fig. 5 (a) Graph showing optimal parameters at fixed microwave power of 150 applied Voltage (2.4 GHz), and (b-c) contour graphs for the possible dissociation of CH₄ and CO₂ with varied flow rate: 50-200 sccm and reaction time: 10-30 min (based on the OES data)

CONCLUSIONS

- Porous Ni_{x%}/Al₂O₃ (X = 5-20 %wt) catalysts derived from MIL-53(Al) was successfully synthesized and was aimed to be used for catalyzing the CH₄ and CO₂ conversion through the microwave plasma catalysis
- The microwave plasma machine for CH₄ and CO₂ conversion was already set up.
- The optimal condition for generating plasma was studied based on OES data and aimed to be a guidance for further optimization of CH₄ and CO₂ conversion conditions in the combined plasma-catalysts.

FUTURE WORKS

- Study the combined plasma-catalysts (porous Ni_{x%}/Al₂O₃ (X = 5-20 %wt) derived from MIL-53(Al)) to yield the highest performance of CH₄ and CO₂ conversion into syngas product (H₂ and CO) with high energy efficiency
- Complete the characterization of the catalyst for understanding the synergy interaction with plasma
- Study the reaction mechanism via the computational model

ACKNOWLEDGEMENTS

This research has received funding support from the NSRF via the Program Management Unit for Human Resources & Institutional Development, Research and Innovation [grant number B13F660124] and Chiang Mai University. Researchers thank to Research Center of Plasma Innovation for Sustainable Quality of Life, Agriculture and Bio Plasma Technology Center, and Plasma and Beam Physics Research Facility for providing us many facilities and instruments in this work.



BRAINPOWER
CONGRESS 2023

ร่วมกันสร้างและขับเคลื่อนงานวิจัยชั้นนำ
สู่อุตสาหกรรมแห่งอนาคต

Cosmic inflation in Minimally Modified Gravity (MMG) theory

Postdoctoral Researcher: Dr Saikat Chakraborty (1)
Principal Investigator: Assoc. Prof. Khamphée Karwan (1)
Co-researcher: Jakkrit Sangtawee (1)
Project Leader: Norraphat Srimanobhas (2)

(1) The Institute for Fundamental Studies, Naresuan University
(2) Chulalongkorn University



Problem Statement

Within the context of cosmology and astrophysics there are many observational motivations to investigate gravity theories beyond Einstein's General Relativity (GR). In general, such "modified gravity" theories add extra dynamical degrees of freedom (d.o.f.) to GR. However, lately there has been significant interest in the so-called **Minimally Modified Gravity (MMG)** theories, which are gravity theories different from GR but still do not add any extra dynamical degree of freedom. Such theories have started a new direction in the modified gravity research.

Our project was to investigate **inflationary cosmology** in one such MMG theories. Inflationary cosmology is the most popular paradigm for early universe.

Results

The main results of our research are the following:

(1) Regarding the particular theory under consideration, earlier research has already identified the conditions for which it becomes an MMG at the linear level. When an extra scalar field is included, which is a more cosmologically relevant scenario, this condition is modified. The resulting theory is an MMG with a scalar field at least up to the linear level.

(2) In the resulting theory, it is possible to have an inflationary attractor solution, which arises asymptotically as time progresses. This solution does not encounter any theoretical instability, making it theoretically viable.

(3) To test the observational viability of the resulting model, we investigate scalar and tensor perturbations, which relate to two important inflationary observables, namely the "scalar spectral index" and the "tensor-to-scalar ratio". We find that, the free parameters in the resulting model allow us to get an observationally viable model.

Methodology

Our work is analytical. For some symbolic tensor calculations we use the software **Wolfram Mathematica** and use specialized packages like the **RGTensor** and **Xtensor**.

We started from a particular theory of gravity, which, in general, appears to propagate extra gravitational d.o.f.. However, previous research has shown that it would propagate no extra d.o.f. at least up to the level of linear perturbation provided there is no additional matter and a certain condition is satisfied. When there is an additional matter component, e.g. a scalar field as required for inflationary cosmology, the condition for having no extra d.o.f. is modified. For an ordinary scalar field, this condition is derived. Applying this condition, we get a theory that has no extra d.o.f. in the gravity sector at least to linear order. Essentially we have an MMG theory with an ordinary scalar field at the linear order. We then apply this theory to inflationary cosmology and calculate inflationary observables.

Conclusions

Early universe cosmology is not as well investigated within the context of MMG theories as late time cosmology is. Our project was a step towards that direction. One may argue that the resulting theory is an MMG only up to the linear perturbation level. However, as far as inflationary observables are concerned, this is sufficient because the inflationary observables are calculated using the linear perturbations around the background.

The project was carried out by Dr Saikat Chakraborty (me), associate professor Dr Khamphée Karwan (mentor) and Mr Jakkrit Sangtawee (PhD student). The research culminated into the paper <https://arxiv.org/abs/2308.09508> which has been submitted to the journal Physical Review D in September.

Acknowledgement: This research has received funding support from the NSRF via the Program Management Unit for Human Resources & Institutional Development, Research and Innovation [grant number B01F650006]. Apart from this particular research, I am also thankful to the financial support from the grant for three of my other works *Fortsch.Phys.* 2023 2300006, *Phys.Rev.D* 107 (2023) 6, 063515, *Phys.Lett.B* 842 (2023) 137962, where the grant is duly acknowledged.

Enhanced the performance of perovskite solar cells and photodetector devices using quantum design

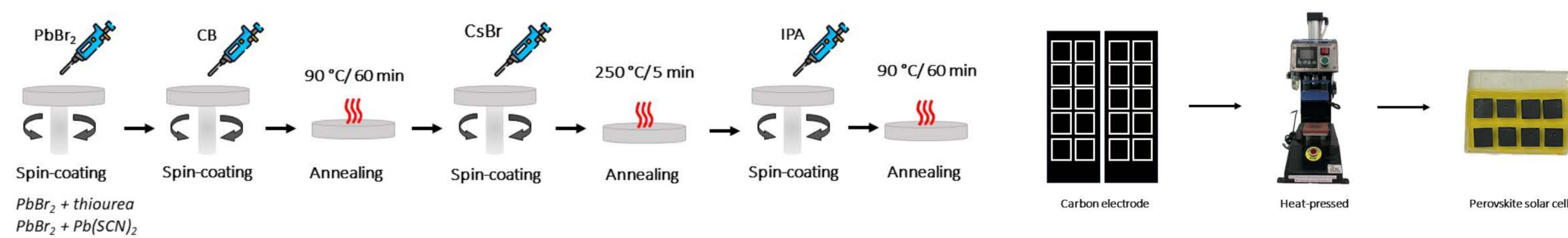
Watcharapong Pudkon^a, Duangmanee Wongratanaphisan^{a,b,c}, Pongsakorn Kanjanaboos^d, Anucha Watcharapasorn^a, Pipat Ruankham^{a,b,c*}

^a Department of Physics and Materials Science, Faculty of Science, Chiang Mai University, 50200, Thailand
^b PBP-CMU Electron Linac Laboratory, Plasma and Beam Physics Research Facility, Department of Physics and Materials Science, Faculty of Science, Chiang Mai University, 50200, Thailand
^c Thailand Center of Excellence in Physics, Ministry of Higher Education, Science, Research and Innovation, Bangkok, 10400, Thailand
^d School of Materials Science and Innovation, Faculty of Science, Mahidol University, Nakhon Pathom, 73170, Thailand

Introduction

Perovskite materials show superior photovoltaic properties, including long exciton diffusion length, and controllable band gap. The power conversion efficiency (PCE) of perovskite solar cells (PSCs) significantly increased to 25.7% since perovskite materials were introduced in 2009 to prepare solar cells. PSCs can be divided into all-inorganic perovskite solar cells and organic-inorganic hybrid perovskite solar cells. Although organic-inorganic hybrid PSCs exhibit excellent PCE, their commercial development is hampered by poor humidity and temperature stability. In the past several years, all inorganic CsPbBr₃ perovskite have attracted great interest owing to their intrinsic advantages of high thermal and light stability and good optical properties. The CsPbBr₃ can easily convert into perovskite phase in air at room temperature, hampering their practical application. All-inorganic CsPbBr₃, with outstanding moisture, oxygen and thermal stability under harsh conditions, emerges as a competitive candidate of light absorbers that is attracting widespread attentions. In general, the perovskite film quality is a key point to greatly improve the efficiency and stability of PSCs, Unfortunately, the one-step solution-processing is not suitable for preparing CsPbBr₃ perovskite film. Therefore, a high-quality CsPbBr₃ perovskite film is fabricated via the multistep spin-coating technique. In addition, additive engineering is an effective strategy for improving the quality of CsPbBr₃ perovskite film.

Methods



Results and Discussion

Surface morphology of PbBr₂ film and CsPbBr₃ perovskite film coated on FTO/ZTO substrate were investigated by FE-SEM as shown in Fig. 1. The PbBr₂ treated by CB film (Fig. 1a) showed good size distribution compared to without CB-treated (Fig. 1b). However, there exists many pinholes on the surface of PbBr₂ film. In this research, thiourea and Pb(SCN)₂ were used as chemical additive to fabricate a high-quality CsPbBr₃ perovskite film. In case of thiourea, the fabricated CsPbBr₃ perovskite film (Fig.1d) showed smooth surface with reduced pinhole and enlarged grain size compared to PbBr₂ film (Fig. 1c). When introduced Pb(SCN)₂ in PbBr₂, it can improve the prepared CsPbBr₃ perovskite film by reducing pinhole and increasing the particle size as shown in Fig.1f compared to PbBr₂ film in Fig. 1e.

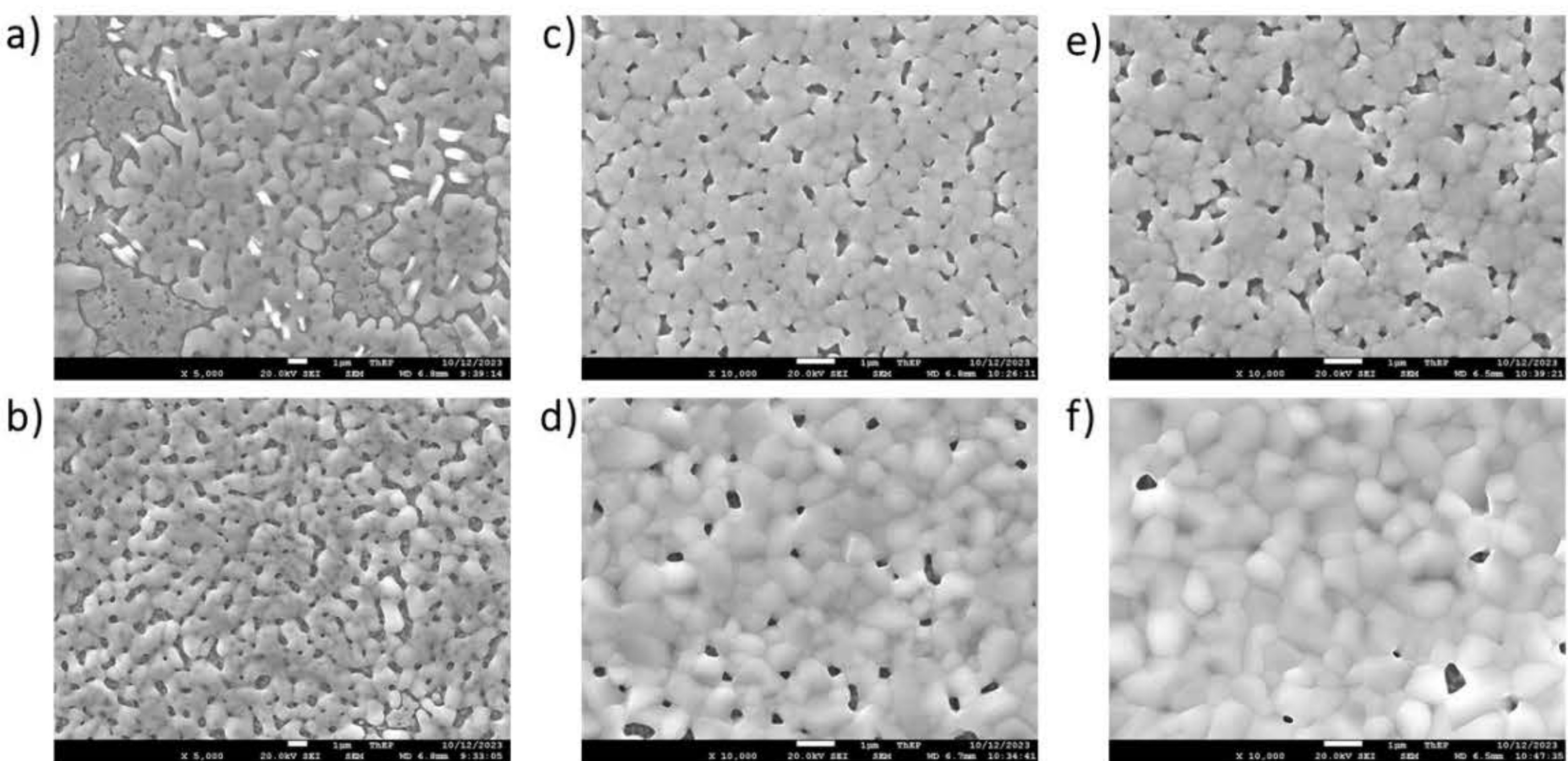


Fig. 1 FE-SEM images of a) PbBr₂, b) PbBr₂ with CB-treated, c) PbBr₂ with 3 mg thiourea, d) CsPbBr₃ with 3 mg thiourea, e) PbBr₂ with 3 mg Pb(SCN)₂ and f) CsPbBr₃ with 3 mg Pb(SCN)₂.

The PSCs based FTO/ZTO/CsPbBr₃/CuSCN/carbon were fabricated to investigate how different chemical additives would affect photovoltaic performance. The photovoltaic parameters including power conversion efficiency (PCE), fill factor (FF), short circuit current density (J_{sc}) and open circuit voltage (V_{oc}) were shown in Table 1. Firstly, the thickness of carbon electrode were studied in 3 groups as thin carbon (150 μ m-250 μ m), normal carbon (250 μ m-400 μ m) and thick carbon (400 μ m-750 μ m) without adding chemical additives. It can be found that the PCE of CsPbBr₃ device increased with increasing carbon thickness and slightly dropped when the carbon thickness was over than 400 μ m. Using normal carbon as electrode showed the highest average PCE as 4.55% with J_{sc} of 6.19 mA/cm², V_{oc} of 1.14 V, and FF of 64.19%. Therefore, the normal carbon was used as electrode for fabrication of CsPbBr₃ solar cell device in this research. In case of adding chemical additives, the amount of additive was varied as 1 mg, 3 mg and 5 mg in both of thiourea and Pb(SCN)₂. When adding thiourea, the average PCE increased with increasing the amount of thiourea from 1 mg to 3 mg. However, when the amount of thiourea is increased from 3 mg to 5 mg, the fabricated PSC shows a decreased PCE.

Conclusion

In conclusion, we have demonstrated that highly efficient CsPbBr₃ PSCs can be fabricated using multistep spin-coating with CB-treated in air ambient condition. The carbon film with thickness as 250 μ m-400 μ m showed a good performance as electrode. As consequence, the average PCE of CsPbBr₃ PSCs without additive showed higher than adding both thiourea and Pb(SCN)₂. It obtains a campion PCE of 4.55% (max. 5.37%) with J_{sc} of 6.19 mA/cm², V_{oc} of 1.14 V, and FF of 64.19%. This enhancement can be mainly attributed to the more effective charge transport by the improved film quality with pinhole-free of the CsPbBr₃ perovskites.

The CsPbBr₃ with 3 mg of thiourea showed the highest average PCE as 3.77% with J_{sc} of 5.69 mA/cm², V_{oc} of 1.09 V, and FF of 61.34%. When adding Pb(SCN)₂, it can be seen that the PCE decreased from 2.87% to 2.07% with increasing the amount of Pb(SCN)₂ from 1 mg to 5 mg. From these results, it can be concluded that the additives can reduced the pinhole on the surface of CsPbBr₃ perovskite film but it can not enhance the solar cell efficiency compared to CsPbBr₃PSC without additive. It has been clearly from FE-SEM images as shown in Fig.2. The CsPbBr₃ perovskite film (Fig. 2b) showed a compact morphology with indistinct grain boundaries and large crystal size compared to PbBr₂ film (Fig. 2a). It is a consensus that the flat and pinhole-free perovskite film with large crystal size would be beneficial for charge transport and extraction, which can largely reduce the charge recombination in fabricated PSCs and lead to a high solar cell efficiency .

Table 1. Photovoltaic parameters of the CsPbBr₃ PSCs with different carbon thickness and chemical additives

Samples	J_{sc} (mA/cm ²)	V_{oc} (V)	FF (%)	PCE (%)
Thin carbon	5.55	1.00	64.03	3.55
Normal carbon	6.19	1.14	64.19	4.55
Thick carbon	5.79	1.07	65.29	4.07
1 mg thiourea	5.01	1.13	59.52	3.38
3 mg thiourea	5.69	1.09	61.34	3.77
5 mg thiourea	4.76	1.12	56.06	2.98
1 mg Pb(SCN) ₂	5.83	1.05	47.08	2.87
3 mg Pb(SCN) ₂	5.98	0.95	46.11	2.66
5 mg Pb(SCN) ₂	5.48	0.86	43.30	2.07

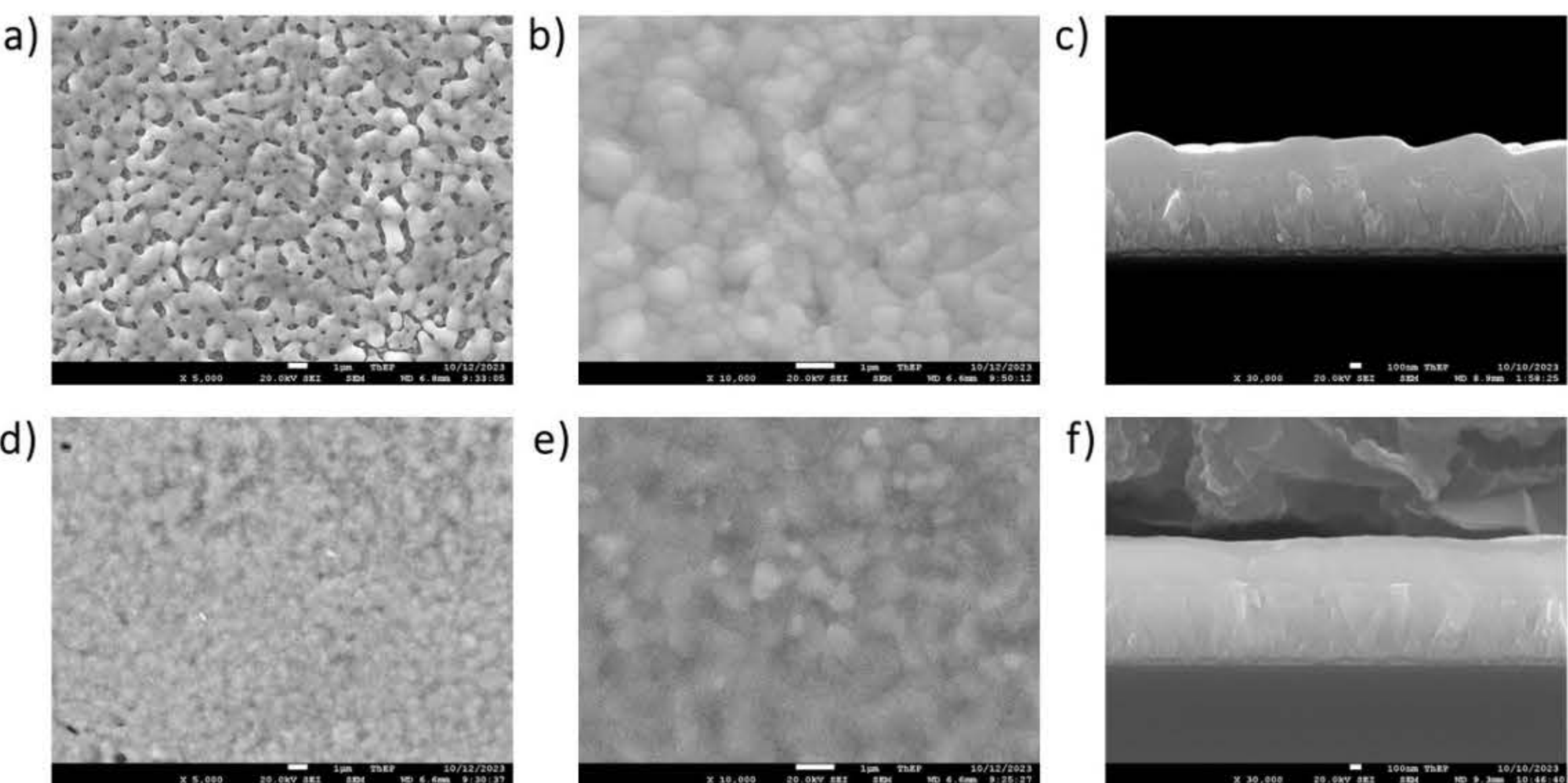


Fig. 2 Top-view FE-SEM images of a) PbBr₂ and b) CsPbBr₃ and cross-section SEM image of c) CsPbBr₃. Top-view FE-SEM images of d) and e) CsPbBr₃ perovskite solar cell, and cross-section of f) CsPbBr₃ perovskite solar cell.

Acknowledgements

This research has received funding support from the NSRF via the Program Management Unit for Human Resources & Institutional Development, Research and Innovation [grant number B13F650006]



BRAINPOWER
CONGRESS 2023

ร่วมกันสร้างและขับเคลื่อนงานวิจัยชั้นแนวหน้า
สู่อุตสาหกรรมแห่งอนาคต



Enhancing the performance and stability of perovskite photodetectors for the commercialization purposes

Sadeq Abbasi^{1, 2}, Pipat Ruankham^{2, 3, 4}, Woraprom Passatorntaschakorn², Warunee Khampa², Wongsathon Musikpan², Chawalit Bhoomanee², Hong Liu¹, Duangmanee Wongrataphisan^{2, 3, 4}, Wenzhong Shen^{1*}

¹Key Laboratory of Artificial Structures and Quantum Control, Institute of Solar Energy, School of Physics and Astronomy, Shanghai Jiao Tong University, Shanghai 200240, P. R. China.

²Department of Physics and Materials Science, Faculty of Science, Chiang Mai University, Chiang Mai, 50200, Thailand.

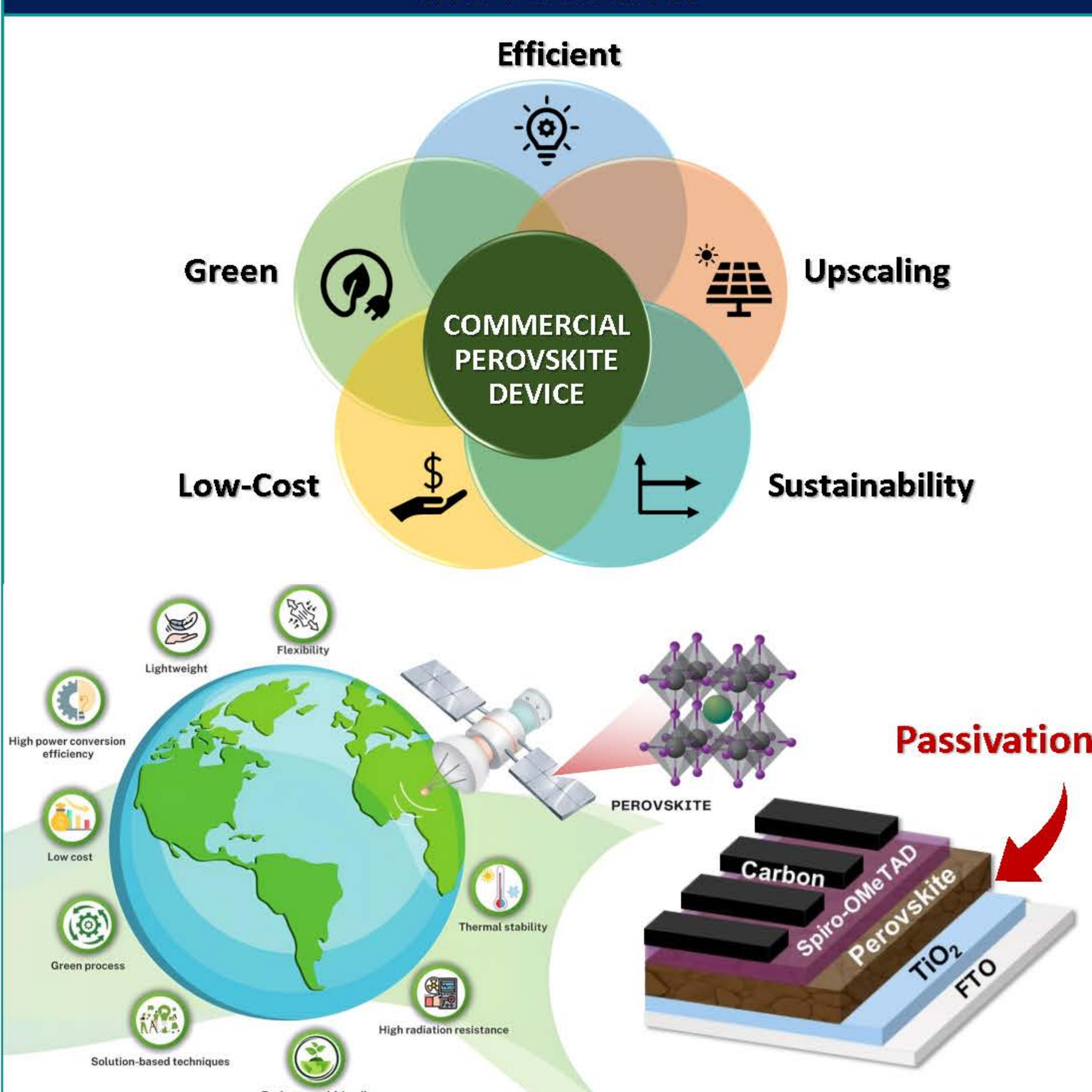
³Research Center in Physics and Astronomy, Faculty of Science, Chiang Mai University, Chiang Mai 50200, Thailand.

⁴Thailand Center of Excellence in Physics (ThEP center), Ministry of Higher Education, Science, Research and Innovation, Bangkok, 10400, Thailand.

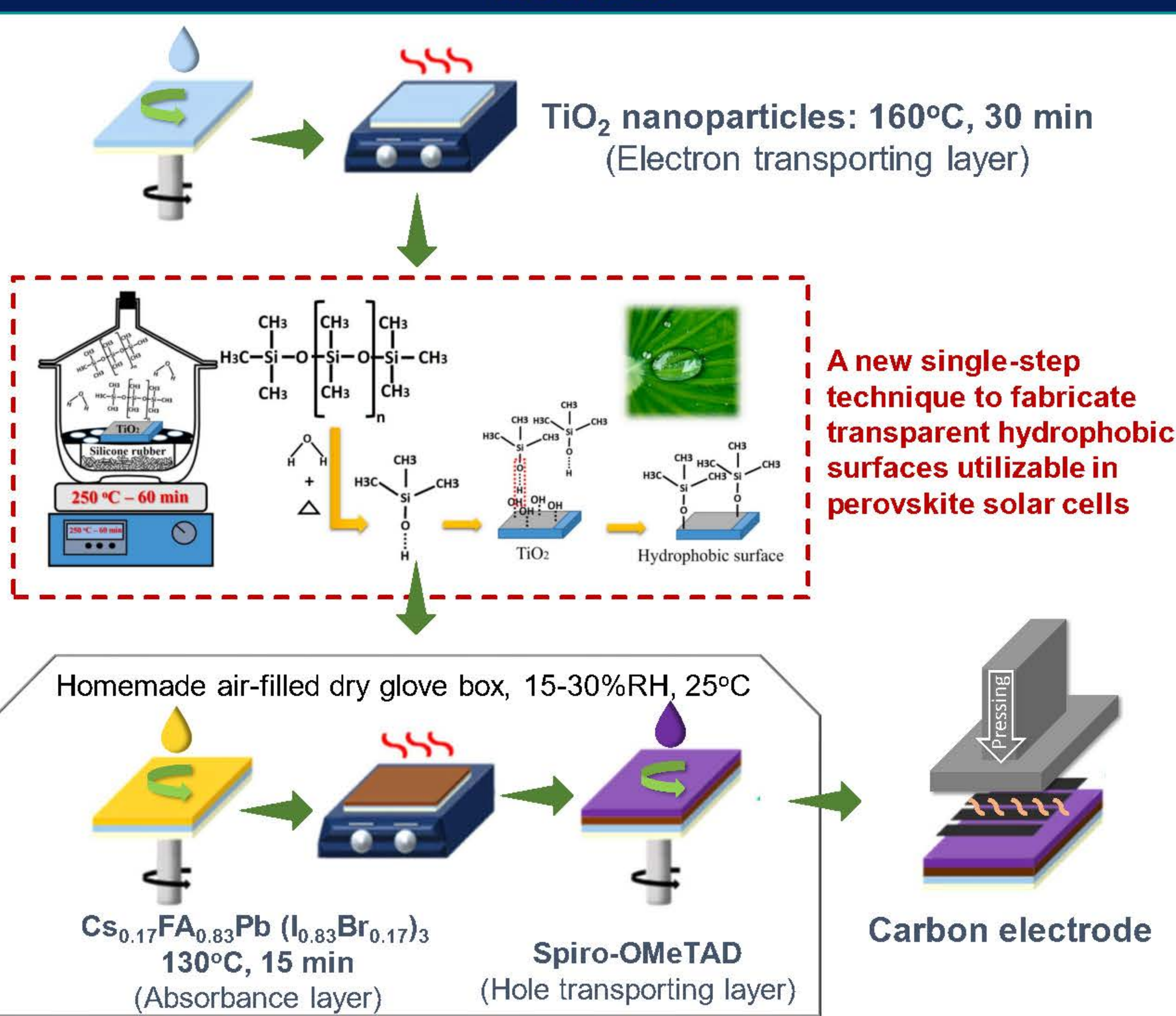
*Corresponding author: duangmanee.wong@cmu.ac.th



Introduction



Methods

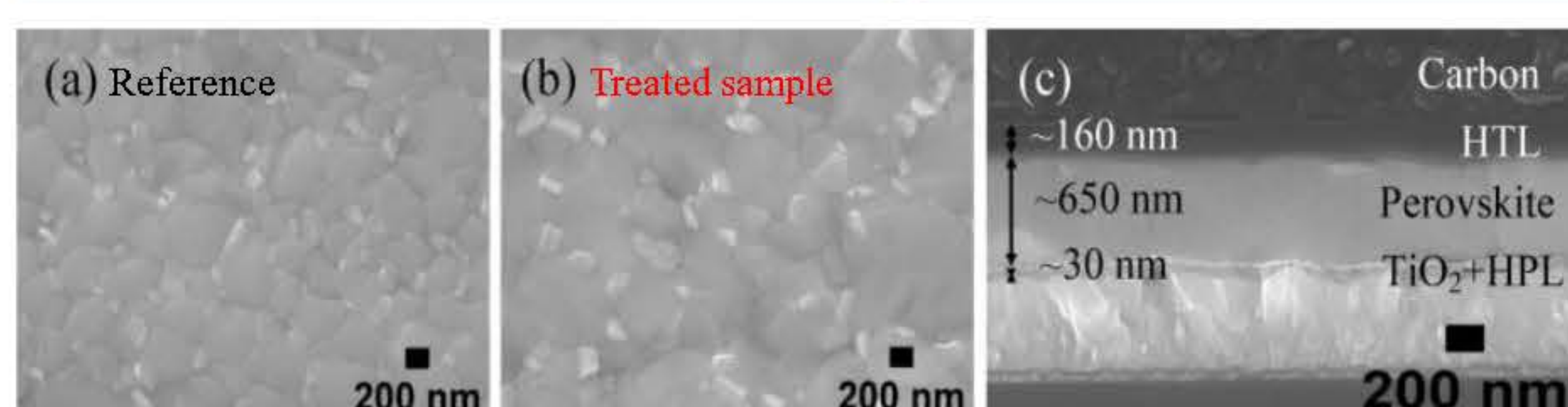


Results & Discussion

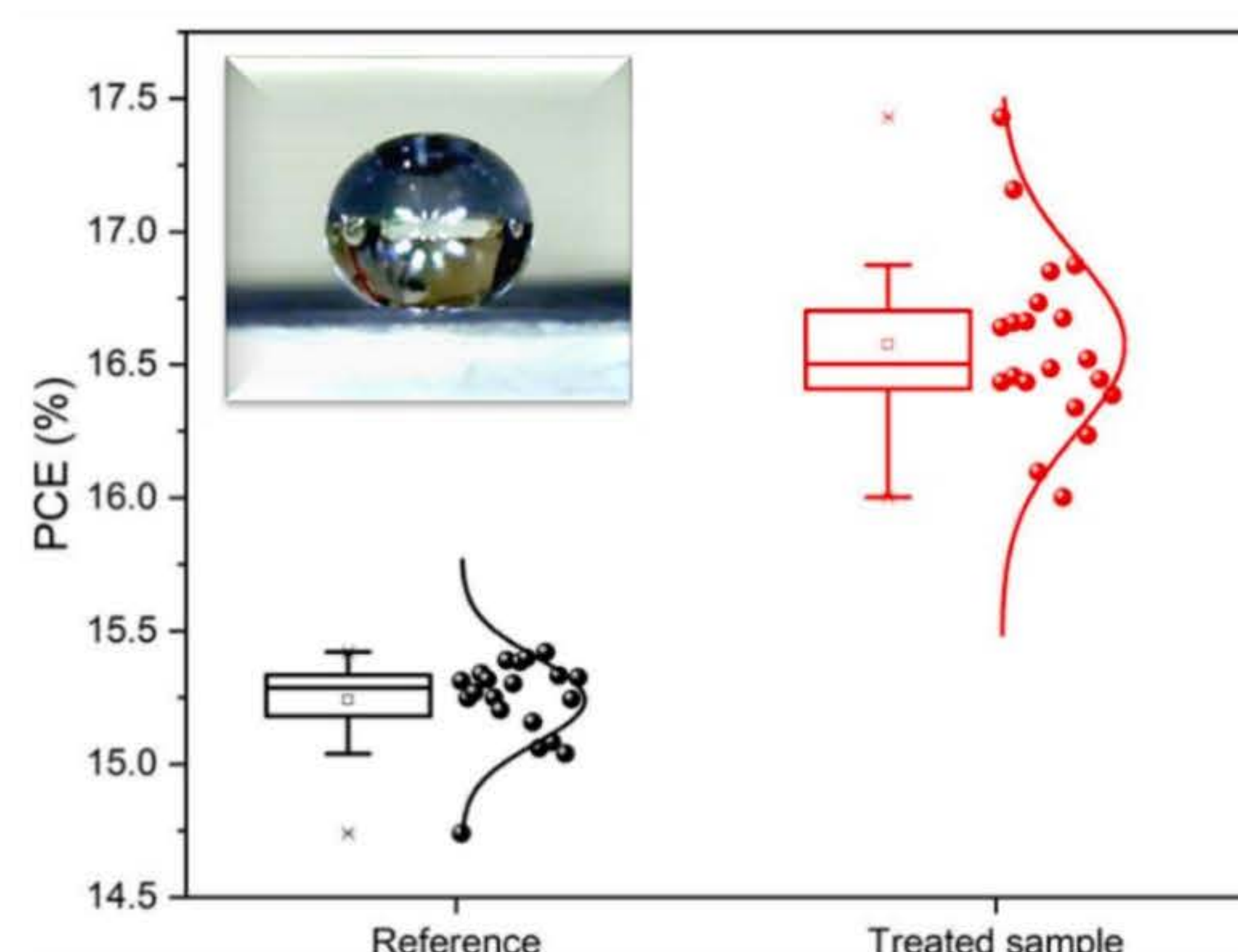
Effects of Passivation

- ✓ By using passivation layers, it is possible to improve the charge-separation and transfer processes.
- ✓ Grain boundaries and traps can be passivated by introducing a passivation layer.
- ✓ A hydrophobic passivation layer (HPL) can protect the active layer against moisture and heat.
- ✓ In our project, both improving in efficiency and sustainability can be achieved by applying a transparent hydrophobic layer on the active layer as a passivation layer.

SEM images

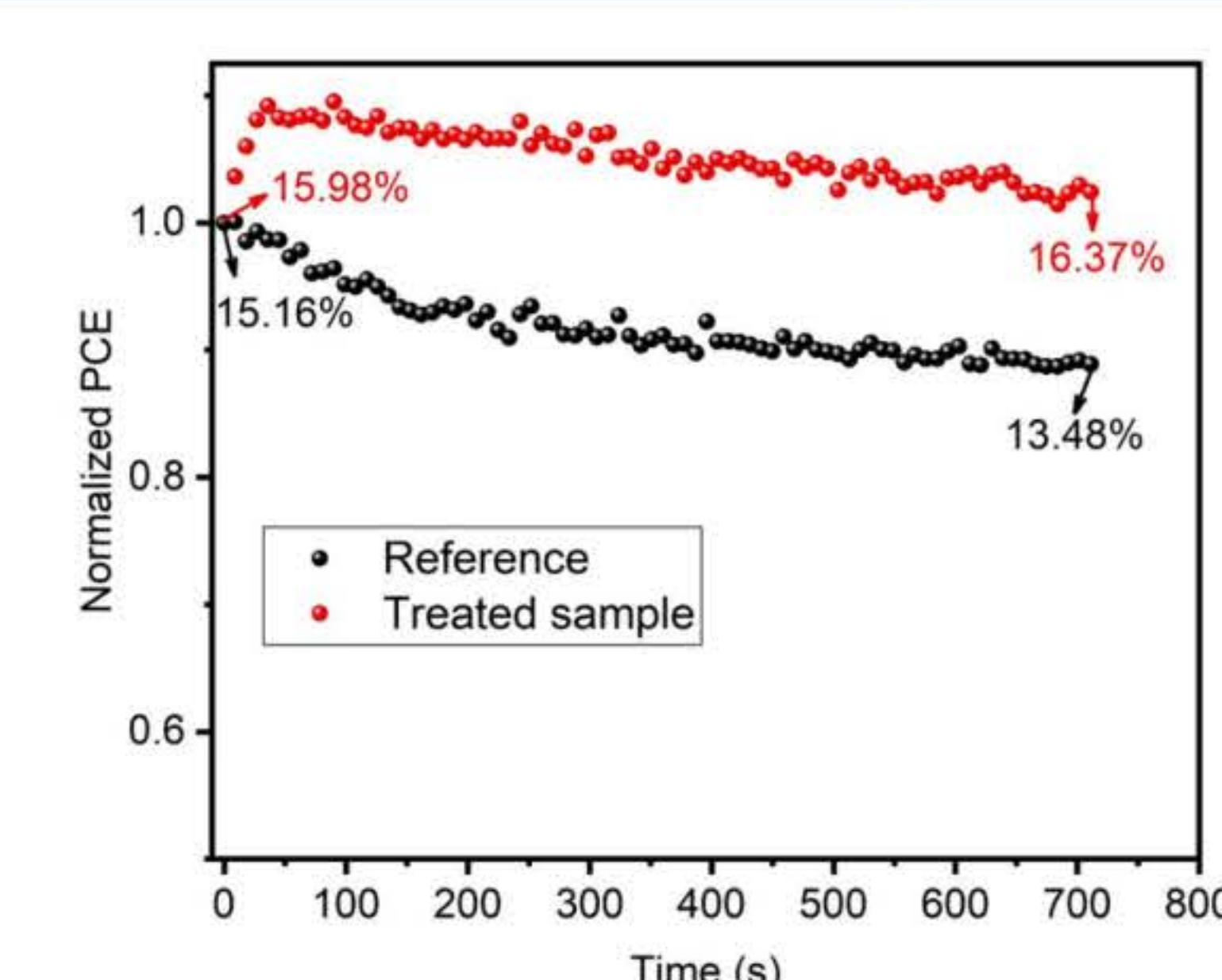


Energy conversion efficiency

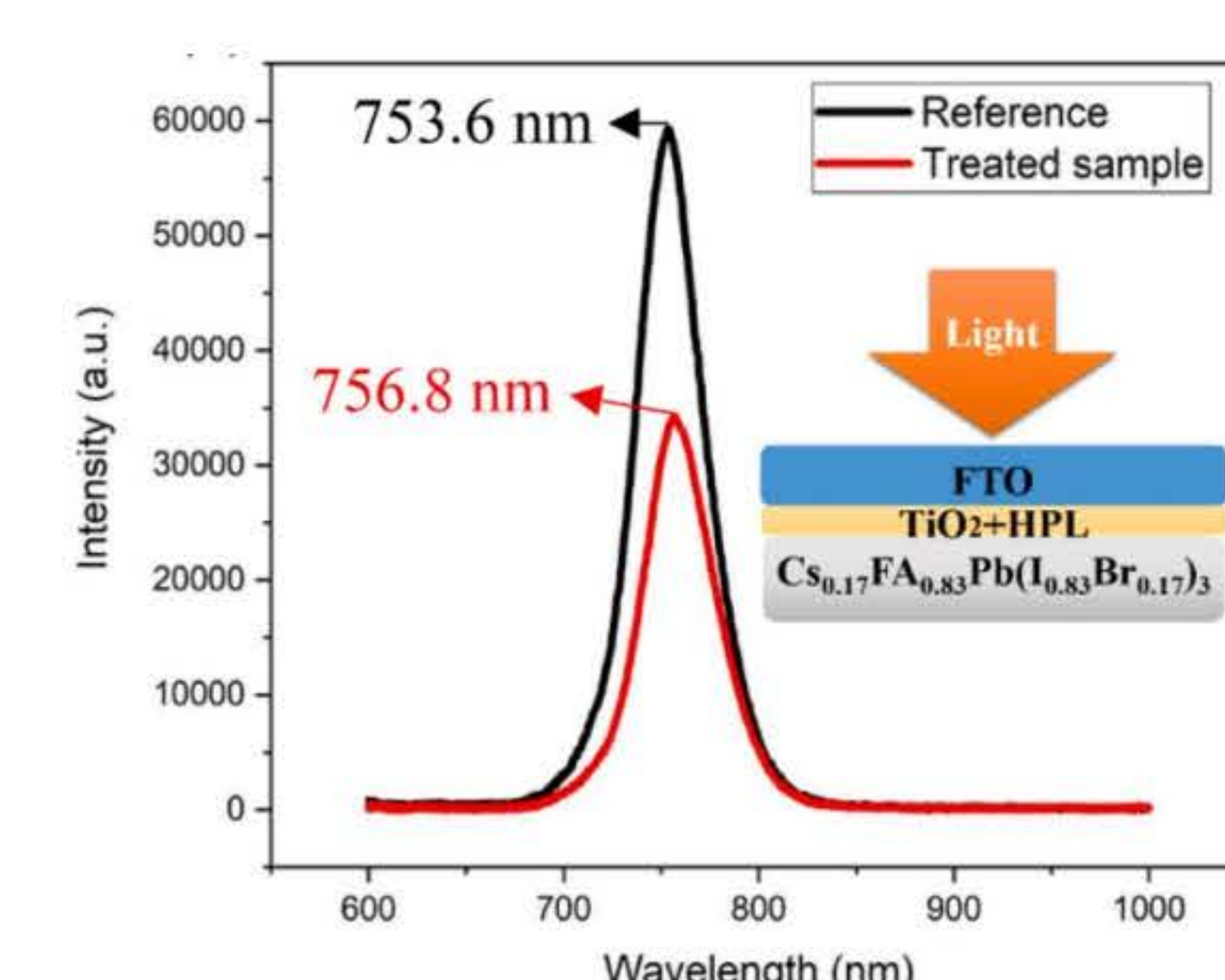


Hydrophobic $-\text{Si}(\text{CH}_3)_3$ groups bonded to the TiO_2 substrate by hydrolysis of silicone rubber evaporation. The champion PCE value of 17.42% was obtained for treated perovskite solar cell device.

Photostability



Photoluminescence analysis



Conclusion

In summary, a cost-effective technique applied a hydrophobic ultrathin film to a perovskite solar cell, yielding a champion PCE of 17.42% with enhanced stability. Ongoing work explores lower-temperature methods, promising advancements for hydrophobic surfaces and the solar cell industry.

Acknowledgements

This research has received funding support from the NSRF via the Program Management Unit for Human Resources & Institutional Development, Research and Innovation [grant number B01F650006].

References

- Abbasi, Sadeq, et al. "A new single-step technique to fabricate transparent hydrophobic surfaces utilizable in perovskite solar cells." *Applied Surface Science* 613 (2023): 155969.
- Abbasi, Sadeq, et al. "Proper annealing process for a cost effective and superhydrophobic ambient-atmosphere fabricated perovskite solar cell." *Materials Science in Semiconductor Processing* 155 (2023): 107241.
- Passatorntaschakorn, Woraprom, et al. "Room-temperature carbon electrodes with ethanol solvent interlacing process for efficient and stable planar hybrid perovskite solar cells." *Energy Reports* 7 (2021): 2493-2500.

Contact Information

Solar Cell Research Laboratory (SCRL)
Faculty of Science, Chiang Mai University
<http://www.physmats.science.cmu.ac.th/scrl/index.php>





BRAINPOWER
CONGRESS 2023

ร่วมกันสร้างและขับเคลื่อนงานวิจัยชั้นแนวหน้า
สู่อุตสาหกรรมแห่งอนาคต



CHIANG MAI UNIVERSITY

KINETICS



attocube
WITTENSTEIN Group

High-temperature superconducting nanocomposite devices based on the Josephson effect and vortex pinning for extremely low-level signal measurement and non-invasive medical diagnostics

Muthukkumar Karthikeyan, Kattaliya Chaipisan and Anucha Watcharaporn*

*Corresponding author: anucha@stanfordalumni.org

Center of Excellence in Quantum Technology, Faculty of Engineering, Chiang Mai University, Chiang Mai 50200, Thailand

Department of Physics and Materials Science, Faculty of Science, Chiang Mai University, Chiang Mai 50200, Thailand

Center of Excellence in Materials Science and Technology, Materials Science Research Center, Faculty of Science, Chiang Mai University, Chiang Mai 50200, Thailand

Problem statement

Developing high-temperature superconducting nanocomposite devices based on the Josephson effect and vortex pinning holds significant promise for extremely low-level signal measurement and non-invasive medical diagnostics. Exploring boron-doped YBCO materials, renowned for their exceptional superconducting properties and suitability for Josephson junction devices, presents a critical gap in comprehensive understanding and optimization. Despite the successful fabrication of YBCO|BNT|YBCO Josephson junctions utilizing Pulsed Laser Deposition (PLD) and the introduction of the novel topological insulator BNT ($\text{Bi}_{0.5}\text{Na}_{0.5}\text{TiO}_3$), challenges persist in fully realizing the potential of this composite system for medical applications. A key problem lies in the need for further research to optimize boron-doping and superconductivity measurement in YBCO materials, as well as the refinement of the YBCO|BNT|YBCO Josephson junction to harness its unique properties for sensitive signal measurement and non-invasive medical diagnostics. Addressing these challenges is essential for advancing high-temperature superconducting nanocomposite devices and facilitating their integration into cutting-edge medical diagnostic technologies.

Methods

Boron-Doped YBCO Material Synthesis:

- Synthesize boron-doped YBCO samples with controlled doping concentrations.
- Employ characterization techniques for structural and superconducting property assessments.

YBCO|BNT|YBCO Josephson Junction Fabrication:

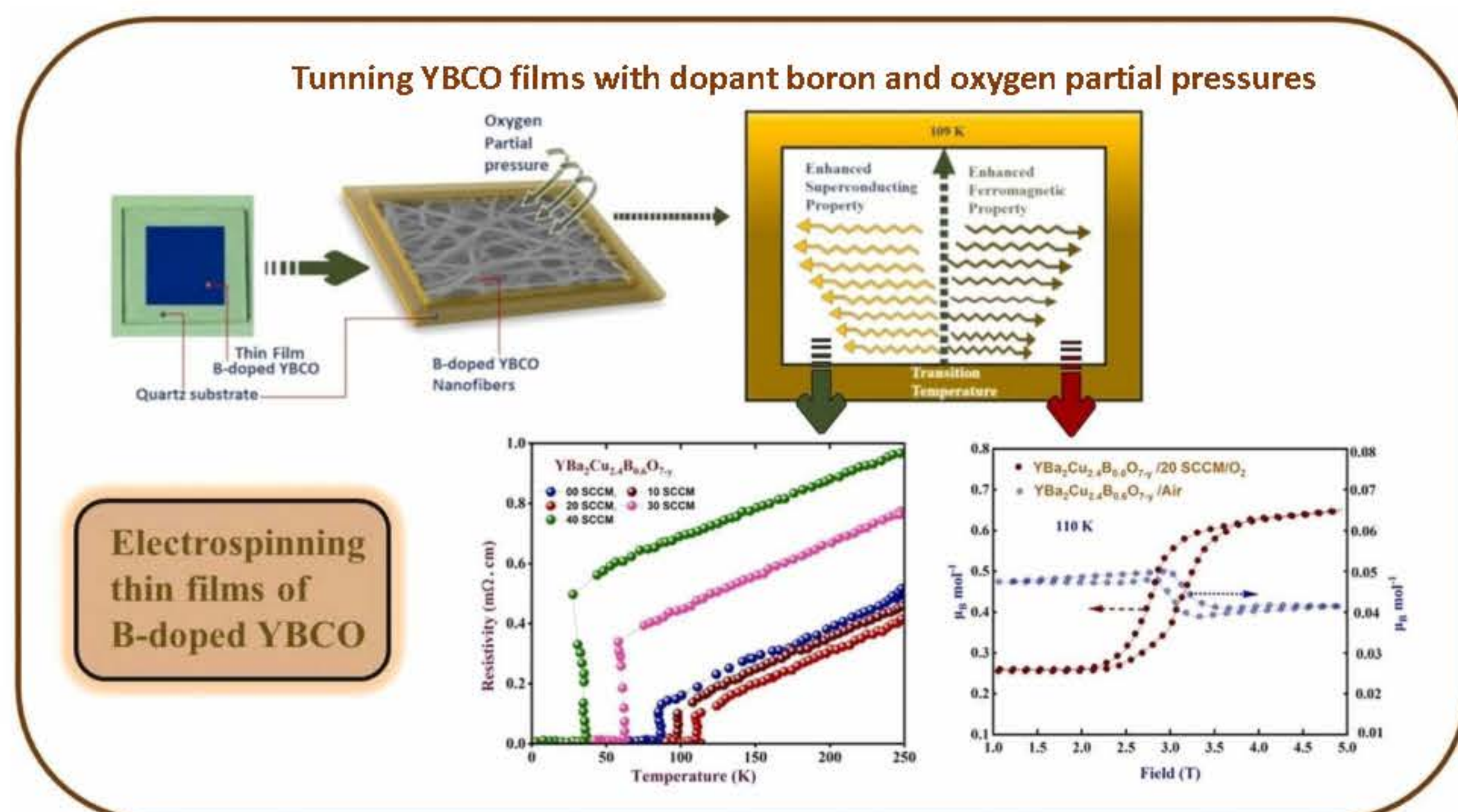
- Use Pulsed Laser Deposition for precise fabrication of YBCO|BNT|YBCO Josephson junctions.
- Optimize layer thicknesses and composition for enhanced electrical and superconducting properties.

Integration into Medical Sensors:

- Integrate optimized Josephson junctions into sensor platforms for low-level signal measurement in medical diagnostics.
- Conduct experiments to evaluate sensitivity and reliability in detecting relevant medical signals.

Results & Discussion

This study establishes a novel pathway for tuning both superconducting and ferromagnetic properties in YBCO thin films through the strategic use of dopant boron and oxygen partial pressure.



Dual Enhancement of YBCO Films:

- Report the simultaneous enhancement of superconductivity and ferromagnetic properties in YBCO films for the first time.
- Achieve dual enhancement through tuning with dopant boron and oxygen partial pressures.

Fabrication Process:

- Electro-spin coat thin films of $\text{YBa}_2\text{Cu}_{3-x}\text{B}_x\text{O}_{7-y}$ with varying B concentrations and oxygen partial pressures.

Systematic Optimization:

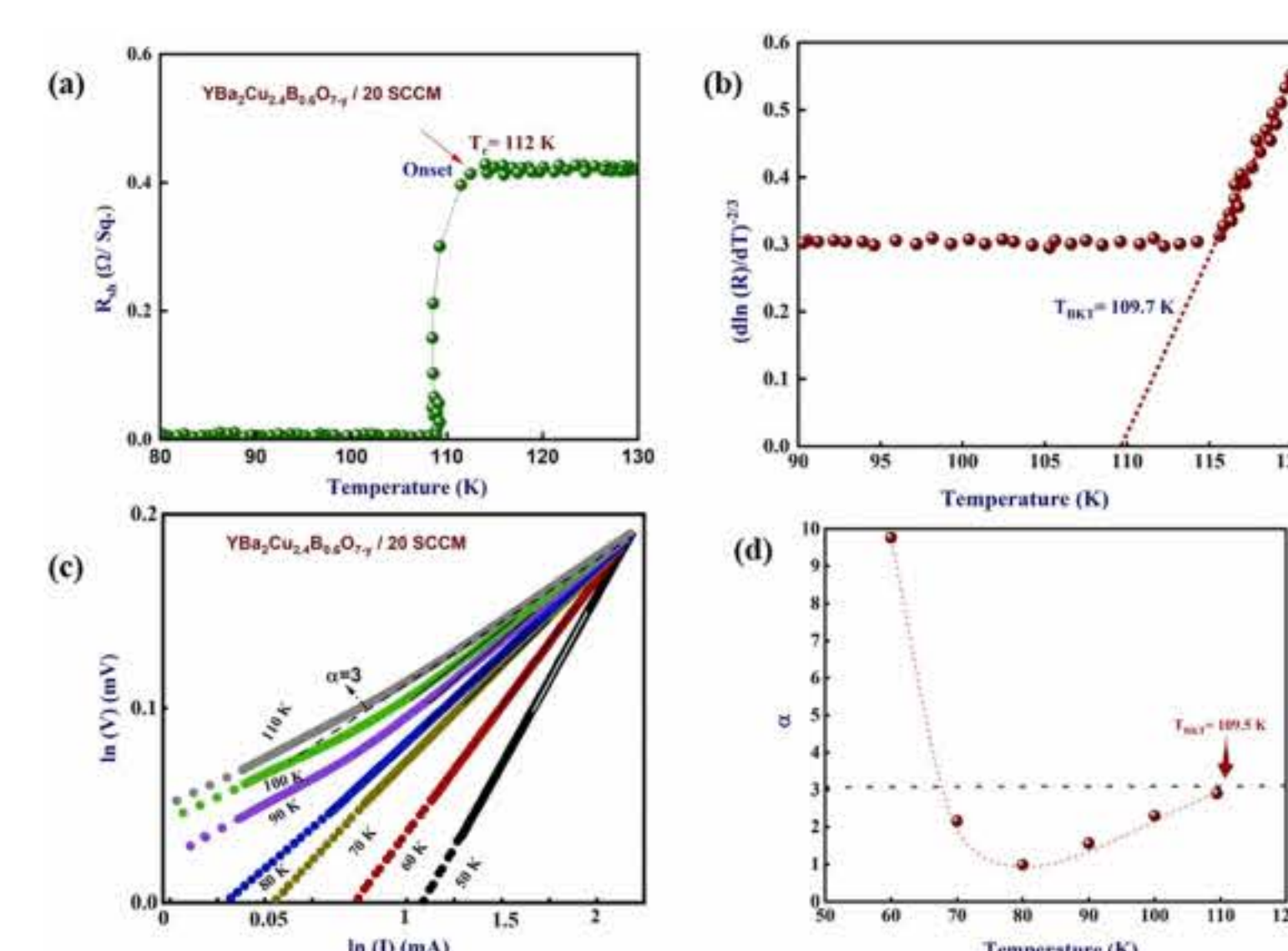
- Study the microstructural, electrical, optical, and magnetic properties to systematically optimize B concentration and oxygen partial pressure in YBCO films.

Optimal Conditions:

- Identify optimal conditions, revealing that a YBCO film doped with 20 mol% B and 20 SCCM O_2 pressure exhibits outstanding superconducting and magnetic properties.

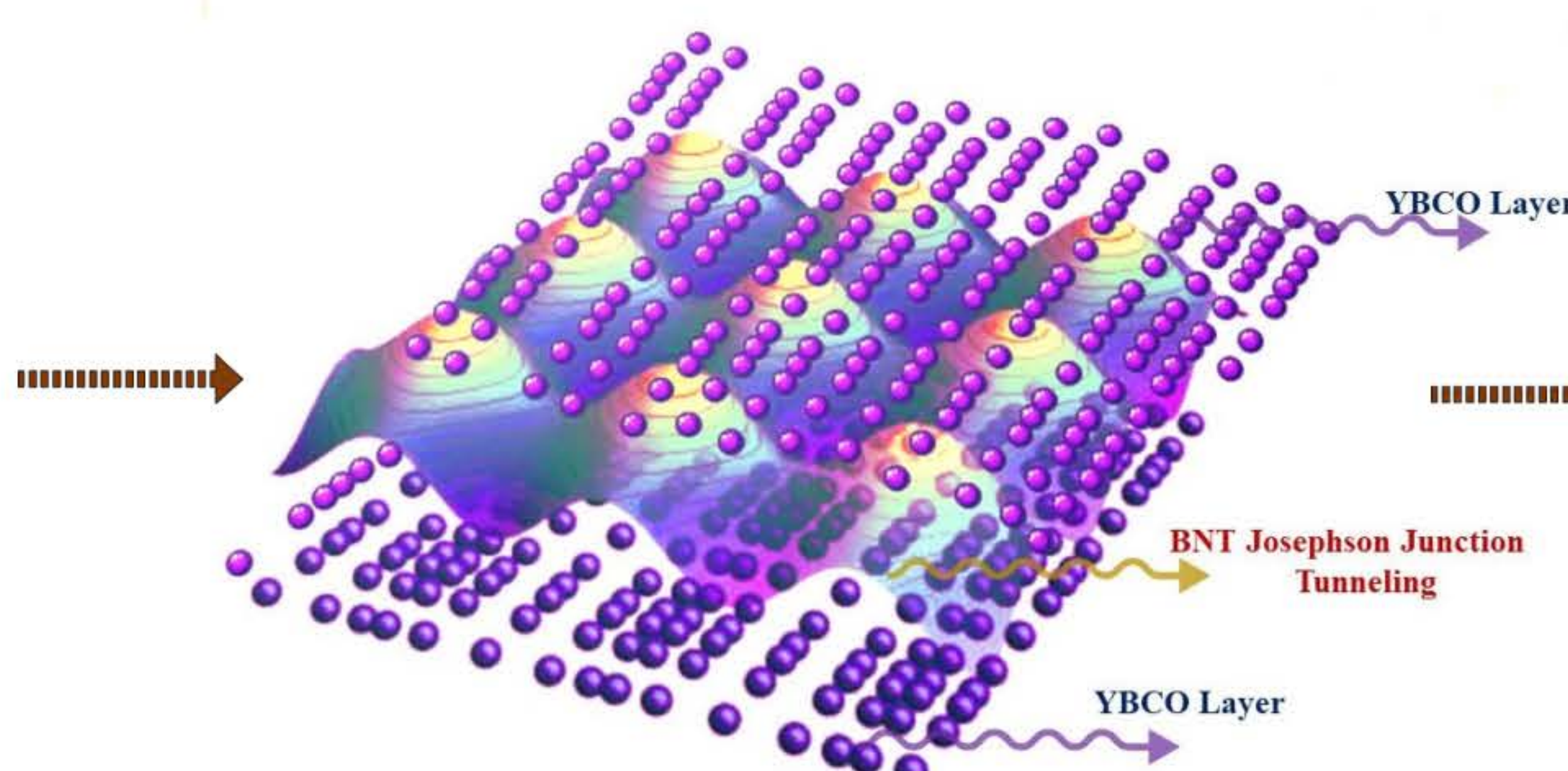
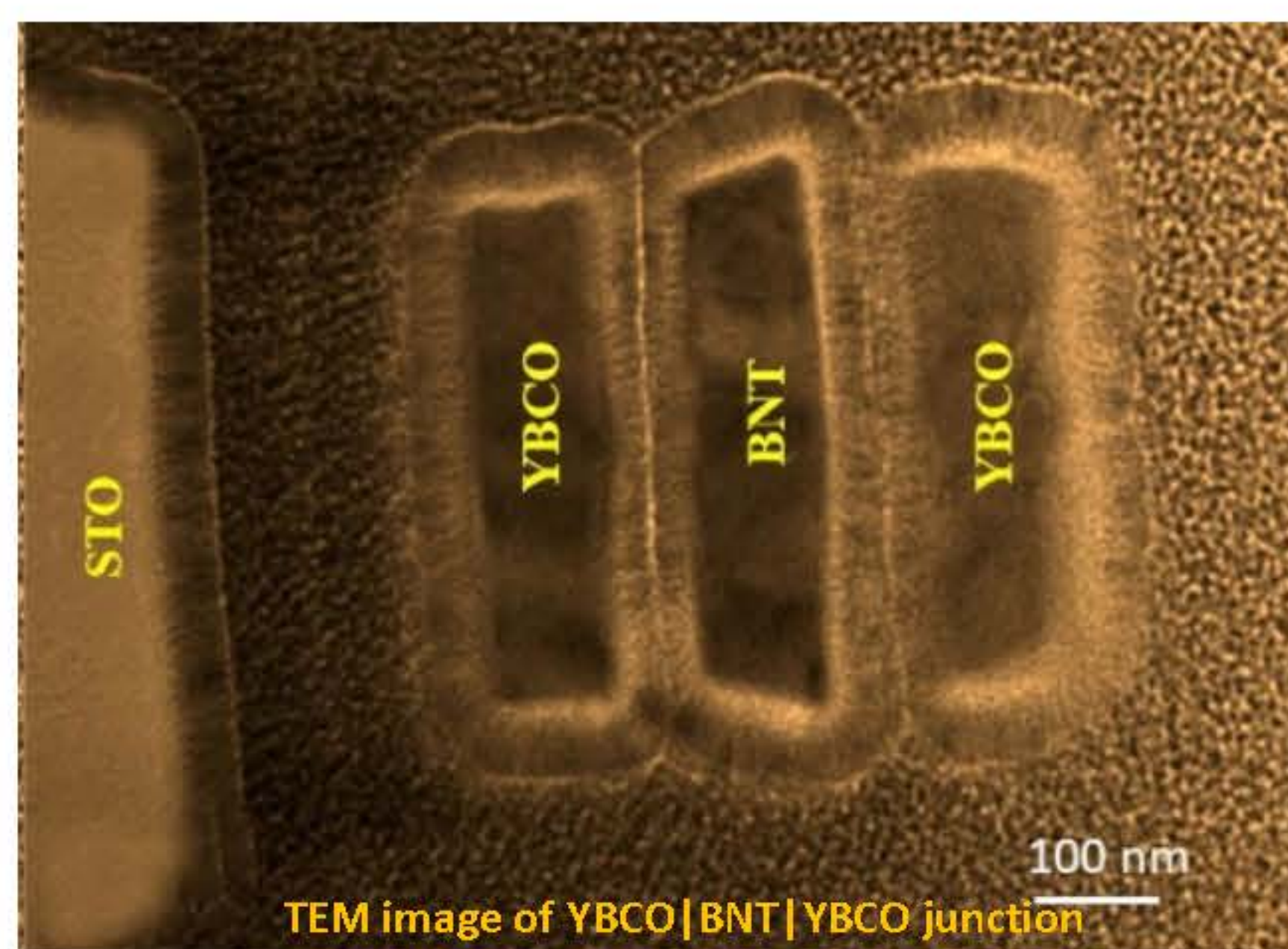
Breakthrough in YBCO Films:

- Highlight the breakthrough in $\text{YBa}_2\text{Cu}_{2.8}\text{B}_{0.2}\text{O}_{7-y}/20$ SCCM films, demonstrating enhanced superconducting and ferromagnetic properties near the transition temperature (T_c) of 109 K.



Low-temperature transport measurement of $\text{YBa}_2\text{Cu}_{2.8}\text{B}_{0.2}\text{O}_{7-y}/20$ SCCM films showing superconducting onset $T_c = 112$ K. (b) the logarithmic plot of (a) for the extraction of T_{BKT} . (c) V-I plots of $\text{YBa}_2\text{Cu}_{2.8}\text{B}_{0.2}\text{O}_{7-y}/20$ SCCM films at different temperatures from black (50 K) to gray (110 K). (d) Exponent α deduced from fitting data in (c) near the transition temperature and T_{BKT} is obtained 109.5 K at $\alpha = 3$.

YBCO-BNT-YBCO sandwiched junctions using the pulsed laser deposition technique



Innovative Junction Design:

- Design and fabricate YBCO-BNT-YBCO sandwiched junctions using the pulsed laser deposition technique, introducing the insulator BNT ($\text{Bi}_{0.5}\text{Na}_{0.5}\text{TiO}_3$) for the first time.

Novel Material Combination:

- Introduce a pioneering approach by combining YBCO with insulator BNT, marking the first instance of such a material combination in this study.

Superconducting Proximity Effect:

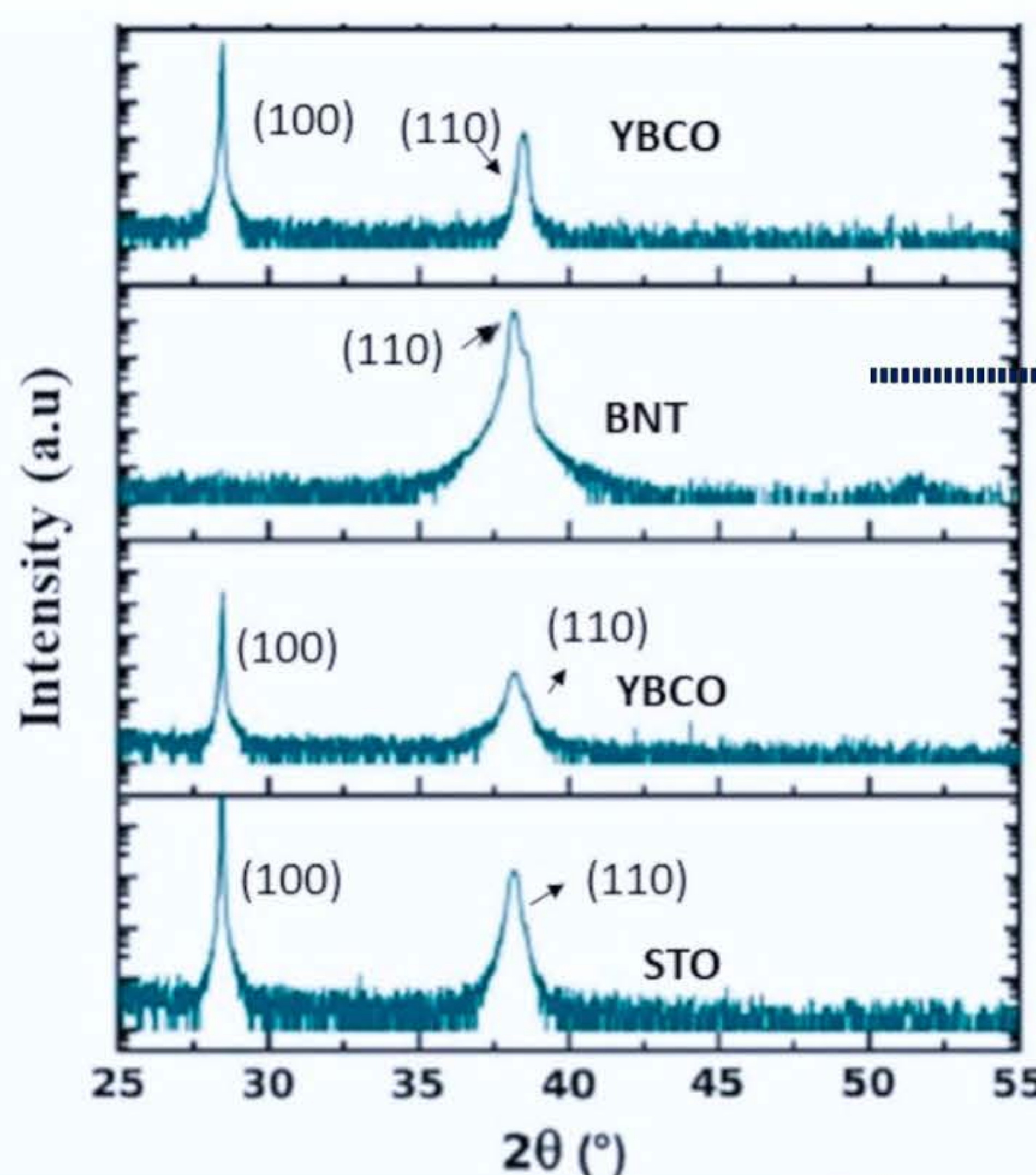
- Conduct comprehensive electron transport measurements at low temperatures, revealing a remarkable superconducting proximity effect between BNT and YBCO.

Josephson Current Formation:

- Observe the establishment of a Josephson current spanning several microns laterally between two YBCO electrodes placed on the BNT surface.

Versatile Platforms for Quantum Phenomena:

- Highlight the potential of these Josephson devices as versatile platforms for exploring phenomena, including the elusive Majorana fermions, with implications for condensed matter physics and quantum electronics.



Precise Preferred Orientation:

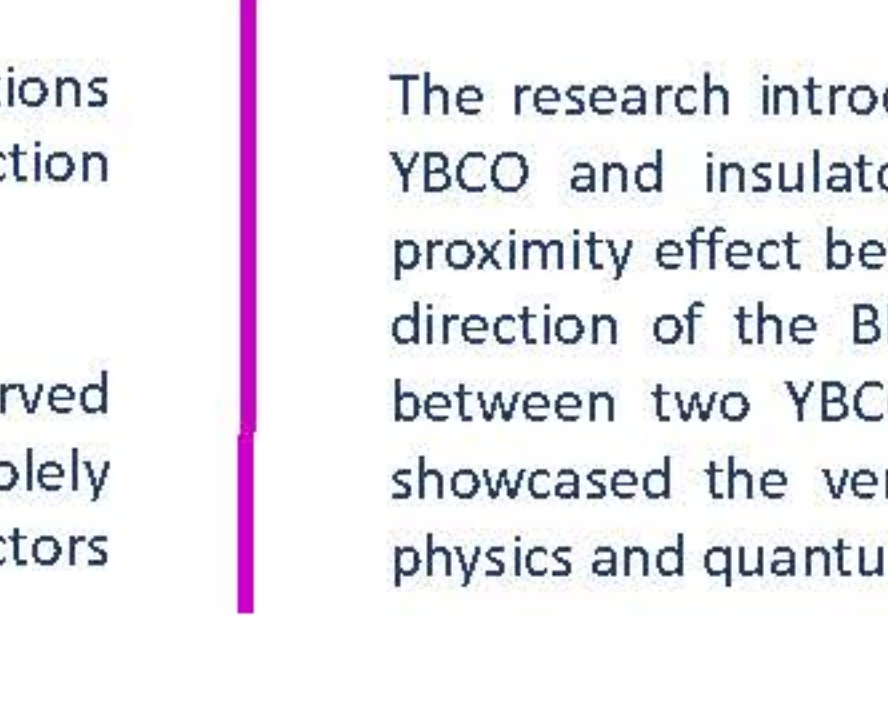
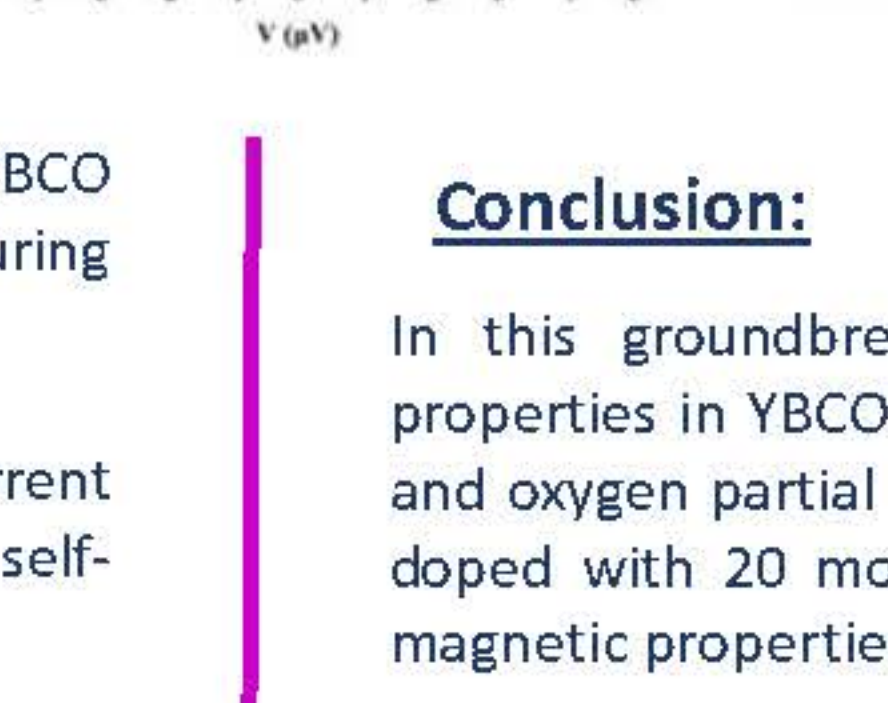
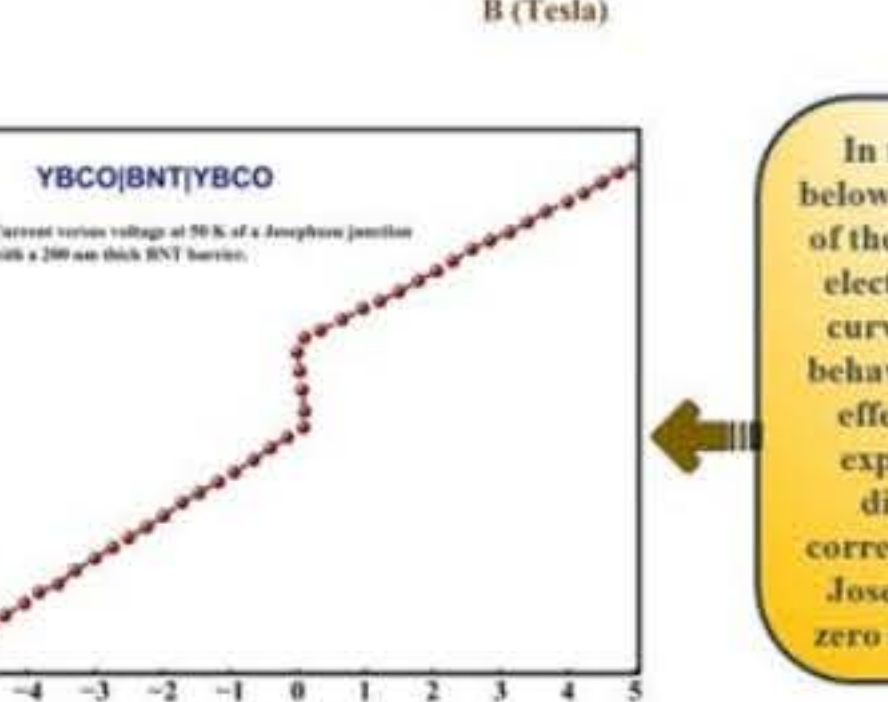
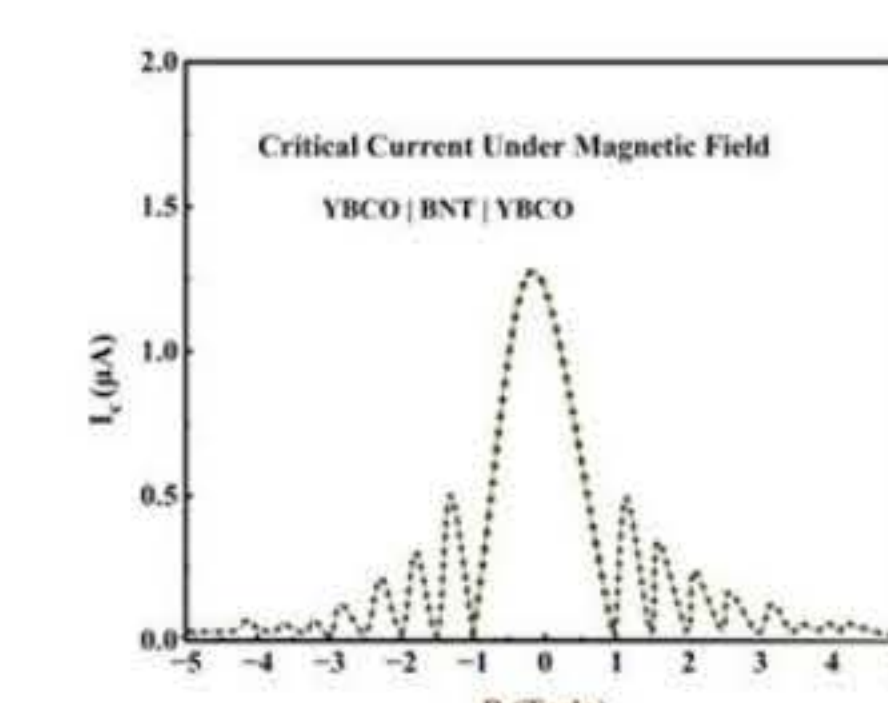
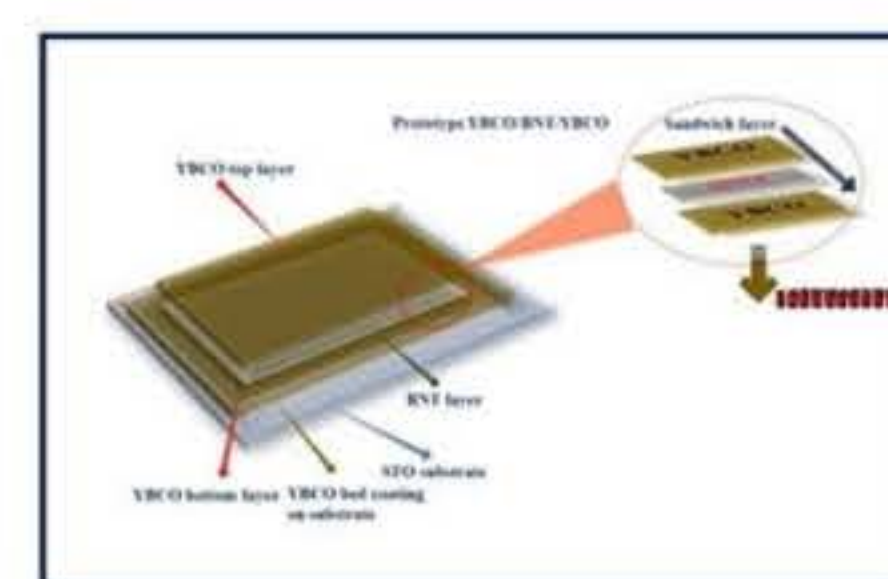
- Investigate the precise preferred orientation behavior of pulsed laser deposition (PLD) films of YBCO/BNT/YBCO on STO substrates, focusing on alignment along the (100) and (110) planes.

Significance for Josephson Junctions:

- Recognize the importance of the observed orientation behavior, especially concerning its implications for the performance and characteristics of Josephson junctions.

XRD Pattern Analysis:

- Utilize X-ray diffraction (XRD) patterns of YBCO/BNT/YBCO on STO to characterize and understand the orientation behavior, providing valuable insights into the structural properties of the film on the substrate.



Conclusion:

In this groundbreaking study, dual enhancement of superconductivity and ferromagnetic properties in YBCO films was successfully achieved through the strategic tuning of dopant boron and oxygen partial pressures. The optimization of YBCO film characteristics, exemplified by a film doped with 20 mol% B and 20 SCCM O_2 pressure, displayed outstanding superconducting and magnetic properties.

The research introduced YBCO-BNT-YBCO sandwiched junctions, pioneering the combination of YBCO and insulator BNT. Notably, the investigation revealed a remarkable superconducting proximity effect between BNT and YBCO, observed as a supercurrent flowing along the thickness direction of the BNT layer. The establishment of a Josephson current in the lateral direction between two YBCO electrodes on the BNT surface and the construction of SQUIDS further showcased the versatile potential of these devices for exploring intriguing condensed matter physics and quantum electronics phenomena.

Acknowledgment

The authors extend sincere gratitude for the partial funding support provided to M K from the National Science and Research Foundation (NSRF) through the Program Management Unit for Human Resources & Institutional Development, Research, and Innovation (PMU-B), Thailand, under Grant Numbers B01F650006 and B05F640218. Additionally, A. W. expresses appreciation for funding and access to facilities provided by Chiang Mai University. These contributions were instrumental in advancing the research and innovation endeavors outlined in this work.



BRAINPOWER
CONGRESS 2023

ร่วมกันสร้างและขับเคลื่อนงานวิจัยชั้นแนวหน้า
สู่อุตสาหกรรมแห่งอนาคต

Inflation from Supersymmetry breaking

Hiroshi Isono (Chulalongkorn University)



collaboration with: Yermek Aldabergenov, Ignatios Antoniadis, Auttakit Chatrabhuti, Rob Knoops

Introduction 1: elementary particles and supersymmetry

supersymmetry makes a pair of spin s and $(s \pm 1/2)$ particles

SUSY invariant theories: invariant under the interchange of the particles in the pair

SUSY pairs

spin 0: Higgs

spin 0: squarks, sleptons

spin 1: photon, W, Z, gluon

spin 2: graviton

spin 1/2: Higgsino

spin 1/2: quarks, leptons

spin 1/2: photino, Wino, Zino, gluino

spin 3/2: gravitino

blue: standard model particles, already found

red: SUSY partner not found

Paired particles have an equal mass, as long as a theory is invariant under SUSY.

BUT, one of the paired particles is not found. Therefore, SUSY must be broken (SUSY breaking), generating mass difference between paired particles.

Q: Does SUSY really exist?

A: Nobody knows. But, for example, string theory, a candidate theory of highest energy scales, naturally possesses it.

Also, Standard Model is not satisfactory: dark matter, baryogenesis, neutrino mass...

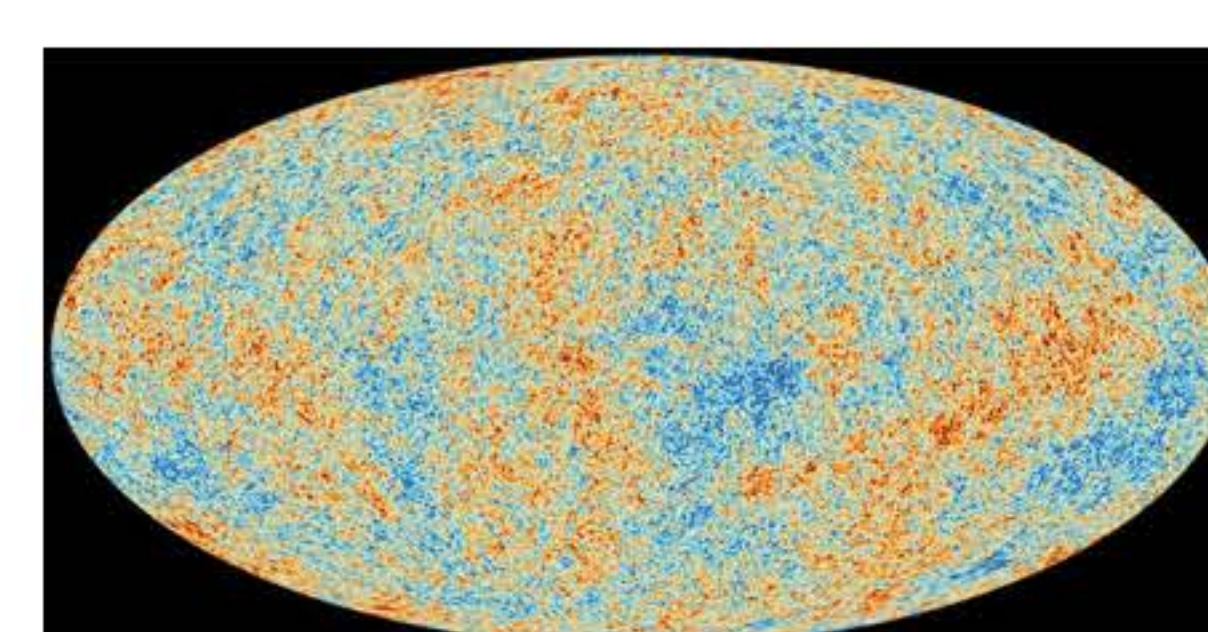
Various models with SUSY have been proposed to resolve these issues

Popular assumption: SUSY exists but is broken at some higher energy Λ_s so does not exist at lower energy scales Λ_{SM} around Standard Model.

Introduction 2: Cosmological inflation

temperature distribution of the universe (Cosmic Microwave Background)

— almost homogeneous, isotropic with tiny but non-negligible fluctuations



(PLANCK satellite, 2018)

Q1: Why so homogeneous in such a giant scale?

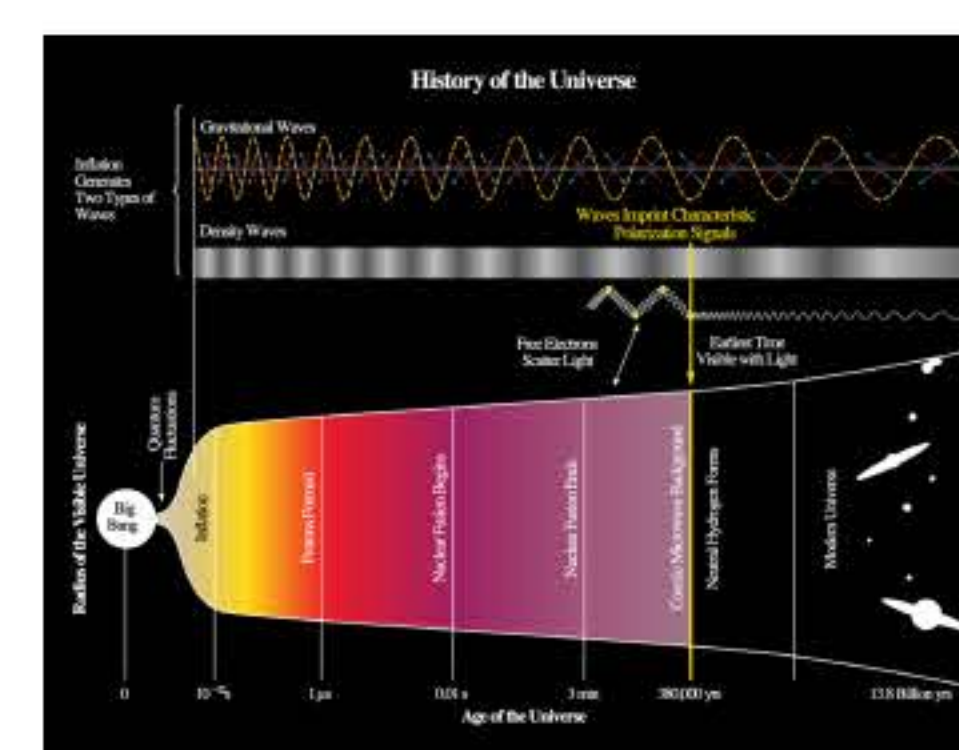
Why is the universe spatially so flat (beyond a horizon scale)?

Q2: What is the origin (seed) of structures like galaxies against such an almost homogeneous universe?

A powerful and promising idea to solve them: inflation period before big bang: very high-energy period $\gg \Lambda_{SM}$: arena for beyond Standard Model

inflation period: energy = - pressure

universe expands exponentially rapidly, so everything is diluted drastically



Q: How is such a situation realised?

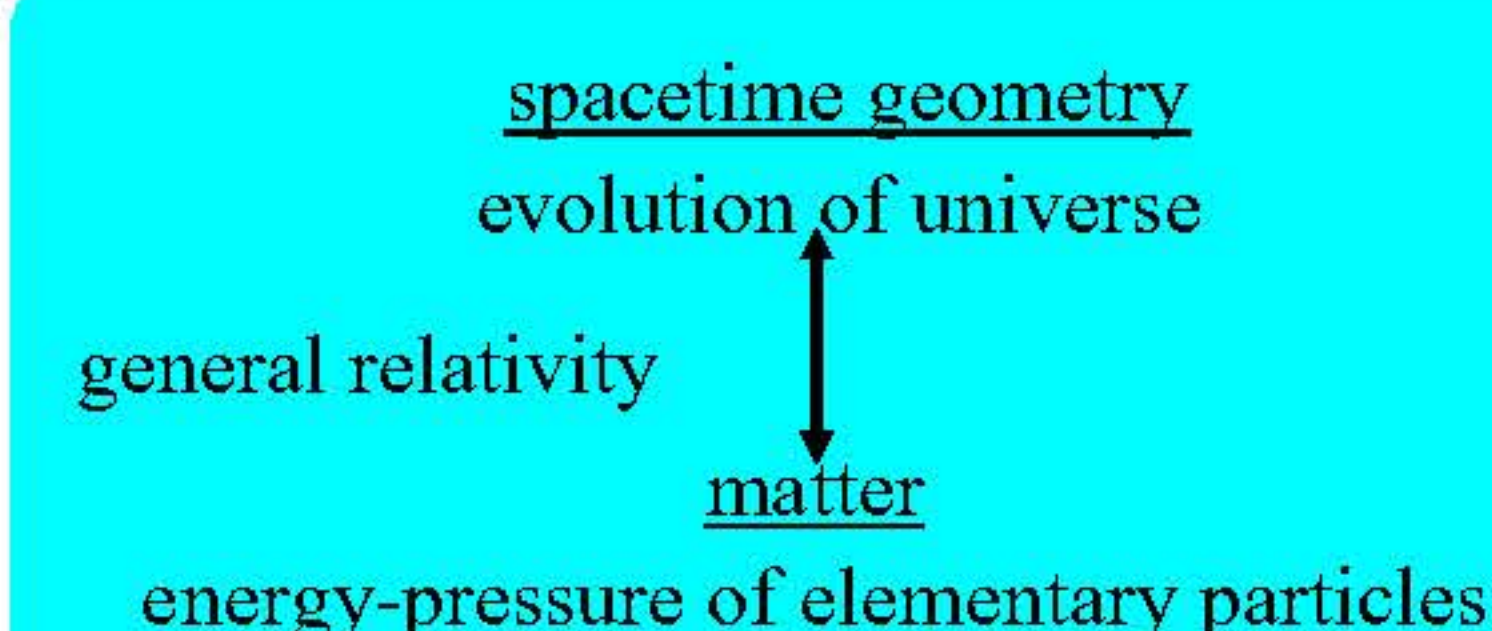
A: Introduce a particle called inflaton.

But, NO such a particle in standard model (see above) has been found.

Another motivation to extend Standard Model

particle physics: physics of spin 0 particle is characterised by scalar potential: energy profile of the particle

To realise energy = - pressure, we can use very flat but rolling-down potential (slow-roll inflation)



Goal

1: realise inflation models in SUSY framework

2: unify cosmological constant, inflation energy scale, SUSY breaking scale in a single model

cosmological constant: confirmed by the expansion of the current universe, but no consensus about WHY from the particle physics point of view

One striking feature of our goals: relate the inflation scale with SUSY breaking scale: relating two scales in different sectors

Method

cook up the scalar potential for the inflaton using machinery of SUSY

machinery of writing down potentials has been established, so we are free to apply it.

1. give a list of particles including inflaton (jargon: supermultiplets describing the SUSY pairs).
2. give characterising functions (jargon: Kahler potential, superpotentials, w/o gauge kinetic function).
3. write down a theory with a scalar potential for inflaton, following the rules and machinery of SUSY.

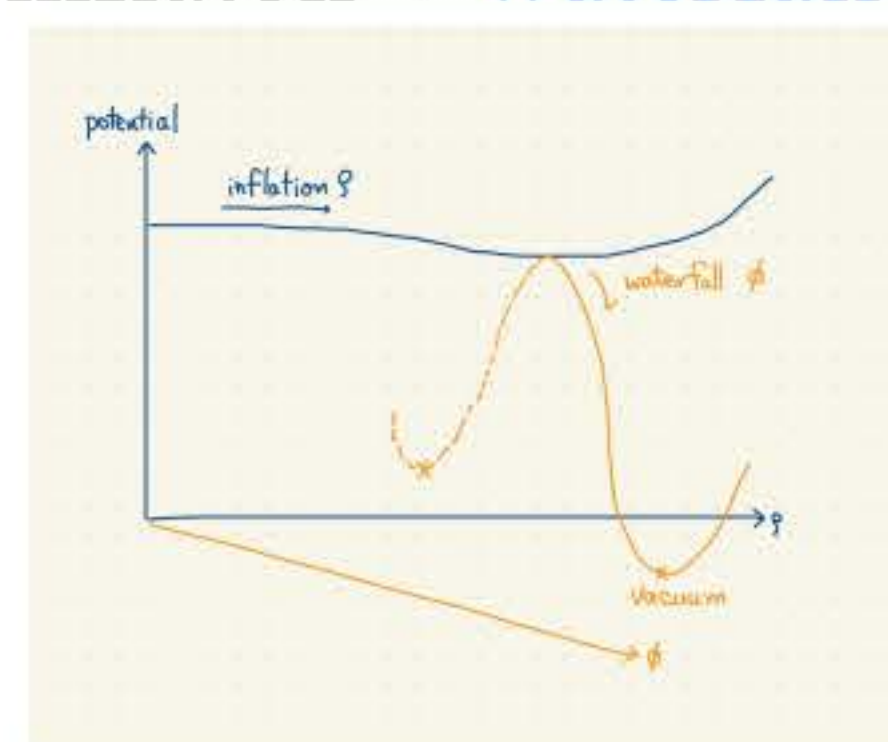
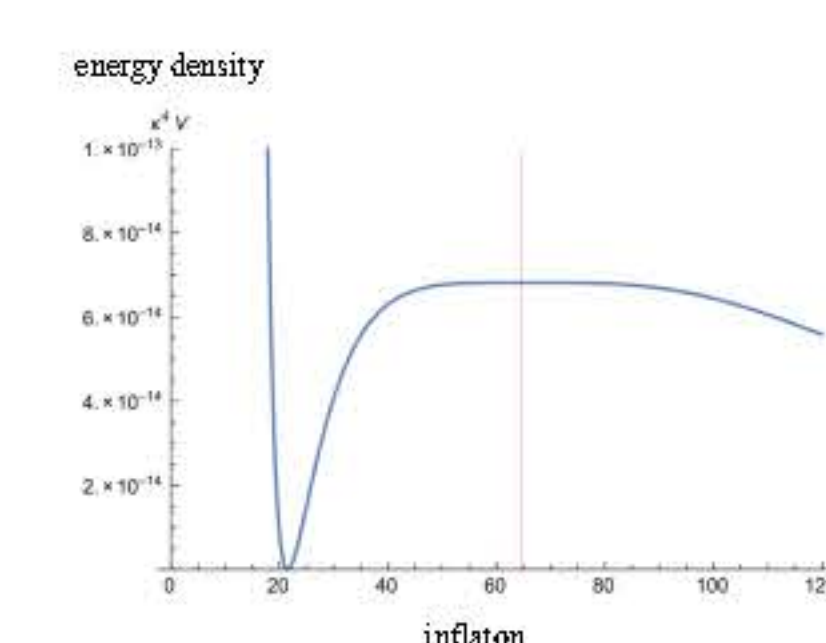
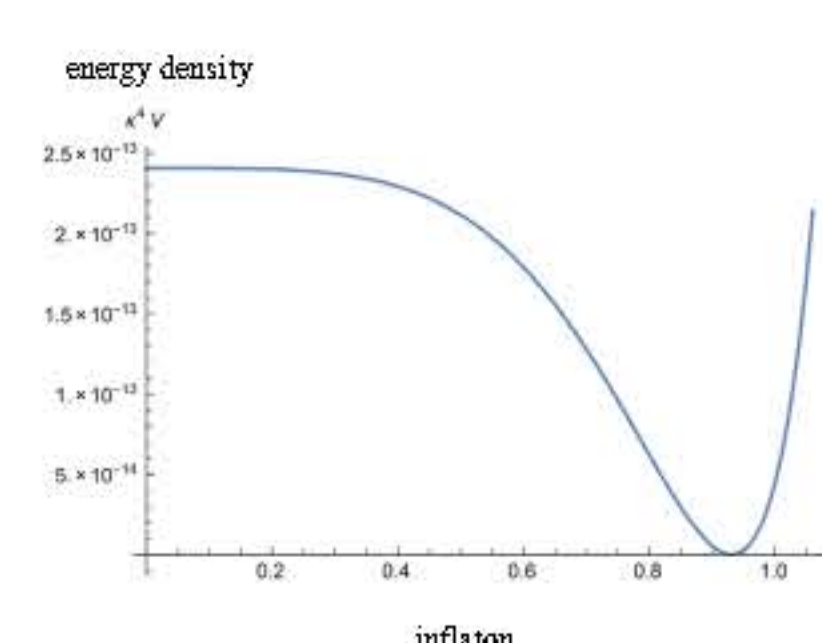
Results

We have proposed various types of inflaton potentials.

— coupling with Standard Model, computing reheating temperature etc.

[arXiv: 1608.02121, 1706.04133, 2009.02233, 2103.11217] (All of them have been published in Q1 journals.)

We are working on the following potential: inflaton + waterfall



Future direction as Concluding remarks:

combine the models with Standard Model relation with gravitational wave physics? relation with dark matter? ...

Acknowledgement

This research has received funding support from the NSRF via the Program Management Unit for Human Resources & Institutional Development, Research and Innovation [grant number B01F650006 and B05F650021].



BRAINPOWER
CONGRESS 2023

ร่วมกันสร้างและขับเคลื่อนงานวิจัยชั้นแนวหน้า
สู่อุตสาหกรรมแห่งอนาคต



De Sitter Universe from anti-de Sitter fluctuations

Anxo Biasi, Oleg Evnin, Spyros Sypsas

Physical Review Letters, 129 (2022) 251104 (editors' suggestion)

- De Sitter space describes the beginning and the current asymptotic geometry of our Universe but it is very hard to obtain de Sitter space as a solution of a fundamental theory (e.g., string theory, supergravity)
- Anti-de Sitter space (negative cosmological constant) is easier to obtain but unstable
- Regular black holes (objects with horizon but no singularity at the center) are expected in quantum gravity

We put together these three seemingly unrelated subjects in a 4D gravitational theory with spherically symmetric scalar matter: $\Psi(r)$

$$S = \frac{1}{2} \int dt dr \sqrt{g} [XR - U(X)\partial X^2 - 2V(X) - h^2(X)\partial\Psi^2],$$

We choose the model such that it has asymptotic AdS solutions and regular black hole solutions that mimic de Sitter space:

$$V(r) = -\frac{1}{2} \left(1 + 3k^2 r^2 - \frac{2\mu^3}{r^3} \right), \quad U(r) = -r \frac{r^3 - 2\mu^3}{(r^3 + \mu^3)^2} X(r) = \frac{r^2}{2} - \frac{\mu^3}{r}, \quad h(X(r)) = r$$

We then evolve numerically the eom: we give small quantum fluctuations to the scalar field (initial conditions), these grow due to AdS instability and collapse to regular BH

$$T_{\mu\nu}(X) + T_{\mu\nu}(\Psi) = 0,$$

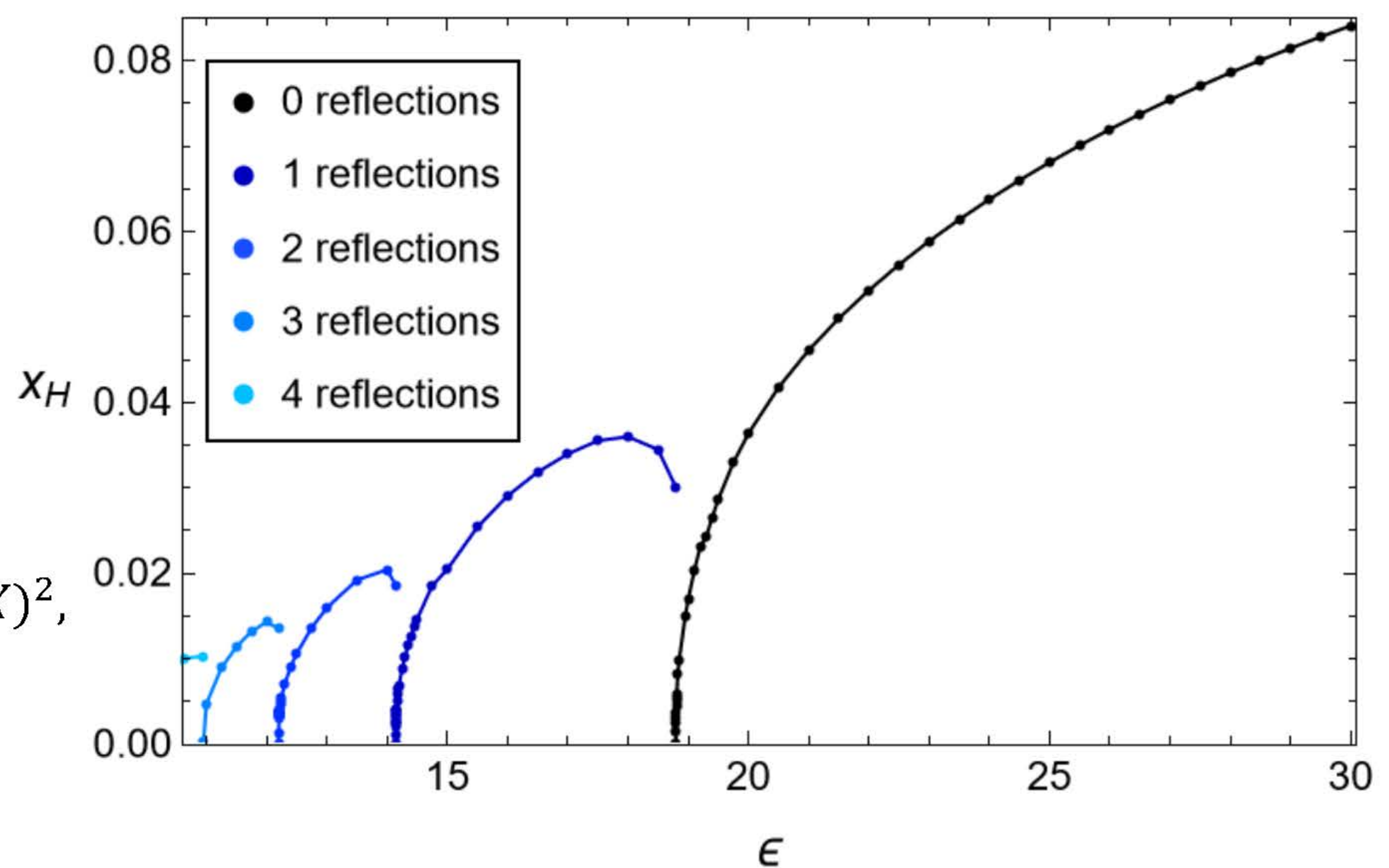
$$V_X + 2UV - \frac{1}{2} \partial_X U (\partial X)^2 + 2h \partial_X h (\partial\Psi)^2 = \frac{1}{2} R,$$

$$\nabla_\mu (h^2(X) \partial^\mu \Psi) = 0$$

with

$$T_{\mu\nu}(X) = \nabla_\mu \partial_\nu X + g_{\mu\nu} V + U \partial_\mu X \partial_\nu X - \frac{1}{2} g_{\mu\nu} U (\partial X)^2,$$

$$T_{\mu\nu}(\Psi) = 2h^2 \partial_\mu \Psi \partial_\nu \Psi - g_{\mu\nu} h^2 (\partial\Psi)^2$$



An example of how to dynamical generate a bubble that looks like our Universe but can be embedded in a fundamental theory

Follow-up research: how a regular BH attains a vacuum configuration? This is currently under investigation using an effective theory of Hawking radiation to drain the matter out of the BH and end up with a vacuum regular BH

This research has received funding support from the NSRF via the Program Management Unit for Human Resources & Institutional Development, Research and Innovation [grant numbers B01F650006, B05F650021]